Minimally Invasive Diagnostic Imaging using High Resolution Optical Coherence Tomography

by

Paul R. Herz

B.S. Engineering Physics, University of California at Berkeley (1995)
M.S. Electrical Engineering, Massachusetts Institute of Technology (2000)

Submitted to the Department of Electrical Engineering and Computer Science in Partial Fulfillment of the Requirements for the Degree of

Doctor of Philosophy

at the

Massachusetts Institute of Technology

August 2004

[September 2004]

Signature of Author: _____
Department of Electrical Engineering and Computer Science
August 10, 2004

Certified by: _____
James G. Fujimoto, Professor of Electrical Engineering
Thesis Supervisor

Accepted by: _____
Arthur C. Smith, Chairman, Committee on Graduate Students

Minimally Invasive Diagnostic Imaging using High Resolution Optical Coherence Tomography

by

Paul R. Herz

Submitted to the Department of Electrical Engineering and Computer Science August 10, 2004
in Partial Fulfillment of the Requirements for the Degree of
Doctor of Philosophy in Electrical Engineering

Abstract

Advances in medical imaging have given researchers unprecedented capabilities to visualize, characterize and understand biological systems. Optical Coherence Tomography (OCT) is a high speed, high resolution imaging technique that utilizes low coherence interferometry to perform cross-sectional tomographic imaging of tissue in real time and *in vivo*. The design, development, and implementation of ultrahigh resolution OCT systems in both laboratory and clinical experiments has been pursued in this work. Biomedical imaging studies in the areas of arthroscopy, cardiology, and endoscopy have been investigated with ultrahigh resolution capability achieved through the use of broadband femtosecond oscillators such as Ti:Sapphire and Cr:Forsterite light sources. OCT image resolutions of 1-5um in tissue have been realized, an order of magnitude greater than conventional MRI or ultrasound resolutions. In addition, through the use of coherent heterodyne detection techniques, the capability to visualize pathological tissue architecture *in vivo* for both animal and human experimental trials has been demonstrated. Because OCT can perform such "optical biopsy" with resolutions approaching that of conventional excisional biopsy and histology, it has the potential to become a powerful diagnostic tool in the field of medical imaging. In combination with small fiber-optic catheters, endoscopes, and other imaging devices, minimally invasive OCT imaging was carried out with novel diagnostic devices also developed in this work. The development and implementation of advanced OCT systems for both research and clinical applications will be presented as well as future directions for the technology.

Thesis Supervisor: James G. Fujimoto
Title: Professor of Electrical Engineering and Computer Science

Acknowledgments

And now for the most important part of the thesis.

To Professor James Fujimoto for providing me with the opportunity to complete this work using the extensive resources of the ultrafast optics lab at MIT. For demanding the highest level of excellence from me so that I could set higher standards for myself both personally and professionally.

To Mathew Varghese, a friend who is like a brother to me and whom I have had the great fortune of knowing for almost 15 years now. Your intelligence, enthusiasm, and strength of character are constant sources of inspiration. And also to his incredible wife Sharon Francis for whom I have the greatest respect and admiration.

To Dario Gil, for your wisdom, depth, and insight into human nature. Our engaging conversations late into the night and your wonderful family in Spain constitute some of my best memories from MIT.

To Rajesh Menon, for your companionship and integrity as well as for showing me how to stay light-hearted in the face of adversity.

To Euclid Moon, for your perpetual good humor and even better nature. You can call on me anytime to take more roadtrips together with you and the iPod.

To Tayo Akinwande, an incredible mentor and advisor from my tenure in the Microsystems Technology Laboratory. Your kindness, generosity, and fairness as an advisor are unparalleled.

To David Pflug, a great colleague and my best office mate out of all my years here. Congratulations and best wishes for you, Patricia, and the new baby.

To Fred Cote and Toby Bradshaw, for teaching me how to shape and weld metal in my copious free time. I hope to continue machining, forging, and avoid blowing up any more acetylene torches.

To Thomas Feurer, for inspirational experiments in the laser lab and many good chats over bad coffee.

To Phil Baddour, my constant friend since elementary school. I promise you won't have to drive across the country again or fight off any more strange animals in Africa. Thanks for always being there.

To Yohei Sato, for many good memories from our time in Tokyo, San Francisco, New York, and Boston.

To my co-workers in the lab and collaborators in the hospital, it was an amazing experience working together and I was privileged to have had you as friends and colleagues.

To my wonderful extended family in Cape Town and Harare, you are always in my heart and mind and I will be back to see you all soon.

Finally to my mother and sister, without your love and support none of this would have been remotely possible.

Dedication

This work is dedicated to my mom and sister, who have both taught me about the most important things in life.

Contents

Chapter 4. Delivery Systems and Minimally Invasive Diagnostics

Chapter 5. Biological Imaging in Animal Models

Chapter 6. Clinical Imaging in Humans

Chapter 7. Conclusion

List of Figures

Chapter 4. Delivery Systems and Minimally Invasive Diagnostics

Chapter 5. Biological Imaging in Animal Models

Chapter 6. Clinical Imaging in Humans

Chapter 1 – Introduction

Motivation

Over the past 50 years, medical imaging has become one of the most powerful investigative tools in both the clinical and laboratory environment. It has provided doctors and researchers not only with unprecedented capability to explore and characterize biological processes, but has also allowed them to diagnosis and treat a wide variety of medical conditions. The key metric of any imaging technology is its ability to *visualize* a system or process of interest. Whether the technique uses optical, acoustic, magnetic, or mechanical energy, the most relevant question to address is if the imaging method allows the visualization of a process that is of clinical relevance or scientific interest. For the field of medical diagnosis and in particular medical imaging, the ability to visualize biological processes can allow for both the understanding and treatment of disease states.

At the heart of an imaging technique is the radiation source that provides a signal which interacts with the system under investigation. In the area of optical imaging, the use of electromagnetic radiation has allowed the development of a diverse range of powerful technologies to visualize biological processes. The simple light microscope has been in use since the 18th century and has played a critical role in the fields of biology and medicine. The development of the laser in the past century enabled major advances in several fields and its use in the medical arena has been demonstrated in applications ranging from tissue ablation and photorefractive surgery [1, 2] to multiphoton, fluorescence, and confocal microscopy [3-5].

Imaging techniques using radiation outside of the visible spectrum have also advanced the field of medical imaging in leaps of technological achievement. The use of x-rays allowed for the first time full-body imaging and material characterization. Imaging technologies such as computed tomography and magnetic resonance imaging with increased capabilities are routinely used in hospitals today [6]. Despite these advances however, few optical imaging techniques in use today take advantage of the many physical properties of light. Even systems that employ lasers as light sources use them primarily as a source of illumination for image recording or as a tool for localized heating of a specific tissue. By utilizing the more fundamental properties of light such as coherence, polarization, and spectral information, there exists a much greater potential to make advances the field medical imaging. These advances can in turn have profound impact in areas of fundamental research as well as in clinical environments where diagnostic imaging is used. Optical Coherence Tomography (OCT) is a relatively new imaging technology

that uses the coherence properties of light to generate cross-sectional or three-dimensional images of tissue samples [7]. Visualization of tissue architecture with near micron-level resolution is possible. OCT can also use the spectral and polarization characteristics of light radiation to visualize additional characteristics of the biological systems under investigation such as and spectral [8, 9], absorption [10, 11], and birefringence properties [12, 13]. With it's capability to image biological specimens at high resolution with minimally invasive diagnostics, OCT has the potential to be an important imaging technology in several areas of biomedical research.

Background

OCT has its origins in optical time domain reflectometry (OTDR), a temporal analog to OCT where the time-of-flight delay of optical pulses is measured for optical ranging within a medium. While initially used for fiber-optic and network component fault analysis [14], the potential for biological applications was soon recognized and demonstrated in the cornea and other biological tissues [15-17]. Further advances in the area of optical time domain reflectometry led to the development of optical coherence domain reflectometry (OCDR), a one dimensional optical ranging technique that had its foundations in white-light interferometry. OCDR uses a low coherence light source to create an interference signal from a sample and reference arm in a Michelson interferometer configuration. Initial work using OCDR for waveguide characterization showed high dynamic ranges (>100 dB) and spatial resolutions on the order of 10um-60um [18-21]. Studies involving the eye [22-25] and other turbid medium [26, 27] soon followed and demonstrated the efficacy of the technique for imaging biological tissue. As work continued, the capability of OCDR was increased to enable two-dimensional scanning of the eye [28, 29] and was subsequently renamed optical coherence tomography (OCT). The application of OCT for both research and clinical purposes has been demonstrated for many biological systems with applications in ophthalmology [30, 31], endoscopy [32, 33], coronary disease [34-36], orthopedics [37, 38] and developmental biology [39, 40] to name a few. The scientific and medical potential for OCT is very promising as it enables a new imaging technique to investigate and characterize biological systems in real time and at high resolution.

Imaging Modalities

A broad spectrum of diagnostic imaging technologies exist today which are in use for biomedical applications. Several important factors must be taken into consideration when determining which imaging technique may be best suited for a given biological system or

diagnostic purpose. Immediate and obvious constraints such as patient or sample exposure limits, required resolution, imaging depth (sample penetration), safety concerns, physical dimensions of the system, and device delivery must be recognized and defined in order to choose the most appropriate technology. Other concerns such as portability, cost, complexity, reliability and accuracy must be considered as well.

Illustrated in Figure 1-1 is a plot of image resolution versus penetration depth for several diagnostic imaging technologies that are currently used in clinical and research environments. As can be seen, OCT has a unique capability in that it can achieve micron level resolution while maintaining depth penetration of several millimeters in biological samples. While the penetration depth is significantly lower when compared to MRI or X-ray techniques, these length scales are optimal for the imaging and diagnosis of several clinical pathologies and disease states within the body. An overview of several imaging modalities will be presented to understand the utility of OCT within the context of diagnostic biomedical imaging techniques.

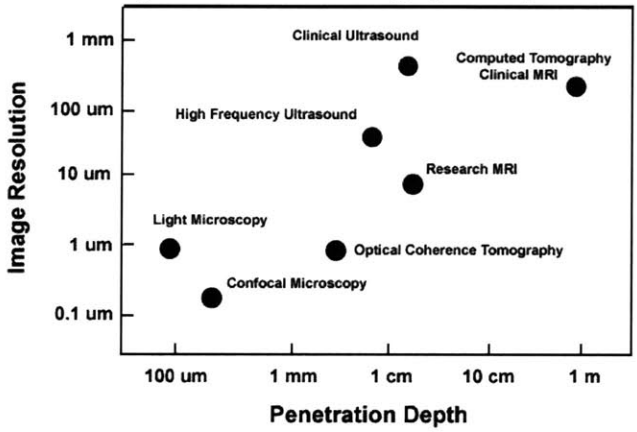

Figure 1-1. Image Resolution vs. Sample Penetration Depth

For each imaging modality there exists a tradeoff between image resolution and penetration depth. The lower right quadrant is the most desirable region of operation with high image resolution and high sample penetration.

Computed Tomography

Computed tomography (CT) is an imaging method that uses X-rays to generate cross-sectional images of the body, tissues, and organ systems [41]. Due to the high energy and short wavelength of X-rays it is possible to visualize both soft and hard tissue as well as bone and cartilage. Modern CT equipment utilizes x-rays emitted in a fan pattern across the patient which are collected by a series of detectors located on the opposite side of the area being imaged. Because a monochromatic radiation source is used the transmitted intensity is proportional to the total attenuation across the path traveled by the X-rays. The patient is positioned between the

source and detector arrays which are rotated over 360 degrees to collect full volumetric data. Images are reconstructed using computer algorithms based on the source and detector positions at each imaging location. Iodine or barium radionuclide dyes can be administered orally or intravenously to increase image contrast in specific organ systems of interest such as the gastrointestinal tract or coronary vasculature. Due to it's capability to image through the whole body, CT is often used to diagnose cancers in solid organs, musculoskeletal disorders and cardiovascular abnormalities.

Imaging resolution in CT is dependent on several factors including the number and orientation of the source and detector arrays, imaging speed, radionuclide concentration, and x-ray energy. Typical systems can achieve 500-1000 um resolution with full body depth of field. New spiral scanning systems have demonstrated rapid image acquisition rates with the capability to capture full body 3D data sets in 10-20 seconds [42]. Higher imaging speed is beneficial in general but especially so for elderly, pediatric, or critically ill patient in where longer scan times can be problematic. While CT has become a standard in clinical care for full body imaging, there are some disadvantages including the large instrument size and high systems cost which can range from $500,000 to $750,000 dollars. In addition exposure to x-ray radiation is in general undesirable and can be harmful if not monitored carefully.

Ultrasound

Medical ultrasound (US) uses high frequency sound waves to generate images of tissue and organ structure [43]. Images are created by measuring the time of flight and signal intensity of reflected acoustic waves from inside the body. The variations in the velocity of sound within tissues of different composition are the mechanism by which image contrast is generated. To create the sound waves a piezoelectric material is vibrated at high frequency and functions as the ultrasonic transducer. The design and engineering of miniaturized transducers for minimally invasive imaging in endoscopic and intravascular has been demonstrated as well.

Clinical systems typically operate with transducing frequencies in the range of 10-20 MHz which provide image resolutions on the order of 100-200 um. Imaging depth of field is typically 10-20 cm with imaging speeds of 30-60 frames per second. High frequency ultrasound has been shown to have higher resolution capability but suffers from reduced depth penetration as the depth of field decreases as the sound wave frequency is increased. There are three modes of imaging with ultrasound devices. A-mode, or amplitude mode, is a one dimensional ultrasonic sonic which displays the amplitude of a reflected acoustic signal as a function of time lag between the transmission of the ultrasonic pulse and the arrival of the echo at the transducer. The time lag

is correlated into a physical distance by accounting for the sound velocity in the tissue specimen. Thus a plot of echo strength (vertical axis) against tissue depth (horizontal axis) is created. The most common technique, B-mode or brightness mode ultrasound, generates a 2D cross-sectional image of an area being imaged. The image is created by either having an array of transducers that sequentially emit an ultrasound beam or by having one transducer that is translated to scan the beam across the region of interest. In this way a signal B-mode image is composed of multiple adjacent A-mode scans with the A-mode signal intensity mapped to brightness in the image. A final mode of ultrasound imaging is M-mode or motion mode. In this technique individual A-mode echo data is displayed as a function of tissue depth (vertical axis) and time (horizontal axis). The brightness at each point in the plotted data corresponds to the echo signal strength. This technique can provide detailed information on the velocity of reflecting structures within the imaging field and is useful in the imaging of blood flow or cardiac motion by color Doppler sonography, continuous and pulsed Doppler ultrasound, and time domain correlation methods.

Overall ultrasound is a relatively inexpensive, fast, and radiation free method to image and diagnosis a number of organs and conditions non-invasively. In addition ultrasound systems are small when compared to CT or MRI equipment and have a price range of $50,000-$100,000 dollars. Ultrasound has found its main application in obstetrics and gynecology as it allows safe imaging of the human fetus. Increased development in the field of ultrasound technology have led to its use in areas such as intravascular ultrasound (IVUS) for the detection and treatment of atherosclerosis and coronary heart disease [44], endoscopic ultrasound for diagnosis of gastrointestinal cancer and diseases of the esophagus [45, 46], imaging of breast tissue [47], and guided needle biopsy. The main limitations of ultrasound are its resolving capability and the necessity of an index-matching material to be placed between the transducer and the area to be imaged.

Magnetic Resonance Imaging

Magnetic resonance imaging (MRI) is an imaging technique that uses radio frequency (RF) pulses to create cross sectional images of the body [48, 49]. MRI works by using a strong magnetic field and the principles of nuclear magnetic resonance to measure changes in spin magnetization of nuclei and in particular hydrogen nuclei. Two different energy states exist for the hydrogen atom depending on the orientation of its nuclei spin relative to the external magnetic field. Although the energy difference between the two states is small (0.01 - 0.1 eV), organic tissues contain a very large number of hydrogen atoms per unit volume and therefore a macroscopic magnetization can be measured. In addition to the main magnetic field in a MR

system (usually created by a permanent, resistive, or cryomagnet) gradient fields are generated within the patient by use of additional coils within the magnet system. These gradient fields permit spatial variation of the magnetic field strength in three spatial dimensions and in time for the localization of magnetization signals and thus image generation. For the MR scan, an RF antenna, also called a transmit coil, irradiates the patient with RF pulses that disturb the spin orientations of hydrogen nuclei. The RF frequency and thus the RF energy is swept across a certain range during a scan. If the RF energy is equal to the energy difference between the two spin states, absorption of the pulse will occur. The energy is then reradiated by the hydrogen with an intensity and temporal behavior that is dependant on the tissue type, pulse energy, and pulse sequence used. From these signals several types of contrast mechanisms can be generated in MR imaging. The two main ones are T1 and T2 relaxation processes but additional structural and functional information can be gained by measuring mobile proton density, spin diffusion, bulk flow, and chemical shifts for MR spectroscopy.

The resolution of MRI is determined by the strength of the magnetic field used. Clinical systems typically operate at 1-2 Tesla and can achieve resolutions of 500-1000 um. Higher fields typically cannot be used in a clinical setting however due to patient discomfort. In MRI there exist several methods to generate image contrast exist and it is possible to do full body imaging with 3D reconstructions. There are several drawbacks to MRI however that makes it accessible only at large medical hospitals and institutions. One is the large system size which typically encompasses a full room for the magnet bore and associated electronics. Another is the high system cost which ranges from $1.5 to $2 million dollars. Finally extreme precaution must be taken that no metallic or magnetic materials be present when operating MRI systems as severe system damage or fatal patient injury can occur.

Microscopy

The area of microscopy is highly diverse and has enabled powerful visualization of biological systems and processes. While a gold standard in the practice of medicine, due to the scattering properties of biological specimens microscopy is mainly limited to the imaging of structures within the first 0-500 um of tissues. Light microscopy has been in use for several hundreds of years however advances in optical elements and contrast techniques such as optical filters, phase masks, bright and dark field imaging, and chemical staining of specific tissue structures has allowed for insight into a wide range of phenomena.

Histological stains such as hematoxylin and eosin, toluidine blue, Buoin solution, and trichrome selectively attach to specific cell and tissue types and allow for sub-cellular resolution of architectural details. In addition, various microscopy techniques such as confocal, fluorescence, and two photon imaging have enabled microscopy to achieve incredible results for both structural and functional imaging *in vivo* and in real time. Microscope systems are present in almost every medical facility however advanced systems can range in price from $100,000 dollars to over $1 million dollars depending on the system capabilities.

Optical Coherence Tomography

Optical Coherence Tomography (OCT) is an imaging technique based on low coherence interferometry and utilizes near infrared light to image tissue non-invasively. With OCT visualization of morphological architecture and tissue microstructure on the micron scale is possible with a 2-3cm depth of field. While the depth of field is much smaller than MRI, CT or ultrasound imaging techniques, image resolution is improved by 2 to 3 orders of magnitude. This imaging regime is highly significant as several disease states initially manifest as cellular or structural changes (1-10 um size scales) near the uppermost tissue layers (1-2 mm below the tissue surface).

As the image penetration of OCT is small relative to the size of the body or an organ, the development of minimally invasive imaging probes is critical for the demonstration and application of OCT for disease states within the body. The most readily accessible organ systems for these devices are the coronary, gastrointestinal and ocular systems. Originally demonstrated for non-invasive imaging of the eye [7], OCT has become a powerful clinical tool in the detection and diagnosis of ophthalmic disease. However as the eye is a highly transparent organ, it is relatively easy to transmit light into it to generate cross sectional image scans. For turbid tissues it is somewhat more challenging to obtain diagnostically relevant information not only because of the highly scattering properties of the tissue but also due to the highly varied tissue architecture in both normal and pathologic specimens. Increased interest in the field has spurred development of high speed, high resolution systems [50] as well as engineering of several minimally invasive diagnostic probes [51, 52]. As OCT represents a unique imaging modality it has the potential to significantly impact the field of medical diagnostic techniques.

Table 1-1. Summary of Diagnostic Imaging Techniques

Technique	Resolution	Depth of Field	Scan Speed	Cost	Imaging example
Computed Tomography	500-1000 um	Full body	1-2 seconds	$500,000	
MRI	500-1000 um	Full body	5-10 minutes	$1,000,000	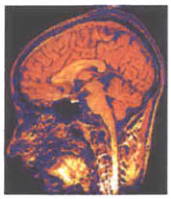
Ultrasound	100-200 um	10-20 cm	Video rate	$50,000	
OCT (eye)	1-10 um	1-2 mm	250 msec	$50,000 - $100,000	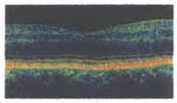
OCT (other)	4-20 um	2-3 mm	250 msec	$50,000 - $100,000	
Light Microscopy	0.2-1 um	10-50 um	Video rate	$10,000 - $100,000	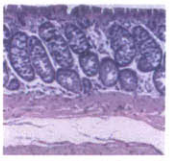
Confocal Microscopy	0.2-1 um	200-300 um	Video rate	$50,000 - $150,000	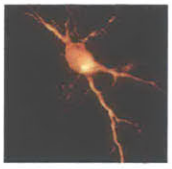
Fluorescence Microscopy	0.2-1 um	50-100 um	Video rate	$20,000 - $150,000	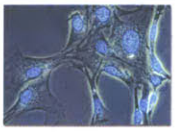

Images are from references [53-58]

Clinical and Biological Systems of Interest

A wide array of clinical pathologies and biological systems of interest exist that could benefit from the high resolution imaging capability of OCT. In order to demonstrate the potential benefits of OCT for the clinical and scientific communities several areas were investigated in this work. As the tissue penetration ability of OCT is limited to a few millimeters, the development and implementation of minimally invasive diagnostic devices to access internal body imaging sites was focused upon as well. In particular handheld imaging probes, catheter and endoscope based devices, and microscope platforms were used to investigate imaging in the clinically significant areas of arthroscopy, cardiology, and endoscopy.

Scope of the Thesis

The utility of OCT has been demonstrated in both medical and non-medical applications. While initial application of the technology has been shown, there exist several areas to be investigated in order to increase both its adoption and efficacy in the clinical setting. In particular the ultimate resolution capability of OCT to distinguish and diagnosis biological systems or disease states of interest is still unclear. The demonstration of OCT has progressed from *in vitro* tissue specimens to *in vivo* animal and human models at standard resolutions. Ultrahigh resolution studies have shown the improved diagnostic capability of OCT but have been limited to mainly ophthalmic applications [50, 59]. The use of ultrahigh resolution OCT for imaging turbid tissues has not been fully explored. The goal of this thesis is to explore the potential of ultrahigh resolution OCT for *in vivo* imaging of clinically significant pathologies with minimally invasive catheter-based and handheld diagnostic devices. To this end, the scientific and technological development of OCT systems and their application to several biological and clinical systems of interest has been pursued to demonstrate OCT imaging at resolutions of 3-4 um in tissue. Achieving this capability is significant as many clinical pathologies and disease states induce architectural disruption at the cellular or glandular level. The size scales of these disruptions are on the order of 5-10um therefore the development of OCT imaging systems that can distinguish and quantify these changes would represent a significant advance in the field of biomedical imaging.

To achieve these goals, the development high resolution OCT systems which implement broadband light sources and has been pursued. Using these light sources in conjunction with advanced system design has enabled high performance OCT imaging to be achieved. In addition,

portable OCT systems have been constructed for clinical and surgical imaging studies. Rapid scanning delay line technology as well as optical elements which support broadband operation have been implemented as well to achieve high speed, high resolution imaging capability.

While the ability to image and visualize tissue structure is critical, the importance of light delivery is often overlooked by scientists and clinicians. Light delivery probes can have a significant and determining impact on the efficacy and capabilities of an imaging system. This applies for both diagnostic and therapeutic areas of application. To this end the development of minimally invasive diagnostic probes using novel micro-mechanical and micro-electromechanical systems has been demonstrated in this work. The fundamental design, construction, and implementation of these devices has been carried out using mechanical, optical, electrical, and ergonomic performance criteria. The capabilities of these diagnostic probes are demonstrated in both animal and human models for *in vivo* and clinical imaging.

Because OCT uses a variety of advanced technologies across a broad range of disciplines this thesis is organized into several sections which can be read somewhat independently. Chapter 2 provides the fundamental theory behind OCT and discusses several factors which affect system performance. An overview of low coherence light sources and their role is provided to give the reader an understanding of this fundamental and critical component in the OCT imaging system. Image quality and physical processes that affect it are discussed. Chapter 3 goes into the detailed specifics of the systems developed for this work and describes optimal design configurations for optical, mechanical, and electronic components. Chapter 4 describes OCT delivery devices and details new diagnostic probes that were designed and fabricated for minimally invasive imaging experiments. Chapter 5 presents *in vivo* imaging results for animal models achieved with the high speed, high resolution systems that were developed. In Chapter 6 experimental results from clinical imaging in humans are presented.

References

1. J. A. Izatt, N. D. Sankey, F. Partovi, M. Fitzmaurice, R. P. Rava, J. Itzkan, and M. S. Feld, *"Ablation of calcified biological tissue using pulsed hydrogen fluoride laser radiation,"* IEEE Journal of Quantum Electronics, **26**, 2261-70 (1990).
2. J. M. Krauss and C. A. Puliafito, *"Lasers in ophthalmology,"* Lasers in surgery and medicine, **17**, 102-59 (1995).
3. J. Bewersdorf, R. Pick, and S. W. Hell, *"Multifocal multiphoton microscopy,"* Opt Lett, **23**, 655-658 (1998).
4. W. Denk, J. Strickler, and W. Webb, *"Two-photon laser scanning fluorescence microscopy,"* Science, **248**, 73-76 (1990).
5. R. H. Webb, G. W. Hughes, and F. C. Delori, *"Confocal scanning laser ophthalmoscope,"* Appl Opt, **26**, 1492-1499 (1987).
6. T. Lazarus-Karaoglan, *"Medical electronics [technology 1999 analysis and forecast],"* IEEE Spectrum, **36**, 79-83 (1999).
7. D. Huang, E. A. Swanson, C. P. Lin, J. S. Schuman, W. G. Stinson, W. Chang, M. R. Hee, T. Flotte, K. Gregory, C. A. Puliafito, and J. G. Fujimoto, *"Optical coherence tomography,"* Science, **254**, 1178-81 (1991).
8. M. D. Kulkarni and J. A. Izatt, *"Spectroscopic optical coherence tomography,"* CLEO '96. Summaries of Papers Presented at the Conference on Lasers and Electro Optics, **9**, 59-60 (1996).
9. D. L. Farkas and D. Becker, *"Applications of spectral imaging: detection and analysis of human melanoma and its precursors,"* Pigment cell research / sponsored by the European Society for Pigment Cell Research and the International Pigment Cell Society, **14**, 2-8 (2001).
10. W. G. Zijlstra and W. P. Meeuwsen-van der Roest, *"Absorption spectra of human fetal and adult oxyhemoglobin, de-oxyhemoglobin, carboxyhemoglobin, and methomoglobin,"* Clin. Chem., **37**, 1633-1638 (1991).
11. W. F. Cheong, S. A. Prahl, and A. J. Welch, *"A review of the optical properties of biological tissues,"* IEEE Journal of Quantum Electronics, **26**, 2166-85 (1990).
12. J. F. De Boer, T. E. Milner, M. J. C. van Gemert, and J. S. Nelson, *"Two-dimensional birefringence imaging in biological tissue by polarization-sensitive optical coherence tomography,"* Optics Letters, **22**, 934-6 (1997).
13. Y. Yang, L. Wu, Y. Feng, and R. K. Wang, *"Observations of birefringence in tissues from optic-fibre-based optical coherence tomography,"* Measurement Science & Technology, **14**, 41-6 (2003).
14. M. Tateda and T. Horiguchi, *"Advances in optical time domain reflectometry,"* Lightwave Technology, Journal of, **7**, 1217-1224 (1989).
15. J. G. Fujimoto, S. De Silvestri, E. P. Ippen, C. A. Puliafito, R. Margulis, and A. Oseroff, *"Femtosecond Optical Ranging in Biological Systems,"* Opt. Lett., **11**, 150-152 (1986).
16. D. Stern, W.Z. Lin, C..A. Puliafito, J.G. Fujimoto, *"Femtosecond Optical Ranging of Corneal Insision Depth,"* Invest. Opthalm. and Vis. Sci., **30**, 99 (1989).
17. S. L. Jacques, *"Time resolved propagation of ultrashort laser pulses within turbid tissues,"* Appl Opt, **28**, 2223-2229 (1989).
18. H. H. Gilgen, R. P. Novak, R. P. Salathe, W. Hodel, and P. Beaud, *"Submillimeter optical reflectometry,"* IEEE Journal of Lightwave Technology, **7**, 1225-1233 (1989).
19. K. Takada, I. Yokohama, K. Chida, and J. Noda, *"New measurement system for fault location in optical waveguide devices based on an interferometric technique,"* Applied Optics, **26**, 1603-1608 (1987).
20. R. Youngquist, S. Carr, and D. Davies, *"Optical coherence-domain reflectometry: a new optical evaluation technique,"* Optics Letters, **12**, 158-60 (1987).
21. C. Chamon Cde, C. K. Sun, H. A. Haus, and J. G. Fujimoto, *"High-speed optical coherence domain reflectometry,"* Optics Letters, **17**, 151-3 (1992).
22. A. F. Fercher, *"Optical coherence tomography,"* Journal of Biomedical Optics, **1**, 157-173 (1996).
23. C. K. Hitzenberger, *"Optical measurement of the axial eye length by laser Doppler interferometry,"* Invest Ophthalmol Vis Sci, **32**, 616-624 (1991).

24. J. A. Izatt, M. R. Hee, E. A. Swanson, C. P. Lin, D. Huang, J. S. Schuman, C. A. Puliafito, and J. G. Fujimoto, "*Micrometer-scale resolution imaging of the anterior eye in vivo with optical coherence tomography,*" Archives of Ophthalmology, **112**, 1584-1589 (1994).
25. E. A. Swanson, D. Huang, M. R. Hee, J. G. Fujimoto, C. P. Lin, and C. A. Puliafito, "*High-speed optical coherence domain reflectometry,*" Opt. Lett., **17**, 151-153 (1992).
26. X. Clivaz, F. Marquis-Weible, and R. P. Salathe, "*Optical low coherence reflectometry with 1.9 μm spatial resolution,*" Electronics Letters, **28**, 1553-1554 (1992).
27. J. M. Schmitt, A. Knuttel, and R. F. Bonner, "*Measurement of optical-properties of biological tissues by low-coherence reflectometry,*" Applied Optics, **32**, 6032-6042 (1993).
28. D. Huang, Swanson, E. A., Lin, C. P., Schuman, J. S., Stinson, W. G., Chang, W., Hee, M. R., Flotte, T., Gregory, K., Puliafito, C. A., Fujimoto, J. G., "*Optical coherence tomography,*" Science, **254**, 1178-1181 (1991).
29. E. A. Swanson, J. A. Izatt, M. R. Hee, D. Huang, C. P. Lin, J. S. Schuman, C. A. Puliafito, and J. G. Fujimoto, "*In vivo retinal imaging by optical coherence tomography,*" Opt Lett, **18**, 1864-1866 (1993).
30. M. Ramaswamy, A. S. Gouveia-Neto, D. K. Negus, J. A. Izatt, and J. G. Fujimoto, "*In vivo retinal imaging by optical coherence tomography,*" Optics Letters, **18**, 1864-6 (1993).
31. M. R. Hee, J. A. Izatt, E. A. Swanson, D. Huang, C. P. Lin, J. S. Schuman, C. A. Puliafito, and J. G. Fujimoto, "*Optical coherence tomography of the human retina,*" Archives of Ophthalmology, **113**, 325-332 (1995).
32. K. Kobayashi, J. A. Izatt, M. D. Kulkarni, J. Willis, and M. V. Sivak, "*High-resolution cross-sectional imaging of the gastrointestinal tract using optical coherence tomography: preliminary results,*" Gastrointestinal Endoscopy, **47**, 515-523 (1998).
33. B. E. Bouma, G. J. Tearney, C. C. Compton, and N. S. Nishioka, "*High-resolution imaging of the human esophagus and stomach in vivo using optical coherence tomography,*" Gastrointestinal Endoscopy, **51**, 467-474 (2000).
34. J. G. Fujimoto, S. A. Boppart, G. J. Tearney, B. E. Bouma, C. Pitris, and M. E. Brezinski, "*High resolution in vivo intra-arterial imaging with optical coherence tomography,*" Heart, **82**, 128-133 (1999).
35. M. E. Brezinski, G. J. Tearney, B. E. Bouma, S. A. Boppart, M. R. Hee, E. A. Swanson, J. F. Southern, and J. G. Fujimoto, "*Imaging of coronary artery microstructure (in vitro) with optical coherence tomography,*" Am J Cardiol, **77**, 92-93 (1996).
36. M. E. Brezinski, G. J. Tearney, B. E. Bouma, S. A. Boppart, M. R. Hee, E. A. Swanson, J. F. Southern, and J. G. Fujimoto, "*High-resolution imaging of plaque morphology with optical coherence tomography,*" Circulation, **92**, 103-103 (1995).
37. J. M. Herrmann, C. Pitris, B. E. Bouma, S. A. Boppart, J. G. Fujimoto, and M. E. Brezinski, "*High resolution imaging of normal and osteoartheritic cartilage with optical coherence tomography,*" Journal of Rheumatology, **26**, 627-635 (1999).
38. P. R. Herz, S. Martin, P. Hsiung, X.D. Li, A.D. Aguirre, N. Patel, K. Saunders, D. Stamper, T.H. Ko, J.G. Fujimoto and M. Brezinski, "*High Resolution in vivo Imaging of Osteoarthritic Cartilage,*" OSA Biomedical Meeting, **MD6(1)**, 331-333 (2002).
39. S. A. Boppart, M. E. Brezinski, B. E. Bouma, G. J. Tearney, and J. G. Fujimoto, "*Investigation of developing embryonic morphology using optical coherence tomography,*" Developmental Biology, **177**, 54-63 (1996).
40. M. D. Kulkarni, W. Tobocman, and J. A. Izatt, "*Optical coherence tomography of embryonic morphology during cellular differentiation,*" OSA Trends in Optics and Photonics on Advances in Optical Imaging and Photon Migration, **2**, 231-3 (1996).
41. A. M. Cormack and G. N. Hounsfield, "*1979 Nobel Prize in Physiology or Medicine: The development of computer assisted tomography,*" (1979).
42. J. H. Duyn and Y. Yang, "*Fast Spiral Magnetic Resonance Imaging with Trapezoidal Gradients,*" Journal of Magnetic Resonance, **128**, 130-134 (1997).
43. F. Kremkau, *Diagnostic ultrasound: principles, instrumentation, and exercises*. 2nd ed. 1984, Philadelpha: Grune and Stratton.

44. S. E. Nissen, J. C. Gurley, D. C. Booth, and A. N. DeMaria, "*Intravascular ultrasound of the coronary arteries: current applications and future directions,*" American Journal of Cardiology, **69**, 18H-29H (1992).
45. R. H. Hawes, "*New staging techniques: Endoscopic ultrasound,*" Cancer, **71**, 4207-4213 (1993).
46. H. Yanai, T. Yoshida, T. Harada, Y. Matsumoto, M. Nishiaki, and T. Shigemitsu, "*Endoscopic ultrasonography of superficial esophageal cancers using a thin ultrasound probe system equipped with switchable radial and linear scanning modes,*" Gastrointestinal Endoscopy, **44**, 578-582 (1996).
47. A. T. Stavros, C. L. Rapp, and S. H. Parker, *Breast Ultrasound.* 2003: Lippincott Williams & Wilkins.
48. *Computed Tomography and Magnetic Resonance Imaging of the Whole Body.* 4 ed, ed. R.C. Gilkeson. 2002: Mosby.
49. J. P. Hornack, "*The Basics of MRI,*" http://www.cis.rit.edu/htbooks/mri/inside.htm (2004).
50. W. Drexler, U. Morgner, R. K. Ghanta, F. X. Kärtner, J. S. Schuman, and J. G. Fujimoto, "*Ultrahigh-resolution ophthalmic optical coherence tomography,*" Nature medicine, **7**, 502-7 (2001).
51. S. A. Boppart, G. J. Tearney, B. Bouma, J. G. Fujimoto, and M. E. Brezinski, "*Single mode fiber-optic catheter/endoscope for optical coherence tomography,*" CLEO '96. Summaries of Papers Presented at the Conference on Lasers and Electro Optics, **9**, 57-8 (1996).
52. A. Katsevich, J. George, and A. Ramm, "*Biomedical diagnostics using optical coherence tomography,*" OSA Trends in Optics and Photonics on Advances in Optical Imaging and Photon Migration, **2**, 196-9 (1996).
53. Y. Romero, A. J. Cameron, D. J. Schaid, S. K. McDonnell, L. J. Burgart, C. L. Hardtke, J. A. Murray, and G. Locke, "*Barrett's Esophagus: Prevalence in SYmptomatic Relatives,*" Am. J. Gastroenterol., **97**, 1127-1132 (2002).
54. G. W. Falk, "*Barrett's Esophagus,*" Gastroenter., **122**, 1569-1591 (2002).
55. A. J. Cameron, B. J. Ott, and W. S. Payne, "*The incidence of adenocarcinoma in columnar-lined (Barrett's) esophagus,*" N Engl J Med, **313**, 857-859 (1989).
56. W. Hameeteman, G. Tytgat, and H. J. Hoffman, "*Barrett's esophagus: Development of dysplasia and adenocarcinoma,*" Gastroenter., **96**, 1249-1256 (1989).
57. A. J. Cameron and H. A. Carpenter, "*Barrett's Esophagus, High-Grade Dysplasia, and Early Adenocarcinoma: A Pathological Study,*" Am. J. Gastroenterol., **92**, 586-591 (1990).
58. T. Rosch, "*Gastroesophageal Reflux Disease and Barrett's Esophagus,*" Endoscopy, **32**, 826-835 (2000).
59. W. Drexler, U. Morgner, F. X. Kartner, C. Pitris, S. A. Boppart, X. D. Li, E. P. Ippen, and J. G. Fujimoto, "*In vivo ultrahigh-resolution optical coherence tomography,*" Optics Letters, **24**, 1221-3 (1999).

Chapter 2 – Optical Coherence Tomography

Introduction

OCT is a relatively new imaging modality that allows non-invasive imaging of tissue structure with micron-level resolution [1]. Imaging is performed by using low coherence interferometry to obtain depth dependent signal information that correlates to scattering and absorption processes within the sample under investigation. An axial depth scan comprised of many localized interferometric signals is generated by scanning the reference arm mirror in the optical interferometer. The intensity envelope of these interference signals is obtained by electronic demodulation and filtering and is subsequently mapped to physical locations within the tissue (Figure 2-1 left). A two-dimensional cross sectional image of the tissue structure can be created by scanning the optical beam across the tissue surface and combining several axial scans at adjacent positions (Figure 2-1 right). Arbitrary scan protocols can be applied to generate rectangular, cylindrical, or circular cross sectional imaging planes. High power light sources and rapid scanning technologies can be utilized to perform *in vivo* imaging in real time.

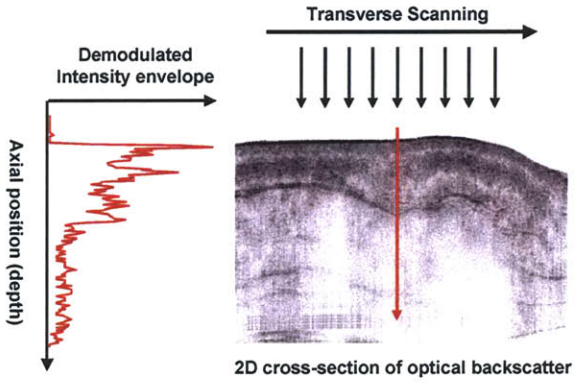

Figure 2-1. Axial scanning and image formation in OCT

The optical sectioning capability of OCT allows it to image tissue microstructure at depths beyond the reach of conventional bright-field and confocal microscopy. Light penetration of 1-2mm beneath the tissue surface can be achieved even for highly scattering tissues such as skin and cervix [2, 3]. For transparent biological systems such as the eye or frog embryos, imaging depths of 2cm or more have been reported [4, 5]. OCT systems are highly compact and portable and can be used for imaging studies in clinical settings where operating space is minimal. In addition, with recent advances in light source technology OCT systems can be

relatively inexpensive when compared to MRI and ultrasound imaging systems. Both *in vitro* and *in vivo* studies can be performed with various minimally invasive handheld, catheter, or needle-like probes [6-9].

With broadband laser light sources it has been shown that OCT can achieve resolutions sufficient to distinguish microscopic and cellular level features in several transparent and non-transparent biological tissues [10, 11]. One of the unique capabilities of OCT is that it can provide high resolution imaging capability (1-10μm) while simultaneously having a sample penetration of 2-3mm which is sufficient in several clinically relevant disease pathologies.

System Overview

There are several components within an OCT system which will be analyzed to understand the principles behind OCT and how a working system can be realized. A schematic of a simple OCT system is shown in Figure 2-2 with the main functional components.

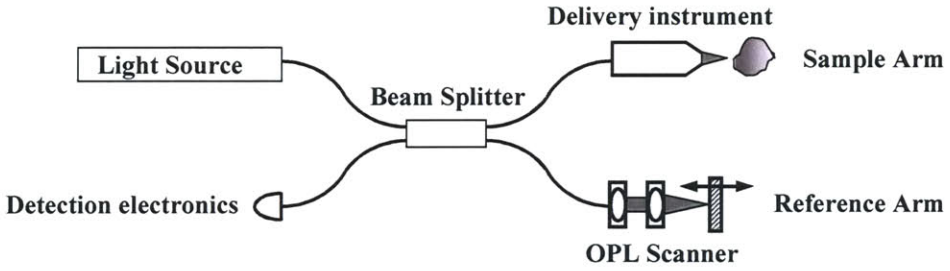

Figure 2-2. Simplified OCT schematic

A basic OCT system consist of 5 main components: a broadband light source, interferometeric beam splitter, optical path length scanner in the reference arm, beam delivery instrument in the sample arm and detection electronics.

Low coherence light is coupled into a fiber-optic Michelson interferometer. The input signal is split into the sample and reference arms with the splitting ratio determined by the coupling ratio of the interferometer. Ideally the spectral energy is equally divided between both the reference and sample arms however due to several factors such as wavelength dependent coupling and polarization sensitivity in the optical components, this may not be the case. This is particularly true for broadband light sources and can results in significantly altered system performance. After passing through the interferometer, the sample signal is coupled into a beam delivery instrument which acts as an interface between the OCT system and the biological sample. The delivery instrument has transverse (x-y) scanning capability and is used to raster the sample beam across the specimen. In the reference arm, a mechanism to scan the optical path length is used to vary the depth location of the detected heterodyne signal within the sample. This

allows a single axial (z-axis) profile, or A-scan, to be obtained by rapidly changing the position of the reference arm mirror and simultaneously recording the resulting interference signal. By synchronizing a 1-dimensional raster scan of the optical beam across the sample, a sequence of A-scans can be combined to form a cross-sectional B-scan image of the sample. If a 2-dimensional scanner in the delivery instrument is used, a volume tomogram can be also constructed. The main limitation in volumetric imaging is the tradeoff between image acquisition speed and the signal to noise ratio. The back-reflected signals from the sample and reference arms are then recombined at the detector where the optical fields are converted into an electrical signal. Detection electronics amplify, filter and demodulate the interferometric heterodyne signal. Intensity as a function of scan position is then used to form two or three dimensional images of the tissue sample. All of the scanning, data acquisition, and image display functions are computer controlled with in-house software and digital acquisition cards. While the system is conceptually simplistic, a substantial amount of design and expertise is required for each component to achieve a system that can have clinically significant diagnostic impact.

Interferometry

At the core of the OCT system is the interferometer that is used to create the optical coherence function from which an OCT image is generated. In this section the fundamental concepts that underlie interference and coherence techniques used in OCT will be discussed. The Fourier transform relationships between the light source spectrum and the longitudinal point spread function (axial resolution) will also be explored.

In its most simple form, how an OCT system functions can be visualized in terms of a Michelson interferometer setup shown in Figure 2-3. For a standard interferometer with a monochromatic light source, a standing wave of constructive and destructive interference is seen at the detector as a function of the relative phase separation between the sample and reference arm electromagnetic wave signals. If one arm of the interferometer is physically translated, this gives rise to a periodic modulation in signal intensity. The frequency of this modulation is determined by the light wavelength as each cycle corresponds to a 2π phase shift in interference. Consider a simplified Michelson interferometer shown in Figure 2-3 where the incident optical wave is split to sample and reference fields, E_R and E_S.

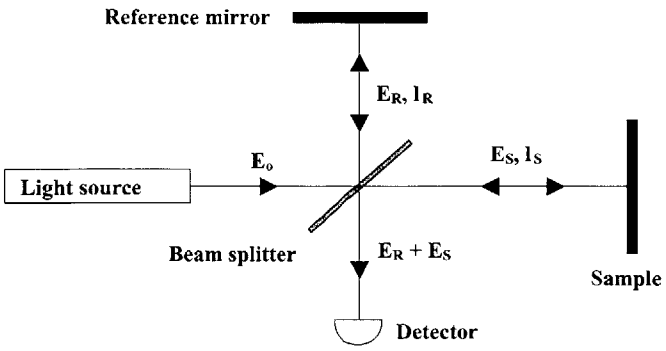

Figure 2-3. Simplified Michelson Interferometer

A monochromatic plane wave is split into two separate fields. The field amplitudes are determined by the slitting ratio of the beamsplitter. The relative phase of each field is determined by the optical path length traveled in each arm of the interferometer.

If we assume a monochromatic light source, the sample and reference fields may be represented by wave functions with harmonic time dependence

$$\vec{E}_R = E_r(\vec{r})\cos[\omega t + \phi_r(\vec{r})] \qquad \text{and} \qquad \vec{E}_S = E_s(\vec{r})\cos[\omega t + \phi_s(\vec{r})]$$

where E_r and E_s the respective field amplitudes from the sample and reference arms and ω is the angular frequency of the light source. The relative phase of each field, ϕ_r and ϕ_s may be expressed as a function of the interferometer arm lengths, l_R and l_S and the fields may be expressed in phasor form such that

$$E_R = E_r e^{-j(2\beta_r l_r - \omega t)} \qquad \text{and} \qquad E_S = E_s e^{-j(2\beta_s l_s - \omega t)}$$

Here β is the propagation constant and the factor of two arises due to the roundtrip propagation of light from the sample and reference mirrors. In general the electric fields are vector quantities and have explicit space dependence. We will initially assume parallel polarization directions for both fields and drop the vector notation for notational simplicity. We have also assumed a 50% beam splitting ratio which will determine the relative field amplitudes that propagate into the sample and reference arms and sets

$$E_r = E_S = \frac{1}{2}E_o$$

The resulting superposition of the complex wave functions at the detector gives an optical intensity

$$I_D = |E_R + E_S|^2 = \tfrac{1}{2}|E_r|^2 + \tfrac{1}{2}|E_s|^2 + \tfrac{1}{4}E_R^* E_S + \tfrac{1}{4}E_R E_S^*$$
$$= \tfrac{1}{2}|E_r|^2 + \tfrac{1}{2}|E_s|^2 + \tfrac{1}{2}\Re e\{E_R^* E_S\}$$
$$= \tfrac{1}{2}I_r + \tfrac{1}{2}I_S + \tfrac{1}{2}\sqrt{I_r I_S}\cos(2\beta_r l_r - 2\beta_s l_s + \phi(t))$$

where $\phi(t)$ is the relative phase difference between the two back propagating waves. If $\phi(t) = 0$ and the propagation constants in the sample and reference arms are identical, $\beta_r = \beta_s = \beta$, then the phase difference between the two fields is related to the optical path length difference Δl by

$$\Delta\varphi = \frac{2\pi}{n\lambda}(2l_r - 2l_s) = \frac{2\pi\ \Delta l}{n\lambda}$$

Since the detected optical intensity is sensitive to the phase difference, small variations in path length Δl, refractive index n, or wavelength λ, can be measured. For example if $\Delta l/\lambda = 10^4$, a relative index of refraction variation of $\Delta n = 10^{-4}$ can be measured in the sample. If the reference arm mirror is moving with constant velocity parallel to the direction of light propagation, the pathlength difference becomes a linear function of time, $\Delta l = vt$, and a Doppler shift is induced in the reflected light with a Doppler frequency of $f_D = v/\lambda$. The optical intensity at the detector is correspondingly

$$I_D = \tfrac{1}{4}I_r + \tfrac{1}{4}I_s + \tfrac{1}{2}\sqrt{I_r I_s}\cos(2\pi f_D t)$$

The first two terms represent the DC component of the signal while the last term is the oscillatory AC component whose oscillation frequency is a function of the relative path length difference in both arms. For a perfectly monochromatic light source the interference signal can be detected over an infinite range in path length difference and fringes will be detected at all times as shown in Figure 2-4.

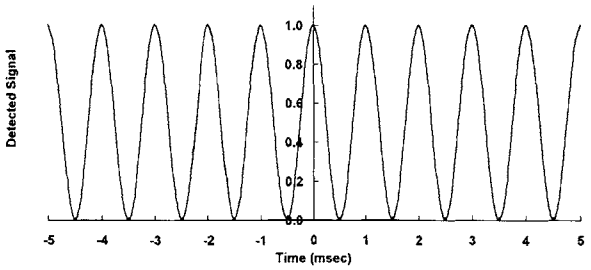

Figure 2-4. Interference fringes for a monochromatic light source

An idealized monochromatic light source when used for interferometry generates an infinetly long train of fringes as a fucntion of optical path length difference in the sample and reference arms.

It is clear that any real light source has a finite spectral bandwidth and therefore is not monochromatic. If additional spectral components are added to the light source, a periodic signal modulation will not be seen at any arbitrary position but is rather confined to a specific spatial region defined by the coherence length of the light source. This envelope function effectively localizes the region from which an interference signal can be detected providing in essence, the axial resolving capability of the system. Thus if a semi-transparent sample is present in the sample arm of the interferometer and the position of the reference arm mirror is changed, only the backscattered light from an area localized at a specific depth within the tissue will generate an interference signal. The degree of localization is inversely proportional to the optical bandwidth (spectral width) of the light source used [12]. Thus a short coherence length, broadband light source can be used to provide high image resolution (signal localization) in the axial (depth) dimension of the interferometric detection scheme. OCT images are constructed by detecting the backscattered light intensity of this localized signal at several depths from within a tissue sample. By using a heterodyne detection technique, very small signal levels (up to -100dB) can readily be discriminated. To investigate this situation more rigorously the coherent properties of light and its role in low coherence interferometry will be discussed in the following sections.

Low Coherence Interferometry

Coherence refers to the degree to which a light field maintains a definite, nonrandom phase relationship in space and time. It is also a measure of how well the light source can exhibit stable interference phenomena [13]. The time over which this phase relationship maintains nearly constant is called the coherence time, τ_c. The coherence time is approximately equal to $1/\Delta\nu$, where $\Delta\nu$, is the optical frequency bandwidth of the light source. A light source with a long coherence time (large τ_c) will be sharply peaked in the spectral domain (small $\Delta\nu$). In the limit of an infinitely coherent source, the optical spectrum would be composed of a single frequency. Correspondingly a light source with a continuous superposition of frequency components will have a short coherence time and constitutes a broadband light source.

The path length over which the light remains coherent is appropriately called the coherence length. Over this distance, the electromagnetic radiation is "nicely" sinusoidal or in other words, it is the spatial and temporal space over which the phase relationship of the light signal can accurately be predicted. Figure 2-5 illustrates how increasing the number of sinusoidal frequency components in a signal decreases the coherence length. This effectively localizes the position over which an interference signal is observed.

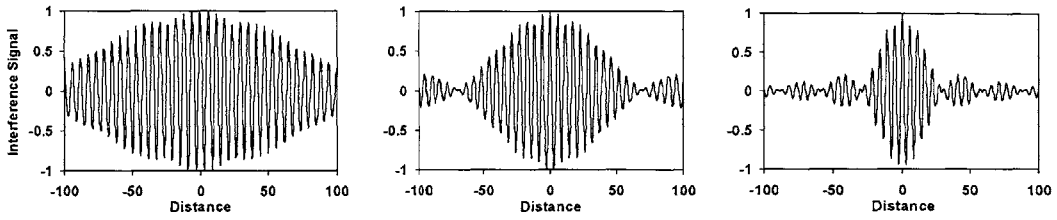

Figure 2-5. Coherent interference from multiple spectral components
Interference patterns for sinusoidal waveforms containing 10, 30 and 50 frequency components. A continous superposition of frequencies generating a larger spectral bandwith results in a corresponding decrease in coherence length.

Consider now the use of a broadband, low coherence light source in the interferometer of Figure 2-3 with a scattering tissue specimen in the sample arm instead of a perfectly reflecting mirror. The optical intensity at the system detector will now be

$$I_D = \tfrac{1}{2} I_r + \tfrac{1}{2} I_s' + \tfrac{1}{2} \Re e\left\{ E_r^* E_s' \right\}$$

where I_r and I_s are again the dc signal intensities but the reflected field from the sample arm, E_s', is now modified due to the scattering and absorption properties of the sample. The degree to which an interference signal forms and the inherent structure of the signal's fringes are dependent upon the temporal and spatial coherence of E_r and E_s'. In this way the interferometer functions as a cross-correlator between the sample and reference arm signals. The strength of the interference signal can be interpreted as a measure of the autocorrelation amplitude of the two electric fields. The correlation amplitude can be obtained by summing over all spectral frequencies and can be written in the Fourier domain as

$$I_D = \Re e\left\{ \frac{1}{2\pi} \int_{-\infty}^{\infty} E_r(\omega) E_s^*(\omega) d\omega \right\} = \Re e\left\{ \frac{1}{2\pi} \int_{-\infty}^{\infty} S(\omega) e^{-i\Delta\varphi} d\omega \right\}$$

where $S(\omega)$ is the convolution of the recombined spectral intensities returning from the sample and reference arms. When the returning spectra are identical across all frequencies and unmodified from the input spectrum, $S(\omega)$ is the power spectral density of the light source. Assuming that the sample and reference arm propagation constants are the same $\beta_r = \beta_s = \beta(\omega)$, $\Delta\varphi$ is the relative phase difference between each frequency component of the sample and reference signals. It is given by

$$\Delta\varphi(\omega) = 2\beta(\omega)(l_r - l_s) = \beta(\omega)\Delta l$$

The temporal coherence function can be related to the power spectral density through the Fourier relationship

$$G(\tau) = \frac{1}{2\pi}\int_0^\infty S(\omega)e^{-i2\pi\tau}d\omega$$

By doing a Taylor expansion of the optical frequencies such that

$$\beta(\omega) = \beta(\omega_o) + \beta'(\omega_0)(\omega - \omega_o)$$

we see that

$$I_D = \Re e\left\{\frac{1}{2\pi}\int_{-\infty}^{\infty} S(\omega)e^{-i\Delta l[\beta(\omega_o)-\beta'(\omega_o)(\omega-\omega_o)]}d\omega\right\}$$

$$= \Re e\left\{\frac{1}{2\pi}e^{-i\beta(\omega_o)\Delta l}\int_{-\infty}^{\infty} S(\omega)e^{-i\beta'(\omega_o)(\omega-\omega_o)\Delta l}d\omega\right\}$$

$$= \Re e\left\{\frac{1}{2\pi}e^{-i\omega_o\Delta\tau_p}\int_{-\infty}^{\infty} S(\omega)e^{-i\Delta\tau_g(\omega-\omega_o)}d\omega\right\}$$

where $\Delta\tau_p$ and $\Delta\tau_g$ are the phase and group delays given by

$$\Delta\tau_p = \frac{\beta(\omega_o)}{\omega_o}\Delta l = \frac{\Delta l}{v_p}$$

$$\Delta\tau_g = \beta'(\omega_o)\Delta l = \frac{\Delta l}{v_g}$$

with v_g and v_p as the group and phase velocity. It is apparent from the above result that the autocorrelation function is equal to the inverse Fourier transform of the power spectral density. This result can be verified and is formalized in the Wiener-Khinchin theorem. If a Gaussian input spectrum is used for the power spectral density

$$S(\omega) = \sqrt{\frac{2\pi}{\sigma_\omega^2}}\; e^{-\frac{(\omega-\omega_o)^2}{\sigma_\omega^2}}$$

then the optical intensity at the detector is

$$I_D = \Re e\left\{\frac{1}{2\pi}e^{-i\omega_o\Delta\tau_p}\int_{-\infty}^{\infty}\sqrt{\frac{2\pi}{\sigma_\omega^2}}\; e^{-\frac{(\omega-\omega_o)^2}{\sigma_\omega^2}}\; e^{-i\Delta\tau_g(\omega-\omega_o)}d\omega\right\}$$

Making a simple substitution of $x = \omega - \omega_o$ and using an integral identity of

$$\int_{-\infty}^{\infty} e^{2bx-ax^2}dx = \sqrt{\frac{\pi}{a}}\; e^{\frac{b^2}{a}}$$

we reach

$$I_D = \Re e\left\{ e^{-i\omega_o \Delta\tau_p} \sqrt{\frac{1}{2\pi\sigma_\omega^2}} \int_{-\infty}^{\infty} e^{2bx - ax^2} dx \right\}$$

where

$$a = \frac{1}{\sigma_\omega^2} \qquad \text{and} \qquad b = \frac{-i\Delta\tau_g}{2}$$

Solving the integral equation yields

$$I_D = \Re e\left\{ e^{-i\omega_o \Delta\tau_p} e^{-\frac{1}{2}\Delta\tau_g^2 \sigma_\omega^2} \right\} = \Re e\left\{ e^{-i\omega_o \Delta\tau_p} e^{-\frac{\Delta\tau_g^2}{2\sigma_\tau^2}} \right\}$$

where the spectral bandwidth is inversely proportional to the pulse duration for a transform-limited pulse,

$$\sigma_\omega = \frac{1}{\sigma_\tau}$$

From the above equation it is apparent that the correlation signal is contained within an envelope function of width $2\sigma_\tau$ in time. The number and frequency of fringe oscillations contained within the coherence envelope is dependent on the phase mismatch and phase velocity, $\Delta\tau_p = \frac{\Delta l}{v_p}$. The interference fringes are seen only when the group delay mismatch $\Delta\tau_g$ falls within the coherence envelope

$$-\sigma_\tau \le \Delta\tau_g \le -\sigma_\tau$$

Converting from the frequency domain to temporal-spatial position, the width or standard deviation of the Gaussian envelope is given by

$$\Delta l_{gaussian} = \frac{\sigma_\tau}{k'(\omega_o)} = \frac{v_g}{\sigma_\omega}$$

In free space, we have $v_g = c$ and the full-width half-maximum spectral bandwidth is given by

$$\sigma_\omega = \frac{\Delta\omega_{FWHM}}{2\sqrt{2\ln 2}}$$

Thus the longitudinal distance over which the fringes will be seen, i.e. the coherence window is

$$\Delta l_{FWHM} = \Delta l_{gaussian}\sqrt{2\ln 2} = \frac{c}{\sigma_\omega}\sqrt{2\ln 2} = \frac{4\ln 2}{\Delta\omega_{FWHM}}$$

Converting to the frequency domain in terms of wavelength where

$$\Delta\omega = d\omega = d(2\pi\nu) = 2\pi d\left(\frac{c}{\lambda}\right) = \frac{2\pi c}{\lambda_o^2}\Delta\lambda$$

we see that this axial resolution is given by the coherence length of the light source

$$\Delta l_c = \frac{2\ln 2}{\pi}\frac{\lambda_o^2}{\Delta\lambda}$$

For a low coherence interferometry system, the optical path lengths of the sample and reference beams must coincide with this coherence length in order to see a interference fringe pattern. This coherence gating provides localized signal information at various depths within a scattering tissue sample and provides the axial (depth) resolution of the system. It can be seen from these relationships that the spectral content and coherence properties of the OCT light source will directly affect the correlation amplitude and resultant OCT image resolution. Figure 2-6 illustrates the effect of spectral modulation on the resultant interference fringe and log demodulated signal.

For a Gaussian spectrum with a small amount of spectral noise present in any system (Figure 2-6a), the heterodyne signal has a Gaussian demodulated envelope with a given system noise floor. As the spectrum becomes less Gaussian (Figure 2-6b), sidelobes appear and degrade the system resolution. Increased spectral noise (Figure 2-6c) gives similar resolution however dramatically decreases signal to noise performance by raising the noise floor.

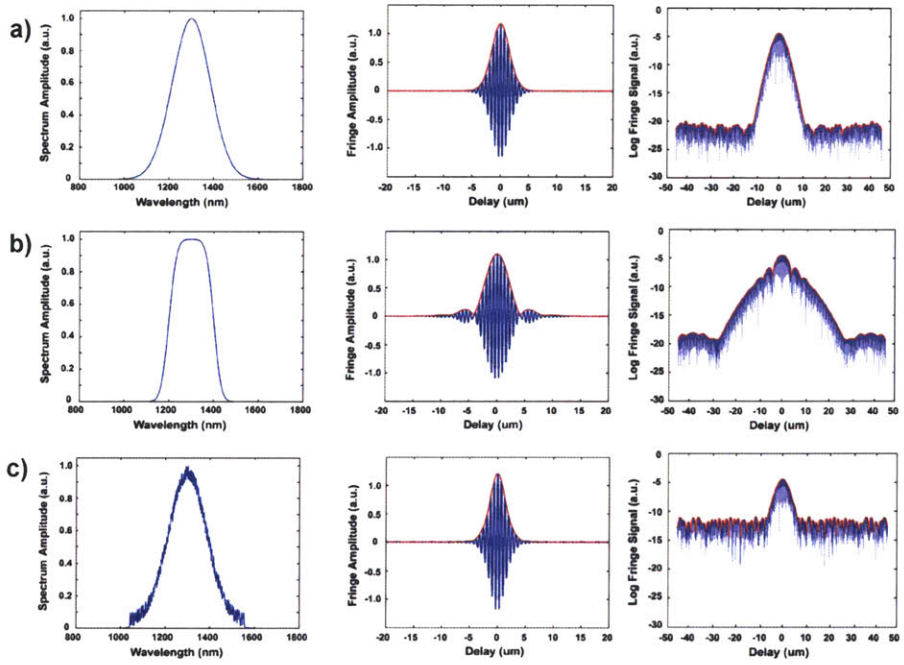

Figure 2-6. Effect of spectral modulation on OCT interference signal

FWHM optical bandwidth 200nm, center wavelength 1300nm, Doppler frequency 14 MHz, Spectral noise 0.5 dB

OCT Considerations

For this work there were several metrics such as image resolution, signal to noise, and system dynamic range that were considered and optimized to achieve the best imaging performance possible. In order to understand how system performance is affected by these variables, factors affecting imaging performance will be discussed below to provide insight into the design of a high performance OCT systems and how these systems were achieved for this work.

Resolution and Depth Penetration

The main component affecting image resolution in OCT is the optical light source. As was seen in the previous section, OCT uses low coherence interferometry to axially localize a signal within a tissue sample. The shorter the coherence length of the light source is, or equivalently the broader the optical bandwidth, the greater the degree of localization, resulting in higher axial resolution. Several types of light sources are available and vary from tungsten filaments to superluminescent diodes to solid-state modelocked lasers. While it is possible to implement almost any light source, the highest performance has usually been obtained through the use of modelocked laser oscillators. The reason for this is two-fold. First is that these sources have high brightness which, after coupling into an optical fiber can provide 30-100 mW of optical power into the OCT system.

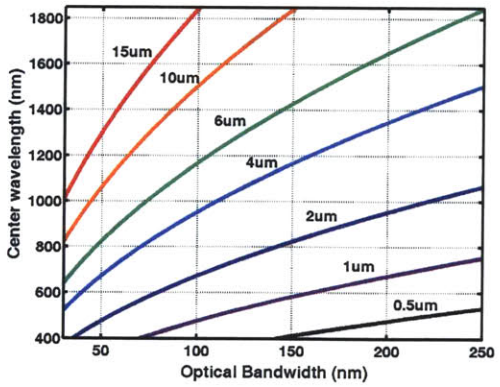

Figure 2-7. OCT resolution as a function of optical bandwidth & center wavelength

Low coherent femtosecond oscillators can typically achieve 1-2um resolutions with a center wavelength of 800nm (Ti:Sapphire) or 4-5um resolutions with a center wavelength of 1250nm (Cr:Forsterite). Superluminescent diodes have until recently been limited to 30-60nm optical bandwidths (10-15um resolution).

Higher power allows not only for increased signal levels at the photodetector but also enables higher speed imaging. This is because with higher power delivered onto the sample, the optical beam can be scanned more rapidly to give the same signal strength for the same amount of energy incident on a sample per unit time and per unit area. The second reason why modelocked lasers have been used is because the optical bandwidth of these sources can reach several hundreds of nanometers. Figure 2-7 shows a contour plot of the theoretical OCT resolution that can be achieved as a function of the light source bandwidth and center wavelength. Previous work has primarily used superluminescent diodes with optical bandwidths of 30-60nm. These give 10-15um resolutions, which are quite good when compared to typical MRI or ultrasound resolution (100-200um). Femtosecond lasers however can increase resolution by almost an order of magnitude using either Ti:Sapphire (800nm center wavelength, 200-300nm bandwidth) or Cr:Forsterite (1250nm center wavelength, 150-250nm bandwidth) oscillators. The main drawbacks to these laser oscillators are their cost, complexity and maintenance. With sufficient expertise however they are capable of providing very high resolution capability for a properly designed OCT system.

Another important factor in OCT imaging is the degree to which light can penetrate turbid, non-transparent tissue media. Figure 2-8 shows a plot of the optical absorption spectra as a function of wavelength in the near infrared. As the main constituent in biological tissue is water, an optical window of low water absorption from 700-1300nm provides an optimal region within which imaging can be done with increased tissue penetration. For this reason the near-IR wavelength range is often referred to as the diagnostic or therapeutic window.

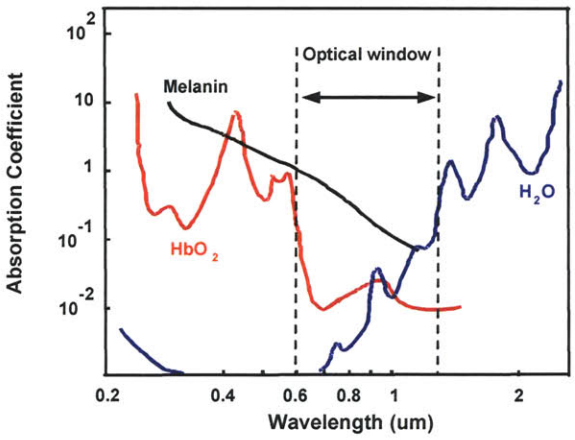

Figure 2-8. Optical absorption as a function of wavelength

An imaging window exhists in the near infrared wavelength range where absorption due to both water and hemoglobin is low. This allows light to penetrate effectively into tissue with significantly less attenuation. Note that the vertical axis for absorption is on a log scale. Reprinted from reference [14].

Depth of field

One of the useful characteristics of OCT is that the axial and transverse resolutions are decoupled from each other. This allows for optimization of parameters affecting the axial resolution without degrading the imaging performance in the transverse dimension. As seen in the previous section, the axial or depth resolution in OCT is governed by the center wavelength and optical bandwidth of the light source used. The transverse resolution is determined by the numerical aperture of the focusing elements used in the sample arm probe and is given by

$$dx = \sqrt{\frac{2b\lambda}{\pi}} = 2\omega_o \qquad \text{or equivalently} \qquad dx = \frac{4\lambda f}{\pi D} \approx \frac{\lambda}{2NA}$$

where b is the confocal parameter, λ is the center wavelength, and ω_o is the full-width half-maximum beam waist at the focus (half the FWHM beam diameter). In the second expression f is the lens focal length and D represents the diameter of the input beam. Axial resolution can be improved by increasing the optical bandwidth of the light source and transverse resolution can be independently modified by changing the numerical aperture of the focusing objective in the sample arm. Figure 2-9 shows the effect of using a low numerical aperture versus high numerical aperture lens on the propagation of the optical beam.

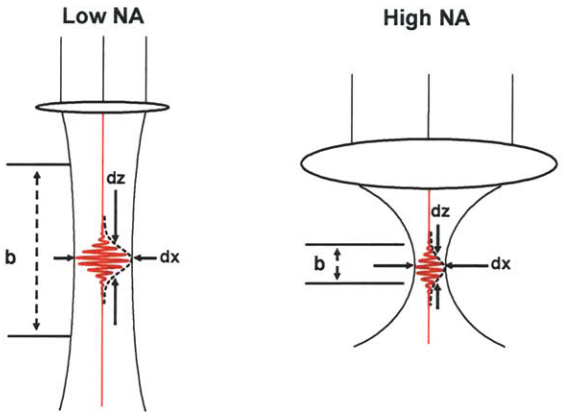

Figure 2-9. Schematic of low NA versus high NA focusing

Using low numerical aperture lens results in a focused beam with an increased depth of field. With a high NA lens the depth of field is reduced however the transverse resolution is increased.

As the optical beam propagates its lateral resolution expands obeying Gaussian beam optics. The beam waist as a function of distance, z, away from the focal point is given by

$$\omega(z) = \omega_o \sqrt{1 + \left(\frac{\lambda z}{\pi \omega_o^2}\right)^2}$$

where ω_o is the waist size at the focus. The transverse resolution is approximately equal to beam diameter at the focus and can be considered as the point at which two Gaussian beam profiles can be resolved with 50% contrast. A parameter that must be considered in the optical design of an OCT system is the depth of field over which the optical beam remains in focus. Higher NA lenses allow for increased transverse resolution but result in a limited depth over which the beam is uniformly focused. As the beam diverges the OCT image quality degrades due to blurring and decreased backscattered signal away from the focus.

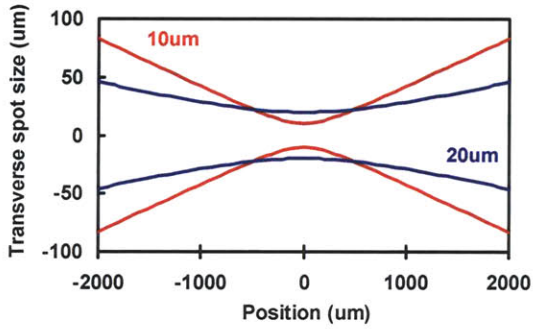

Figure 2-10. Expansion of a Gaussian beam away from its focus

The depth of field for a 20um focused beam is larger by a factor of 4 when compared to a 10um focused beam as the confocal parameter depends quadratically on the beam spot size.

Figure 2-10 shows the profile of two Gaussian beams, one focused to a 10um transverse spot size and one focused to a 20um spot size. As can be seen, the more tightly focused beam diverges rapidly as it propagates away from the focus. This effect causes the transverse resolution in an OCT image to decrease and also results in a loss of signal contrast as the optical energy deposited per unit volume is significantly lower away from the focus. Additionally for the same focused spot size, higher beam divergence and loss of transverse resolution are more pronounced at a higher operating wavelength. Figure 2-11 shows the dependency of the confocal parameter on the transverse spot size resolution as a function of two different wavelengths. A higher confocal parameter implies greater depth of field. While depth penetration in tissue is greater at 1300nm, divergence of the optical beam is more pronounced thus care must be taken to select the optimal focusing parameters to obtain high resolution images across the full OCT scan range.

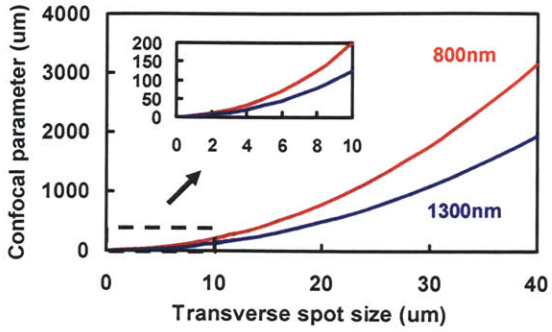

Figure 2-11. Confocal parameter as a function of transverse spot size

For a given transverse resolution, the beam divergence is greater for a higher wavelength. The confocal parameter and corresponding depth of field are therefore lower at higher wavelengths.

Figure 2-12 shows an example of two OCT images of a finger cuticle obtained with different focusing objectives. The image on the left used a 15mm focal length objective to focus the optical beam to a 10um transverse spot size on the sample. For the image on the right, an objective with a 40mm focal length lens was used for a spot size of 20um at the focus.

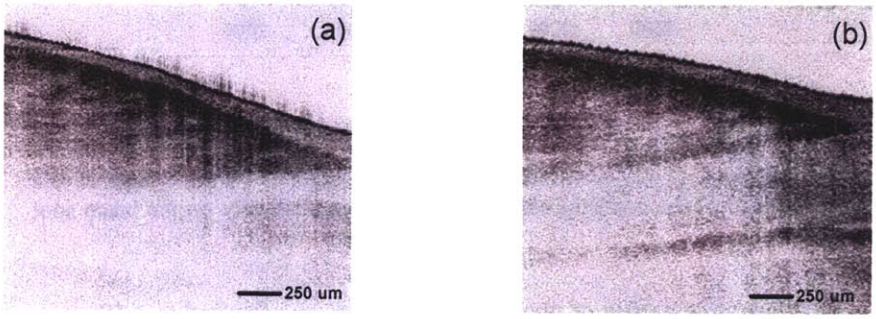

Figure 2-12. Effect of focusing optics on image resolution and depth of field

Tighter focusing with a 10um spot size (a) shows greater feature delineation within the cuticle region. Depth of field is limited however to approximately 1mm. Using a lower numerical aperture for a 20um spot size results in increased depth of field within the image (b) however with lower transverse resolution.

The image penetration in Figure 2-12b appears to be greater. As both images were taken with the same operating wavelength, the increased depth of field is due to the lower divergence of the optical beam within the sample. In the first image a higher level of detail can be seen over the scan range however the focal depth is lower. This example demonstrates the tradeoff in OCT between the transverse resolution and the optical depth of field. When designing an OCT system it is important to choose these parameters carefully so that optimal image quality is achieved for a given imaging objective.

Low Coherence Light Sources

The optical light source used in OCT is one of the most important components which determines system performance. Not only does it directly affect the axial and transverse resolutions, it also influences image contrast, signal levels, noise characteristics, imaging speed, ease of use, and system cost. Table 2-1 summarizes several low coherence light sources that can be used for OCT. These sources all utilize a laser cavity of some sort to achieve a high power, spatially coherent output that can be coupled into an optical fiber. Other light sources that have very broad bandwidth such as tungsten filaments or other white light sources can also be used. They provide the capability to achieve high resolution however at the expensive of low power due to inefficient fiber coupling. This restriction requires these systems to scan an OCT image rather slowly which limits their use for clinical or *in vivo* imaging studies.

Table 2-1	1300nm SLD [15]	800nm SLD [1]	Nd:Glass pumped High NA fiber [16]	Cr:Forsterite oscillator [17]	Ti:Sapphire oscillator [18]	Ti:Sapphire + PCF fiber [19]
Bandwidth	30-60 nm	30-140 nm	140 nm	240 nm	250 nm	1200 nm
Center Wavelength	1300 nm	800 nm	1050 nm	1250 nm	800 nm	800nm
Power	30 mW	5 mW	100 mW	50 mW	60 mW	150 mW
Resolution	12-25 um	2-10 um	5 um	4 um	2 um	1 um
Noise	Low	Low	Medium	Low	Low	High

Superluminescent Diode Laser

For the initial studies in this work, a superluminescent diode (SLD) light source was used. This source provided an optical bandwidth of 65nm at a center wavelength of 1330nm allowing for 10-15um imaging resolution. SLD sources are the most common sources that have been used for OCT imaging to date and have been used in many OCT studies both at 800nm and 1300nm wavelength ranges [20-23]. They have shown great utility and offer several advantages over other light sources such as relatively high power, broad optical spectra, reasonable cost, and turn-key operation. SLD's typically consist of an edge-emitting multiple quantum well structure with angled end facets to minimize optical loss and feedback effects. Figure 2-13 shows a plot of the optical output of a commercially available SLD light source from AFC Technologies.

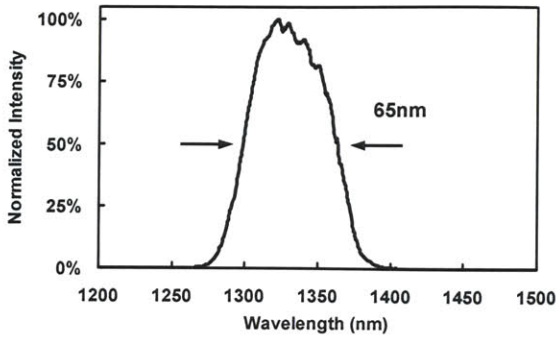

Figure 2-13. Normalized optical spectra of a SLD light source at 1330nm
This turnkey diode laser source is highly useful for reliable operation and long life. A 65nm optical bandwidth allows for OCT axial resolutions of 12um.

As SLD's are continuous wave (CW) sources, it is possible to combine multiple spectra from individual sources with fiber couplers. This generates broader bandwidth (increasing image resolution) however comes at the expense of lower optical power. Some OCT applications though do not need high sample power for imaging. In particular, ophthalmic imaging requires the delivered optical power on the retina to be quite low, on the order of microwatts, in order to stay within safe exposure limits.

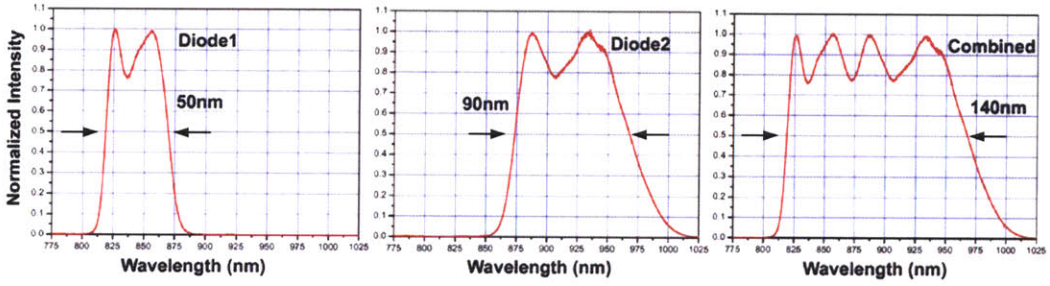

Figure 2-14. Optical spectra of individual and combined SLD spectra
By altering the quantum well structure with the diode, shifts in the emitted center wavelength can be achieved. By combing the optical output of these modified qunatum well structures, a broadband spectra can be achieved.

Figure 2-14 shows the optical output of two diode lasers with slightly modified quantum well structures. By combining these two spectra an optical bandwidth of 140nm at 900nm center wavelength can be achieved. This source is a prototype that has been tested in our laboratory for ophthalmic imaging and may soon be commercially available.

Titanium Sapphire Modelocked Laser

Investigation of imaging at ultrahigh resolution was also done using a modelocked femtosecond Ti:Al_3O_2 solid state laser which produces femtosecond pulses with a center wavelength of 800nm. This laser was originally developed in our laboratory for the demonstration of sub-two-cycle optical pulses of ~5fs in duration [24]. Figure 2-15 shows a schematic diagram of the Ti:Sapphire laser cavity used for high resolution imaging studies in this work.

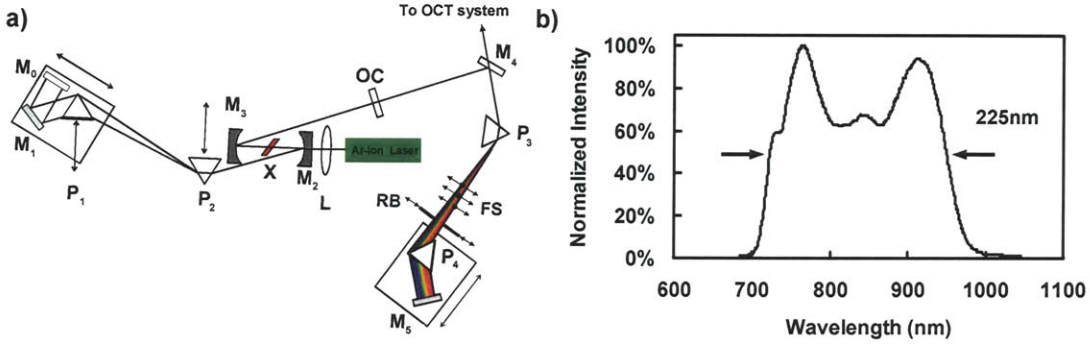

Figure 2-15. Cavity and spectrum of modelocked Ti:Sapphire femtosecond laser

a) Pump lens (L), gain crystal (X), DCM mirrors (M_2, M_3), flat end mirror (M_0) and output coupler (OC). Intracavity CaF2 prisms (P_1, P_2), extracavity quartz prisms (P_3, P_4), fiber splices (FS) and razor blade (RB) slit aperture. b) Output spectrum after spectral shaping. Cavity diagram from reference [24].

A Ti:Al_3O_2 crystal is used as the gain medium and is pumped by a continuous wave argon-ion laser at 5 W. The slope efficiency of the laser is approximately 40 mW/W thereby producing a typical output CW power of 150-200 mW. The resonator is configured in a Z-fold design with the Ti:Al_3O_2 crystal (X) oriented at its Brewster angle to minimize loss. The laser is operated with near zero intracavity dispersion to facilitate modelocking operation. Dispersion control is achieved through the use of specially designed double chirped mirrors (M_1, M_2) [25, 26] and intracavity CaF_2 prisms (P_1, P_2). The double chirped mirrors (DCMs) produce net negative second order dispersion in the optical pulse. This offsets the positive second order dispersion generated by the pulse propagating in the cavity and passing through the Ti:Al_3O_2 crystal. The DCMs however do introduce negative third order dispersion which is balanced out by the intracavity CaF_2 prisms. Fused quartz prisms (P3, P4) are placed extracavity and are used to spread out the laser spectrum and perform manual spectral shaping with fiber splices (FS) and a razor blade (RB) slit aperture. The individual fibers provide spatial line filters for fine bandwidth tuning while the slit aperture can be used to truncate low or high end spectral components. By modifying the laser spectrum to approximate a Gaussian profile, higher OCT

resolution is achieved due to the reduction of sidelobes in the heterodyne interference signal (see Figure 2-6). After the cavity output coupler (OC) the pulse is retroreflected at M6 and coupled into the OCT interferometer system. The very high optical power (100-300mW) and broad bandwidth (>250nm) capabilities of these lasers have made them the tool of choice for high resolution OCT systems. They also have broad application to many areas of research such as femtosecond chemical dynamics, spectroscopy, and nonlinear phenomena. Their widespread use and clinical implementation of these lasers for OCT however is likely to be limited due to the complexity and alignment sensitivity of the laser cavity.

Chromium Forsterite Modelocked Laser

Another laser resonator that was used for high resolution imaging studies in this work was a compact modelocked Cr^{4+}:Forsterite laser developed by Karl Schneider, a visiting researcher to the laboratory. The advantage of this laser is that broadband optical spectra of over 200nm can be generated at 1250nm center wavelength to achieve 4-5um axial resolution in air [17, 27]. This wavelength range has lower absorption in tissue than the Ti:Sapphire 800nm wavelength range and allows for increased depth penetration in the OCT image. A schematic and photograph of the laser are shown in Figure 2-16.

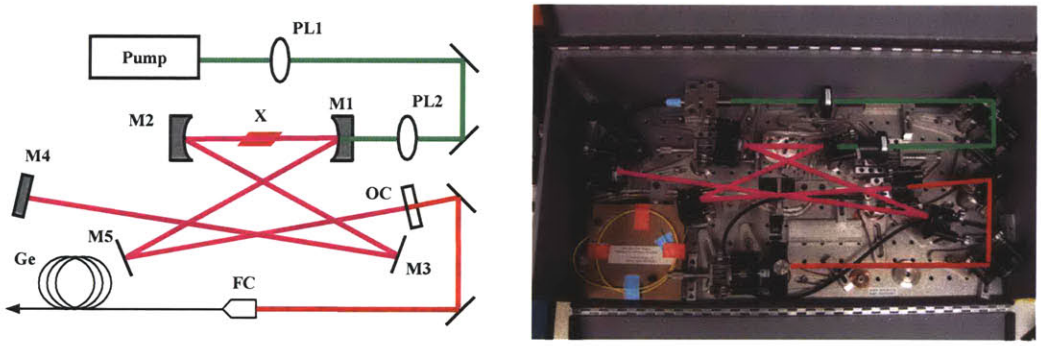

Figure 2-16. Schematic & photograph of compact, broadband Cr^{4+}:Forsterite laser

A prismless x-cavity cavity design is used with double chirped mirrors to compensate for intra-cavity dispersion. Cavity arm lengths of 50 and 67cm with a 11cm DCM seperation give a pulse repetition rate of ~11.7 MHz (confirmed experimentally with pulse measurement).

The cavity is prismless and utilizes double chirped mirrors to operate at near zero intra-cavity dispersion. It is configured in a folded x-cavity design with multiple beam crossings. This makes the laser more sensitive to alignment however allows the system to be highly compact and portable for use in clinical studies. In addition, Forsterite lasers are also more susceptible to thermal lensing effects and birefringence than Ti:Sapphire systems which makes them more

difficult to operate. The laser cavity is pumped by a Nd:Glass fiber laser at 5 watts and uses a Brewster cut Cr^{4+}:Forsterite crystal to generate optical bandwidths of up to 80 nm in modelocked operation. Pulse durations are on the order of 40-50 femtoseconds assuming a transform limited time-bandwidth product. The pulses are coupled into a Germanium doped optical fiber that broadens the spectrum through higher order nonlinear optical effects.

The output coupler is mounted on a moving translation stage that is manually shaken to introduced mode instability and initiate modelocking operation. Once modelocked, extra-cavity turning mirrors and a 3-axis translation stage are used optimize power coupling into the Germanium fiber. Figure 2-17 shows experimental data of generated spectra as a function optical power coupled into the nonlinear fiber. As the spectra are highly symmetric about the zero dispersion point at 1280nm, self-phase modulation is most likely the dominant mechanism for the spectral broadening. Four-wave mixing and soliton self-frequency shifting may also play a role as the modelocked power of 140-150mW is high enough to form optical solitons. The generated optical bandwidth exhibits a square root dependence on input power (Figure 2-17b) which is consistent with experiments on nonlinear continuum generation in optical fibers.

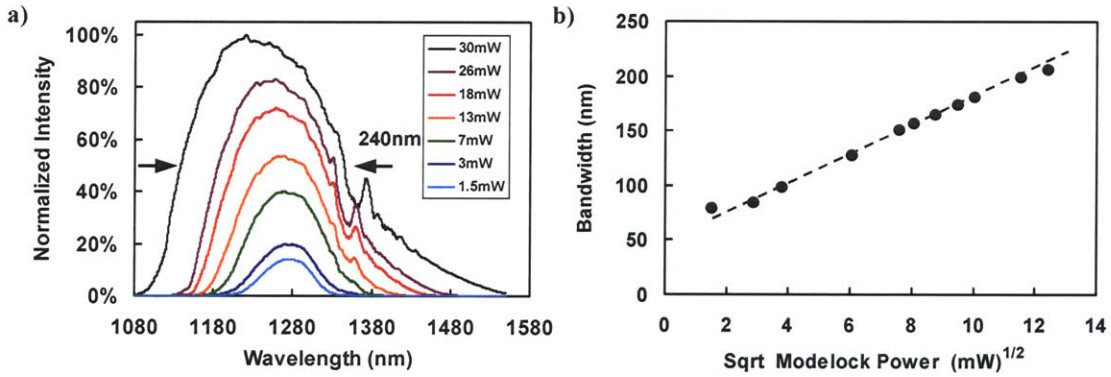

Figure 2-17. Optical spectrum generation with nonlinear Ge-doped fiber

a) Spectral bandwidth generated as a function of fiber-coupled optical power exhibits symmetric broadening about the the zero dispersion wavelength of 1280nm. b) Modelocked output power plotted against bandwidth shows a square root dependence beteen bandwidth and laser power indicative of nonlinear spectral broadening.

During imaging the Forsterite is fairly stable over several hours of operation however periodic retuning of the cavity is necessary to achieve optimal output characteristics. The highest bandwidth and power points are typically respectively located at the inner edge of the outer stability region or the outer edge of the inner stability region where the pump mode and laser mode have the highest overlap.

Diode Pumped Nd:Glass Fiber Laser

While modelocked lasers have proven their capability as high brightness, broadband sources for OCT they have several drawbacks which limit their use in clinical application. Most significant is their lack of stability over extended periods of time (days to weeks) and highly sensitive alignment requirements. Typically individuals with a high level of laser expertise are needed even to operate these systems. Additionally they can be prohibitively expensive with component costs of up to $100,000 including the pump laser, DCM mirrors and optical components. In the past several years, there has been recent development of high power fiber lasers that utilize diode pumping to generate broadband optical spectra. These lasers have the advantage over modelocked lasers in that they are turn-key, reasonably priced, and commercially available. While they do not give the highest performance possible, the optical resolution and power levels are comparable to modelocked lasers.

One such system is a femtosecond Nd:Glass laser made by High Q of Austria. Figure 2-18 shows a photograph of the laser system which is contained within a enclosure. The laser outputs 100-200mW of modelocked power at a center wavelength of 1070nm. This is coupled into a tapered or high numerical aperture fiber which again broadens the spectrum though nonlinear effects and generates up to 95mW of optical power with a spectral bandwidth of 140nm [28].

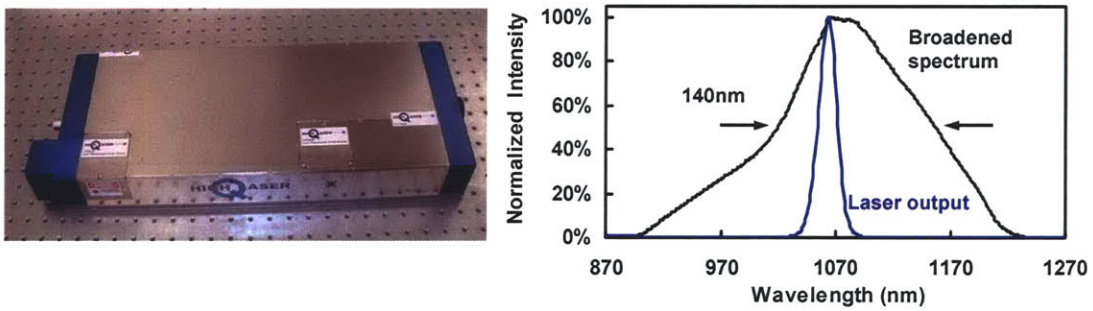

Figure 2-18. Photograph of ND:Glass laser and output spectra

The output laser spectra of 10nm (150 fs pulse width) at 1062nm is spectral broadened in a high NA fiber to generate 140nm of optical bandwidth. Original demonstration in [16].

While the optical bandwidth of this source is lower than the Forsterite laser, the shorter operating wavelength at 1062nm versus 1250nm allows for almost equivalent axial resolutions of 4-5um to be achieved. In addition as this source lies in between the 800nm and 1300nm operating regimes it offers a good compromise between depth penetration and image resolution. One significant change that must be accounted for when using this source is to modify the fiber interferometer and optical components to operate at 1062nm. Typical SMF28 fiber with a 9um

core used in 1300nm systems cannot support singlemode operation below a cutoff wavelength of approximately 1100nm. If this fiber is used in a 1um system, multimode effects will lead to distortion of the interferometric signal and decrease resolution as well as image quality.

Continuum Sources using Photonic Crystal Fiber

In the past several years there has been increasing interest in the use of nonlinear optical fibers to generate broadband light continuum. The use of continuum sources can be used for OCT but also has numerous applications in research areas ranging from laser spectroscopy to ultrashort pulse generation [29, 30]. Use of a continuum source for high resolution OCT imaging was first demonstrated in our group using a microstructured air-silica fiber [31]. By pumping the microstructured fiber with a high intensity femtosecond pulse and coupling into a dispersion shifted fiber, a spectral bandwidth of up to 450nm at a center wavelength of 1300nm was generated. This enabled *in vivo* imaging with 2.5um axial resolutions. Results from this fiber source are shown in Figure 2-19.

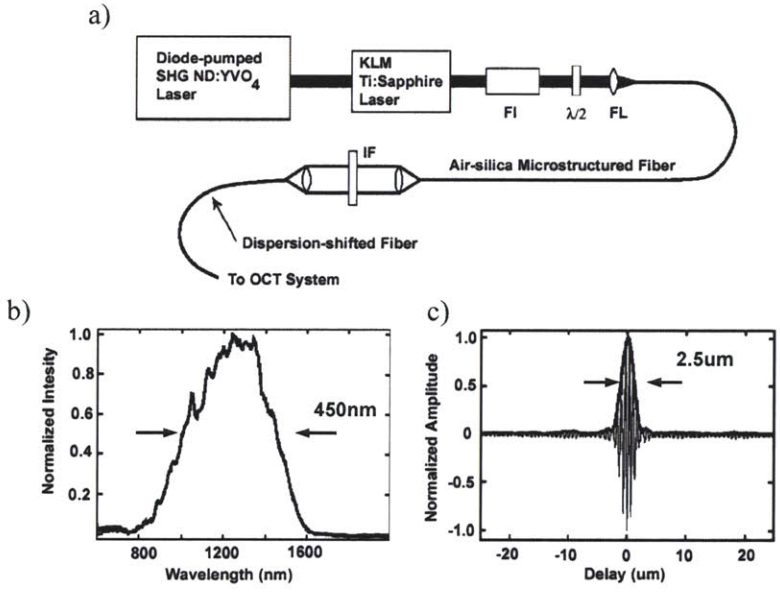

Figure 2-19. Continuum fiber source for OCT using microstructured fiber

a) Schematic of the continuum fiber source for OCT utilizing a diode pumped Ti:Sapphire laser. Femtosecond optical pulses are used to pump an air-silica microstructure and dispersion-shifted fiber for continuum generation and subsequent spectral broadening. b) Optical bandwidth generated at the output of the dispersion shifted fiber and c) axial resolution measurement of the OCT system. Reprinted from reference [31].

This system, while demonstrating high resolution OCT with a fiber based source, is somewhat complex due to the necessity for a pump laser, Ti:Sapphire oscillator, and two types of nonlinear fibers to generate the spectral continuum. Research in this area however is quite active and a light source that was recently developed by Imperial College in London has been tested in our laboratory. It is a continuous wave source that uses a diode-pumped Yb fiber laser and photonic crystal fiber to generate broadband continuum with up to 330mW of output power (Figure 2-20). Previous studies have demonstrated the utility of Yb based fiber sources for OCT imaging [32].

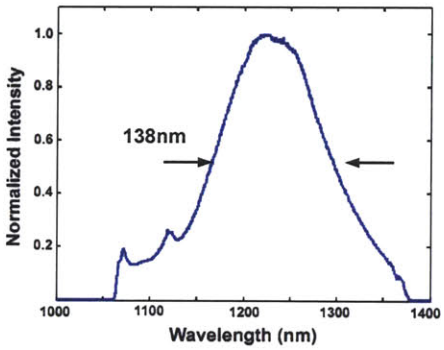

Figure 2-20. Optical spectrum of Ytterbium fiber source

The Ytterbium fber source generates 138nm of bandwidth with 3.8W of output power. Original demonstration of fiber laser in reference [33]

The development of this source and its demonstration in our laboratory shows the increasing possibility of using fiber sources for high resolution OCT studies. It is expected that broadband, high power lasers will soon be readily available for OCT imaging in both laboratory and clinical settings. The availability of compact, portable, and relatively inexpensive broadband light sources for OCT promises to provide researchers the capability to conduct high resolution imaging studies more readily than ever before.

One factor that has not been discussed yet is the noise characteristics of these sources. When high intensity pulses are used to generate continuum, shot to shot variability can result in "noisy" spectra with high background levels of coherent light or large spectral modulations. This effect is reduced by using continuous wave sources such as the Raman-based diode laser developed by Imperial College. Regardless of which optical source used however, it is important to measure the RF spectrum and determine if the noise levels are within acceptable limits at the electronic heterodyne and demodulation frequencies. Additionally care must be taken to minimize optical feedback into these laser cavities as damage and eventual failure will occur.

Optical Properties of Tissue

High resolution optical imaging of biological systems is challenging as most tissues are non-transparent and have a complex architectural structure. The two main processes that influence imaging in tissue are absorption and scattering. These processes are often considered detrimental to imaging however are not necessarily negative aspects and can provide both diagnostic information and enable therapeutic treatment. For example, by using a femtosecond broadband light source, optical absorption can be used to resolve differential spectroscopic properties of tissue structure [34, 35]. Optical excitation of chromophores [36, 37], fluorophores [38, 39], or quantum dot nanoparticles [40, 41] also use absorption processes for diagnostic imaging applications. Finally therapeutic applications such as laser ablation and corneal refractive surgery have been demonstrated utilizing localized heating or vaporization of tissue.

For imaging, the main absorbers in tissue and blood are oxyhemoglobin, deoxyhemoglobin, and water. There exists however an optical window in the near infrared wavelength range where absorption is minimized (see Figure 2-8). This window is used for optical imaging due to the decreased absorption and corresponding increased light penetration in tissue and is often referred to as a diagnostic or therapeutic window. In addition while blood is a strong absorber in this wavelength range, many tissues have a low blood concentration of a few percent.

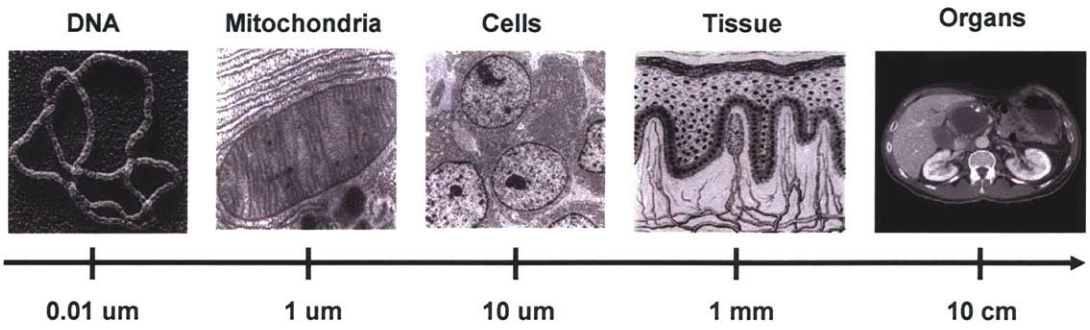

Figure 2-21. Size scale of tissue and cellular structures

Scattering is due to the interaction of light with electrons, molecules and particles within tissue structure. It affects changes in the internal distribution, polarization, and reflection of light. The scattering profile (angular distribution) of incident light can be described for geometrically simple shapes such as spheres however detailed mathematical descriptions are not available for complex biological structures. For most turbid tissues thicker than a few tens of microns, light propagation is typically characterized by multiple scattering. These multiple interactions wash out

the detailed structure associated with individual scattering events and permit a simplification in the description of the scattering process [42]. Figure 2-21 shows a scale of typical structures within tissue and cells. Scattering caused by structures on the same size scale as the incident light wavelength is well described by Mie theory [43-46]. Such scattering centers consist of cellular organelles which are on the order of 1-2 um in size. The size of cell nuclei range from 5-7um while cells sizes can be as large as 10-30 um. If the dimensions of the scattering structures are much smaller than the optical wavelength Rayleigh scattering dominates [47, 48]. Collagen, macromolecular aggregates and cell membranes fall into this range with typical dimensions of 10-100nm. Several numerical simulations using Monte Carlo methods and finite difference time domain methods have also been used to analyze cell and tissue scattering models [49-51].

A well accepted approach to describing light interaction in turbid medium uses radiative transport theory [52-54]. The propagation of optical waves in tissue is quantified in terms of energy loss with effective scattering and attenuation constants. In the case of multiple scattering, an effective scattering coefficient can be defined [55]

$$\mu_s' = \left(1 - \langle \cos\gamma \rangle\right)\mu_s$$

where γ is the scattering angle $1/\mu_s$ is the mean distance between isotropic scattering events. Typical values in tissue of μ_s are on the order of 2-20 cm^{-1} however μ_s' is approximately on tenth of this value. Including absorption processes, the total interaction coefficient is given by $\mu_t = \mu_s + \mu_a$ and the mean free path of the photon between scattering events is $1/\mu_t$. The absorption of the tissue can be described by an exponential decay function known as the Lambert-Beer law

$$P = P_o e^{-\mu_t z}$$

where P_o is the initial power, P is the remaining power, and z is the propagation distance traveled. A theoretical understanding of the optical scattering and light transport in tissue is very powerful and several studies have been done showing the validity of the Lambert-Beer law for the scattering of light in turbid media [56-58].

Tissue Viability

Living tissue is a highly complex system that functions through the careful balance and interplay of many mechanisms on sub-cellular, cellular, and extra-cellular levels. Of these mechanisms the one that most directly affects optical imaging performance in the near infrared

wavelength regime is the balance of osmotic forces to maintain tissue hydration. In its hydrated state, tissue and cellular volume is increased which enables structural features to be resolved more readily by OCT imaging. The presence of subcellular constituents such as melanin, mitochondria, and extracellular fluid also affect the imaging of tissue microstructure as changes in absorption and scattering processes on a macroscopic scale are influenced by these microscopic particles. Needless to say the processes that maintain tissue integrity can only be performed so long as the tissue is maintained in a viable environment that sustains life. Loss of blood flow, oxygen deprivation, injury, or excision can quickly initiate cellular death and tissue autolysis.

Many studies have been conducted imaging tissues both *in vitro* and *in vivo* using OCT [59-65]. In reviewing the literature it is apparent that for many studies the imaging performance and ability to distinguish architectural detail in tissue is greater for viable, living specimens than for excised samples. There are several reasons for this. One as mentioned previously is the degree of tissue hydration which increases cellular volume. An example of this is shown in Figure 2-22 where an excised specimen of rabbit small intestine is imaged *ex vivo*. Initially the tissue is somewhat dehydrated in the first image shown in Figure 2-22a . After buffered saline is applied to the tissue it become more hydrated and architectural features can be distinguished more clearly (Figure 2-22b, c).

Figure 2-22. Effect of tissue hydration on imaging performance
Increasing tissue hydration enables enhanced visualiztion of villous architecture in the rabbit intestine by more closely approximating natural conditions *in vivo*.

In addition to hydration, the integrity of interfacial membranes and tissue layers is another factor that influences image resolution. As contrast in intensity-based OCT imaging is derived from differential changes in reflection within the tissue, interfaces between heterogeneous tissue layers produce highly scattering signals. This is particularly true for high resolution OCT which has the capability to distinguish slight changes in tissue index of refraction due to altered physiological structure. Even slight changes in tissue type or orientation can be detected with sufficiently sensitive OCT systems that employ high resolution, polarization sensitivity or

spectroscopic imaging capabilities. Figure 2-23 shows an example of an *in vivo* OCT image of an animal esophagus exhibiting varying degrees of image contrast.

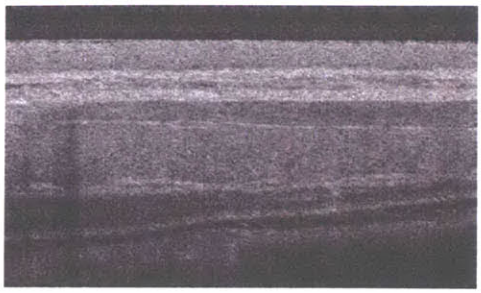

Figure 2-23. Multi-layered structure and tissue differentiation

OCT scan of the rabbit esophagus demonstrates high image contrast and differentiation of layers within the tissue. Interface boundaries and changes in tissue type and orientation alter the backscattered light intensity.

After cell death, many chemical processes are initiated that break down the cell and release its contents into the extracellular space. These constituents, while smaller than the imaging resolution of the OCT beam, affect scattering and absorption processes which subsequently alter the interaction of the light signal with the tissue environment. The net effect is to increase scattering in the tissue which reduces the ability of OCT to resolve structural detail. In addition, optical penetration is reduced causing imaging performance to degrade. Figure 2-24 illustrates the dramatic reduction in image quality for a tissue sample imaged *in vivo* and then excised and imaged *ex vivo*. Despite a time lapse of only 5-10 minutes between the images, it is apparent that after death, the tissue viability is rapidly compromised and imaging capability can be reduced.

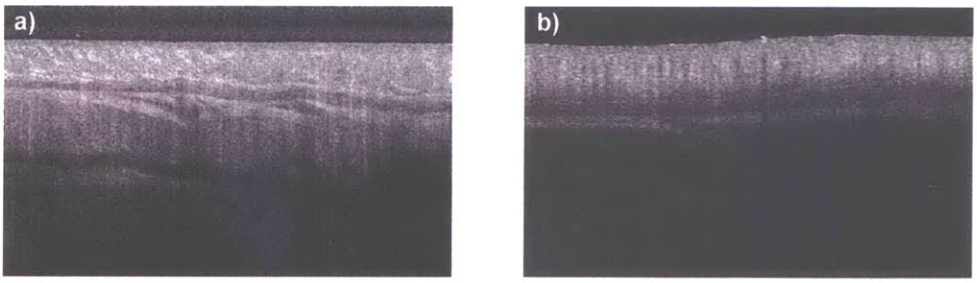

Figure 2-24. OCT image comparison of *in vivo* and *ex vivo* tissue

Imaging of rabbit colon *in vivo* (a) shows increased tissue penetration, image contrast, and structural detail. Imaging the same tissue *ex vivo* (b) shortly after excission illustrates reduced imaging performance.

Histological Staining

A final area that should be considered is the fixation and staining of tissue for comparison with OCT images. Histology processing is the gold standard for the analysis of tissue pathology in medicine [66]. Various preservation and staining techniques can allow for delineation of both tissue structure and function at the sub-cellular level. The most commonly used staining technique uses hematoxylin and eosin (H & E) chemical dyes. Hematoxylin stains acidic structures a purplish blue color. Both nuclei and endoplasmic reticulum strongly absorb this dye respectively due to their high content of DNA and RNA. Eosin is an acidic dye which stains structures which are more basic in pH a red or pinkish hue. For most of the comparative OCT and histology pairs H & E staining has been used in this work. A secondary dye used for stains is Masson's trichrome. Trichrome delineates collective tissue elements well, with collagen or cartilage staining blue and cytoplasm, muscle, and keratin staining a bright red.

References

1. D. Huang, E. A. Swanson, C. P. Lin, J. S. Schuman, W. G. Stinson, W. Chang, M. R. Hee, T. Flotte, K. Gregory, C. A. Puliafito, and J. G. Fujimoto, "*Optical coherence tomography,*" Science, **254**, 1178-81 (1991).
2. J. M. Schmitt, M. Yadlowsky, and R. F. Bonner, "*Subsurface imaging of living skin with optical coherence tomography,*" Dermatology, **191**, 93-98 (1995).
3. C. Pitris, A. Goodman, S. A. Boppart, J. J. Libus, J. G. Fujimoto, and M. E. Brezinski, "*High-resolution imaging of gynecologic neoplasms using optical coherence tomography,*" Obstetrics and Gynecology, **93**, 135-9 (1999).
4. S. A. Boppart, M. E. Brezinski, B. E. Bouma, G. J. Tearney, and J. G. Fujimoto, "*Investigation of developing embryonic morphology using optical coherence tomography,*" Developmental Biology, **177**, 54-63 (1996).
5. M. R. Hee, J. A. Izatt, E. A. Swanson, D. Huang, C. P. Lin, J. S. Schuman, C. A. Puliafito, and J. G. Fujimoto, "*Optical coherence tomography of the human retina,*" Archives of Ophthalmology, **113**, 325-332 (1995).
6. S. A. Boppart, B. E. Bouma, C. Pitris, G. J. Tearney, J. G. Fujimoto, and M. E. Brezinski, "*Forward-imaging instruments for optical coherence tomography,*" Optics Letters, **22**, 1618-1620 (1997).
7. A. H. Gandjbakhche, V. Chernomordik, R. F. Bonner, R. Nossal, and G. H. Weiss, "*High resolution intraarterial imaging with optical coherence tomography,*" OSA Trends in Optics and Photonics on Advances in Optical Imaging and Photon Migration, **2**, 200-2 (1996).
8. G. J. Tearney, M. E. Brezinski, S. A. Boppart, B. E. Bouma, N. Weissman, J. F. Southern, E. A. Swanson, and J. G. Fujimoto, "*Catheter-based optical imaging of a human coronary artery,*" Circulation, **94**, 3013 (1996).
9. X. D. Li, C. Chudoba, T. Ko, C. Pitris, and J. G. Fujimoto, "*Imaging needle for optical coherence tomography,*" Optics Letters, **, in review** (2000).
10. J. G. Fujimoto, C. Pitris, S. A. Boppart, and M. E. Brezinski, "*Optical coherence tomography: an emerging technology for biomedical imaging and optical biopsy,*" Neoplasia, **2**, 9-25 (2000).
11. W. Drexler, U. Morgner, F. X. Kärtner, C. Pitris, S. A. Boppart, X. D. Li, E. P. Ippen, and J. G. Fujimoto, "*In vivo ultrahigh resolution optical coherence tomography,*" Optics Letters, **24**, 1221-1223 (1999).
12. E. A. Swanson, D. Huang, M. R. Hee, J. G. Fujimoto, C. P. Lin, and C. A. Puliafito, "*High-speed optical coherence domain reflectometry,*" Opt. Lett., **17**, 151-153 (1992).
13. *Biomedical Photonics Handbook*, ed. T. Vo-Dinh. 2003.
14. J. L. Boulnois, " *Photophysical processes in recent medical laser development: A review,*" Lasers Med. Sci., **1**, 47-66 (1986).
15. J. G. Fujimoto, M. E. Brezinski, G. J. Tearney, S. A. Boppart, B. Bouma, M. R. Hee, J. F. Southern, and E. A. Swanson, "*Optical biopsy and imaging using optical coherence tomography,*" Nature Medicine, **1**, 970-2 (1995).
16. S. Bourquin, A. D. Aguirre, I. Hartl, P. Hsiung, T. H. Ko, J. G. Fujimoto, T. A. Birks, and W. J. Wadsworth, "*Ultrahigh resolution real time OCT imaging using a compact femtosecond Nd:Glass laser and nonlinear fiber,*" Optics Express, **11**, 3290-3297 (2003).
17. B. Bouma, G. Tearney, I. Bilinsky, B. Golubovic, and J. Fujimoto, "*Self-phase-modulated Kerr-lens mode-locked Cr:forsterite laser source for optical coherence tomography,*" Optics Letters, **21**, 1839-42 (1996).
18. B. Bouma, G. J. Tearney, S. A. Boppart, M. R. Hee, M. E. Brezinski, and J. G. Fujimoto, "*High-resolution optical coherence tomographic imaging using a mode-locked Ti:Al/sub 2/O/sub 3/ laser source,*" Optics Letters, **20**, 1486-8 (1995).
19. Y. Wang, Y. Zhao, J. S. Nelson, Z. Chen, and R. S. Windeler, "*Ultrahigh-resolution optical coherence tomography by broadband continuum generation from a photonic crystal fiber,*" Optics Letters, **28**, 182-4 (2003).

20. E. A. Swanson, J. A. Izatt, M. R. Hee, D. Huang, C. P. Lin, J. S. Schuman, C. A. Puliafito, and J. G. Fujimoto, "*In vivo retinal imaging by optical coherence tomography,*" Optics Letters, **18**, 1864-6 (1993).
21. M. R. Lee, J. A. Izatt, E. A. Swanson, D. Huang, J. S. Schumun, C. P. Lin, C. A. Puliafito, and J. G. Fujimoto, "*Optical coherence tomography for ophthalmic imaging: new technique delivers micron-scale resolution,*" IEEE Engineering in Medicine and Biology Magazine, **14**, 67-76 (1995).
22. Y. Pan and D. L. Farkas, "*Noninvasive imaging of living human skin with dual-wavelength optical coherence tomography in two and three dimensions,*" Journal of Biomedical Optics, **3**, 446-55 (1998).
23. C. K. Hitzenberger, M. Danner, W. Drexler, and A. F. Fercher, "*Measurement of the spatial coherence of superluminescent diodes,*" Journal of Modern Optics, **46**, 1763-74 (1999).
24. U. Morgner, F. X. Kartner, S. H. Cho, Y. Chen, H. A. Haus, J. G. Fujimoto, E. P. Ippen, V. Scheuer, G. Angelow, and T. Tschudi, "*Sub-two-cycle pulses from a Kerr-lens mode-locked Ti:sapphire laser,*" Optics Letters, **24**, 411-413 (1999).
25. F. X. Kartner, N. Matuschek, T. Schibli, U. Keller, H. A. Haus, C. Heine, R. Morf, V. Scheuer, M. Tilsch, and T. Tschudi, "*Design and fabrication of double-chirped mirrors,*" Optics Letters, **22**, 831-833 (1997).
26. N. Matuschek, "*Theory and design of double-chirped mirrors,*" Swiss Federal Institute of Technology: Zurich (1999).
27. G. D. Sanders, C. K. Sun, B. Golubovic, J. G. Fujimoto, and C. J. Stanton, "*Self-phase-modulated Kerr-lens mode-locked Cr:forsterite laser source for optical coherence tomography,*" Optics Letters, **21**, 1839-41 (1996).
28. I. Hartl, P. Hsiung, T. H. Ko, J. G. Fujimoto, W. Wadsworth, T. Birks, U. Bunting, and K. Kopf. *High resolution OCT imaging using a spectrally broadened femtosecond Nd:Glass laser.* in *Conference on Lasers and Electro-Optics*. 2002. Long Beach, CA: Optical Society of America and IEEE.
29. W. Watanabe, Y. Masuda, and K. Itoh, "*Dispersive coherence spectrotomography with white-light continuum,*" Optical Review, **6**, 455-8 (1999).
30. N. Nishizawa and T. Goto. *Generation and characterization of widely broadened supercontinuum using highly nonlinear fibers and fiber laser.* in *OFC 2002*. 2002.
31. I. Hartl, X. D. Li, C. Chudoba, R. K. Ghanta, T. H. Ko, J. G. Fujimoto, J. K. Ranka, and R. S. Windeler, "*Ultrahigh-resolution optical coherence tomography using continuum generation in an air-silica microstructure optical fiber,*" Optics Letters, **26**, 608-610 (2001).
32. M. Bashkansky, M. D. Duncan, L. Goldberg, J. P. Koplow, and J. Reintjes, "*Characteristics of a Yb-doped superfluorescent fiber source for use in optical coherence tomography,*" Optics Express, **3** (1998).
33. S. V. P. A.V. Avdokhin, J.R. Taylor, "*Continuous-wave, high-power, Raman continuum generation in holey fibers,*" Opt Lett, **28**, 1353-1355 (2003).
34. M. Hammer, D. Schweitzer, L. Leistritz, M.Scibor, K. Donnerhacke, and J. Strobel, "*Imaging Spectroscopy of the Human Ocular Fundus In Vivo,*" J. Biomed. Opt., **418** (1997).
35. U. Morgner, W. Drexler, X. Li, F. X. Kaertner, C. Pitris, S. A. Boppart, E. P. Ippen, and J. G. Fujimoto, "*Spectroscopic optical coherence tomography,*" Optics Letters, **25**, 111-113 (2000).
36. J. Herbst, K. Heyne, and R. Diller, "*Femtosecond Infrared Spectroscopy of Bacteriorhodopsin Chromophore Isomerization,*" Science, **297**, 822-825 (2002).
37. M. Kohl, U. Lindauer, U. Dirnagl, and A. Villringer, "*Separation of changesin light scattering and chromophore concentrations during cortical spreadingdepression in rats,*" Opt. Lett., **23**, 555 (1998).
38. S. W. Hell, K. Bahlmann, M. Schrader, A. Soini, H. Malak, I. Gryczynski, and J. R. Lakowicz, "*Three-Photon Excitation in Fluorescence Microscopy,*" J. Biomed. Opt., **71** (1996).
39. M. Dellinger and M. Gèze, "*Detection of mitochondrial DNA in living animal cells with fluorescence microscopy,*" Journal of Microscopy, 196-202 (2001).
40. Y. C. Cao, R. Jin, and C. A. Mirkin, "*Nanoparticles with Raman Spectroscopic Fingerprints for DNA and RNA Detection,*" Science, **297**, 1536-1540 (2002).

41. F. Tokumasu and J. Dvorak, "*Development and application of quantum dots for immunocytochemistry of human erythrocytes,*" Journal of Microscopy, **211**, 256-261 (2003).
42. S. A. Prahl, N. Kollias, and R. R. Anderson, "*Light scattering in biologic tissues,*" Photochem. Photobiol., (1992).
43. H. van de Hulst, *Light Scattering by Small Particles*. 1957, New York: John Wiley & Sons.
44. L. T. Perelman, V. Backman, M. Wallace, G. Zonios, R. Manoharan, A. Nusrat, S. Shields, M. Seiler, C. Lima, T. Hamano, I. Itzkan, J. Van Dam, J. M. Crawford, and M. S. Feld, "*Observation of periodic fine structure in reflectance from biological tissue: a new technique for measuring nuclear size distribution,*" Physical Review Letters, **80**, 627-630 (1998).
45. L. T. Perelman, W. Jun, C. Kun, I. Itzkan, R. R. Dasari, and M. S. Feld, "*Photon paths in turbid media: from smooth to random,*" OSA Trends in Optics and Photonics on Advances in Optical Imaging and Photon Migration, **2**, 18-20 (1996).
46. C. F. Bohren and D. R. Huffman, *Absorption and Scattering of Light by Small Particles*. 1983, New York: John Wiley & Sons.
47. A. Maki, Y. Yamashita, Y. Ito, E. Watanabe, and H. Koizumi, "*Origins of tissue optical properties in the UVA, visible, and NIR regions,*" OSA Trends in Optics and Photonics on Advances in Optical Imaging and Photon Migration, **2**, 364-71 (1996).
48. J. S. Saidi, S. L. Jacques, and F. K. Tittel, "*Mie and Rayleigh modeling of visible-light scattering in neonatal skin,*" Appl. Opt., **34**, 7410 (1995).
49. R. Drezek, A. Dunn, and R. Richards-Kortum, "*Light scattering from cells: finite-difference time-domain simulations and goniometric measurements,*" Applied Optics, **38**, 3651-3661 (1999).
50. A. Dunn and R. Richards-Kortum, "*Three-Dimensional Computation of Light Scattering From Cells,*" IEEE Journal of Selected Topics in Quantum Electronics, **2**, 898-905 (1996).
51. Y. Pan, R. Birngruber, J. Rosperich, and R. Englehardt, "*Low-coherence optical tomography in turbid tissue: theoretical analysis,*" Appl Opt, **34**, 6564-6574 (1995).
52. A. E. Profio, "*Light transport in tissue,*" Appl Opt, **28**, 2250-2255 (1989).
53. W. F. Cheong, S. A. Prahl, and A. J. Welch, "*A review of the optical properties of biological tissues,*" IEEE Journal of Quantum Electronics, **26**, 2166-85 (1990).
54. A. H. Hielscher, R. E. Alcouffe, K. M. Hanson, and J. S. George, "*Comparison of finite difference transport and diffusion calculations for photon migration in homogenous and heterogeneous tissues,*" OSA Trends in Optics and Photonics on Advances in Optical Imaging and Photon Migration, **2**, 55-9 (1996).
55. S. Prahl, " *http://omlc.ogi.edu/classroom/ece532/class3/index.html,*").
56. M. Kempe, A. Z. Genack, W. Rudolf, and P. Dorn, "*Ballistic and diffuse light detection in confocal and heterodyne detection,*" J. Opt. Soc. Am. A, **14**, 216-223 (1997).
57. J. M. Schmitt, A. Knuttel, and R. F. Bonner, "*Measurement of optical-properties of biological tissues by low-coherence reflectometry,*" Applied Optics, **32**, 6032-6042 (1993).
58. G. Popescu and A. Dogariu, "*Ballistic attenuation of low-coherence optical fields,*" Appl Opt, **39**, 4469-4472 (2000).
59. M. E. Brezinski, G. J. Tearney, B. E. Bouma, S. A. Boppart, M. R. Hee, E. A. Swanson, J. F. Southern, and J. G. Fujimoto, "*Imaging of coronary artery microstructure (in vitro) with optical coherence tomography,*" The American journal of cardiology, **77**, 92-3 (1996).
60. S. Jackle, N. Gladkova, F. Feldchtein, A. Terentieva, B. Brand, G. Gelikonov, V. Gelikonov, A. Sergeev, A. Fritscher-Ravens, J. Freund, U. Seitz, S. Soehendra, and N. Schrodern, "*In vivo endoscopic optical coherence tomography of the human gastrointestinal tract--toward optical biopsy,*" Endoscopy, **32**, 743-9 (2000).
61. W. Jung, B. Kao, K. M. Kelly, L.-H. L. Liaw, J. S. Nelson, and Z. Chen, "*Optical coherence tomography for in vitro monitoring of wound healing after laser irradiation,*" IEEE Journal of Selected Topics in Quantum Electronics, **9**, 222-6 (2003).
62. A. V. D'Amico, M. Weinstein, X. Li, J. P. Richie, and J. Fujimoto, "*Optical coherence tomography as a method for identifying benign and malignant microscopic structures in the prostate gland,*" Urology, **55**, 783-7 (2000).
63. J. G. Fujimoto, "*Optical coherence tomography for ultrahigh resolution in vivo imaging,*" Nature biotechnology, **21**, 1361-7 (2003).

64. E. V. Zagaynova, O. S. Streltsova, N. D. Gladkova, L. B. Snopova, G. V. Gelikonov, F. I. Feldchtein, and A. N. Morozov, "*In vivo optical coherence tomography feasibility for bladder disease,*" The Journal of urology, **167**, 1492-6 (2002).
65. U. Seitz, J. Freund, S. Jackle, F. Feldchtein, S. Bohnacker, F. Thonke, N. Gladkova, B. Brand, S. Schroder, and N. Soehendra, "*First in vivo optical coherence tomography in the human bile duct,*" Endoscopy, **33**, 1018-21 (2001).
66. *Functional Histology*, ed. P.R. Wheater, H.G. Burkitt, and V.G. Daniels. 1987: Churchill Livingston.

Chapter 3 – System Development and Characterization

Introduction

This chapter discusses the analysis and design methodologies that were used to develop high resolution OCT systems capable of real-time *in vivo* imaging. The considerations covered were applied to construct and optimize several high performance OCT systems. By understanding both the theoretical aspects of the design space as well as the necessary criteria for practical implementation, optimal system performance can be achieved. The first sections of this chapter discuss noise and signal to noise in an OCT system. As noise from both electronic and optical sources can have a significant impact on system performance, factors affecting noise behavior are discussed. An analysis of signal to noise in shot-limited operation is done and experimental methods to measure signal to noise are described. System component design is reviewed with respect to the optimal interferometer configuration, electronic signal detection, and reference arm scanning techniques. The effects of bandwidth throughput and dispersion on system performance are analyzed and experimental data is presented.

Signal to Noise

At the most fundamental level, OCT involves the localized detection of an optical signal and the differentiation of that signal from its surroundings. Every aspect in the design of an OCT system is geared towards optimizing both the ability to accurately detect these signals with a high level of sensitivity while minimizing possible source of system noise. This goal applies not only to OCT imaging but to almost all fields of engineering and science where a signal is detected, be it electrical, optical, chemical, or mechanical. The common metric that conveys the degree of system sensitivity is the signal to noise ratio (SNR). High SNR is necessary as very low intensity levels (-110dB) of backscattered light are detected to form an OCT image. Increased SNR results in better OCT image contrast therefore much effort is made to optimize this system parameter.

Statistical Properties of Noise

Noise signals in general contain a great deal of information and appear almost random in nature as each noise value in time and space is highly uncorrelated with a signal at another point. Because of this noise sources can often be analyzed in probabilistic terms with the mathematical description depending on the physical basis of the noise source. When analyzing noise sources it is important to keep in mind that noise can be described as a statistical process and that noise sources can exhibit different statistical distributions (Gaussian, Poisson, etc) however because

OCT systems are implemented with narrow-band detection the sources can be considered as white noise. For optimal operation the time-averaged noise level in the OCT system will approach the shot-noise detection limit. An often used measure of noise [1] is the root mean square (rms) standard deviation σ or mean square variance σ^2 of the noise power spectral density. This can be expressed as

$$\sigma^2 = \frac{1}{N}\sum_{n=1}^{m}\left(I_{noise,n}\right)^2$$

where N is the number of measurements and m is the number of noise sources. Each noise source contributes to the total noise photocurrent as an rms term. Over time stochastic noise sources will tend to cancel in summation while the signal of interest will be enhanced. In principle the SNR improvement with averaging, as seen from the equation above, is equal to the square root of the number of samples. Figure 3-1 shows a demodulated OCT signal from a glass coverslip demonstrating this concept. By time averaging the demodulated signal an appreciable increase in the signal to noise ratio can be achieved. The non-averaged interference signal from the coverslip is shown as a dark trace below the demodulated signal. High speed OCT systems allow for the implementation of this noise reduction technique as a simple method to improve image contrast.

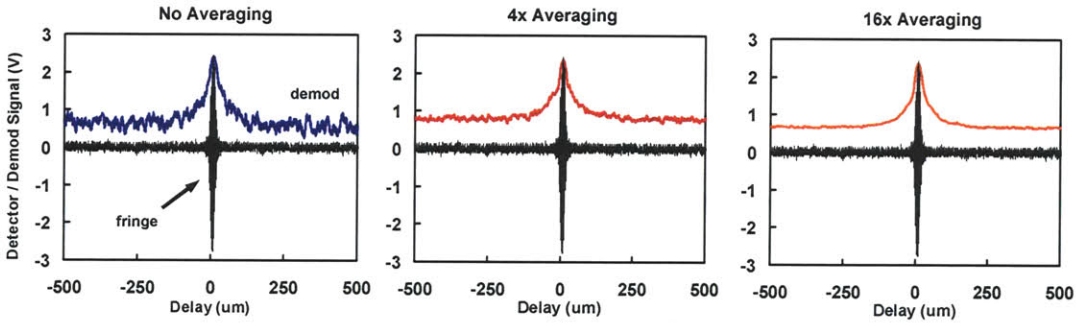

Figure 3-1. Noise reduction of a demodulated OCT interferogram by averaging
Interference signals (black) and demodulated OCT signals from a mirror surface at 1x, 4x, and 8x averaging.

The noise in an OCT system arises from three main sources that contribute to the detected photocurrent noise. These are electronic receiver noise, excess intensity and beat noise from the light source, and photon shot noise. Summing these components, the mean square photocurrent noise can be written as

$$\left\langle \sigma^2 \right\rangle = \left\langle \sigma_{rec}^2 \right\rangle + \left\langle \sigma_{ex}^2 \right\rangle + \left\langle \sigma_{beat}^2 \right\rangle + \left\langle \sigma_{shot}^2 \right\rangle$$

These noise sources can be approximated as Gaussian-distributed white noise sources and with proper optimization of the OCT system it is possible to operate near the theoretical shot-noise detection limit. Each noise component will be discussed to describe the factors affecting them and how they can be minimized.

Receiver Noise

Receiver noise has three components that can affect the system signal to noise. These are thermal noise, temperature noise, and amplifier noise which will be discussed below. Thermal noise arises from the random thermal motion of electrons in the photodiode resistor and is given by

$$\sigma_{th}^2 = \frac{4k_B TB}{\mathrm{R}_{eff}}$$

where k_B is Boltzmann's constant, T is the temperature, and B is the electronic detection bandwidth used for the receiver. R_{eff} is the effective load resistance of the photodiode resistor and amplifier load. Temperature noise is caused by random temperature fluctuations between the detector and its surroundings. It can be expressed in terms of the mean square radiant power fluctuations [2]

$$\sigma_{temp}^2 = 4k_B T^2 KB$$

If the detector is assumed to be in equilibrium with the background, $K = 4\varepsilon\sigma T^3 A$ so that

$$\sigma_{temp}^2 = 16\varepsilon\sigma k_B T^5 AB$$

where ε is the vacuum permeability, σ is the Stefan-Boltzmann constant and A is the detector area. Finally the amplifier noise is

$$\sigma_{amp}^2 = \frac{4k_B(T_A + T_R)G^2 B}{R_{eff}}$$

G is the amplifier gain while T_A and T_R are the noise temperatures of the amplifier and detector load resistor. In practice it is difficult to evaluate the receiver noise however a lower limit can be calculated from the manufacturer specifications of the receiver noise equivalent power or input current noise (ICN). The receiver noise current can then be given by [3]

$$\sigma_{rec}^2 = (ICN)^2 B$$

Typical input current noise values of $3pA/\sqrt{Hz}$ [4] can be achieved in commercially available photoreceivers.

Photon shot noise

In addition to receiver noise, the conversion of light into an electronic signal generates noise. As photon energy is quantized, the arrival of photons at random intervals is detected as noise called photon shot noise. The photon shot noise current can be written as

$$\sigma_{shot}^2 = 2qBi_{dc},$$

q is the electrical charge, and B is the electrical bandwidth as before. i_{dc} is the mean detector photocurrent given by

$$i_{dc} = S_v\left(P_{ref} + P_{inc}\right)$$

S_v is the photodiode responsivity, P_{ref} is the backreflected reference arm power, and P_{inc} is the incoherent light power reflected from components the system that arrives back at the detector. The second term, P_{inc}, can significantly increase the system noise level if there are highly reflecting surfaces within the OCT sample arm probe. Care must be taken to minimize these back reflections even if they are beyond the OCT scan range. Normalizing to 1 Hz of bandwidth, the optical shot noise power can be expressed as

$$P_{shot} = I^2 R_{det} = {\sigma_{shot}}^2 R_{det} = 2qi_{dc}R_{det}$$

For a $50\,\Omega$ photodetector input resistance, a typical OCT reference arm dc photocurrent of 20uA will generate a shot noise power of -185 dBm/Hz (~3.2 x10^{-19} mW).

Excess intensity noise

Intensity noise, also termed relative intensity noise, is a result of fluctuations in the optical intensity of the local oscillator (laser source). If components of the laser noise spectrum lie within the detection bandwidth of the OCT system excess noise is introduced. This deteriorates the system sensitivity and results in operation above the quantum fluctuation detection limit. In theory it is possible to use a balanced configuration receiver that can remove this excess intensity noise from the signal and achieve quantum limited performance [5-7]. The excess intensity noise can be expressed as [3, 8]

$$\sigma_{ex}^2 = (1+V^2)i_{dc}^2\frac{B}{\Delta\upsilon}$$

where V is the light source degree of polarization, B is the electrical bandwidth, and $\Delta\upsilon$ is the optical bandwidth given by

$$\Delta\upsilon = \sqrt{\frac{\pi}{2\ln 2}} c \frac{\Delta\lambda}{\lambda_o^2}$$

The dc photocurrent is given by the photodiode responsivity times the power reflected from the reference arm

$$i_{dc} = S_v P_{ref}$$

Measuring laser intensity noise

In order to fully characterize the sensitivity limit for an OCT system it is necessary to accurately measure the relative intensity noise of the laser source and determine its impact on system performance. A precise measurement can be performed using an rf spectrum analyzer and appropriate detector (silicon for 700-1000nm range, InGaAS or InP for 1000-1500nm range) with a frequency response on the order of 1-10 GHz. Figure 3-2 shows measured rf spectra from both a SLD light source and a fiber laser source. As can be seen the intensity noise for the SLD is near the system detection limit of -147dBm at higher frequencies of 100kHz to 10MHz. In OCT, the heterodyne carrier frequency is determined by the speed at which the optical delay line in the reference arm is scanned and the center wavelength Slower systems with scan speeds of 50-500 mm/sec have demodulation frequencies in the 1-100 kHz range. Depending on the noise characteristics of the light source it may be beneficial to operate at higher or lower Doppler frequency. As can be seen in Figure 3-2, a fiber based source can have considerably higher noise characteristics. In general however it is beneficial to operate away from baseband to avoid 1/f noise.

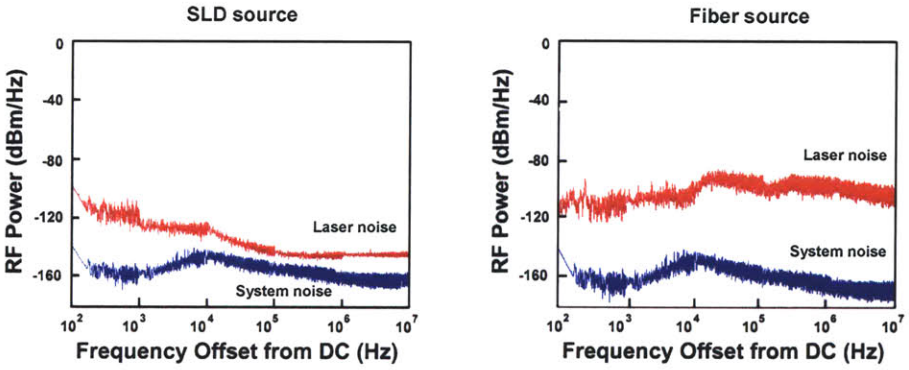

Figure 3-2. RF noise spectrum of SLD and fiber laser sources

As the SLD is a continous-wave (CW) laser there can be considerable 1/f noise near the baseband DC frequency. Operating at high heterodyne detection frequency avoids this region of noise. Fiber based sources can have very high excess noise which results in significantly decreased sugnal to noise performance.

When a mode-locked femtosecond laser source is used several factors can contribute to the noise. Some of these include variation in spontaneous emission, vacuum or gain fluctuations, and pump laser noise [9-11]. When characterizing the local oscillator noise it is necessary to measure the rf spectrum away from the carrier frequency. This can be done by measuring the noise intensity at the first harmonic of the laser as shown in Figure 3-3. The location of the first harmonic is determined by the repetition rate of the laser cavity as identical noise peaks will exist at multiples of the pulse repetition rate [12]. Measuring at the first harmonic removes 1/f noise located at the baseband frequency and isolates noise intrinsic to the oscillator.

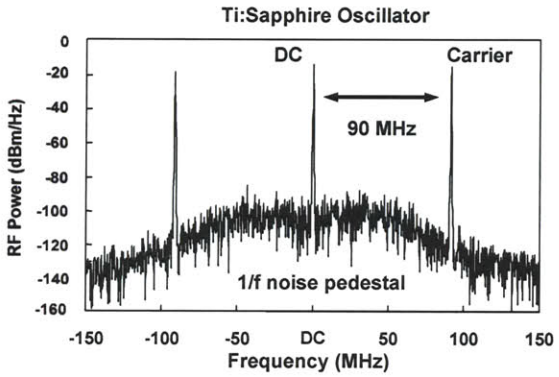

Figure 3-3. RF spectrum of Ti:Sapphire laser with 90MHz repition rate

The carrier frequency of the laser is ~90MHz and is determined by the cavity round-trip propagation time of the optical pulse. Subsequent higher order harmonics are spaced in frequency by the cavity repition rate. Optical power on the detector = 1 mW.

Figure 3-4 shows two noise spectra obtained from the broadband laser oscillators used for the ultrahigh resolution imaging in the work. Both exhibit significant amounts of noise in the kHz to MHz frequency ranges demonstrating the need to cancel out the relative intensity noise in the OCT system.

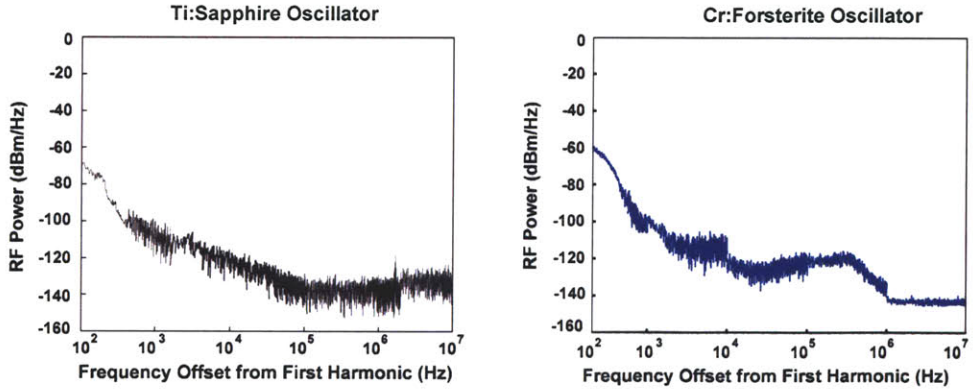

Figure 3-4. RF noise spectrums of broadband Ti:Sapphire and Cr:Forsterite lasers

Noise spectrums for both oscillators show better noise performace at higher frequencies.

It is possible to suppress the excess intensity noise of the optical light source through a dual balanced detection scheme. This effectively allows the interference heterodyne signal to add while canceling the noise generated from the local oscillator. The principles behind dual balancing and experimental measurements will be presented in the following section. In addition to excess intensity noise however, there is a noise source termed beat noise that cannot be removed through dual balancing.

Beat noise

Beat noise is a result of coherent mixing of the electrical field signals within a heterodyne detection scheme and can also be thought of as the shot noise arising from a dual balanced interferometer geometry. Beat noise results when various frequency components of the broadband spectrum of the light source beat with spectral components of back reflected signals from within the sample and reference arms.

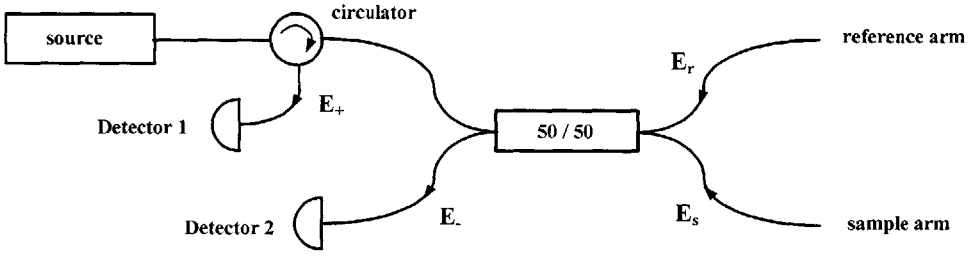

Figure 3-5. Dual balanced geometry with an ideal optical circulator
The optical circulator allows for full transmission of the source power through to the second coupler as well as full transmission of the return signal to the first photodetector.

Looking at a dual detector geometry with an ideal circulator and 50-50 beam splitter the electric fields in the two detector arms are

$$E_+ = \frac{1}{\sqrt{2}}\left(E_r e^{-i\omega t} + E_s e^{-i\left(\omega t + \frac{\pi}{2}\right)} \right) \qquad E_- = \frac{1}{\sqrt{2}}\left(E_r e^{-\left(\omega t + \frac{\pi}{2}\right)} + E_s e^{-i\omega t} \right)$$

The corresponding intensities are therefore

$$I_+ = \left\langle |E_+|^2 \right\rangle = \frac{1}{2}\left\langle \left(|E_r|^2 + |E_s|^2 + E_r E_s^* e^{i\pi/2} + E_r^* E_s e^{-i\pi/2} \right) \right\rangle$$

$$I_- = \left\langle |E_-|^2 \right\rangle = \frac{1}{2}\left\langle \left(|E_r|^2 + |E_s|^2 + E_r E_s^* e^{-i\pi/2} + E_r^* E_s e^{i\pi/2} \right) \right\rangle$$

When the two signals are subtracted in a balanced detector the intensity terms cancel thereby removing the intensity noise in the system.

$$I_+ - I_- = \frac{1}{2}\left\langle\left(e^{i\pi/2} - e^{-i\pi/2}\right)\left(E_r E_s^* - E_r^* E_s\right)\right\rangle = i\left\langle E_r E_s^* - E_r^* E_s\right\rangle$$

The interference terms which generate the signal however do not cancel and each of these terms beats with the electric field vacuum fluctuations in the system giving rise to the beat noise of the system. The beat noise can be quantified as [13]

$$\sigma_{beat}^2 = \frac{2S_v^2(1+V^2)P_{ref}P_{inc}B}{\Delta\upsilon}$$

where S_υ is the responsitivity of the photodiode and P_{ref} is the optical power on the detector reflected from the reference arm. The beat noise current increases linearly with the amount of backreflected power and decreases inversely with the bandwidth of the light source. The shot noise detection limit is proportional to the amount of power on the sample however when significant back reflections are present the minimum detectable reflectivity is limited by the beat noise. Using a broadband light source reduces the beat noise nonetheless care should be taken to minimize back reflections within the system.

Coherent Noise (Speckle)

Speckle arises from the interference of waves of random phase. Much work has been done to understand speckle [14] and even utilize it for measurement techniques [15, 16]. In OCT imaging however, speckle is a source of background noise that reduces the ability to distinguish tissue structure and is usually minimized as much as possible [17, 18].

Speckle is generated in an OCT image as a result of multiple wavelet signals from different backscattering locations in the tissue sample interfering with each other [19]. These backscattering sites are located within the coherence volume defined by the numerical aperture of the sample arm optics and the coherence length of the optical light source. The wavelets have random phase due to the random depth distribution of scattering sites in the sample and fluctuations in the sample index of refraction. Any additional speckle intensity signals from regions outside the coherent volume will be filtered out by heterodyne detection. Figure 3-6 shows two OCT images of a stationary tape phantom, both taken at 4 frames per second capture rate. Figure 3-6a has noticeable background speckle noise however this noise is considerably reduced by four frame averaging (Figure 3-6b). The subtracted images show the background noise intensity distribution.

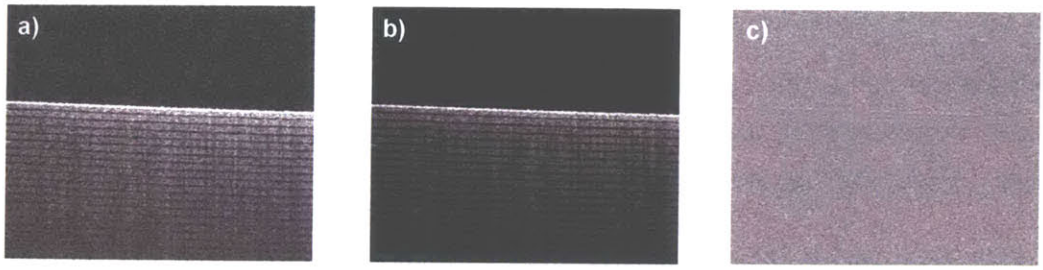

Figure 3-6. Reduction of background speckle by frame averaging

a) Tape phantom image acquired in 250msec. b) Tape phantom imaged with 4 frame averaging shows higher image contrast and reduced speckle. c) Image subtraction shows speckle intenisty distibution.

1/f noise

A final source of noise that can reduce sensitivity in almost any system is 1/f noise. This noise is very ubiquitous and occurs in systems ranging from electronic receivers and lasers to biological phenomena. There has been a great deal of research into the causes and behavior of 1/f noise [20], however the main effect that we need to address is its effect on system sensitivity. In electronic amplifiers 1/f noise typically has approximately a 3dB per octave slope from dc to ~10kHz and laser diodes can exhibit this noise characteristic up to several 100kHz. Not much can be done to remove this type of noise in a system however it is possible to avoid 1/f noise from deteriorating system performance by operating and detecting the signal of interest in a higher frequency range. OCT systems therefore have heterodyne Doppler frequencies from several 100 kHz to the MHz range and demodulate at these higher frequencies to avoid

System Sensitivity

As the system sensitivity is a critical parameter in OCT, it is instructive to look at its behavior under the influence of the various sources of noise. Using the above results, the full expression for SNR is given by

$$SNR = \frac{\langle i_{ac} \rangle^2}{\langle \sigma_{rec}^2 \rangle + \langle \sigma_{ex}^2 \rangle + \langle \sigma_{beat}^2 \rangle + \langle \sigma_{shot}^2 \rangle}$$

$$= \frac{2S_v{}^2 P_{sam} P_{ref}}{(ICN)^2 B + \frac{(1+V^2) S_v^2 P_{ref} B (P_{ref} + 2P_{inc})}{\Delta \upsilon} + 2qBS_v (P_{ref} + P_{inc})}$$

Using 50/50 single interferometer configuration we have $P_{sam} = R_{sam}(P_{source}/4)$ and $P_{ref} = R_{ref}(P_{source}/4)$ where R_{ref} and R_{sam} are the reference and sample arm reflectivity. Setting the sample reflectivity equal to one for a perfectly reflecting mirror we can plot the signal to noise behavior as function of reference arm reflectivity. A plot of OCT system sensitivity as a function of reference arm reflectivity and optical bandwidth is shown in Figure 3-7. The constraining parameter for the sensitivity in this case is the excess laser noise. Higher optical bandwidth reduces excess noise and allows for operation closer to the shot noise limit thereby showing the benefit of using broadband light sources for OCT.

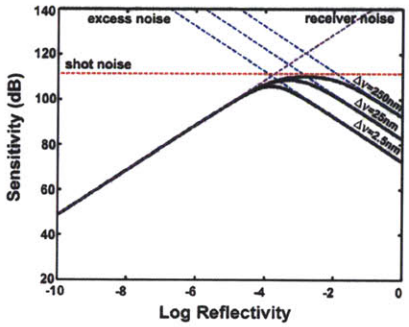

Figure 3-7. OCT system sensitivity as a function of reference arm reflectivity

Sensitivity dependancy of shot noise, excess laser intensity noise, and receiver noise is shown for optical bandwidths of 2.5nm, 25nm, and 250nm. P_{source}=25mW, electrical bandwidth B=200kHz, responsivity S_v=0.7, receiver noise current=0.5pA/$\sqrt{Hz}$.

Looking at additional dependencies, Figure 3-8a shows that a larger electrical bandwidth decreases the maximum possible sensitivity that can be achieved by decreasing the shot noise limit. This relates to the optical scanning speed and heterodyne signal Doppler frequency. As the OCT reference arm is scanned faster as is often necessary for real-time imaging applications, there is an increase in the Doppler frequency of the interference signal. Higher Doppler frequencies need a corresponding larger electrical bandwidth to collect the full signal and result in decreased system sensitivity.

Another factor that can reduce sensitivity is the incoherent light that is reflected back from the system to the detector. These reflections can occur in both the sample and reference arms at any location where an optical interface exists. The back reflected light increases the dc photocurrent level at the detector. The effect at increasing incoherent power reflectivity is shown in Figure 3-8b. A reflectivity value of one corresponds to one-fourth of the input optical power being reflected back to the photodetector. As even low levels of reflected incoherent light ($1/100^{th}$

the sample arm power) can result in a 4-5dB signal loss, care must be taken to minimize excess reflections within the system.

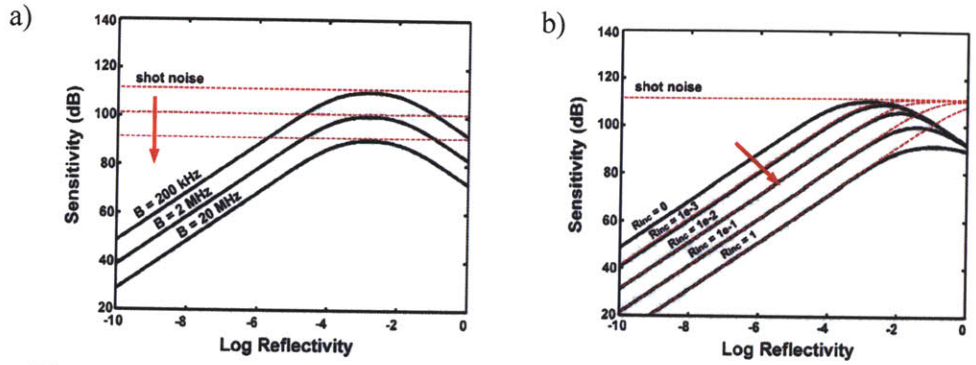

Figure 3-8. Sensitivity dependency on electrical bandwidth and reflections

As scan speed is increased, the heterodyne doppler frequency and corresponding increase in electronic bandwidth result in lower sensitivity. Incoherent light reflected for within the system raise the dc photocurrent and also result in decreased sensitivity. Optical bandwidth $\Delta\upsilon$=250nm, P_{source}=25mW, responsivity S_v=0.7, receiver noise current=0.5pA/$\sqrt{Hz}$.

Signal to Noise in the shot-noise limit

With proper system design and optimization it is possible to minimize system noise and operate near the theoretical shot noise limit. Analytically the signal to noise ratio is the ratio of the mean-square current of the detected signal, over the detected current variance. In a shot noise limited system, this corresponds to

$$SNR = \frac{\langle i_{ac} \rangle^2}{\langle \sigma_{shot}^2 \rangle}$$

where $\langle i_{AC} \rangle^2$ is the mean-square current of the interferometric signal, and $\langle \sigma_{shot}^2 \rangle$ is the shot noise current variance. Looking first at the signal component in a heterodyne system, the current flowing through the photodiode is given by

$$i = S_v[P_{ref} + 2\sqrt{P_{sam}P_{ref}}\cos(\omega t + \varphi)]$$

where P_{ref} and P_{sam} are the optical powers on the detector reflected by the sample and reference arms.The signal of interest is the AC component of the last formula

$$i_{ac} = S_v 2\sqrt{P_{sam}P_{ref}}\cos(\omega t + \varphi)$$

The mean-square value is given by

$$\langle i_{ac} \rangle^2 = S_v{}^2 4 P_{sam} P_{ref} \frac{1}{T} \int_0^T \cos^2(\omega t + \varphi) \; dt$$

i.e.

$$\langle i_{ac} \rangle^2 = S_v{}^2 2 P_{sam} P_{ref}$$

Concerning the noise, optimal operation is achieved in the shot noise limit, i.e., when all other noise sources are below the shot noise level. This is the case when dc optical power detected is strong enough to generate a shot noise component higher than all other noise sources. Using the expressions above, it is seen that the excess intensity noise will dominate when

$$i_{dc} > 2q\Delta\upsilon$$

This corresponds to approximately $i_{dc} \geq 10\mu A$. This dc noise current is often exceeded however it can be partly removed by using a dual-balance detector scheme. From before the shot noise is given by

$$\left\langle \sigma_{shot}^2 \right\rangle = 2qBS_v \left(P_{ref} + P_{inc} \right)$$

We are now able to calculate the SNR of the system

$$SNR = \frac{\langle i_{ac} \rangle^2}{\left\langle \sigma_{shot}^2 \right\rangle} = \frac{S_v{}^2 2 P_{sam} P_{ref}}{2qBS_v (P_{ref} + P_{inc})} = \frac{S_v P_{sam} P_{ref}}{qB(P_{ref} + P_{inc})} = \frac{\eta}{h\upsilon B} \frac{P_{ref}}{(P_{ref} + P_{inc})} P_{sam}$$

where η is the diode quantum efficiency, υ is the center optical frequency, and B is the detection bandwidth. In the case where the incoherent back reflected power is small this reduces the familiar formula used to calculate theoretical signal to noise in OCT

$$SNR = \frac{\eta}{h\upsilon B} P_{sam}$$

This is the formula to calculate the theoretical signal to noise in OCT. In decibel units, the formula is given by

$$SNR \;\; [dB] = 10Log\left[\frac{\eta}{h\upsilon B} P_{sam} \right]$$

Noise Equivalent Power

The noise equivalent power (NEP) is defined as the lowest amount of power that can be detected by the system to give a signal just above the noise level, i.e. when the SNR is equal to unity. In our case,

$$NEP = \frac{h\upsilon B}{\eta}$$

Dynamic Range

In addition to SNR, dynamic range is an additional parameter that is used to characterize an OCT system. While SNR gives a measure of how small of an optical signal can be detected, e.g. 120dB sensitivity for detection of a signal power of 10^{-12} times the incident power, dynamic range measures the difference between the SNR and the maximum detectable signal. The dynamic range is thus defined as the highest optical power over the lowest optical power that can be detected by the system. It is usually lower than the sensitivity value, due to the saturation of the detection electronics.

Typically maximum detectable back reflections from tissue are -50 to -60 dB giving a dynamic range of approximately 70 dB. Several advanced OCT systems use digital signal demodulation which allows for increased dynamic range. Analog demodulation and signal digitization however is still prevalent which can further limit the dynamic range. For an n-bit A/D converter the dynamic range is

$$DR(dB) = 10\log(2^n)$$

Thus a 12-bit A/D converter is limited to 36dB of dynamic range. Higher resolution 14-bit or 16-bit cards may be used for 42dB or 48dB of dynamic range however can be limited in acquisition rate. In practice, the dynamic range is usually measured as the ratio of the maximum power that can be detected by the receiver (saturation limit) divided by the minimum power (sensitivity). These powers are determined by placing increasingly higher value neutral density filters into the sample arm until no signal is seen.

Measuring Signal to Noise

As SNR is an important system metric, its practical measurement will be discussed. There are several methods to measure SNR which all yield slightly different values. The most common and straightforward approach is to use a reflective mirror in the sample arm and look at the demodulated heterodyne interference signal on either an oscilloscope or the visual display

monitor. As the mirror will reflect a large amount of power back to the detection electronics, the input source power is reduced to avoid detector saturation. Neutral density filters of increasingly higher value are inserted into the sample arm until no signal is seen. The SNR in units of dB is twice the ND filter value as the light attention occurs in both the forward and reverse directions. In most systems the sample arm optical beam is focused with an objective lens. The ND filter will slightly alter the focal position and it is necessary to slightly move the objective lens to refocus the beam onto the reflecting mirror surface. Failure to do this will result in a lower SNR measurement than the actual value.

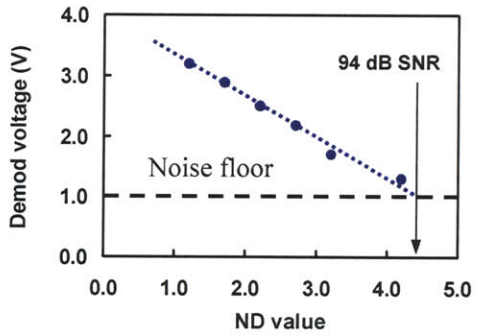

Figure 3-9. Measurement of SNR with neutral density filters

By inserting ND filters in the sample arm optics, the SNR can be measure by monitoring the demodulated signal voltage. When the demod voltage falls below the signal noise level the SNR in dB can be calculated as 2x the ND filter value multiplied by 10.

A second method can be used to measure SNR in an OCT system involves analyzing the filtered interference fringe and noise signals before demodulation. For this technique the squared amplitude of the interference waveform signal is divided by the variance of its noise after log demodulation.

Interferometer Design

As OCT is at the fundamental level a technique using low coherence interferometry, an optical interferometer is an essential component of every OCT system. Most systems implement a fiber-optic Michelson interferometer as a matter of course however the use of fiber optics while convenient, is not essential. Free space optics may also be used and can have several advantages over a fiber based system. These include the availability of broadband mirrors and beam splitters at several wavelength ranges. The main disadvantage of a free space system is the increased optical alignment that is necessary.

There are two main types of interferometer configurations that are commonly used. The first is a single interferometer in an unbalanced system shown in Figure 3-10. The optical transmission across the interferometer is characterized by a transmission ratio, α. This option has the benefit of simplicity and lower cost however it performs poorly if the optical source has a large amount of excess intensity noise. In addition, any dc photocurrent generated from back reflections within the system add to the interference signal. This can result in detector saturation and loss of dynamic range.

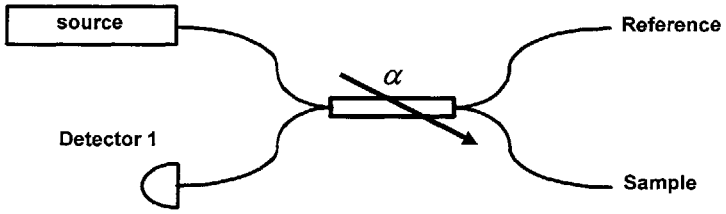

Figure 3-10. Unbalanced interferometer design

A fiber interferometer splits the light source electric field between the sample and reference arms. The coupling ratio across the interferometer can be configured in the fabrication process.

For the unbalanced system there is an optimal interferometer split ratio that will maximize the signal level received at the photodetectors. The optical power delivered to the sample in this case is equal to

$$P_{sample} = \alpha P_{source}$$

while the signal received at the detector is equal to

$$P_{detector1} = (1-\alpha) P_{signal}$$

where P_{signal} is the maximum signal power in the return path before the interferometer. If a mirror is placed in the sample arm as is done when measuring the system SNR, the power at the detector is given by

$$P_{detector1} = \alpha(1-\alpha) P_{source}$$

assuming there are no additional losses in the system. The detected signal is maximized for an α split ratio of 50%. This is shown numerically in Figure 3-11. The optical power delivered onto the sample in this case is equal to 50% of the original source power. Increasing the split ratio coefficient will increase the delivered power however results in decreased signal power therefore is unfavorable.

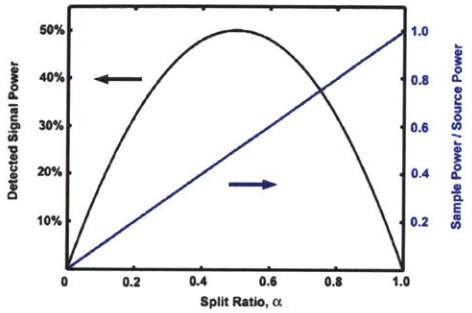

Figure 3-11. Sample and detected signal power for an unbalanced system

For a dual balanced system the situation is slightly more complicated. A schematic of a balanced interferometer setup is shown in Figure 3-12. In a balanced configuration, the background and intensity noise are cancelled by subtracting the photocurrent signals at the two detectors. This is done by placing the photodetectors in a back to back electrical configuration, thereby inverting one of the signals by 180 degrees. Thus any positive dc offset or intensity noise seen at one detector is cancelled by the inverted dc offset value in the second detector. The interference signals do not cancel but instead add at the two detectors as they are out of phase with each other by 180 degrees before the electrical inversion [21].

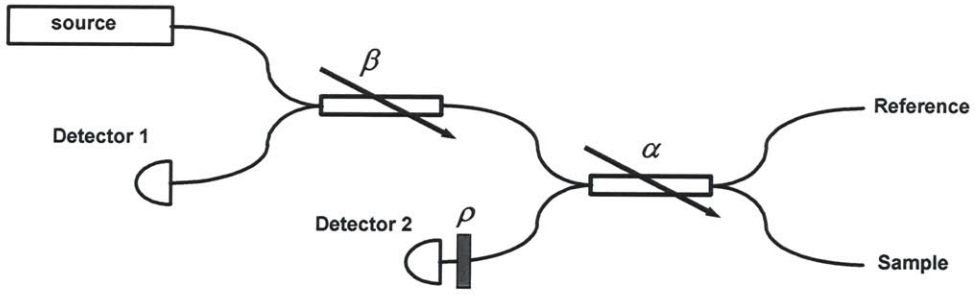

Figure 3-12. Balanced interferometer design

The transmission across each of the interferometers is determined by the transmission ratios α and β. A signal traversing the interferometer without crossing, for example from the sample to detector 2, is transmitted by the reciprocal amount, $1-\alpha$ in this case. Normalizing to the input source power, the optical power delivered into the sample and reference arms are

$$P_{sample} = \alpha\beta \qquad \text{and} \qquad P_{reference} = (1-\alpha)\beta$$

On the return path assuming no additional losses in the system, the signal power at detectors from the sample arm and reference arm will be

$$P_{detector1_{SAMPLE}} = \alpha^2\beta(1-\beta) \qquad P_{detector1_{REFERENCE}} = \beta(1-\alpha)^2(1-\beta)$$

$$P_{detector2_{SAMPLE}} = \alpha\beta(1-\alpha) \qquad P_{detector1_{REFERENCE}} = \alpha\beta(1-\alpha)$$

For any combination of interferometer split ratios, the optical power incident on detector 2 will be greater than the optical power at detector 1. As the goal in a dual balanced system is to cancel out the dc and noise signal components, the signal power at detector 2 must be attenuated to a level equal to the dc signal at detector 1. It can be shown that the attenuation factor needed to achieve equal power levels is given by

$$\rho = \frac{(1-\alpha)(1-\beta)}{\alpha}$$

Figure 3-13 shows the parameter space for a dual balanced interferometer system. The signal power at the photodetectors is maximized at both the highest and lowest values for the transmission coefficient, β, in the first coupler and with a 50-50 split ratio in the second coupler. For the highest transmission β value, the maximum optical power is delivered to the sample thereby increasing the amount of power on the return path. For the lowest β value, the delivered sample power is lower however the back reflected signal has the high transmission returning to detector 1.

An optimal dual balanced design actually utilizes an optical circulator in place of the first interferometer. Ideally this device allows the full optical power to be transmitted in the forward direction and all the signal power to be transmitted in the return path as well (see Figure 3-5). With an optical circulator the detected signal power is twice that of a standard dual balanced interferometer design allowing for a 3dB increase in SNR performance. The gain in SNR performance achieved by using a dual balanced detection configuration is simply given by

$$G_{SNR} = 2\beta$$

where for an optical circulator β will be equal to 1. It should be noted however that optical circulators often cannot support the full optical bandwidth of broadband sources. Most commercially available circulators to date cannot support more than 200nm at a center wavelength of 1300nm. Performance capabilities in the 800nm wavelength range are typically even lower thereby precluding the use of circulators in 800nm OCT systems.

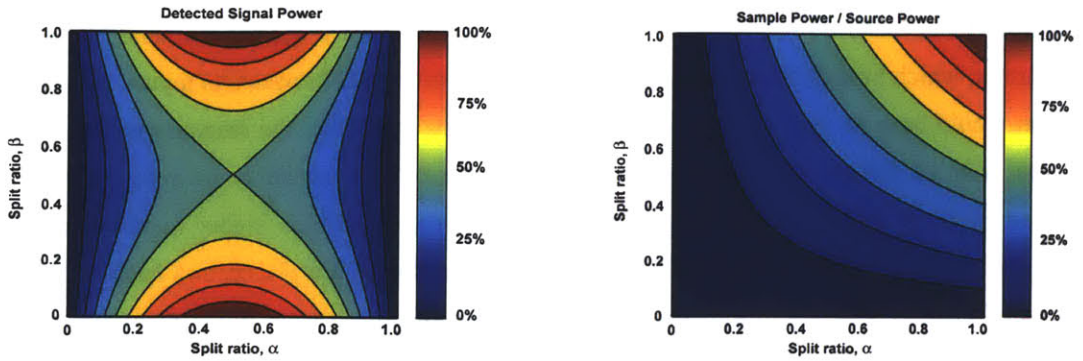

Figure 3-13. Parameter space for dual balanced interferometer design
Variation in Detected Signal Power and optical power on the Sample as a function of split ratios for a dual balanced interfoerometer configuration.

In practice however several factors determine the best interferometer configuration to use. The most influential factor is the optical light source and its performance characteristics. Table 3-1 summarizes several design options that can be implemented for various light sources.

Table 3-1. Optimal design configurations for OCT system interferometers [22]

Design	Light source	β	α	Sample power	D1 power	D2 power	ρ
Standard	Low cost 800nm/1300	0.5	-	0.50 P_{source}	0.50 P_{signal}	-	-
Dual balanced standard	Noisy Broadband	0.5	0.5	0.25 P_{source}	0.25 P_{signal}	0.25 P_{signal}	0.5
Dual balanced with circulator	Bandwidth <200nm	1.0*	0.5	0.50 P_{source}	0.50 P_{signal}	0.50 P_{signal}	0
Dual balanced With high power	High power	0.1	0.5	0.05 P_{source}	0.45 P_{signal}	0.45 P_{signal}	0.9
Dual balanced high efficiency	Low noise <200nm	1.0*	0.9	0.90 P_{source}	0.90 P_{signal}	0.90 P_{signal}	-

* Indicates use of an optical circulator

Dual Balanced Detection

Dual balanced detection is a technique that can be used to suppress the excess laser noise within an OCT system and operate closer to the shot noise limit. Theoretically, a balanced interface can reject any interference as long as it produces identical voltages on each of the signal lines and the resulting peak voltages don't exceed the capabilities of the receiver. Any voltage that

appears on both inputs top the receiver, because it is common to both inputs, is called a *common-mode voltage*. A balanced receiver uses a differential device, either a specialized amplifier or a transformer, which inherently responds only to the voltage difference between its inputs. An ideal receiver would have no response to common-mode voltages. In reality, the response is not zero, and the ratio of differential gain to common-mode gain of this device is its *common-mode rejection ratio,* or *CMRR*. It is usually expressed in decibels, in which higher numbers mean better rejection. In a dual balanced OCT system, two photodiodes are placed in a back-to-back configuration such that the common-mode voltage into the receiver is the sum of the two photodiode signals. An electrical schematic of the photodiode configuration is shown in Figure 3-14.

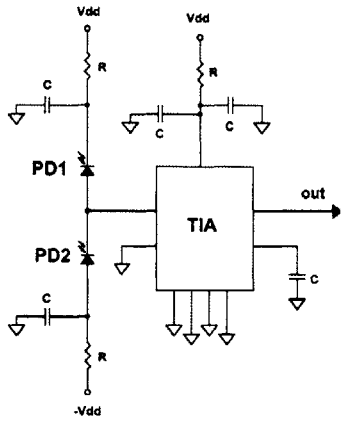

Figure 3-14. Electrical layout for a dual balanced photodetection and receiver.
The two photodidoe detectors (PD1, PD2) are placed back-to-back to cancel out common-mode laser intensity noise.

The output of the photodetectors (PD1, PD2) are combined and input into a high speed transimpedance amplifier which converts the photodiode current into a voltage signal. It can be shown that by the two beat signal arriving to the detectors have a 180 degree phase shift between them [23]. Thus if signal at PD1 is negative, in a reversed back-to-back photodiode configuration the two beat signals will add constructively while the in phase local oscillator intensity noise will cancel. The resulting laser oscillator noise suppression is similar to that obtained in a microwave balanced mixer [24] however in the case of an optical signal, the photodetector outputs are random point processes driven by parameters related to the laser intensity noise [25].

.

When building a dual balanced OCT system a subtle point that is often overlooked is that in addition to matching the path length in the sample and reference arms to obtain an interference signal within the coherence length of the laser source, it is also necessary to match the path lengths of the optical signals traveling to the photodetectors. As the optical path length in the backwards direction from the second interferometer to Detector 1 is longer (see Figure 3-12), a fiber jumper must be inserted before Detector 2 to match the back-traveled path lengths. This allows the signals to combine (or subtract in the case of the laser noise) precisely at the photodetectors. If the backward path lengths are not matched, the optical signals do not arrive at the same instant in time. This results in non-cancellation of the laser noise contained within the pulse signals.

As the two signals are combined in the back-to-back photodiode configuration, the optimal noise reduction is obtained when the two signals arrive at exactly the same time to the photodetector. By minimizing the path length mismatch the excess laser noise is reduced and system SNR is increased. Ideally, perfectly matched path length would result in complete noise cancellation. Using a dual balanced detection system not only reduces excess intensity laser noise as described earlier but also removes any DC photocurrent level thereby improving the system signal to noise performance. Figure 3-15 shows a noise measurement characteristic of the OCT system comparing a single detector configuration to one with dual balanced detection. With dual balancing a theoretical 3 dB improvement in the signal level can be achieved however the reduction and cancellation on noise terms results in a significant improvement in the SNR performance of the system. The frequency range of 5-50 MHz is of relevance as the system uses high speed scanning in the reference arm and has a Doppler demodulation frequency of 10-20 MHz.

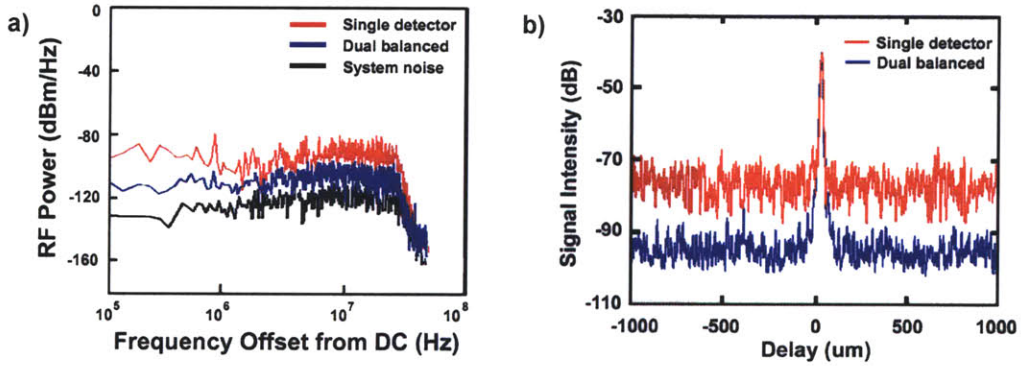

Figure 3-15. Comparison of system noise performance with dual balancing

a) Single (upper trace) and dual balanced (middle trace) RF noise spectra. b) Logarithmic demodulation signal of the OCT heterodyne fringe. Using dual balancing give better performance that is closer to the shot noise limit and results in better SNR.

Considerations with Pulsed Oscillators

It is possible to perform OCT with both pulsed and continuous wave light sources. Femtosecond laser oscillators such as Ti:Sapphire, Cr:Forsterite, and Cr:LiCAF however have traditionally provided the highest resolutions for OCT imaging as they are capable of generating optical bandwidths often in excess of 200nm [26, 27]. While more complicated in terms of alignment and stability these sources enable coherence lengths on the order of 1-2um and can have several hundred milliwatts of output power. In addition as many the OCT systems used in this work were built using single mode fiber-based components, optical coupling of the symmetric output laser mode is more efficient than coupling of asymmetric diode modes.

When using pulsed oscillators there are several considerations that must be taken into account to ensure safe operation and achieve optimal imaging performance. First and foremost is patient and operator safety. With typical sample powers of 5-10uW in ophthalmic imaging, pulse power can approach picojoules with 20-100 femtosecond pulse durations. In order to reduce the peak pulse intensity, the pulse is temporally broadened through several hundred meters of fiber. This is most relevant in ophthalmic imaging where the laser light is directly incident on the patient's retina.

For imaging in tissue other than the eye, sample powers of 5-10mW are typically used with a focused transverse spot size of approximately 10um. This corresponds to an energy density of 10 kW/cm^2. It is important that the scanning speed is sufficiently high such that the incident optical energy is within safe ANSI exposure limits. This holds true whether CW or pulsed sources are used. For human skin and non-retinal tissue, the CW exposure limit at 1300nm is approximately 10 mW [28]. For a pulsed source the calculations are more complicated but exposures are within acceptable safety limits if the incident power of the sample is kept below 15 mW [29, 30].

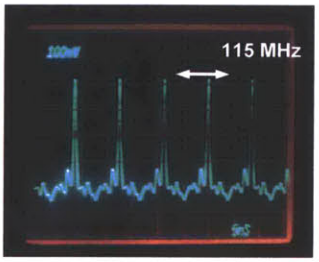

Figure 3-16. Pulse output of Cr:Forsterite laser

Pulse repetition rate should match the round trip cavity time for the oscillator. Pulse duration cannot be determined by this method for femtosecond systems as the detector response time is too slow. Scale 5 nsec/div.

There are other factors to consider and be aware of when using pulsed oscillators for OCT imaging. One of these is the pulse stability and operating mode of the laser. In order to characterize the laser output, a fast photodetector with a response time 4-5x faster than the pulse repetition rate should be used. Figure 3-16 shows a measured output pulse train from the Cr:Forsterite laser described in Chapter 2 and used for several of the high resolution imaging studies in this work.

For femtosecond oscillators, the detector response time (~500 psec) is not sufficient to resolve the individual pulse durations. Autocorrelation and cross correlation measurement techniques [31, 32] should be employed for this purpose. However the transient response of the photodiode allows for characterization of the pulse dynamics from the oscillator. The pulse train should also be checked on a longer timescale to verify that the laser output is stable and single pulsing.

Figure 3-17 illustrates the output pulse characteristics for stable, modelocked operation and for at operating point where Q-switching like behavior is observed. This behavior is caused by the population inversion dynamics within the laser. During the period of lower energy emission (cycle troughs) the laser is able to output couple all the light energy generated by the pump. However more energetic pulses rapidly build up within the cavity and cause higher and higher pulse intensities to be generated. This continues until a peak energy is reached where the stimulated emission probability has increased enough to couple out the additional energy (as a results of the stimulated emission probability being proportional to the pulse intensity). This increase in stimulated emission causes a decrease in the inverted population which reduces the pulse energies again. The timescale of this oscillation is approximately 1.75 usec which is on the order of the carrier lifetime for the Cr:Forsterite laser crystal.

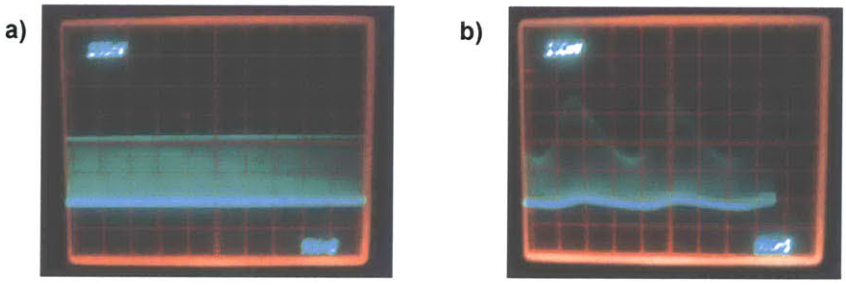

Figure 3-17. Modelocked and Q-switched modes of operation

a) Stable, modelocked operation exhibits uniform pulse intensity while b) Q-switched operation exhibits modulations in pulse energy on a . Scale 500 nsec/div.

Bandwidth Support

In order to achieve high resolution imaging it is necessary that the electrical and optical components within the OCT system support the broadband optical bandwidth of the laser light source. To this end the fiber interferometers and optical circulators used in the OCT system were characterized to determine their performance. For an ideal fiber coupler, the coupling ratio would be constant across the full wavelength range of the light source. In practice however the coupler can have non-uniform optical transmission as well as loss. Fiber components at the 1300nm wavelength range have in general better performance components at 800nm due to development of devices in the telecommunications wavelength range.

Figure 3-18 shows a transmission plot of two 50-50 fiber couplers across 1000-1500nm. The couplers were tested using a broadband white light source which, while low power, emits a large spectrum for testing the broadband performance of optical components. The resulting transmission curves are plotted relative to the input light power.

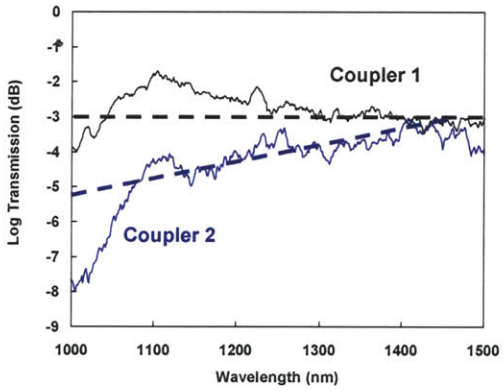

Figure 3-18. Coupler transmission of two 50-50 fiber interferometers
Flat coupling across the required spectral bandwidth allows maximum uniform bandwidth transmission and optimal resolution performance.

Coupler 1 shows a fairly flat and uniform transmission characteristic with a 3dB coupling ratio across most of the spectrum. This is near ideal performance and is helpful when designing and configuring the OCT interferometer. In contrast, Coupler 2 shows a significant decrease in coupling at lower wavelengths, a skewed transmission profile, and higher insertion loss. Using this coupler would result in sub-optimal system performance as the optical transmission in both the forward and backward directions is affected.

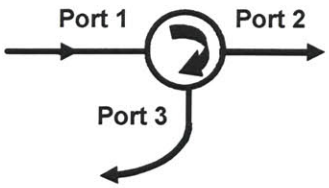

Figure 3-19. Schematic of an optical circulator

In the previous section it was seen that several optimal interferometer configurations implemented optical circulators to achieve high signal levels at the photodetectors (Figure 3-13, Table 3-1). An optical circulator is a three port fiber device where the optical input at Port 1 is completely transmitted through to Port 2. The unique property of these devices is that any back reflected signal is routed to Port 3 with (ideally) no loss of signal back into Port 1 (Figure 3-19). These devices are ideal for an OCT system as high power throughput into the system is desired as well as maximal back reflected signal transmission to Detector 1 in a dual balanced interferometer configuration (Figure 3-12). The design calculations for this system layout however were performed under the assumption of ideal forward transmission through Port 1 and back transmission through Port 3.

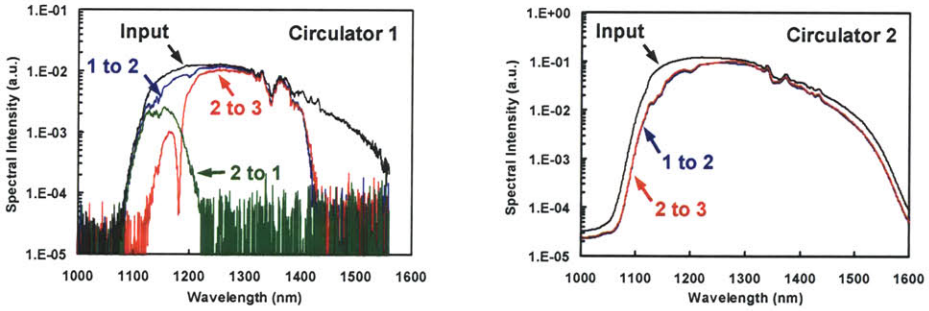

Figure 3-20. Transmission characteristics for two optical circulators

Optical circulator transmission characterists from JDS Uniphase (Circulator 1) and Oplink (Circulator 2) vendors.

As the wave guiding properties of circulators are more sensitive and difficult to maintain over a broad bandwidth, characterization of these components is important is they are to used in an OCT system. Figure 3-20 shows the transmission curves of two different circulators demonstrating that the second circulator has much better performance.

Dispersion

In the previous sections, it was shown that increased resolution performance can be achieved through the use of broadband light sources. An important factor that was considered in the use of broadband optical sources for the high resolution systems developed was the dispersion characteristics of the elements within the OCT systems built. As was derived previously, the coherence length of an optical light source is inversely proportional to its spectral bandwidth. Larger spectral bandwidth corresponds to higher axial resolution in OCT imaging. For a 1300nm light source with a bandwidth of 40-60nm, the effects of optical dispersion is minimal as the zero dispersion point in optical fibers and most glass elements is near 1300nm. Precise balancing of the optical dispersion is necessary to maximize system resolution and achieve optimal imaging performance.

Material dispersion in optical fibers arises from the frequency dependence of the index of refraction

$$n^2(\omega) = \chi^2(\omega) + 1$$

where χ is the electric susceptibility. Once this relationship is known the fiber mode propagation constant

$$\beta_1 = \frac{1}{v_g} = \frac{n}{c} + \frac{\omega}{c}\frac{dn}{d\omega}$$

can be determined. The group velocity, v_g, can be thought of as the spectral center of mass velocity of the optical pulse . Higher order dispersion terms are found by taking derivatives of the mode propagation constant. For example the second order dispersion, called the group velocity dispersion (GVD), is given by

$$\beta_2 = \left(\frac{d^2\beta}{d\omega^2}\right)_{\omega=\omega_o} = \frac{1}{c}\left(2\frac{dn}{d\omega} + \omega\frac{d^2n}{d\omega^2}\right)$$

The GVD describes how spectral components within the pulse are delayed or advanced with respect to the pulse's spectral center of mass. In the normal dispersion regime, shorter wavelength components of the spectrum travel slower than longer wavelengths ($\beta_2 > 0$) while in the anomalous dispersion regime ($\beta_2 < 0$), the opposite is true.

As the susceptibility is difficult to determine experimentally, the Sellmeir formalism can be used to calculate dispersion characteristics of optical elements. The wavelength dependence of material index is given by

$$n(\lambda)=\sqrt{1+\frac{A\lambda^2}{\lambda^2-D^2}+\frac{B\lambda^2}{\lambda^2-E^2}+\frac{C\lambda^2}{\lambda^2-F^2}}$$

where the variables A-F are the Sellmeir coefficients. Using the relationship

$$\frac{\omega}{c}=\frac{2\pi}{\lambda} \qquad \text{and} \qquad d\omega=\frac{-2\pi c}{\lambda^2}d\lambda$$

the second order dispersion in terms of wavelength can be written as

$$\beta_2=\frac{\lambda^3}{2\pi c}\frac{d^2n}{d\lambda^2}$$

Often a dispersion parameter D is used in place of β_2 in the literature. The two such that negative dispersion parameter ($D<0$) corresponds to the normal dispersion regime while a positive dispersion parameter ($D>0$) corresponds to the anomalous dispersion regime. In terms of wavelength, the dispersion parameter is given by

$$D=10^{21}\frac{\lambda^3}{2\pi c^2}\frac{d^2n}{d\lambda^2}$$

With λ in units of um, D will be in units of ps^2/km. For silica fibers, $D\approx 50 ps^2/km$ in the visible portion of the spectrum but becomes negative in the infrared with zero dispersion near 1300nm. A plot of dispersion as a function of wavelength is shown in Figure 3-21 for several common optical materials.

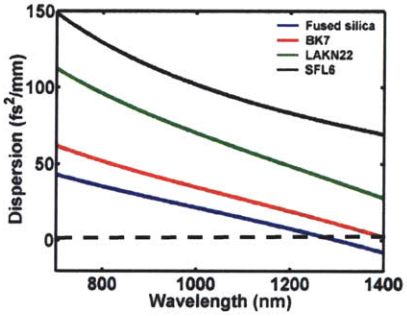

Figure 3-21. Group delay dispersion for various optical materials

Dispersion is minimzed in optical fibers near 1300nm. Operating at lower wavelength requires more sensitive balancing of material dispersion in the sample and reference arms of the OCT system. The plot shows the increase in dispersion for 1mm of material.

As can be seen the GDD due to even a small amount of material can be significant. This is more pronounced at lower wavelengths and matching dispersion of optical elements in the sample and reference arm paths of the OCT system must be done precisely. Figure 3-22 shows of the effect of dispersion mismatch on the OCT heterodyne signal at 1300nm wavelength. Dispersion matching characterization is done by placing varying amounts and types of glass blanks into the reference arm to the OCT interferometer. The interference trace at the systems zero delay position is measured from a mirror interface. A high resolution OCT system with the Cr^{4+}:Forsterite laser is used with 240nm of operating bandwidth.

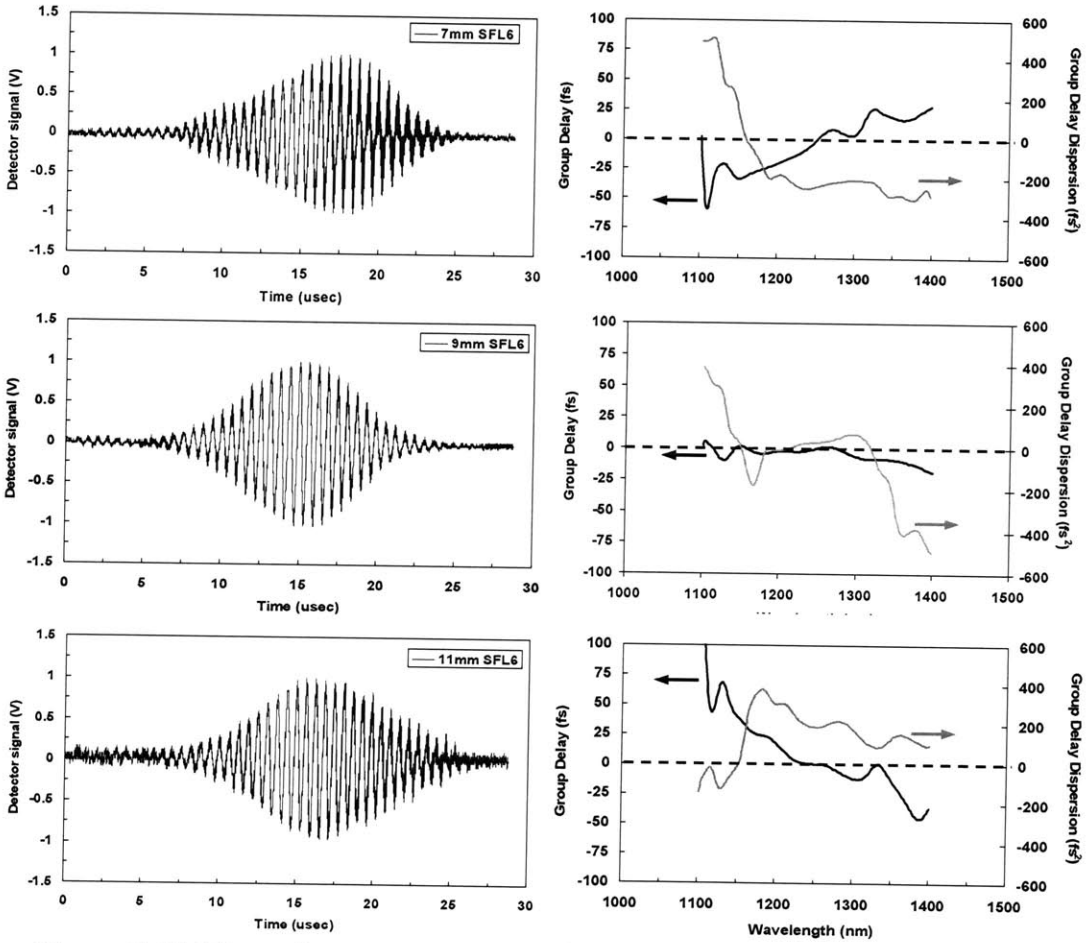

Figure 3-22. Dispersion matching of a Cr^{4+}:Forsterite light source at 1300nm

Left figures show interferometric heterodyne traces for different amounts of glass inserted into the system reference arm. Right figures show corresponding group delay and group delay dispersion calculated from the interference signal. Optimal dispersion matching is seen for 9mm of SFL6 glass giving flat group delay over the optical bandwidth [33].

To obtain the group delay the phase information of the interferogram Fourier transform was differentiated with respect to frequency. The characteristic for the group delay dispersion was obtained by taking the second derivative of the phase. When the dispersion is precisely matched, minimal chirp is observed in the interference signal, group delay over the optical bandwidth range is flat, and GDD is almost zero. When the system is not optimally matched, a positive or negative slope of ~200 fs^2 can be seen for the group delay. When using glass blanks or prisms to match dispersion important to consider that each interface introduces back reflections into the system which can increase the dc noise level. There is also an approximate 4% loss in optical power at each surface if the elements do not have an anti-reflected coating which decreases the system heterodyne gain.

Figure 3-23 shows the change in group delay relative to center wavelength at 800nm and 1300nm operating points. Of note is the significantly higher relative group delay of spectral components around an 800nm central wavelength. Thus for high resolution OCT at 800nm with the Ti:Sapphire laser, dispersion matching is very sensitive to even millimeter variations in material.

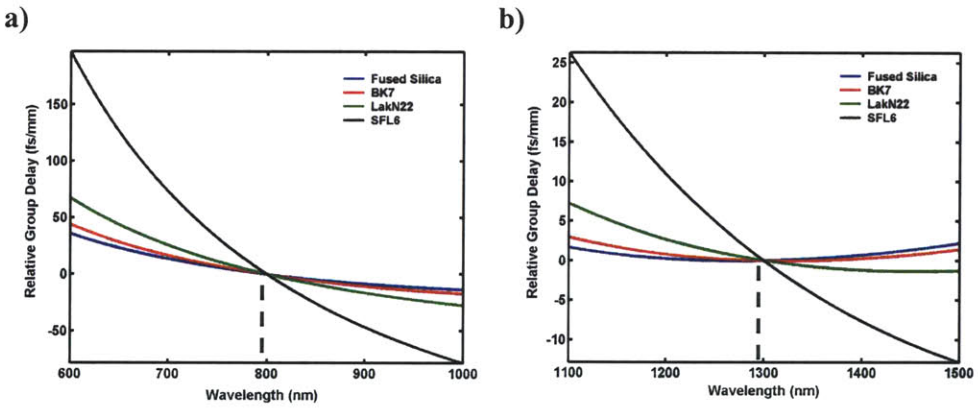

Figure 3-23. Relative group delay as a function of wavelength for different materials

a) Relative group delay for 800nm and b) 1300nm center wavelength. For all materials shown the dispersion of wavelengths around 800nm is significantly larger than for wavelengths about 1300nm (note vertical scale difference).

It is also seen that at 1300nm there is a zero derivative of group velocity for silica. Therefore optical fiber contributes only a parabolic variation of group velocity at this wavelength. It is difficult to compensate this type of variation and the only solution is to precisely match both the fiber length and types of materials in the system. As shown in Figure 3-22 dispersion balancing at 1300nm was possible by inserting the correct type of glass in the reference arm of the system. Positive and negative chirp was observed for modifications of +/- 2mm SFL6

corresponding to 30-40 fs change in relative group delay over the laser bandwidth range of 240nm.

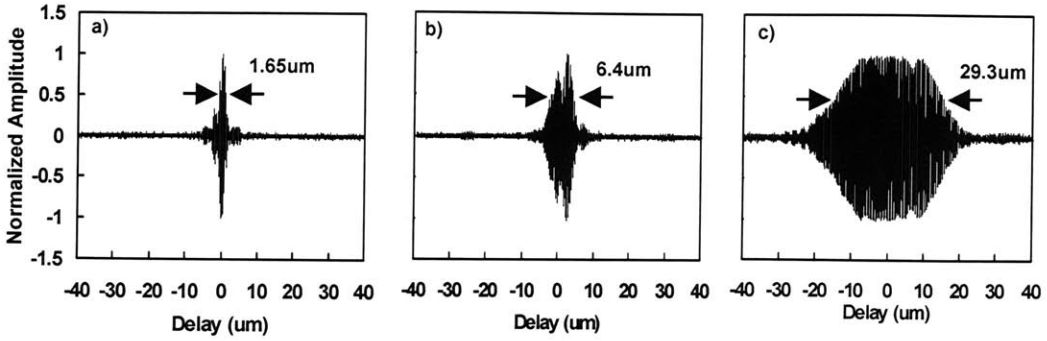

Figure 3-24. Loss of resolution due to dispersion mismatch in Ti:Sapphire system

Axial resolution of 1.65um is achieved with precise dispersion matching in the sample and reference arms. Insertion of 1mm fused silica (b) or 1mm SFL6 (c) glass into the system reference arm causes a 4-fold and respective 17-fold decrease in resolution.

A demonstration of the high-resolution OCT system's sensitivity to optical dispersion at 800nm is shown in Figure 3-24. In Figure 3-24a, an interferometric heterodyne trace is shown for the system with the dispersion balanced. An operating bandwidth of 250nm centered at 800nm yields an axial resolution of 1.65um in air. To observe the effect of unmatched material dispersion, a 1mm glass blank of fused silica glass was inserted into the reference arm. The resulting interferogram exhibits a four fold decrease in resolution (Figure 3-24b). Replacing the fused silica with 1mm of SFL6 results in a 17-fold decrease in resolution. If the dispersion variation is mostly linear as was the case in Figure 3-22 then a single material can be used to compensate the dispersion. However, if there is a significant curvature, then a combination of materials is necessary to match the material and optical path length in the sample and reference arms.

Dispersion Management for High Resolution Imaging

For the high resolution imaging studies in this work it was necessary to carefully balance the optical dispersion in the Michelson interferometer sample and reference arms. As shown in previous chapters, even a slight mismatch of optical dispersion can cause significant reduction of the OCT system resolution and imaging performance. In the OCT reference arm (e.g. mechanical galvanometer or cam scanner) there is typically 15-18cm of air path to allow for optical elements such as focusing lenses or turning mirrors. The optical dispersion introduced by the reference arm

air path can be generally compensated for in OCT sample arms that implement microscope-based or handheld probe sample arms as shown in Figure 3-25.

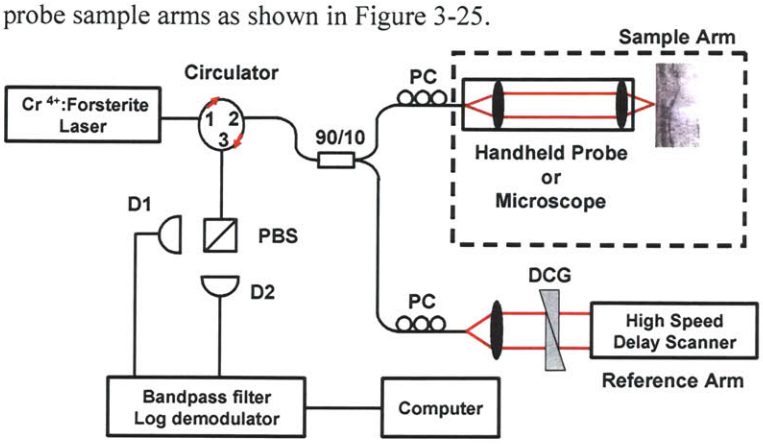

Figure 3-25. Dispersion balancing in a Probe-based OCT System

Dispersion balancing of the reference arm air path is achieved by the air spacing in the sample arm diagnostic device. Dispersion compensating glass (DCG) is needed in the reference arm to balance the corresponding glass elements in the sample arm.

In a catheter based system however no such air path exists in the sample arm and it was necessary to build an optical air coupling of the same length as the air path in the system reference arm. A schematic of one such system implemented is shown in Figure 3-26. It is also necessary to maximize optical throughput of the signal in the air gap coupling (AGC) so that the reflected sample signal is not reduced on the return path to the photodiode detectors. Because of this requirement, the fiber path lengths were configured such that no dispersion compensating glass would be necessary to insert in the AGC as each glass blank would introduce at least a 4% reflection loss at each surface interface.

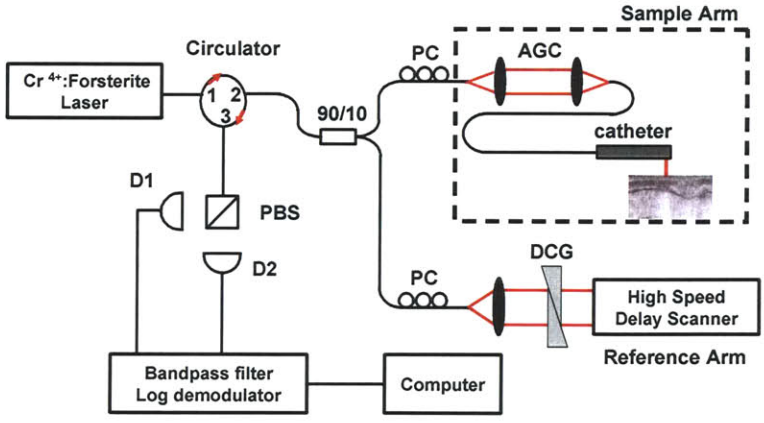

Figure 3-26. Dispersion balanced Catheter-based OCT system

Implementation of an air gap coupling in the sample arm allows for high resolution imaging in a catheter based OCT system. This air coupling can be inserted into all catheter systems where an equivalent air path is needed to balance the air path length in the system reference arm.

The air coupling implement for high resolution imaging consisted of two fiber pigtailed GRIN lens collimators with a working distance equal to the reference arm path length. This corresponded to each GRIN lens' beam waist positioned at a position equal to half the working distance. With this configuration the system had an optical beam waist centered between the two collimator lenses which proved to be more efficient than trying to couple the light directly from two collimated beams. The reason for this is that even with two highly collimated beams, due to the Gaussian beam distribution of the propagating light, the beams will only be matched exactly at a flat beam waist position as illustrated in Figure 3-27. Higher bandwidth support is also achieved in this configuration as chromatic aberrations are less severe.

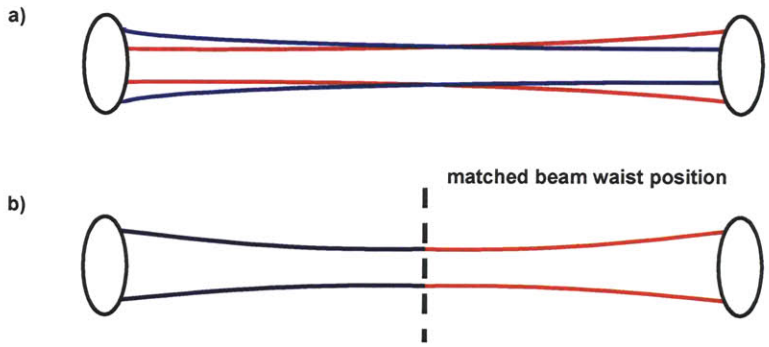

Figure 3-27. Gaussian beam propagation for air coupling configurations
a) Using two collimated beams results in sub-optimal coupling efficiency as the beam wavefronts do not match at any location over the propagation path. b) Configuring the lens system such that a flat beam waist exists in the middle of the optical system enables optical coupling efficiency and bandwidth support.

Characterization of both the power throughput and bandwidth capacity of the air coupling was conducted. Figure 3-28 shows that it was possible to support up to 260nm of optical bandwidth from the modelocked Cr:Forsterite laser. As the GRIN lens collimators were designed for beam propagation at 1300nm it is likely that the use of a different wavelength range, such as 700-1000nm for a Ti:Sapphire based system, would require an independently configured air coupling for high resolution catheter based imaging. Power efficiency was measured to be as high as 95.7% in each direction, resulting in less than 0.4 dB total roundtrip loss.

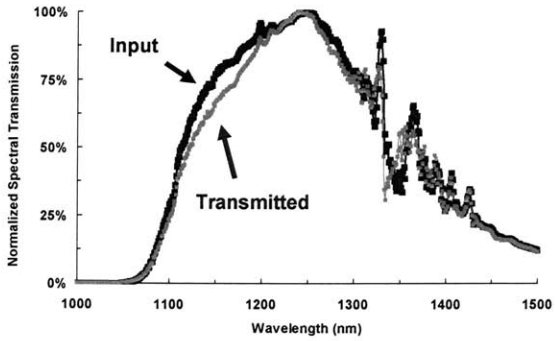

Figure 3-28. Air coupling bandwidth support

Careful optical and component design of the air coupling enable high resolution imaging with broad bandwidth support (>250nm) and minimal power loss (>95% coupling efficiency). Note that transmitted spectrum has not been normalized to the peak of the input spectrum and accurately represents 95.7% coupling efficiency.

Polarization Control

Not mentioned until now is the effect of the light polarization state on the heterodyne interference signal. As interference only occurs between two fields of similar polarization, when the two reflected optical signals from the sample and reference arms recombine at the interferometer the degree to which the polarization states are similar affects the signal strength. In general the polarization is a combination of either linear or circularly polarized states which is not precisely controlled in the OCT system. Birefringence caused by mechanical stress in the optical fibers can change the polarization state unless polarization preserving fiber is used. The polarization states can however be altered to optimize the interference signal by inserting polarization paddles into the sample and reference arm paths. These paddles introduce a repeatable mechanical stress by bending optical fiber loops and can control the polarization in a consistent manner. By using three paddles in a $\lambda/4:\lambda/2:\lambda/4$ configuration, polarization control over the entire Poincare sphere can be achieved for a monochromatic light source. As most OCT light sources are broadband and cover a large optical spectrum, exact control of the polarization is not possible. However by configuring the fiber loops near the center wavelength of the light source, one can obtain reasonably good polarization control. The governing equation to determine the number of fiber loops necessary for the $\lambda/4:\lambda/2:\lambda/4$ configuration is

$$N = \frac{1}{2\pi n}\frac{R}{r^2}W\lambda$$

where n is the fiber index of refraction, R is the loop radius, r is the fiber core diameter, λ is the center wavelength, and W is the waveplate order, ¼ for $\lambda/4$, and ½ for $\lambda/2$.

It is also possible to use the polarization state of the light to interrogate the sample being imaged with polarization sensitive OCT. Several experiments have demonstrated this capability to gain additional information about the tissue state [34-38]. Some tissue types, such as articular cartilage, exhibit birefringence which can be observed by changing the polarization state of the incident light. In addition the polarization states can be separated before the optical photodetectors using a polarizing beam splitter or fiber polarizer. Both these implementations to observe birefringence in tissue will be shown in the subsequent chapter on biological imaging studies.

Axial Scanner Technologies

The reference arm of the OCT interferometer is another important system component and enables the axial depth scanning of the heterodyne fringe signal. Because OCT is a low coherence interferometry technique, by changing the optical pathlength in the reference arm the depth location of the interference signal is similarly altered in the sample arm. In essence, the reference arm scanner is an electrical, acoustic, or mechanical method to change the optical path length of the OCT interferometer in a controlled and repeatable manner. Several scanning technologies have been developed using mechanical galvanometers with retro-reflectors [39, 40], optical phase delay lines [41, 42], and piezoelectric fiber stretchers [43, 44]. High speed scanning systems have also been realized using resonant galvanometers [45], rotating cubes [46, 47] and rotary cam scanners. This section will review some of the scanning techniques and reference arm systems constructed and used for studies in this work.

Mechanical Galvanometer

One of the most basic reference arm designs implements a retro-reflecting mirror placed on the arm of a mechanical galvanometer. An optical fiber from the fiber interferometer is interfaced to a collimating lens placed on a translation stage as shown schematically in Figure 3-29. Optical elements such as glass or prisms can be placed in the reference arm to balance dispersion for high resolution operation. By adjusting the degree of collimation and optical alignment, the amount of back-coupled light can be readily modified. The reference arm back coupled optical power is important as it affects the heterodyne gain of the system. Care must be taken to set the back coupled power for optimal SNR while avoiding saturation of the optical detectors.

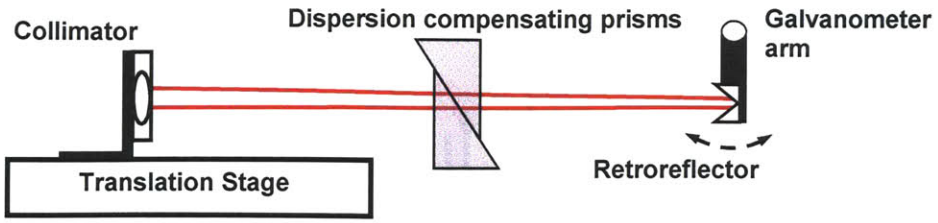

Figure 3-29. Mechanical galvanometer reference arm

A retroreflector placed at the end of a galvonometer swing arm reflects incident light back into the system. The degree of collimation or focusing onto the retroreflector can be changed to control the amount of back coupled light. Back to back prisms are used for dispersion compensation and a translation stage is used to adjust the zero delay position of the interference fringe.

Some of the advantages in using a mechanical galvanometer in the OCT reference arm are the availability of components and ease in optical alignment. In addition there are only a few optical elements used, it is possible to support broad optical bandwidths. The main disadvantage of these reference arm scanners is their relatively low scanning speeds of 50-250 Hz. For an OCT image consisting of 250 A-scans per image this corresponds to a imaging rate of 2 frames per second or less even if a triangle waveform is used to image on both the forward and return galvanometer stroke.

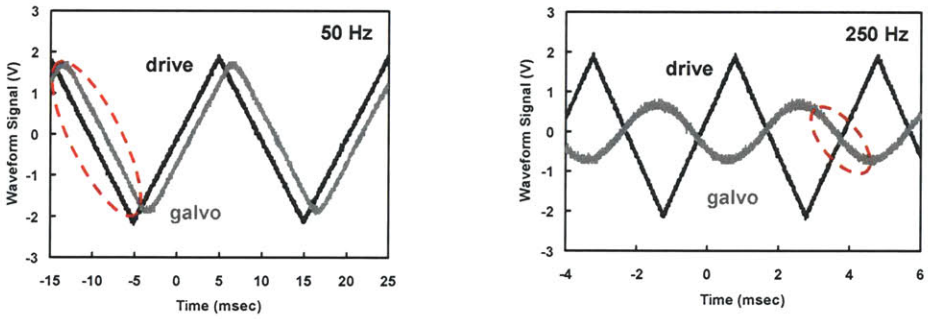

Figure 3-30. Drive frequency effect on galvanometer response

At slower scan frequencies the galvanometer position (gray) can closely approximate the drive waveform (black). Increasing the scan speed however often results in a reduction of the amplitude response and a decreased linear scan range. Linear scan range is indicated by the dotted ellipse in each plot.

Another limitation of mechanical galvanometers is their non-linear response at higher driving frequencies. Figure 3-30 illustrates the response function (monitored position out feedback signal) of the galvanometer with respect to its drive signal at two drive frequencies. For slow scanning at 50 Hz the position of the galvanometer closely matches the input drive

waveform. At a higher scan speed however there is a decrease in the response amplitude and degree of scan linearity.

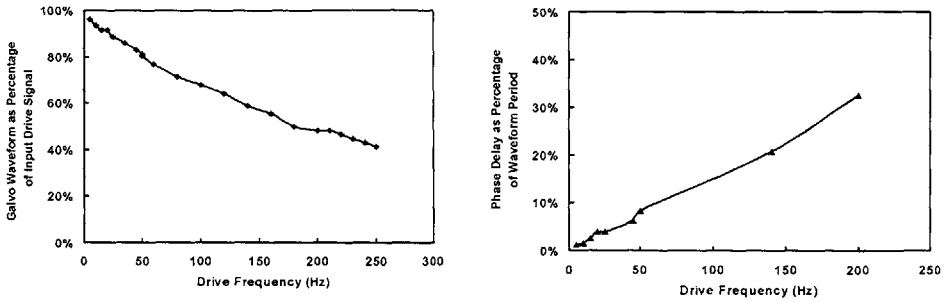

Figure 3-31. Amplitude reduction and phase offset for scanning galvanometer
At increased drive frequency, mechanical galvonometers exhibit worse amplitude and phase performance.

This results in a shorter linear scan region (dotted circles) that can be used. In addition the relative phases of the drive waveform and response function are non-congruous. Figure 3-31 shows the decrease in the galvanometer position waveform amplitude and relative phase difference as a function of increasing drive frequency. The slope of the amplitude reduction is significant and the amount of linear stroke length that can be used decreases rapidly at higher frequencies. Also important is that the galvanometer phase relative to the drive waveform changes. This is not beneficial as the reference arm scanner drive signal is often used as a reference signal for timing, data acquisition, and image display purposes.

Phase Delay Line

In order to enable real time imaging with OCT it is necessary to scan the reference arm optical delay by 2-3mm at frequencies approaching or exceeding 1000 A-scans per second. Retro-reflecting galvanometers while simple in operation and alignment, are quite limited in their scan speed and scan range capabilities. To remedy this situation a high speed Fourier domain phase delay line was developed by Tearney [41]. Figure 3-32 shows a schematic of the elements in the optical delay line.

The system operates on the principles similar to those used in grating-based scanners for chirped pulse amplification and temporal shaping [48, 49]. The incident optical beam is spectrally dispersed by the delay line grating element and focused onto a flat scanning mirror. If the grating and scanning mirror are placed at the focal length positions of the lens, the optical beam is focused at the Fourier plane. When the mirror undergoes a rotational scan a linear phase ramp is imposed onto the spectrally dispersed spectrum.

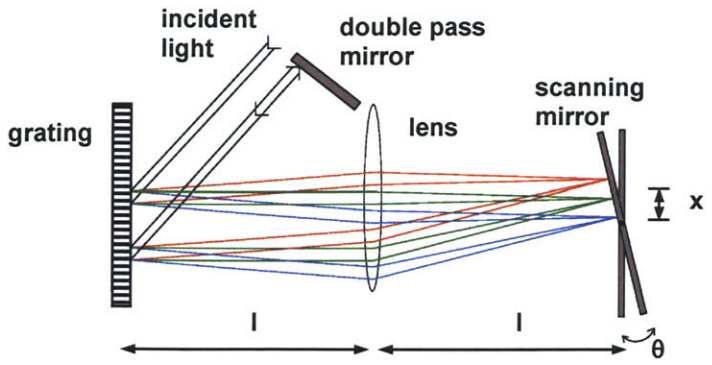

Figure 3-32. Fourier domain optical phase delay line

Incident light is spectrally dispered by a diffraction grating and focused the the system Fourier plane on the mirror surface. A double pass mirror is used to reflect the light back into the system. The center wavelength (green) is offset from the mirror axis of rotation by a distance, x. Modified from reference [50].

This wavelength dependent phase shift in the frequency domain maps to a group delay in the time domain by the Fourier relation

$$x(t-t_o) \quad \overset{\Im}{\rightleftarrows} \quad X(\omega)e^{-j\omega t_o}$$

By scanning the mirror a time-dependent group delay is produced. If the grating is aligned such that the center wavelength of the spectrum is diffracted normal to the grating surface and passes through the center of the lens, group velocity dispersion (GVD) is minimized. If the grating is offset such that it is not aligned normal to the lens optical axis GVD can be introduced into the optical propagation if desired [41, 51]. It can be shown [50] that in a double pass configuration shown the phase shift as a function of mirror tilt angle θ can be written as

$$\phi(\lambda) = \frac{8\pi\theta x}{\lambda} + \frac{8\pi\theta l(\lambda-\lambda_o)}{p\lambda} \qquad \text{or} \qquad \phi(\omega) = \frac{4\theta x\omega}{c} - \frac{8\pi\theta l(\omega-\omega_o)}{p\omega}$$

where l is the focal length of the lens, p is the grating pitch, and x is the optical beam offset distance from the scanning mirror's axis of rotation. With the phase and group delay defined respectively as $\tau_p = \phi(\omega_o)/\omega_o$ and $\tau_g = \partial\phi/\partial\omega\big|_{\omega=\omega_o}$ they are given by

$$\tau_p = \frac{4\theta x}{c} \qquad \text{and} \qquad \tau_g = \frac{4\theta x}{c} - \frac{4\theta l\lambda_o}{cp}$$

Figure 3-33 shows the phase and group delay characteristics of the scanner plotted as a function of mirror offset position. Taking the ratio of the delay terms in Figure 3-33b, there are two unique operating points

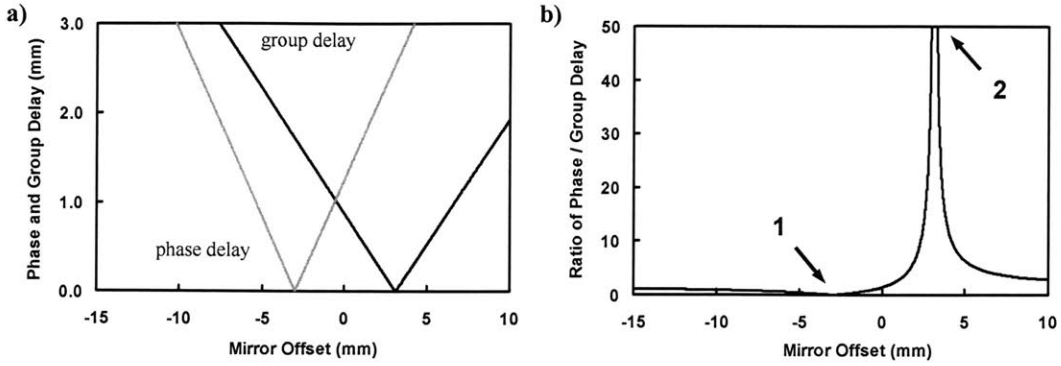

Figure 3-33. Phase and group delay characteristics for optical delay line

a) Plot of phase (grey) and group delay (black) as function of mirror offset position. b) Ratio of pahse delay to group delay shows operating points of zero phase and zero group delay. Grating denisty 50 l/mm, center wavelength 1250nm, bandwidth 180nm, scan frequency 2000 A-scans/sec, Doppler frequency 6 MHz.

which can be achieved for the phase delay line. The first unique operating point 1 has only a group delay is imparted to the optical signal with zero phase delay. This setting can be used to have minimal dispersion introduced by the delay line in the system reference arm. It is important to reduce dispersion of course when using high resolution, broadband light sources. With correctly chosen parameters, a second operating point 2 can be achieved where a phase delay is introduced to the signal however with no group delay. This pure phase modulation was shown by Zvyagin and Sampson [52] and can be used for other scanning techniques such as optical coherence microscopy [53, 54].

Coherent detection

In optical transmission systems, signal measurements were initially performed by directly detecting intensity modulated waveforms [55]. It was realized that coherent detection could significantly improve system performance by enabling shot-noise limited sensitivity rather than being limited by thermal receiver noise for the case of direct detection techniques. While the principles of coherent detection were well established for radio frequencies [56], they were only demonstrated in the optical domain after development of the gas laser [57, 58]. While direct detection methods only allow for measurement of the optical carrier amplitude, with coherent detection it is possible to extract amplitude, phase, and frequency information of the optical signal [59].

Coherent systems can be divided into two categories dependent on whether homodyne or heterodyne detection is used. In both detection techniques, a local oscillator signal is added to the

incoming signal at the receiver. The relevant signal information is retrieved by converting the optical signal into an electrical signal and removing unwanted frequency components by filtering operations. For homodyne systems the local oscillator signal is at the same frequency as the carrier. While this gives increased signal to noise performance over heterodyne techniques [60], extraction of signal information is more complex as the carrier frequency of infrared light is on the order of 10^{14} Hz. For heterodyne systems the local oscillator frequency is significantly offset from the carrier. By using this characteristic signal demodulation can be performed at frequencies amenable to electronic filtering and amplification in the kHz or MHz range. For this reason OCT systems implement heterodyne detection to retrieve and process optical signal information.A block diagram of the receiver electronic system originally developed by Swanson, *et. al.* [61] is shown in Figure 3-34.

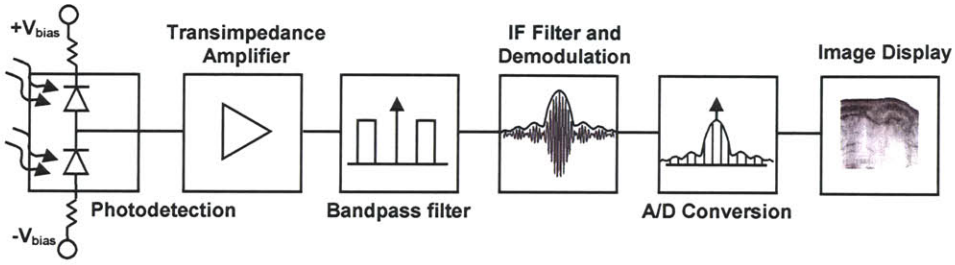

Figure 3-34. Functional block diagram of OCT receiver electronics

The sample signal and local oscillator reference signal are combined in an optical coupler and the resultant signal is discriminated by a photodetector stage. Either a single (unbalanced) or dual (balanced) photodiode configuration may be used. A dual balanced design is beneficial when excess intensity noise from the laser source is significant. By using back-to-back photodiodes as shown it is possible to suppress out the laser noise in a balanced receiver [62, 63]. It is important that the electronic response characteristics of the photodiodes be well matched to achieve optimal noise reduction. The transimpedance amplifier converts the photocurrent into an electrical voltage signal with amplification equal to the heterodyne gain of the system. Typically the local oscillator signal is much larger than the sample signal and thereby determines the signal gain.

In a heterodyne receiver the output from the transimpedance amplifier is centered about an intermediate frequency (IF) that is determined by the scanning speed of the system reference arm mirror. This intermediate frequency is often referred to as the Doppler frequency of the system. The signal is first processed by a bandpass filter which must reject any non-relevant frequency components in the signal while at the same time be wide enough such that the passband contains the IF signal spectrum. After filtering the signal is demodulated with a linear or logarithmic demodulation method. While linear demodulation allows for increased resolution, it

suffers from decreased dynamic range. For this reason logarithmic demodulation is often employed as the signals in OCT can typically span over 100 dB in optical intensity. Finally a baseband filter can be applied after demodulation to remove any remaining low frequency noise.

Photodetection

While often overlooked, the photodetector plays a critical role in the system performance. A semiconductor photodetector functions by creating a depleted region of space charge between multiple layers of selectively doped material. When photons enter the material electron-hole pairs created in the depletion layer generate an electrical drift current which flows under the internal electric field. The response time of this current is fairly fast, on the order of nanoseconds, as the electron and hole mobilities are appreciably high. For the 700-1000nm wavelength range, silicon photodiodes offer good conversion of photons into electrons as the photon energy is greater than the silicon bandgap of 1.1eV. For higher wavelengths from 1100-1400nm InGaAs on Ge photodiodes can be used as the material bandgap is smaller and therefore more sensitive to the lower photon energy. Figure 3-35 shows the spectral sensitivity behavior for several commonly used photodiodes in the near IR. The spectral sensitivity which is defined as the ratio of the photo-generated electrical current over the incident optical power can be written as

$$\sigma = \frac{\eta e \lambda}{hc}$$

where η is the diode quantum efficiency. As a system design issue, one should try to obtain the best performing photodiodes as possible. The extra investment is well worth it when one considers that these system components are directly responsible for converting the optical light energy into the one electrical signal that directly and significantly impacts imaging performance. In addition it is beneficial to reduce the detector size in order to minimize Johnson or lattice noise which is proportional to the detector active area. The detector should be large enough however to accommodate the full optical beam from the interferometer system and collect all of the incident light. Pigtailed photodiodes can provide a reliable, off-the-shelf solution to optimal fiber to detector alignment however some drawbacks exist to this approach. One drawback is the inability to measure optical power and spectral bandwidth arriving at the detectors for system characterization purposes. The second is that often it is necessary to attenuate one detector signal in a dual balanced OCT configuration to achieve noise cancellation and optimal signal to noise performance (see Table 3-1). Fiber attenuators can be used however usually cannot support the full optical bandwidth of high resolution OCT systems. A more standard and versatile approach is

to either slightly misalign the fiber and photodiode (for a non-pigtailed setup) thereby reducing the optical power received as necessary.

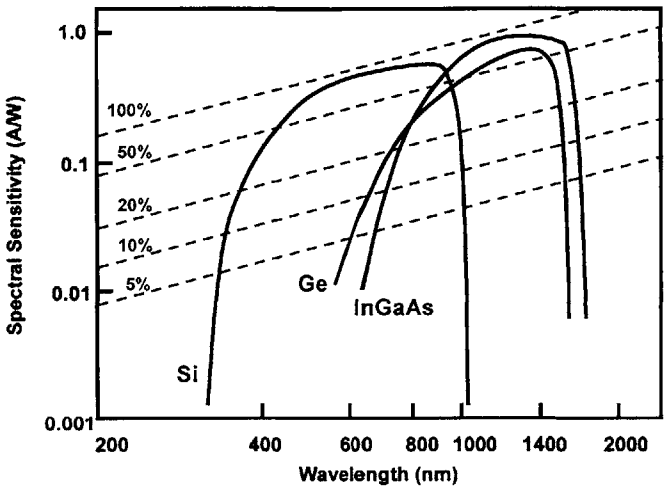

Figure 3-35. Spectral sensitivity curves for photodiodes in the NIR
Silicon diodes exhibit good spectral response in the lower infrared regime while Ge and InGaAs diodes perform better in the 1000-1400nm wavelength ranges. Dashed lines with percentages represent levels of constant quantum efficiency. Modified from reference [64].

Two important figures of merit for the receiver are sensitivity and dynamic range. Fortunately the conversion of optical energy into an electronic signal by a photodetector aids in the signal to noise performance of the system. This is because the photodetector produces an electrical current that is proportional to the incident optical *power*, or square of the optical field. The corresponding electrical power is proportional to the square of the electrical current and therefore to the square of the incident optical power. Thus the signal to noise ratio in the electrical domain will be twice the optical signal to noise ratio expressed in units of dB. The detector photodiodes are reverse biased to minimize leakage current and present an almost purely capacitive load to the transimpedance amplifier.

Transimpedance Amplifier

The function of the transimpedance amplifier is implicit in its name. Power amplification of the input photoelectron current from the photodiodes is performed and a corresponding voltage is produced at the output. In a conventional operational amplifier the open loop gain is usually very large in order to obtain electrical characteristics approaching those of an ideal circuit. At higher frequencies however (>1 MHz) the time delay around the feedback loop of the amplifier becomes significant thereby preventing operational behavior. It is therefore necessary to have a

circuit that provides high speed with a fast feedback loop at the expense of some gain, hence the transimpedance amplifier. The output voltage from the amplifier is typically produced with a significantly lower impendence in order to allow for a large current signal to be obtained. A schematic of a basic transimpedance amplifier circuit is shown in Figure 3-36.

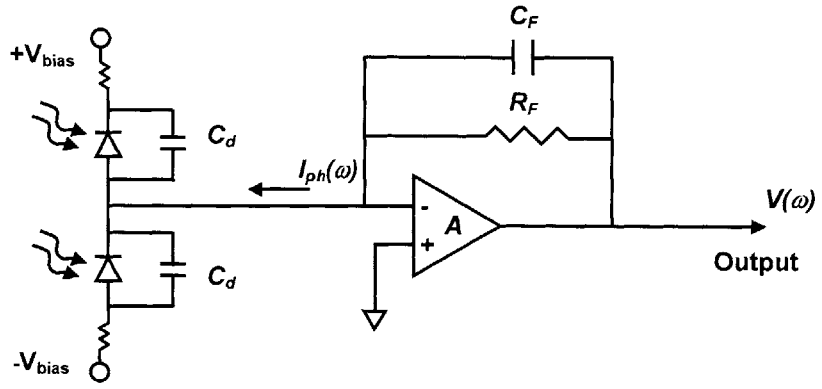

Figure 3-36. Transimpedance amplifier circuit

A low-noise transimpedance amplifier is utilized to amplify the signal photocurrent from the dual balanced photodetectors.

Although no current is drawn by the inverting input of the amplifier, feedback creates a virtual ground at the input which is pinned close to zero volts. This causes photodiode current to be diverted to the load where it produces a voltage signal equal to $-I_{ph}R_F$. Assuming the gain has a single pole cutoff such that

$$A = \frac{A_o}{1 + j\omega/\omega_o}$$

where A_o is the dc gain and ω_o is the cutoff frequency. It can be shown [64] that the amplifier has a two pole, second order response given by

$$\frac{V(\omega)}{V(0)} = \left(1 + \frac{2\chi\omega}{\omega_3^2} + \frac{\omega^2}{\omega_3^2}\right)^{-1}$$

where ω_3 is the 3dB cutoff frequency given by

$$f_3 = \frac{1}{2\pi}\sqrt{\frac{\omega_o A_o}{R_F(C_i + C_F)}} = \frac{\omega_3}{2\pi}$$

and χ is a damping factor of the frequency response

$$\chi = \frac{1}{2}\left[\left(\frac{1}{C_i + C_F}\right)\left(\sqrt{\omega_o A_o R_F C_F} + \left(\frac{R_i + R_F}{R_F}\right)\sqrt{\frac{1}{R_F \omega_o A_o}}\right) + R_F\sqrt{\frac{\omega_o (C_i + C_F)}{A_o}}\right]$$

The term R_i corresponds to the internal resistance of the operational amplifier while C_i it the added internal capacitance of the amplifier and photodiodes. The 3dB cutoff frequency can also be written in terms of the cutoff frequency due to the feedback resistance f_R, and the gain-bandwidth product of the operational amplifier (GB)

$$f_3 = \sqrt{f_R (GB)}\ , \qquad f_R = \frac{1}{2\pi R_F (C_i + C_F)}, \qquad (GB) = \frac{\omega_o A_o}{2\pi}$$

To avoid ringing in the frequency response it is necessary to have $\chi > 1$. $\chi = 1$ corresponds to the critical damping condition while $\chi < 0.5$ results in significant frequency overshoot. In practice the optimal solution is to carefully select a transimpedance amplifier that fulfills most if not all of the requirements necessary to have good frequency response, low noise, and sufficient speed and bandwidth specifications. Several commercial transimpedance stages are available [65-67] and can be chosen to suit a specific system. A complete dual balanced detection system with transimpedance can even be purchased as a stand alone unit [4] however performance specifications may not be optimal for all experiments. After the transimpedance stage fixed or variable gain stages can also be implemented to increase signal strength. The gain stages should be configured to optimize dynamic range and sensitivity. In addition the resistance should be chosen to be as high as possible to provide the maximum gain while maintaining the necessary bandwidth performance required for the signal.

Bandpass Filtering

After electrical conversion and amplification of the optical signal it is often desirable to perform electronic filtering on the signal to remove unwanted noise. In an OCT system, the heterodyne modulation frequency is determined by the optical wavelength and scanning speed of the reference arm. This frequency, termed the Doppler frequency, is given by

$$f_D = \frac{2v_s}{\lambda_o}$$

where v_s is the scan velocity and λ_o is the center wavelength of the light source. For slow scanning systems implementing mechanical galvanometers, a 2-3mm optical delay can be produced at 200 Hz. This results in Doppler frequencies in the range of 1-2 kHz. For the high speed OCT systems used in this work scan speeds of 2000-3000 Hz were achieved with 4.5mm

scan lengths. This results in Doppler frequencies in the 10-20 MHz range and introduces significantly more demanding requirements on the electrical filtering and demodulation stages in the receiver. For the high speed system, discrete 2nd order, 4-pole bandpass filters were built using passive RLC components. A schematic of the bandpass filter design is shown in Figure 3-37.

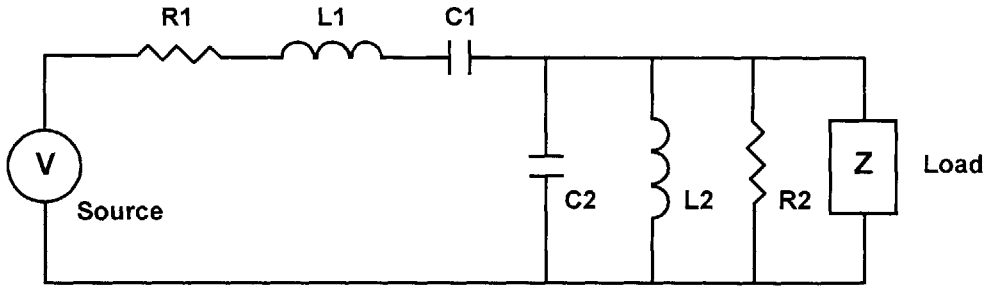

Figure 3-37. Bandpass filter schematic

A frequency response plot of the magnitude and phase of one filter used is shown in Figure 3-38. The filter shows good response characteristics with sharp cutoffs at the low and high frequency corners outside of the passband. To filter bandwidth should be approximately equal to if not slightly larger than the signal bandwidth to obtain the best performance. While a small percentage of the signal will be lost, the SNR is maximized when the filter's frequency response is nearly identical to the signal power spectrum.

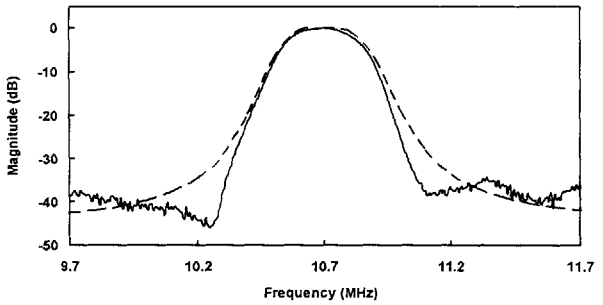

Figure 3-38. Frequency response of 2nd order bandpass filter

Good agreement is achieved between simulated (dashed curve) and measured (solid curve) frequency responses of the system bandpass filter.

A larger bandwidth introduces additional noise and any smaller of a bandwidth clips too much of the signal. A rough estimate of the OCT signal electronic bandwidth can be measured by performing an FFT decomposition of the fringe signal either with a FFT-enabled oscilloscope or in a computational program such as Matlab.

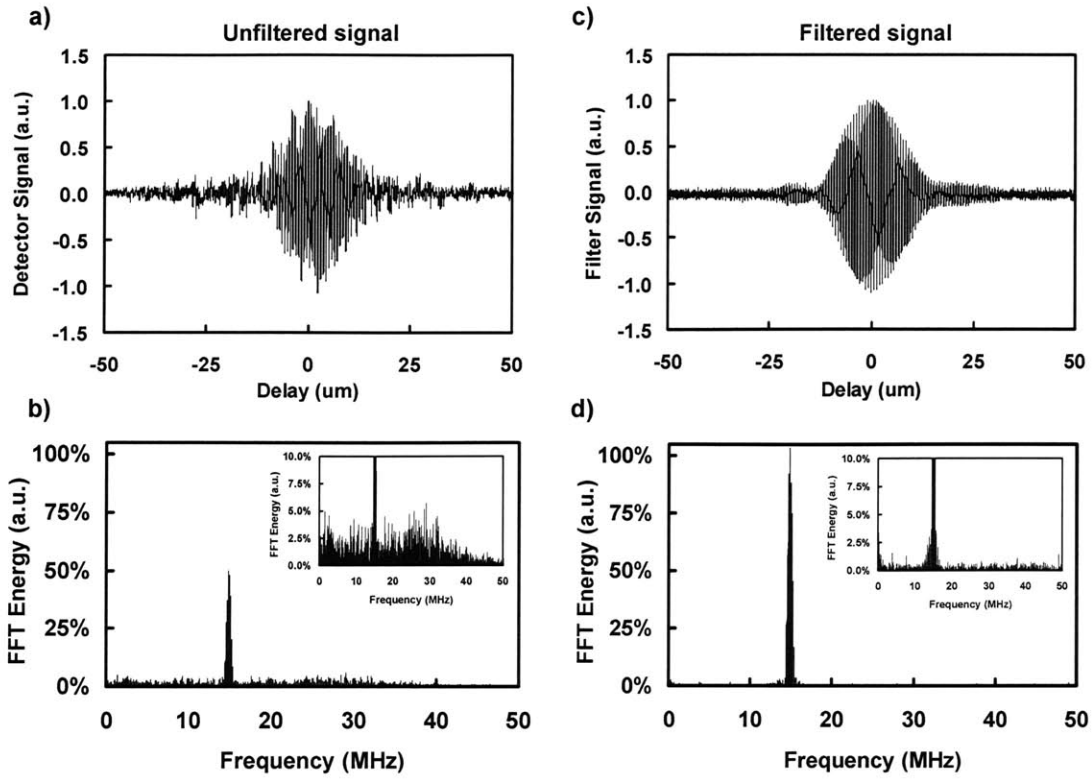

Figure 3-39. Effect of filtering on the OCT signal frequency spectrum

OCT heterodyne signal and FFT enery spectrum for before (a,b) and after (c,d) bandpass filtering. Frequency components both above and below the system Doppler frequency (15 MHz) are removed allowing increased signal isolation and detection.

With the previously described rotary cam scanner in the reference arm it is possible to adjust scanning speed and center the Doppler frequency in the middle of the filter response curve. This is more practical than trying to precisely design an exact frequency response for a discrete component, multi-pole filter.

Figure 3-39 shows the heterodyne fringe pattern and FFT frequency spectrum of the OCT signal before and after bandpass filtering. The importance of filtering process can be seen by the significant decrease in the noise and number of frequency components in the signal spectrum after bandpassing.

Demodulation

There exist several options for demodulation of the OCT signal. Due to the high sensitivity of the heterodyne detection technique however, signal levels spanning over 100 dB were readily achieved for the high resolution systems used in this work. For this reason a

logarithmic amplifier was implemented after the bandpass filtering stage to visualize signal levels over the full dynamic ranges achieved. The purpose of the logarithmic amplifier is not to amplify but rather to compress a signal of wide dynamic range into its decibel equivalent. A more appropriate nomenclature might be that of a logarithmic converter as the input signal is converted from one form to another via the nonlinear transformation

$$V_{OUT} = V_Y \log\left(\frac{V_{IN}}{V_X}\right)$$

where V_Y and V_X are the slope and intercept voltages and as illustrated in Figure 3-40. For the calibration of the amplifier the formula

$$V_{OUT} = V_{slope}\left(P_{in} - P_{ref}\right)$$

can be used where V_{slope} is the logarithmic slope expressed in volts per decade, P_{in} is the input power, and P_{ref} is a reference power level. For the log demodulator used a slope of 25mV/dB was measured. For its functionality, the log demodulator employs a series of nonlinear amplifiers cascaded in series to generate the logarithmic transform of the incoming electrical signal. For the demodulating amplifier used an overall gain of 20,000 (86 dB) with a bandwidth of 500 MHz was specified. The resulting gain-bandwidth product (GB) is equal to 10 THz, a factor of approximately 10^6 times larger than that of a typical operational amplifier. This high GB product is necessary in order to have accurate operation under small signal conditions at high frequencies.

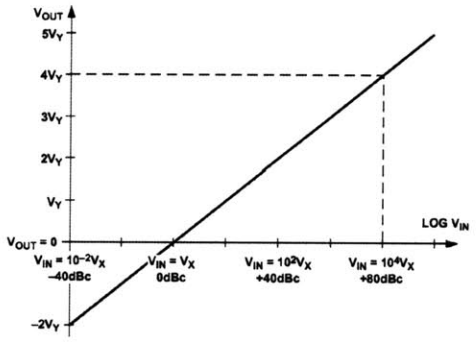

Figure 3-40. Logarithmic voltage transformation

Graphical representation of voltage signal compression to its decibel equivalent. Reprinted from reference [68].

It should be kept in mind that the amplifier responds to the applied voltage at its input, not the incoming power. As the input impedance of the amplifiers are typically much greater than $50\,\Omega$ (usually $>1\ k\Omega$ even at low frequencies) the use of a well designed matching network can considerably improve the power sensitivity of the amplifier. In addition, because logarithmic

amplifiers have very high gain and large bandwidth they are susceptible to a broad frequency range of signals at their input. Without pre-filtering, these signals will have the effect of increasing the noise floor and lowering the system dynamic range. For this reason a solid ground for the amplifier should be implemented as well as any necessary shielding and power supply decoupling.

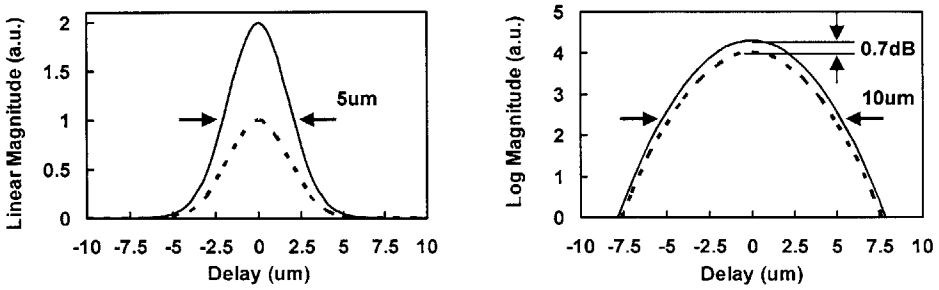

Figure 3-41. Effect of log demodulation on resolution and contrast
Log demodulation results in a decrease in SNR sensitivity and reduction in resolution.

There is a disadvantage however when using log demodulation on the OCT signal to generate an image. While the process of taking the logarithm enables a large dynamic range and allows for the visualization of very low backreflected signal levels, it also results in decreased image resolution and contrast of the fringe envelope function. As shown in Figure 3-41, a 5um FWHM axial OCT resolution on a linear scale broadens to twice that on a log scale (at a -2.5dB level or 50dB of dynamic range). In addition a two fold increase in signal strength on the linear scale results in only a 0.7dB difference out of ~100dB in the OCT image

Analog to Digital Conversion

The goal of an A/D converter (ADC) is to transform the analog voltage OCT signal into a quantized, digital representation that can be processed and manipulated by the system computer. There are two main functions of the A/D data acquisition card, sampling of the signal in the time domain and quantization of the signal amplitude. Sampling of the data signal is performed at discrete time intervals set by the A/D card clock frequency. It is possible to completely reconstruct the time domain signal by sampling at or above the Nyquist sampling frequency. This frequency is just twice the maximum frequency contained within power spectrum of the signal of interest. Sampling at a lower frequency, i.e. undersampling, results in aliasing of the original signal and can result in unwanted signal components appearing in the desired frequency band of interest which cannot be differentiated from the actual signal. A graphical example of aliasing is

shown in Figure 3-42. Once a signal has been aliased it is in general not possible to recover the original function without introducing additional error.

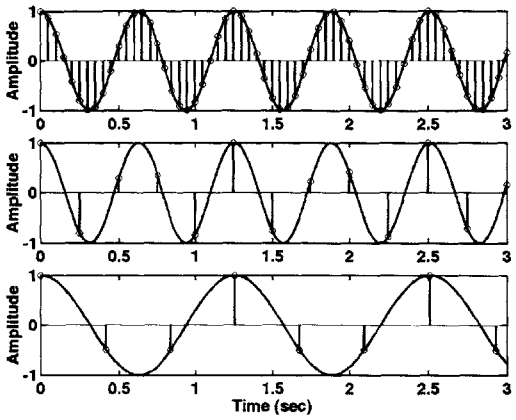

Figure 3-42. Signal aliasing due to undersampling

The original signal is accurately reconstructed when oversampled or sampled at Nyquist (top and middle). Undersampling results in signal aliasing and loss of the original signal information upon reconstruction (lower).

The second function of the A/D card is to quantize the sampled signal into digital integer values. The resolution of the quantization is determined by the bit resolution of the card and theoretically an N-bit ADC can provide 2^n discrete quantization levels or steps corresponding to a specified analog signal amplitude range with each bit corresponds to 6 dB of available dynamic range [69]. Thus a 12-bit ADC would have a theoretical 72 dB of dynamic range with 4096 discrete levels. All of these levels would be usable except that on average some digital values fall in between the discrete levels and produce quantization noise in the ADC output. This quantization noise effectively uses up one bit of resolution termed the least significant bit (LSB). So at best an N-bit ADC functions at best as an (N-1) bit resolution converter. If additional techniques such as sample clock dithering are used for example to reduce the signal noise floor, the ADC resolution would be lower still.

The process of signal amplitude conversion is also inherently error prone and information is lost in the transformation of the analog signal into digital form. This arises due to the discrete binning of the analog signal into quantized amplitude levels and is demonstrated in Figure 3-43 for a three bit ADC. The converter has 8 separate integer levels (ranging from 0 to 7) from within which it can bin the incoming signal.

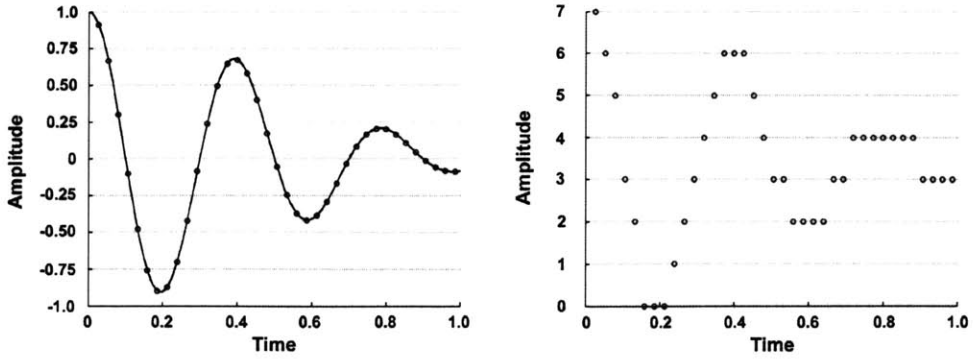

Figure 3-43. Loss of signal veracity due to amplitude quantization

ADC quantization leads to inherent signal distortion due to the transformation from continous to discrete signal levels. This can be reduced however not eliminated by using more bits in the A/D conversion.

The quantization level is defined as the range of values which are assigned to the same digital integer value. In the case of the three bit ADC example, the quantization interval is 0.25; in general it is equal to 2^{1-N} where N is the bit resolution of the ADC.

Hardware Configuration, Timing, and Image Acquisition

Critical to any OCT system is the control software that is used for data acquisition, image display, and timing synchronization of optical, electrical, and mechanical sub-systems. The software control systems used for several of the studies in this work was originally developed by Tony Ko [70] in a C++ Windows based shell. Modifications were made to acquire and control signals for new high speed scanning systems. Figure 3-44 shows the hardware configuration for the high speed OCT imaging system constructed in this work. The system was made to be highly compact and portable so that it could be transported easily and used in clinical settings. The control software was run on a 2 GHz personal computer and utilized two 12-bit data acquisition cards for I/O operations. A National Instruments 6110E PCI analog to digital (A/D) card and a PCI 6711 digital to analog (D/A) card were used to control the system drive and timing synchronization signals. The sampling and update rates for the two cards were 5 MHz and 2 MHz which were sufficient for non-spectroscopic imaging experiments.

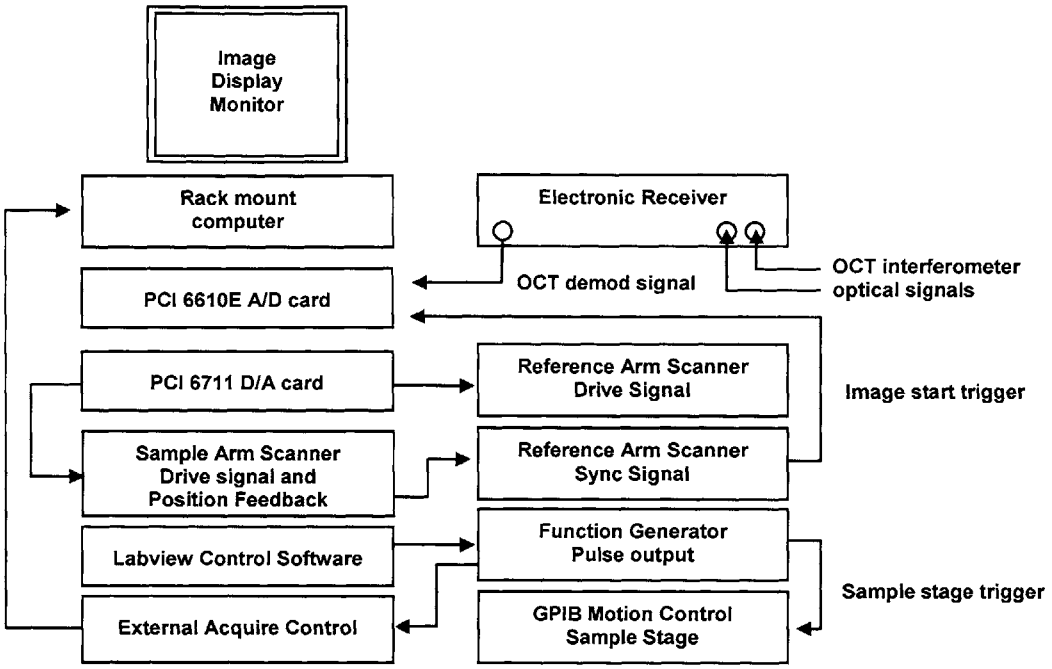

Figure 3-44. Hardware configuration for high speed OCT system

The system functioned by initializing the software interface and generating a drive waveform for the reference arm scanner. For a mechanical galvanometer or phase delay line, this signal consisted of a triangle waveform to scan in the forward and backwards mirror swings. When this was done however the image display needed to be modified to display sequential OCT scans as flipped 180 degrees with respect to the previous scan. This is because the interferometric delay position on the backward stroke of the galvanometer mirror starts at the tissue surface and goes into the sample while on the forward stroke the direction is reversed. For the high speed rotary scanner, the reference arm drive signal consisted of a 5 Volt square pulse with a 50% duty cycle. This pulse actuated the motor shaft and the delay line with a 1:1 relationship between the drive frequency and delay line speed. Thus a 500 Hz square wave resulted in 500 revolutions per second (rps). At high delay line scanning speeds it was necessary to configure the software control to gradually ramp up the drive frequency in order to avoid an excessive current load on the scanner power supply. Figure 3-45 shows a timing diagram of several signals in the OCT system. The reference arm drive is the top trace in Figure 3-45a.

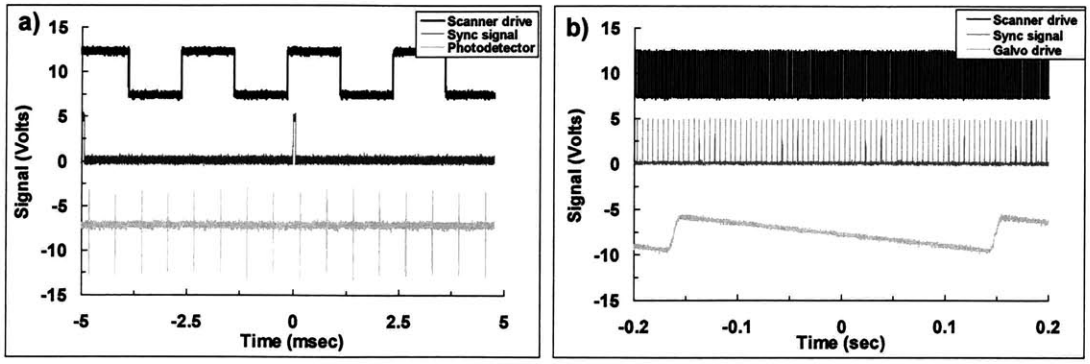

Figure 3-45. OCT system timing diagram

a) Scanner drive, frame sync signal, and photodetector output. b) Increased time scale with scanner drive, sync signal, and x-galvo drive waveform for OCT image scan.

In order to consistently display a OCT image, a starting reference point must be defined in the system timing. Each cross-sectional image is created by scanning the sample arm and collecting many axial depths scans at different scan positions on the tissue surface. Thus a logical reference point to begin the image acquisition would be at the start of the sample arm scan sweep. There was one problem with using the sample arm sweep signal as the image start trigger. Due to the fact that the delay line offsets were not identical and a zipper offset was required, it was necessary to have the image acquisition starting point be referenced to a specific position on the scanner. This was implemented by painting a black mark on the top of the reflective scanner surface and using an LED and photodetector to measure the signal reflectivity off of this top surface. When the scanner underwent actuation, a voltage difference was detected, inverted and transformed into a 5 Volt TTL pulse. This trigger pulse occurred once per scan revolution and is shown as the middle trace in both Figure 3-45a and Figure 3-45b. An AND operation was performed on the trigger pulse and the sample arm scan signal to begin image acquisition on a specific mirror position at the beginning of a sample arm scan (lower trace shown in Figure 3-45b). For each A-scan, an interference signal from the OCT system was generated by the dual balanced photodetectors and is shown as the lower trace in Figure 3-45a and upper trace of Figure 3-45b. This interference signal was filtered and demodulated by the electronic receiver and sent to the 12 bit A/D card for image display (Figure 3-44).

In one particular system configuration, a modification was made to automatically acquire OCT images with no operator input necessary to enter a save keystroke. This was done for the purpose of collecting high density 3D volume-imaging data sets. As each data set consisted of

several hundred scans it was not feasible to manually save each image. For this system configuration, the sample was placed on a motion control stage with a GPIB interface. Additional control code was written in LabView and Matlab to generate stage motion control and image acquisition TTL pulses via a function generator. When the OCT sample arm mirror was scanned across a tissue specimen, an acquire pulse was sent to the computer system and an image was saved. The motion control stage was then moved automatically to an adjacent tissue location and another OCT scan was performed. This process was repeated in order to generate full 3D volume data sets of OCT tissue specimens.

Imaging at High Resolution

A great deal of work was done in this thesis to realize high resolution imaging with OCT as well as develop a high speed imaging system capable of being used in a clinical setting. In order to achieve this optimization and understanding of several important factors affecting system performance was done. These factors included the optical light source, fiber-based system components, photodetection, electronic filtering and receiver configuration, dispersion compensation, reference arm scanning systems, and sample arm beam delivery devices. In addition the hardware implementation for signal timing and image acquisition using in house software control was carried out.

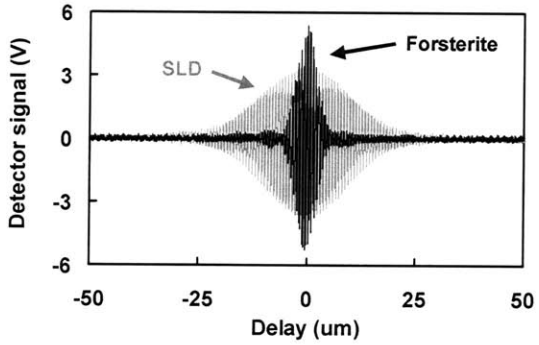

Figure 3-46. Axial resolution comparison of SLD versus Cr:Forsterite laser
A 3x improvement is possible with the Forsterite laser achieving axial resolutions of <5um in tissue.

As a representative example of OCT resolution performance a comparison of system axial resolution and image quality was made at 1300nn center wavelength between a broadband SLD (AFC Technologies) with a 60nm optical bandwidth and the Cr^{4+}:Forsterite laser at 180nm bandwidth. Figure 3-46 shows the interferometric fringe signals from the source at the matched zero delay optical path position. With the AFC source, a measured axial resolution of 15um was obtained. In comparison, it was possible to achieve <5um resolution with the Forsterite laser

using dispersion matching elements within the system. As dispersion at 1300nm is not as significant for a smaller bandwidth range (see Figure 3-23b), compensating glass was not required nor had any appreciable effect for the AFC source.

Figure 3-47 shows comparative images of OCT images using both the AFC and Forsterite laser sources. Figure 3-47a is a standard resolution OCT scans of a tissue phantom (layers of thin translucent tape), while Figure 3-47b shows the same phantom however acquired with the Forsterite source.

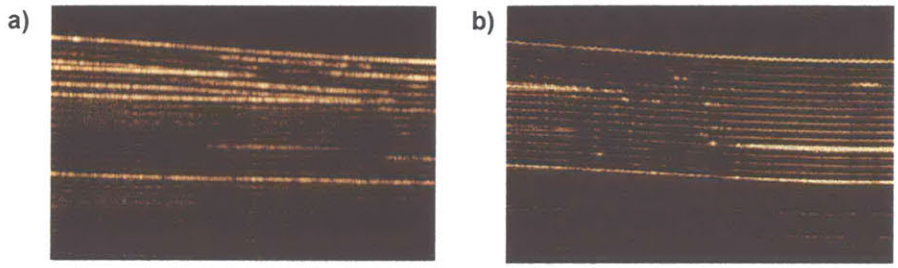

Figure 3-47. Comparison of tissue phantom at high resolution

OCT image of a tissue phantom imaged at standard 15um resolution with the AFC source (a) and at 5um resolution with the Forsterite laser (b).

The higher resolution source clearly shows higher fidelity in distinguishing the individual tape layers. Each interface layer exhibits a high backscattering characteristic that delineates it from the next layered region. This is significant in the context of imaging biological systems as many important regions in tissue are separated by epithelial or mucosal membrane surfaces. It is at these interfaces that a strong backscattered OCT can be detected and identified if the system resolution is sufficient. In addition the disruption of these interfacial surfaces in disease states is often indicative of a pathological condition. The ability to detect, qualify, and quantify these interface disruptions would have significant clinical implications.

A second set of images demonstrates a standard and easily accessible *in vivo* specimen, that of a human inner cheek. While the standard resolution image (Figure 3-48a) does provide some contrast between the structures below the surface, much more detail and architecture can be seen at higher resolution (Figure 3-48b). This is apparent at the higher magnification insets on the right. The capability to visualize such microstructural tissue components can be important when distinguishing subtle differences in tissue architecture and diseased tissue states.

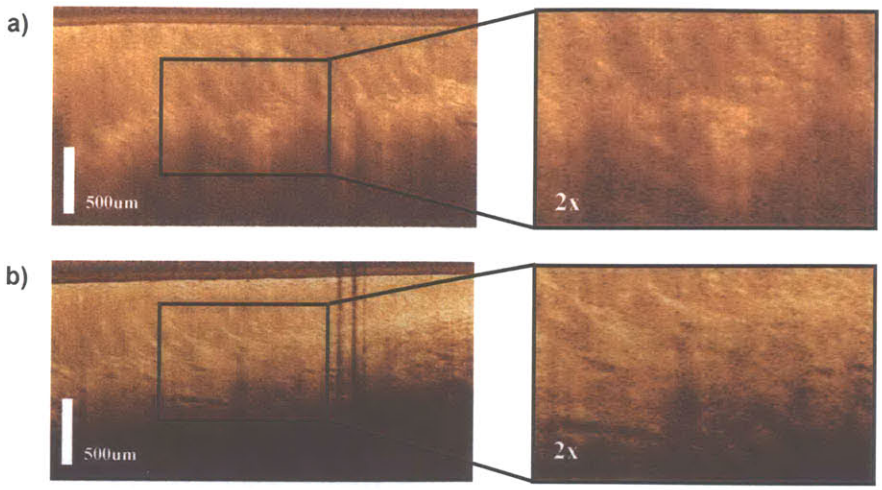

Figure 3-48. Standard and high resolution imaging of human tissue

Greater structural detail and image contrast is seen in the high resolution image (b) with 5um axial resolution over standard 12um axial resolution (a) image. Transverse resolution is 15um ($2w_o$) in both images. Pixel density is 1 pixel / 2um.

A factor that must also be considered when acquiring high resolution data is the imaging frame rate required for a given application and the image pixel density relative to the system resolution. We will first consider the axial resolution of the image. In the depth direction, the number of resolvable spots is determined by the coherence gating of the heterodyne interference signal and the image pixel density.

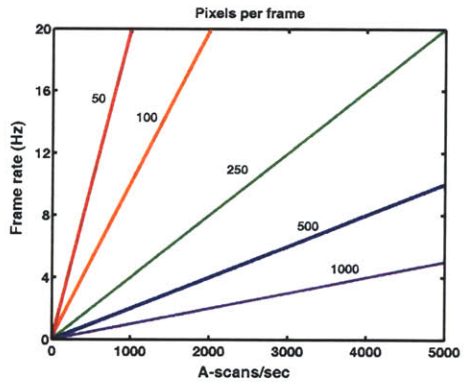

Figure 3-49. Number of pixels per frame as a function of scanning speed

High speed imaging (increased frame rate) rapidly reduces the number of available pixels in a given OCT image frame. For optimal resolution performance the pixel sampling density should be at least twice the axial or transverse resolution.

The high resolution systems used in this work have at minimum a three to five-fold increase in axial resolution over standard SLD sources. In the case of imaging at 1300nm wavelength an axial resolution of 5um was achieved compared to 15um for the SLD. For imaging studies using the Ti:Sapphire laser system even smaller transverse and axial resolutions of 5um and 2um were achieved. In order to maintain image quality and prevent unwanted blurring due to undersampling, high pixel densities are again desirable. Figure 3-49 shows the qualitative relationship between the number of pixels within an OCT imaging frame as a function of the image frame rate and number of axial scans per second.

Most OCT sample arm scanning probes implement a 10-15um transverse spot size in order to maintain a relatively large depth of field through the scan field. For a transverse scan length of 3mm as an example, this corresponds to 300 resolvable axial scan spot locations if the focused spots are directly adjacent to one another. Ideally however the axial scan density will oversample the imaging field to avoid losing feature details. As an example, a 2x oversampling rate this corresponds to 600 axial scans per 3 mm lateral scan. If the sample is scanned at 4 frames per second to give a reasonable real time imaging display the necessary system requirement is to generate 2400 A-scans/second. It is clear that high speed OCT systems are therefore necessary to ensure optimal image resolution and A-scan density across the scan field. This is even more pronounced for longer scanning protocols where as much as 8mm of linear scanning is performed to survey a large tissue field.

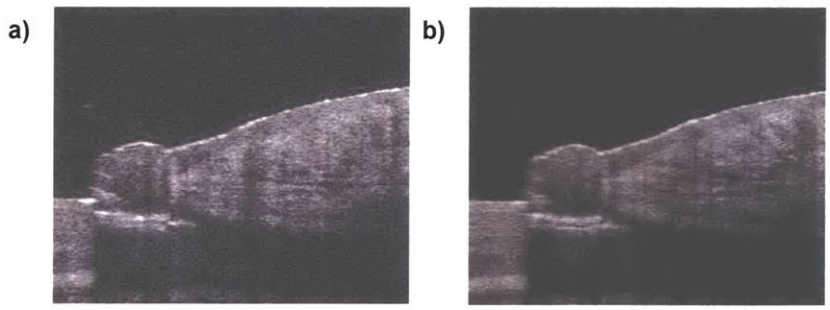

Figure 3-50. Image enhancement with frame averaging

High resolution OCT scans of human nailbed and cuticle a) without and b) with frame averaging. The frame averaged image shows higher contrast, reduced speckle, and greater detail of tissue architecture.

If the OCT system is capable of high speed scanning, imaging performance can be further improved by frame averaging over multiple OCT scans. This increases the image contrast and feature resolution by higher signal to noise performance through reduction of speckle and other noise sources in the image as shown in Figure 3-50. The imaging system however must be

capable of imaging sufficiently rapidly in order to gain the benefits of frame averaging. If the scan speed is too slow or alternatively if the tissue area under examination is prone to movement due to blood flow, breathing, or other factors, image quality is rapidly reduced. Figure 3-51 demonstrates the reduction in OCT image quality when averaging is used and the sample undergoes motion between the averaged scans. This results in blurring and decreased performance.

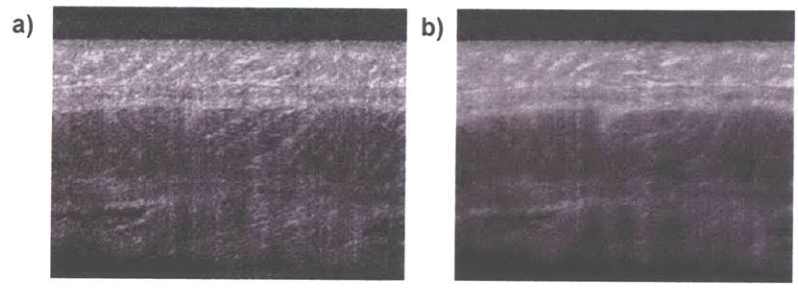

Figure 3-51. Image degradation due to averaging with motion artifact
High resolution scan of rabbit colon recorded at 4 frames per second a) without frame averaging and b) with 2 frame averaging resulting in a blurred image due to motion.

References

1. H. W. Ott, "*Noise Reduction Techniques in Electronic Systems,*" John Wiley & Sons, 2nd edition, (1988).
2. F. Grum and R. J. Becherer, *Radiometry*. Optical Radiation Measurements. Vol. 1. 1979: Academic Press.
3. A. Rollins and J. Izatt. *SNR Analysis of conventional and optimal fiber-optic low-coherence interferometer topologies*. in *Proc. SPIE 3915*. 2000.
4. "*New Focus Nirvana Auto-Balanced Photoreceivers,*"
5. H. Stadt, Astron. Astophys., **36** (1974).
6. B. M. Oliver. in *Proc IRE*. 1961.
7. H. P. Yuen and V.Chan, Opt Lett, **8**, 177 (1983).
8. A. Rollins and J. Izatt, "*Optimal interferometer designs for optical coherence tomography,*" Optics Letters, **24**, 1484-1486 (1999).
9. H. A. Haus and M. Mecozzi, "*Noise of mode-locked lasers,*" IEEE J Quantum Electron, **29**, 983-996 (1993).
10. H. A. Haus, M. Margalit, and C.X.Yu, "*Quantum Noise of a Modelocked Laser,*" Opt. Soc. America., **17**, 1240-1256 (2000).
11. F. Rana and R. J. Ram, "*Noise and timing jitter in active and hyvrid mode-locked semiconductor lasers,*" OSA, 6-7 (2001).
12. F. Rana, H. Lee, R. J. Ram, M. E. Grein, L. A. Jiang, E. P. Ippen, and H. A. Haus, "*Characterization of the noise and correlations in harmonically mode-locked lasers,*" Opt. Soc. America., **19**, 2609-2621 (2002).
13. K. Takada, IEEE J Quant Electron, **34**, 1098-1108 (1998).
14. *Selected Papers on Adaptive Optics and Speckle Imaging*, ed. D.G. Crowe. 1993: SPIE Milestone.
15. J. D. McKinney, M. A. Webster, K. J. Webb, and A. M. Weiner, "*Characterization and imaging in optically scattering media by use of laser speckle and a variable-coherence source,*" Opt Lett, **25**, 4 (2000).
16. R. Feiel and P. Wilksch, "*High-Resolution Laser Speckle Correlation for Displacement and Strain Measurement,*" Applied Optics, **39**, 54 (2000).
17. S. H. Xiang, L. Zhou, and J. M. Schmitt. *Speckle noise reduction for optical coherence tomography*. in *SPIE*. 1997.
18. J. M. Schmitt, S. H. Xiang, and K. M. Yung, "*Speckle in optical coherence tomography,*" Journal of Biomedical Optics, **4**, 95-105 (1999).
19. A. F. Fercher, W. Drexler, C. K. Hitzenberger, and T. Lasser, "*Optical coherence tomography-principles and applications,*" Reports on Progress in Physics, **66**, 239-303 (2003).
20. W. Li, "*1/f Noise,*" http://www.nslij-genetics.org/wli/1fnoise/ (2004).
21. K. Takada, H. Yamada, and M. Horiguchi, "*Optical low coherence reflectometry using a 3x3 fiber coupler,*" IEEE Photon. Tech. Lett., **6**, 1014-1016 (1994).
22. S. Bourquin, "*Internal memo, MIT Ultrafast Optics Laboratory,*" (2001).
23. T. Waite, Proc. IEEE, **54**, 334 (1966).
24. R. H. Dicke, Rev Sci Instrum, **17**, 268 (1946).
25. G. L. Abbas, V. Chan, and T. K. Yee, "*Oscillator excess intensity suppression for homodyne and heterodyne detection,*" Opt. Lett., **8** (1983).
26. W. Drexler, U. Norgner, F. X. Kaertner, C. Pitris, S. A. Boppart, X. Li, M. Brezinski, E. P. Ippen, and J. G. Fujimoto. *In vivo ultrahigh resolution optical coherent tomography using a Kerr-lens modelocked Ti:Al_2O_3 laser*. in *Conference on Lasers and Electro-Optics*. 1999. Baltimore, MD: Optical Society of America and IEEE.
27. U. Morgner, P. Wagenblast, R. Ell, W. Seitz, E. P. Ippen, J. G. Fujimoto, and F. X. Kartner, "*Broadband laser light sources for commercial and biomedical applications,*" Proceedings of SPIE, **4978**, 32-37 (2003).
28. ANSI, "*American National Standard for Safe Use of Lasers, ANSI Z136.1-2000,*" (2000).

29. R. J. Thomas, B. A. Rockwell, W. J. Marshall, R. C. Aldrich, S. A. Zimmerman, and J. R. Rockwell, "*A procedure for multiple-pulse maximum permissible exposure determination under the Z136.1-2000 American National Standard for Safe Use of Lasers,*" Journal of Laser Applications, **13**, 134-140 (2001).
30. B. A. Rockwell, C. P. Cain, W. P. Roach, and R. J. Thomas. *Safe use of ultrashort lasers.* in *Proceedings of the 1999 Commercial and Biomedical Applications of Ultrafast Lasers.* 1999. San Jose, CA.
31. K. K. Ranka, A. I. Gaeta, A. Baltuska, M. S. Pshenichnikov, and D. A. Wiersma, "*Autocorrelation measurement of 6-fs pulses based on the two-photon induced photocurrent in a GaAsP photodiode,*" Opt Lett, **22**, 1344-1347 (1997).
32. J. W. Nicholson, J. Jasapara, W. Rudolph, F. G. Omenetto, and A. J. Taylor, "*Full-field characterization of femtosecond pulses by spectrum and cross-correlation measurements,*" Opt Lett, **24**, 1774-1776 (1999).
33. V. Sharma, "*Acknowledgement to V. Sharma for dispersion measurement code in Labview.,*" (2003).
34. Y. Yasuno, S. Makita, Y. Sutoh, M. Itoh, and T. Yatagai, "*Birefringence imaging of human skin by polarization-sensitive spectral interferometric optical coherence tomography,*" Optics Letters, **27**, 1803-5 (2002).
35. M. C. Pierce, B. Hyle Park, B. Cense, and J. F. de Boer, "*Simultaneous intensity, birefringence, and flow measurements with high-speed fiber-based optical coherence tomography,*" Optics Letters, **27**, 1534-6 (2002).
36. J. F. de Boer and T. E. Milner, "*Review of polarization sensitive optical coherence tomography and Stokes vector determination,*" Journal of Biomedical Optics, **7**, 359-71 (2002).
37. X. D. Li, W. Drexler, C. Pitris, R. Ghanta, C. Jesser, J. Hermann, D. Stamper, D. Golden, S. Martin, J. G. Fujimoto, and M. E. Brezinski. *Imaging of osteoarthritic cartilage with optical coherence tomography: microstructure and polarization sensitivity.* in *Conference on Lasers and Electro-Optics.* 1999. Baltimore, MD: Optical Society of America and IEEE.
38. C. Saxer, J. de Boer, B. Park, Y. Zhao, Z. Chen, and J. Nelson, "*High-speed fiber-based polarization-sensitive optical coherence tomography of in vivo human skin,*" Optics Letters, **25**, 1355-1357 (2000).
39. J. A. Izatt, W. Hsing-Wen, M. Kulkarni, K. Kobayashi, M. I. Canto, and M. V. Sivak, "*Optical coherence tomography and microscopy in gastrointestinal tissues,*" OSA Trends in Optics and Photonics on Advances in Optical Imaging and Photon Migration, **2**, 203-6 (1996).
40. E. A. Swanson, D. Huang, M. R. Hee, J. G. Fujimoto, C. P. Lin, and C. A. Puliafito, "*High-speed optical coherence domain reflectometry,*" Opt. Lett., **17**, 151-153 (1992).
41. G. Tearney, B. Bouma, and J. Fujimoto, "*High speed phase- and group delay scanning with a grating-based phase control delay line,*" Optics Letters, **22**, 1811-13 (1997).
42. A. Rollins, M. Kulkarni, S. Yazdanfar, R. Ung-arunyawee, and J. Izatt, "*In vivo video rate optical coherence tomography,*" Optics Express, **3** (1998).
43. G. Tearney, B. Bouma, S. Boppart, B. Golubovic, E. Swanson, and J. Fujimoto, "*Rapid acquisition of in vivo biological images by use of optical coherence tomography,*" Optics Letters, **21**, 1408-10 (1996).
44. V. Gelikonov, G. Gelikonov, N. Gladkova, V. Leonov, F. Feldchtein, A. Sergeev, and Y. Khanin, "*Optical Fiber Interferometer with PZT Scanning of Interferometer Arm Optical Length,*" Optical Coherence Technologies, Inc. (1999).
45. R. Windecker, M. Fleischer, B. Franze, and H. J. Tiziani, "*Two methods for fast coherence tomography and topometry,*" Journal of Modern Optics, **44**, 967-77 (1997).
46. C. Su, "*Achieving variation of the optical path length by a few millimeters at millisecond rates for imaging of turbid media and optical interferometry: a new technique,*" Optics Letters, **22**, 665-7 (1997).
47. J. Ballif, R. Gianotti, P. Chavanne, R. Walti, and R. Salathe, "*Rapid and scalable scans at 21 m/s in optical low-coherence reflectometry,*" Optics Letters, **22**, 757-9 (1997).
48. J. P. Heritage, A. M. Weiner, and R. N. Thurston, "*Picosecond pulse shaping by spectral phase and amplitude manipulation,*" Optics Letters, **10**, 609-611 (1985).

49. R. Thurston, J. Heritage, A. Weiner, and W. Tomlinson, "*Analysis of picosecond pulse shape synthesis by spectral masking in a grating pulse compressor,*" IEEE J Quantum Electronics, **QE-22**, 682-96 (1986).
50. A. M. Rollins, M. D. Kulkarni, S. Yazdanfar, R. Ung-arunyawee, and J. A. Izatt, "*In vivo video rate optical coherence tomography,*" Optics Express, **3** (1998).
51. O. E. Martinez, "*3000 times grating compressor with positive group velocity dispersion: Application to fiber compensation in the 1.3-1.6um region,*" IEEE J. Quant. Elect., **23**, 59-64 (1987).
52. A. V. Zvyagin and D. D. Sampson, "*Achromatic optical phase shifter-modulator,*" Optics Letters, **26**, 187-190 (2001).
53. J. A. Izatt, M. R. Hee, G. M. Owen, E. A. Swanson, and J. G. Fujimoto, "*Optical coherence microscopy in scattering media,*" Optics Letters, **19**, 590-2 (1994).
54. A. D. Aguirre, P. Hsiung, T. H. Ko, I. Hartl, and J. G. Fujimoto, "*High-resolution optical coherence microscopy for high-speed, in vivo cellular imaging,*" Opt Lett, **28**, 2064-6 (2003).
55. S. D. Personick, *Optical Fiber Transmission Systems*. 1982: Plenum Press.
56. A. B. Carlson, *Communication Systems*. 1975: McGraw Hill.
57. L. H. Enloe and J. L. Rodda, Proc. IEEE, **53**, 165-166 (1965).
58. O. E. Delange and A. F. Dietrich, Bell Syst. Tech. J., **47**, 161-178 (1968).
59. T. G. Hodgkinson, *Coherence, Amplification and Quantum Effects in Semiconductor Lasers*. Pure and Applied Optics, ed. Y. Yamamoto. 1991: John Wiley & Sons.
60. S. D. Personic, Bell Syst. Tech. J., **52**, 843-886 (1971).
61. E. A. Swanson, J. A. Izatt, M. R. Hee, D. Huang, C. P. Lin, J. S. Schuman, C. A. Puliafito, and J. G. Fujimoto, "*In vivo retinal imaging by optical coherence tomography,*" Optics Letters, **18**, 1864-6 (1993).
62. G. L. Abbas, V. W. S. Chan, and T. K. Yee, "*Local-oscillator excess-noise suppression for homodyne and heterodyne detection,*" Optics Letters, **8**, 419-421 (1983).
63. G. L. Abbas, V. W. S. Chan, and T. Yee, "*A dual-detector optical heterodyne receiver for local oscillator noise supression,*" J Lightwave Technol, **2**, 1110-1122 (1985).
64. S. Donati, *Photodetectors: Devices, Circuits, and Applications*. 2000: Prentiss Hall.
65. "*Analog Devices AD8015 Differential Oputput Transimpedance Amplifier,*").
66. "*Anadigics ATA005001 Transimpedance Amplifier,*"
67. "*Vitesse VSC7710 Integrated Photodetector/Transimpedance Amplifier,*"
68. "*Analog Devices AD8310 Logarithmic Amplifier,*"
69. D. Smith, *ARRL Handbook for Radio Communications: Digital Signal Processing*. 2003.
70. T. Ko, "*High Speed Data Acquisition System for Optical Coherence Tomography,*" in *Electrical Engineering and Computer Science* Massachusetts Institute of Technology: Cambridge. p. 59 (2000).

Chapter 4 – Delivery Systems and Minimally Invasive Diagnostics

Introduction

The development of medical technologies has had a profound impact in both fundamental biomedical research and clinical patient care. Traditionally, the area of medical imaging has been used primarily as a diagnostic tool for the visualization and diagnosis of disease pathologies. While this capability in as of itself has transformed the medical and healthcare fields, there exists several opportunities to use imaging technology in increasingly valuable ways. Some of these opportunities include its use as a tool for the staging of disease progression, its implementation in surgical guidance and for interventional procedures, and as a diagnostic methodology to assess therapeutic conditions both before and after treatment.

One of the enabling factors that has enabled imaging to be used as a diagnostic, therapeutic, and interventional tool has been the development of non-invasive or minimally invasive diagnostic technologies. These technologies include both advanced imaging techniques themselves such as ultrasound or MRI as well as sophisticated diagnostic probes that enable the imaging of internal body organs that would otherwise be inaccessible to certain imaging modalities. Such devices are critical for the implantation and realization of OCT as a diagnostic or clinical guidance technique since OCT image penetration is limited to the first several millimeters of a tissue surface.

Table 4-1. Summary of Delivery Systems and Diagnostic Imaging Devices

	Advantages	Disadvantages	Application
High Resolution Microscope	Increased resolution	Slow scan speed	Developmental biology systems
Clinical Microscope	High speed	Lower resolution	Open tissue
Forward Scanning Handheld Probe	High speed Adjustable resolution	Large size	Open tissue
Minimally Invasive Handheld Probe	Small size	Fixed resolution	Arthroscopic & oral imaging
Rotary Scanning Catheter	Small size	Difficult interface	Coronary imaging
Micromotor Catheter	Adjustable focus	Larger size catheter	GI imaging
Advanced Rotary Catheter	Multi-plane imaging	Rotational scan	GI imaging
Linear Scanning Catheter	High res. linear scan	Advanced actuation	GI imaging
MEMS Scanner Catheter	2D scanning	Limited scan range	GI imaging

In this chapter the design, development, and use of a variety of diagnostic devices used in the sample arm of the OCT system will be described. These devices include laboratory and surgical microscopes, handheld imaging devices, and minimally invasive catheter based probes. The design criteria, functionality, and utility of these probes will be discussed. Table 4-1 summarizes advantages and applications for the delivery systems developed in this work.

OCT Imaging Microscopes

One of the most fundamental devices used to visualize biological phenomena and tissue systems is the optical microscope. Even the most basic white light microscopes are capable of achieving sub-micron resolution capabilities that can be used to investigate cellular level architecture and disease pathology. Advanced optical systems and microscope objectives have been continually developed to extend the capabilities of the microscope to achieve diffraction-limited and even sub-diffraction-limited imaging performance [1]. Research and development in the field has resulted in a virtual explosion of microscopy techniques that employ physical, chemical and biological processes to enable high resolution, multi-modality, and functional imaging of biological processes. The use of the ultraviolet, visible, and infrared wavelength ranges combined with laser light source technologies has also contributed to such techniques such as confocal [2, 3], two-photon [4, 5], and fluorescence microscopy [6-8].

In this work two optical microscope designs were used for high resolution imaging studies. Both of these microscopes were designed to operate with optimal performance in the infrared wavelength range used in OCT. The first microscope was developed previously in our laboratory [9] and has been optimized primarily for use at 800nm with the Ti:Sapphire laser system. It is a capable system however employs a slower scanning galvanometer reference arm to achieve high resolution imaging performance. For this reason it has been mainly used within the laboratory for the investigation of *ex vivo* tissue samples or small *in vivo* biological models [10, 11]. The second microscope used was developed by LightLabs Imaging and employs a straightforward optical design for use in the 1300nm wavelength range. It has multiple scanning galvanometers which allow for high speed imaging.

High Resolution Laboratory Microscope

A layout of the high resolution imaging microscope used for several studies is shown in Figure 4-1. The optical design is rather straightforward and consists of simply a fiber collimator and focusing lens. The devil of course is in the details. In particular the optical elements used for beam collimation and focusing are a pair of specialized achromat lenses which can achieve near

diffraction-limited performance with minimal wavefront distortion. The lenses are configured with a broadband anti-reflection coating and are designed to have optimal optical performance in the infrared wavelength range.

The microscope has approximately an 80% throughput efficiency which results in a -2 dB signal loss in both the forward and backward directions. This is a caused by two factors in the microscope design. One is that the collimating lens must be placed such that the optical fiber is located at the back focal plane of the lens. This ensure optimal beam collimation and with minimal aberrations in the focused spot. Since the collimated beam is Gaussian however it is partially clipped by the small clear aperture of the focusing lens. This results in some signal loss. The other factor is that the numerical aperture of the collimating lens does not exactly match that of the optical fiber. Therefore there is some loss introduced when back coupling the optical beam into the OCT fiber interferometer.

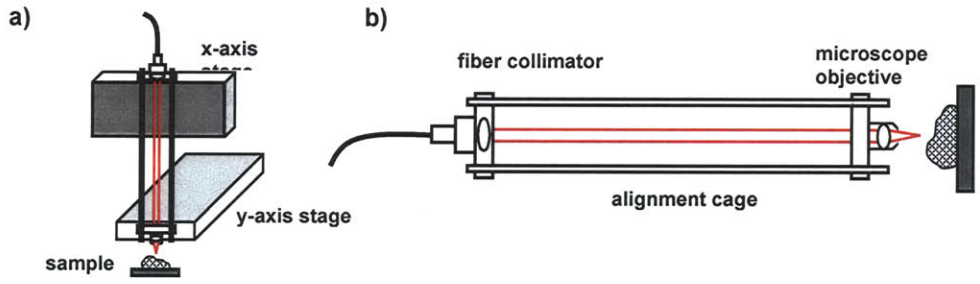

Figure 4-1. High resolution imaging microscope

a) Vertical configuration of the high resolution imaging microscope. OCT scanning is accomplished by using electronic translation stages in the x and y directions. b) Rotated view showing the simple optical configuration.

The magnification of the system is given by the ratio of the focal lengths of the lenses, $M = -f_2/f_1$, with the minus side indicated image inversion. The depth of field is determined by the optical wavelength and focal spot diameter

$$2Z_R = \frac{2\pi\omega_o^2}{\lambda}$$

while the transverse resolution is dependent on the collimated beam diameter and numerical aperture of the focusing lens. For the high resolution imaging studies, super-achromat lenses were used with focal lengths of $f_1 = 10mm$ and $f_2 = 10mm$ giving a 1:1 magnification of the optical fiber core (5 um) in the imaging plane to achieve a transverse post size of approximately 5um.

The microscope was configured with a z-translation stage to manually adjust the beam focal position on the tissue sample. With the focusing optics used a confocal parameter (2 Z_R) of 45 um was calculated for a 5um spot diameter and 1.2mm input beam diameter. A measurement of the focusing lens achromaticity is shown in Figure 4-2 which plots backcoupled optical spectral bandwidth as a function of the z-translation of the focused spot location. Near the beam optical focus the degree of achromatism is apparent as a modulation in the backcoupled spectrum. Shorter wavelength are seen to focus more strongly beyond the focal plane while longer wavelength components in the spectrum are focused slightly before the focal plane (Figure 4-2a). Further away from the focus chromatic aberrations are reduced and the backcoupled optical spectrum is very similar to the spectrum at the focal plane (Figure 4-2b).

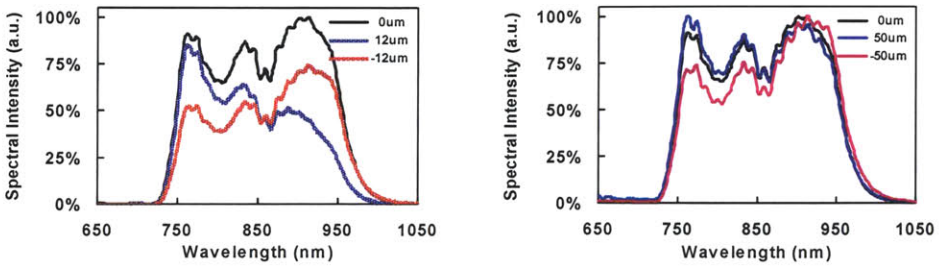

Figure 4-2. Backcoupled optical spectra from the high resolution microscope

Optical scanning in the x- and y-directions was enabled through GPIB motion control stages with 0.1 um and 1 um resolution accuracies. The stage speeds were to 0.5 mm/sec and 2 mm/sec respectively. As the stage motion on either axis was used to generate the cross-sectional OCT scans it was not necessary to employ high speed axial scanning in the system reference arm. Typical reference arm scan velocities of 100 mm/sec allowed 30-40 A-scans per second with high resolution images consisting of 500-1000 A-scans. This required acquisition times on the order of 10-20 seconds per image.

High Speed Clinical Microscope

In order to conduct real-time, *in vivo* imaging of biological specimens at high resolution use of a clinical microscope was implemented. A schematic of the microscope and optical beam path is shown in Figure 4-3. A fiber coupled collimator assembly was used at the microscope input to create a 3.5 mm diameter input collimated beam. The collimated beam was incident upon a pair of high speed mechanical galvanometer mirrors that could scan the beam in the x- or y-directions. The beam diameter was maximized to allow for the highest transverse resolution for the given galvanometer mirror sizes and focusing lens parameters. After reflecting off both of the galvanometer mirrors the beam transverses to a right angle turning mirror and is directed

downwards toward the focusing objective lens. The objective lens was a large diameter near IR achromat with a focal length of 35 mm. With this optical configuration it was possible to generate a focused spot size of 8 um with 1600 resolvable spots (50% contrast at FWHM) across an 8mm scan field.

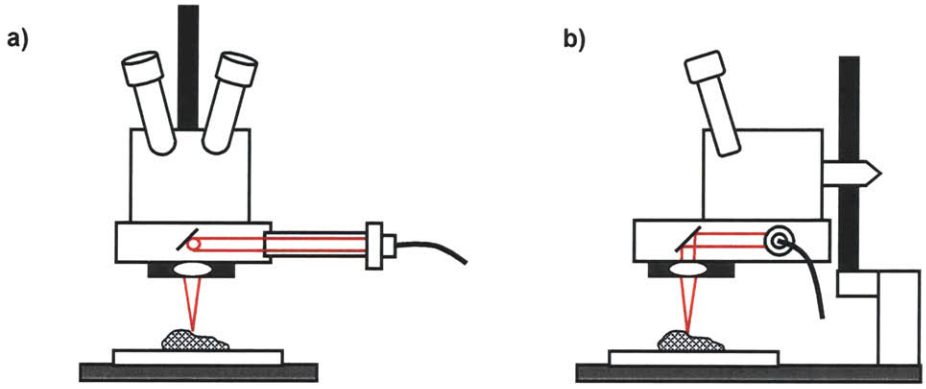

Figure 4-3. Schematic of high speed clinical microscope

Front view (a) and side view (b) of the optical configuration for the clinical microscope diagnostic system. High throughput efficiency of >90% was achieved by using AR coated lenses and gold mirrors.

With control software developed by LightLabs Imaging Corporation it was possible to use the clinical microscope image both *in vitro* tissue samples as well as *in vivo* biological systems at high speed (up to 12 fps) and across a large scan field of view up to 8mm transverse scan length). Custom modifications were made to the timing and control signals of the microscope to create an automatic motion control and image acquisition system (see Chapter 3). This control system was used to generate large 3-D volumetric data sets of excised tissue samples as well as developmental biology systems. Both of these applications will be discussed in detail in subsequent chapters.

Due to the larger transverse resolution design in this microscope it was possible to have an increased depth of field for OCT imaging. Figure 4-4 shows depth-of-field measurements for the 800nm and 1300nm microscope systems. The measurement was done using a technique which quantifies the backcoupled optical power while translating a reflecting mirror through the focus [12]. The research microscope has a FWHM focus depth of 35um in the axial direction which is in close agreement with the calculated confocal parameter of 38um for a 4um focused spot size ($2w_o$). The research microscope has a significantly larger spot size and confocal depth of field which is useful for high speed imaging applications however the inherent tradeoff between transverse resolution and imaging depth is apparent.

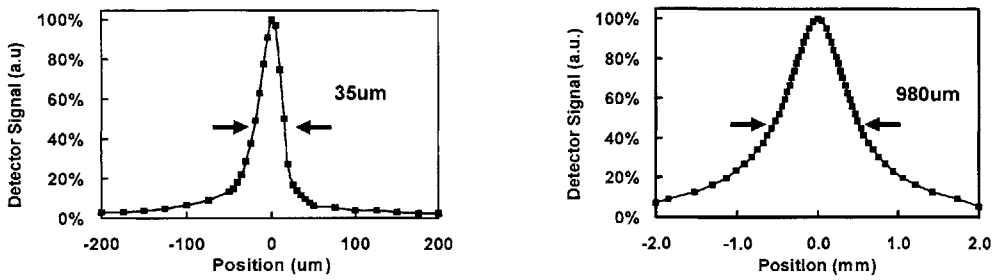

Figure 4-4. Depth of field measurements for research and clinical microscopes

Measurement of the backcoupled optical power as a function of focal spot position for the 800nm and 1300nm microscopes. The corresponding transverse spot size for the research and clinical microscopes are 4um ($2w_o$) and 28um ($2w_o$).

The main drawback to the microscope diagnostic systems is that they are somewhat limited to image small excised tissue samples. *In vivo* imaging can be done however requires rather difficult placement and orientation of the animal system under the microscope objective lens. For this reason, a handheld imaging probe diagnostic was used for *in vivo* imaging applications.

Handheld Imaging Devices

While both OCT microscope designs allowed for high resolution and high speed imaging of biological tissue samples, the implementation of OCT technology in a clinical setting is strongly influenced by the system portability and ease-of-use. As the OCT systems developed and used in this work were fiber optically based, the light source, optical components, electrical hardware and software control systems could be made both portable and compact. The delivery mechanism of the OCT scanning beam is a critical element however that is the interface between the imaging engine and the patient or tissue system under investigation. For imaging open tissue or organ systems such as the human dermis, exposed epithelial tissue (e.g. hamster cheek pouch), or areas accessible during open-field surgical procedures, handheld imaging devices can serve as a compact and portable interface to deliver the OCT optical beam and generate cross-sectional images of the tissue structure. An additional benefit of this type of scanning probe is that it does not need to contact the tissue surface thereby reducing the possibility of tissue infection and removing the need to repeatedly sterilize the OCT probe after use.

Forward Scanning Handheld Probe

In our laboratory a modular, compact handheld probe for *in vivo* imaging of biological specimens was built by Ravi Ghanta and improved upon by Pei-lin Hsiung. The probe

construction consisted of an aluminum housing for two scanning galvanometers and a stainless steel tube that contained the optical lens elements. A photograph of the probe and schematic of the optical design is shown in Figure 4-5. The stainless tube was designed to be easily detached for cleaning and sterilization procedures when needed. To facilitate rapid assembly and precise alignment of the optical elements, hollow copper tubes of specified length were cut to serve as spacers for different telescope lens configurations. The total probe length was 15 cm and main tube diameter was 1.6 cm top accommodate 1.2 cm diameter optical lenses.

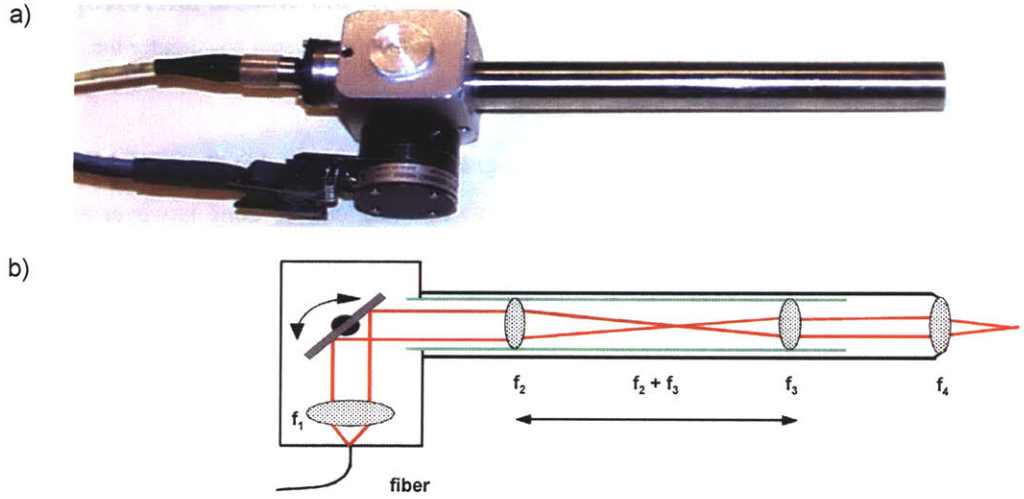

Figure 4-5. Handheld probe for OCT imaging

a) Photograph of probe showing compact and portable design. b) Optical telescope configuration with image magnification given by the ratio of lens focal lengths.

The collimating and focusing lenses were chosen to optimize the optical spot size and working distance of the handheld probe. The lenses were designed and anti-reflection coated for the NIR wavelength ranges to maximize optical focusing and light transmission. The total magnification from the fiber to the objective image plane is given by the ratio of the objective to collimator lens focal lengths and relay lens pair

$$M = (f_4 / f_1)(f_2 / f_3)$$

The scan length Δx depends on the angle of the galvanometer $\Delta\theta$, the relay lenses and objective focal lengths as

$$\Delta x = f_4 * (f_2 / f_3) * \Delta\theta$$

The final lens f_4 is set such that the scanning beam pivots through the center point of the lens. This produces a curved field but uses the full aperture of the lens without clipping. By changing the final lens, the imaged spot size can be readily adjusted. Lens parameters for various

configurations are summarized in Table 4-2. For the studies in this work a typical configuration uses a scan range of 3-5mm, a transverse spot size ($2w_o$) of 18-25um, and a working distance of 2.0-2.6 cm. A galvanometer scan angle of approximately 5.3 degrees was possible without clipping of the optical beam.

Table 4-2. Optical configurations for forward scanning handheld probe

Fiber MFD	f1	f2	f3	f4	Magnification	Working distance	Spot size
9.3um	11mm	40mm	25mm	25mm	3.6	2.1 cm	34um
				18mm	2.6	1.2 cm	24um
	11mm	25mm	40mm	30mm	1.7	2.6 cm	16um
				25mm	1.4	2.1 cm	13um
				18mm	1.0	1.2 cm	9um

The galvanometer scanner in the probe was triggered with control signals generated by OCT software and synchronized with OCT image acquisition. Scan range and scan frequency values could also be adjusted in the software to allow for 2-6mm scan lengths at 1-8 frames per second (1-8 Hz). Scan signal waveforms were configured in either a sawtooth drive pattern or a triangle as shown in Figure 4-6. For the sawtooth drive, image acquisition was done on the long stroke (dashed circle). By implementing a triangle drive higher imaging frame rates were possible by acquiring data on both the forward and backward strokes of the galvanometer and reduces the repetition rate by a factor of two. This also allowed a reduction in the amount of mechanical stress at the turnaround locations.

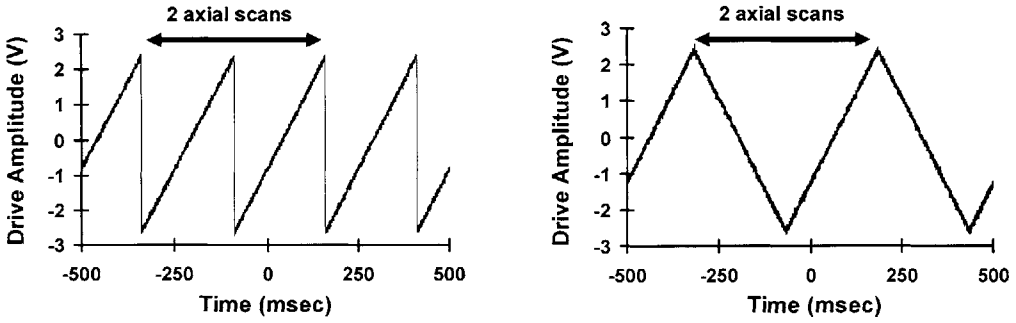

Figure 4-6. Sawtooth and triangle drive waveforms for handheld probe

a) Dashed circle indicates image acquisition on the forward sawtooth stroke of the galvanometer. b) For a triangle drive, data could be acquired on both forward and backward waveform directions.

Image display for the triangle drive configuration was more challenging however as image data was acquired in both the forward and reverse directions during each half stroke cycle

of the galvanometer. Thus the data values were transposed in the image acquisition buffer for each adjacent axial OCT scan. Software modifications implemented by Tony Ko allowed for the 'flipping' of these every other adjacent A-scan and resulted in a correct image being displayed. Figure 4-7 shows the effect and implementation of this A-scan flipping for an acquired OCT image. Figure 4-7a is the original data before flipping and Figure 4-7b is the corrected image. While offline data processing could have been performed this operation as well, the implementation of this capability in real time was critical for high speed, *in vivo* imaging with the handheld probe.

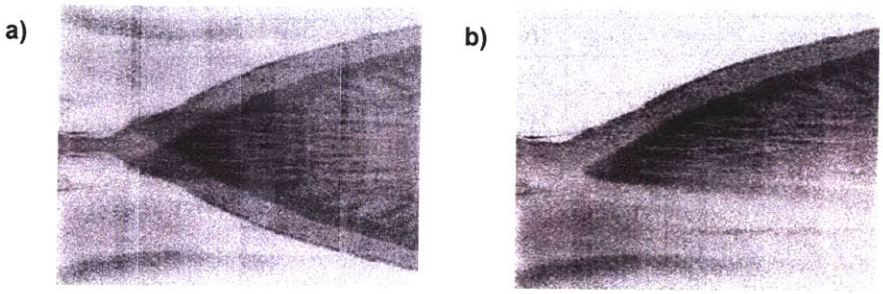

Figure 4-7. Required A-scan flipping for triangle drive acquisition

a) Image acquired on both the forward and reverse galvanometer sweeps without software implemented axial scan flip correction. b) Same image with every other A-scan flipped to account for galvanometer sweep direction.

By using two galvanometers in the probe design, dual axis scanning was possible for en-face imaging. For most of the studies in this work however scanning with a single galvanometer to create cross-sectional OCT images was implemented.

Minimally Invasive Handheld Probe

The handheld probe described in the previous section while relatively compact and modular was most capable in open field imaging situations. This constraint limited the use of the forward scanning probe to situations where the tissue or organ system of interest could be made readily accessible in an open environment. For *ex vivo* imaging of excised tissue specimens this could be easily done as sample placement as well as image registration for the OCT scan beam and histology sectioning could be readily done. For almost all *in vivo* organ systems other than dermis (skin) however, probe access was considerably more complicated. While the use of the forward scanning probe has been demonstrated in our laboratory for the imaging of knee cartilage during open field surgery, positioning of the probe during the surgical procedure exactly 2.5cm above the exposed tissue surface was somewhat difficult (2.5cm is the working distance of the

probe which can only be off by 3-4 mm which is the visible scan range of the OCT system). Imaging in other tissues such as human oral mucosa also was difficult as the diameter of the probe was large relative to the mouth. Also accurate placement of the beam without causing discomfort to the patient was difficult.

Because of the constraints imposed by the forward scanning OCT probe, a second handheld scanning device was developed to access tissue systems in confined spaces and image in a minimally invasive manner. A schematic cutaway cross section of the designed and constructed probe is shown in Figure 4-8. The probe consisted of an ergonomically designed housing which contained a miniature linear drive actuator, a translating stage and clamping assembly, and a small diameter tube (<2mm). The mechanical assembly functioned to create a physical translation of distally located fiber optics to generate a linear scan of the OCT imaging beam. The fiber optics were placed within the mechanical tube which could be of various length depending on the particular application in mind. The tube functioned both to protect the delicate optical fiber and as a mechanism to transmit the stage motion within the probe assembly into linear actuation of the optical beam. As the scan design was independent the optical components used it provided flexibility to adapt or modify these elements as necessary.

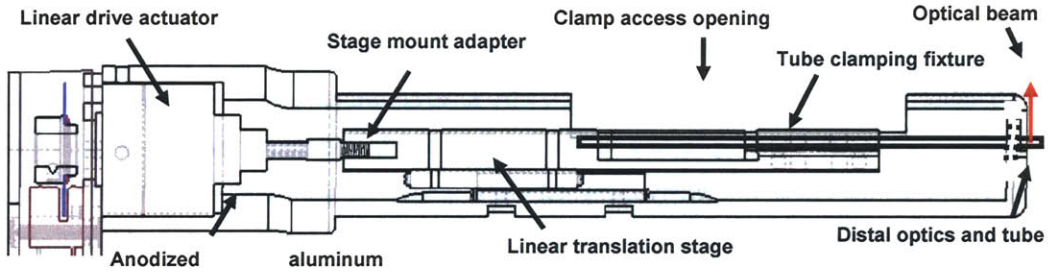

Figure 4-8. Cross section cutaway of minimally invasive handheld probe

Linear translation of the distal optical beam to generate an OCT scan was achieved through micro-stepper drive actuation.

Initial probe design including the mechanical alignment and assembly of components was done using SolidWorks solid model simulator program. This considerably enhanced the design process and allowed for multiple design iterations before the physical building the probe. By using the simulator it was also possible to investigate various component tolerances without the need to machine prototype parts. The probe was specifically designed to fit into a large 10ml plastic syringe which is not depicted in the schematic. A photograph of the fully sheathed device is shown in Figure 4-9. The syringe sheath was used to provide a easily implemented method to

protect the imaging field from contamination. In addition it is a readily available component that is inexpensive, does not require multiple sterilizations, and can be thrown away after a single use.

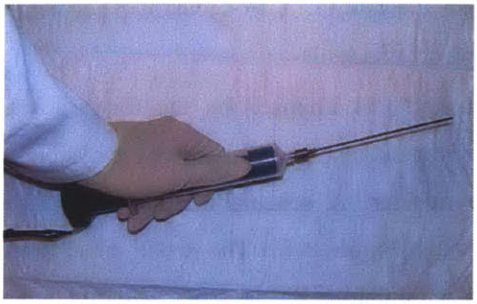

Figure 4-9. Photograph of handheld probe with sheath

Two possible applications for this probe were considered for OCT imaging. The first was for minimally invasive imaging of cartilage in the human knee. This is of particular interest as OCT has been demonstrated to visualize cartilage pathology and degradation in previous studies [13]. Previous work implemented either the forward scanning handheld probe in an open surgical field [14] however was somewhat difficult to use. A small catheter based OCT probe originally developed by Tearney [9] for coronary and endoscopic imaging was also tried to minimally invasively image through a small opening in an *in vitro* knee specimen. It was found however that this catheter device was too fragile and could not be used in the rough bone and cartilage environment inside the knee. The newly designed probe would use the stainless steel housing to protect the catheter fiber optics and generate an OCT scan by translating tube with affixed catheter optics thereby significantly reducing the possibility of breakage.

One of the challenging aspects of the probe design was configuring a drive actuator that could effectively cycle at a high speed with sufficient torque to translate the optical elements over the required OCT scan range. In addition the actuator had to be small and lightweight to fit within a compact and easily manipulated handheld device. The actuator chosen was a micro-stepper drive system shown in Figure 4-10. It implemented a captured shaft design with a Teflon coated lead screw. In order to reduce stepping artifacts a small step angle of 7.5° was specified with a travel distance of 0.001" per step. This corresponds to a 25.4 um motion step per step angle which allowed for equal sampling of the spatial field as the focused optical spot size was also approximately 25 um. While a smaller step size would have been preferable in order to oversample the spatial field, motor speed constraints had to also be considered as discussed below.

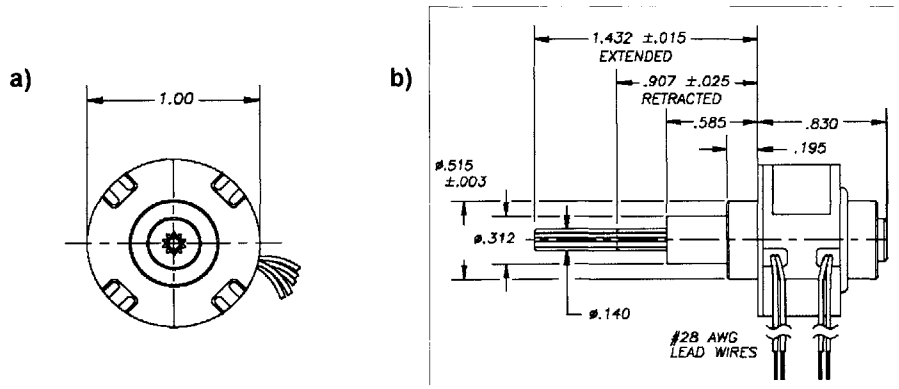

Figure 4-10. Cross sectional views of miniature stepper motor drive actuator

a) Front and b) side views of the stepper motor actuator with dimensioning parameters. Units are in inches.

The final specification on the motor actuator was that it had to be capable of rapidly driving the stage and tubing assembly for sufficient *in vivo* imaging frame rates (2-4 frames per seconds). For a typical OCT transverse scan length of 3 mm, a step rate of at least 500 steps per second would be required (500 steps/second * 25.4 um/step = 12.7mm actuation/second divided by 4 fps = 3.1 mm scan/second). This imposed high torque reversals at the end-of-scan locations. To compensate for this, a motor with both low inductance (4.3 mH per phase) and low resistance (14.7 ohms per phase) was specified. The total motor weight was 34 grams. Figure 4-11 shows the specified thrust versus step rate transfer characteristics for the bipolar drive actuator chosen. As the motor load was minimal (<10 oz) it was possible to achieve high step rate values and sufficient scanning capability.

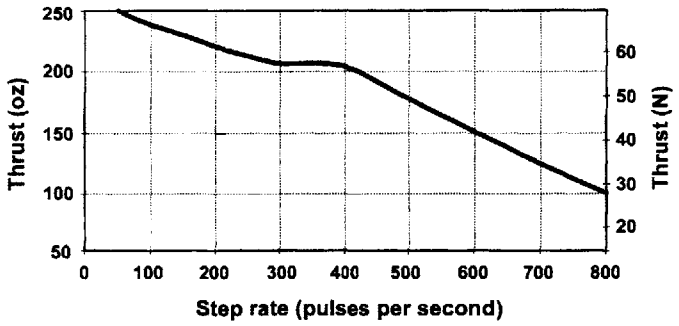

Figure 4-11. Stepper motor thrust curve

Transfer characteristic of handheld probe motor actuator shows the capability of 600-800 steps per second under light load conditions (<30 N). High step rate enables faster imaging frame rates and micro-stepping control for increased image resolution in the transverse direction.

To generate the OCT scan for imaging the motor was driven in a push-pull manner. As the input to step the motor was 5V TTL square pulses with a separate signal to control the motor direction (forward or backward stepping), it was necessary to add these signals into the OCT control software.

Catheter-based Imaging Probes

Catheter based devices play an important role in diagnostic, surgical, and interventional medical procedures. They enable access to regions within the human body with reduced patient risk and without the need for open field surgical procedures. The use of these devices for medical procedures significantly increases patient survival rates, reduces procedural time, and allows for faster patient recovery. The health care benefits as well as financial market size motivates the development and utilization of these devices in the medical field.

High resolution, catheter-based OCT imaging has several potential applications such as the monitoring of disease progression and recovery, early imaging and diagnosis of disease states, and for surgical guidance. To investigate and achieve minimally invasive OCT imaging, catheter based probes were both designed and employed for several studies in this work. Because OCT can be implemented with fiber optic components, the construction of small catheter probes for OCT is possible. Boppart and Tearney et. al. first constructed a fiber optic OCT catheter and demonstrated its use *in vivo* [15, 16]. Catheter based OCT has been demonstrated in arterial and coronary applications [17, 18], respiratory imaging [19], and endoscopic imaging [20-22]. The design of catheter probes used in both *in vivo* animal and *in vivo* human imaging experiments for this work will be discussed.

Catheter Design Considerations

There are several factors that must be considered in the design any catheter based device. Of primary importance is the identification of the parameters that will constrain catheter use and operation in the application of interest. Some of these parameters include the accessibility of the organ system, size of the area to be imaged, biological, chemical and physical environment the catheter will be exposed to, and mechanical control of the catheter within the body. For an OCT catheter device, an important design factor is the capability to effectively deliver light both to the sample as well as to have high optical transmission of reflected light back to the OCT system for detection. Interface reflections both within the OCT imaging scan field and at further locations can severely degrade imaging performance. Figure 4-12 shows a schematic and photograph of components used in the distal end of a constructed OCT catheter. After the light is coupled into

the optical fiber it emerges at the distal end as a diverging point source. To focus the light onto a spot within a tissue sample the light is collimated and then refocused by a lens system. Typically micro gradient index (GRIN) lenses are used for this operation due to their compact size and good optical tolerances. In the schematic shown a GRIN lens is used to collimate the incoming beam and then a separate achromatic lens follows to refocus the optical beam onto the tissue sample.

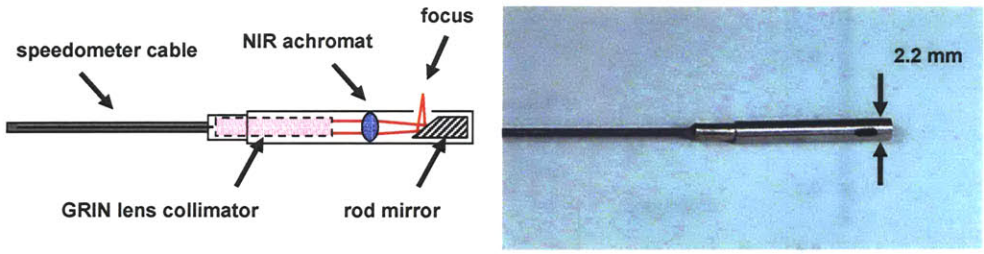

Figure 4-12. Schematic and photograph of OCT catheter distal end

The catheter uses a GRIN lens collimator and NIR achromat to focus the optical beam on the sample. An aluminum coated rod mirror reflects incident light at a 90 degree angle to image outside the catheter sheath (catheter sheath not shown).

The reduction of internal back reflections is important to reduce background noise and achieve maximum signal to noise performance. Figure 4-13a shows the log demodulated light signal from reflections caused by the sheath, front and back focusing lens surfaces, and GRIN lens collimator of the catheter in Figure 4-12. The signal intensity as a function of position along one axial scan is plotted in Figure 4-13b with signal strength normalized to the intensity of the catheter sheath reflection. It can be seen that reflections from the internal optical components in the catheter are very low as the image is on a logarithmic scale. Careful optical alignment and catheter assembly allow for both minimization of reflected light and reduction of multiple reflections from parallel optical surfaces. Figure 4-13 illustrates that reflections can occur well beyond the OCT scan range of 2-3 mm beyond the optical sheath. Thus measurements should be taken by adjusting the reference arm path length through its complete travel range to characterize reflections within the system sample arm. In addition measurement of the total backreflected optical power can be done to quantify the optical performance of the catheter.

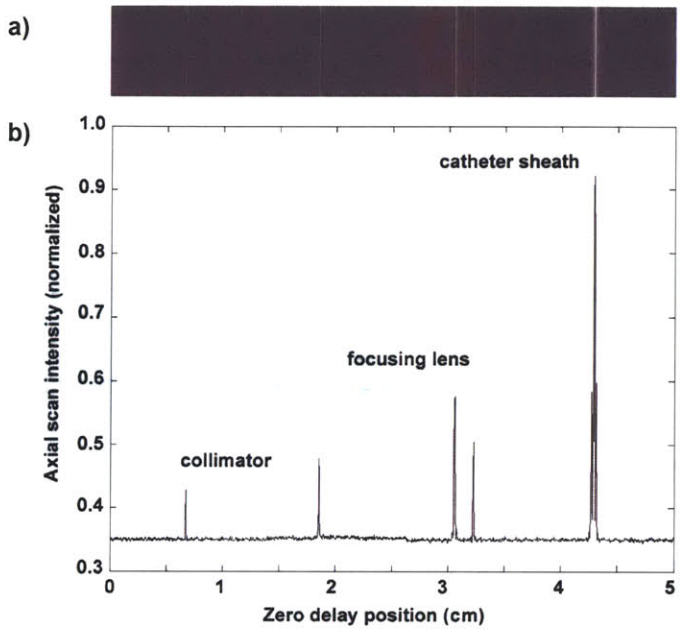

Figure 4-13. Reflections from catheter based OCT probe

a) Log image and b) normalized A-scan signal intensity from the OCT catheter show low levels of back reflected light with no multiply reflections. This enables optimal imaging performance with high signal to noise.

In addition to optical considerations, material and mechanical properties play an important role in the catheter design. Optical fiber is composed of a silica core and cladding region typically 62um or 125um in diameter. While this small size facilitates the miniaturization of optical based probes it imposes mechanical limitations as the fiber can easily break under tensile loads or bending conditions. The use of protective coatings on the optical fiber, hollow metallic speedometer cables, or guidewires can be implemented to improve the robustness of the catheter design. In order to isolate the catheter from the external tissue environment, various extruded medical tubing can be used. Tubing properties such as flexibility, opacity, hydrophobic or hydrophilic properties, and scratch/tear resistance all play important roles in the design process.

As each imaging application has different constraints and requirements, the optimal catheter design is variable for each situation. In coronary imaging for example very small catheter diameters (<1mm) are required to image with confined arterial lumens. In addition long (>2m) and highly flexible catheter sheaths are used thereby making distal actuation of the optical scanning element quite challenging. Endoscopy catheters on the other hand can be relatively large

(2-2.5mm), can be rigid or flexible, and are typically shorter in length (~1.5m) thereby allowing easier mechanical actuation.

Rotary Scanning Catheter

In order to generate a 2-dimensional OCT cross-section it is necessary to scan the optical beam by some mechanical method. For handheld or microscope devices it is possible to employ a scan mechanism at a remote location and allow propagation of the optical beam to generate a line scan (Figure 4-3, Figure 4-5). For a catheter based device however there is insufficient space to allow remote scanning of the optical beam. Thus proximal actuation of the catheter components resulting in distal translation of optical elements is required.

A previously designed rotational scanning catheter is shown in Figure 4-14. This catheter was constructed through the use of a small diameter GRIN lens and right angle microprism affixed to the end of an optical fiber. The microprism directed light out at a 90 degree angle to image tissue structure inside a cylindrical lumen. A stainless steel, reverse coiled speedometer cable (inner sleeve) was attached to the GRIN lens and optical fiber and provided mechanical stability as well as the capability to effectively rotate the catheter optics over the full length of the catheter. A cross sectional rotational OCT scan is generated by rotating the speedometer cable and attached optics at the proximal end by a rotary coupling shown in Figure 4-14a.

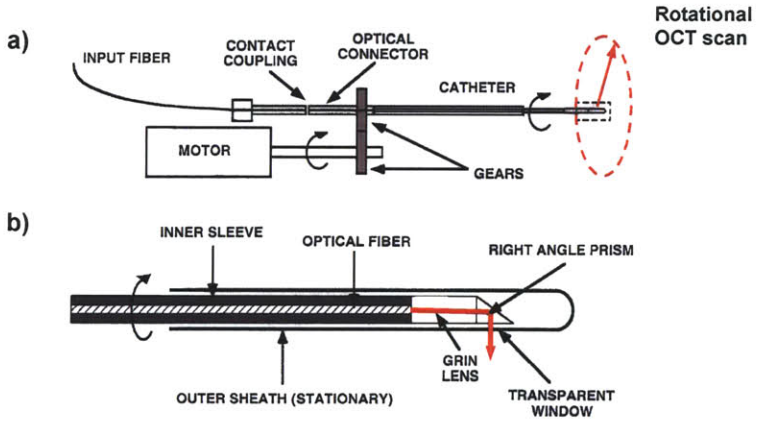

Figure 4-14. Rotational scanning OCT catheter design

a) Light form the OCT system input fiber is coupled into the catheter via a fiber splice connector. b) Rotation of the catheter distal optics generates a 2-dimensional rotational OCT scan. Reprinted from reference [15].

The rotary coupling functions by using an optical splice connector to join two flat-cleaved optical fibers at the contact coupling. The more proximally located fiber which is

connected to the OCT system (leftmost fiber in the figure) is fixed in place while the catheter fiber is made to rotate by a dc motor and gear configuration. Control of the gear ratio and motor speed allows accurate and repeatable rotational scan speeds to be achieved. This catheter was used for initial studies in this work imaging *ex vivo* coronary vessels with an improved rotary coupling stage for greater stability and improved imaging performance.

Adjustable Focus Micromotor Catheter

The rotational imaging OCT catheter described above has been adopted and implemented by several OCT research groups for both coronary and endoscopic imaging applications. Various improvements on the original design have been made however the fundamental scanning concept has remained the same, i.e. distal scan actuation via proximal mechanical rotation. While functional, this scanning technique can introduce non-uniform rotational distortion which causes the slowing or speeding up of the mechanical cable rotation due to frictional effects. This variability in the rotational scanning speed of the catheter results in a de-synchronization of the OCT image. The frame acquisition software correspondingly captures an OCT scan that is either compressed or extended in the angular direction and the acquired OCT image is difficult to interpret. A second limitation of the proximal scanning catheter design is that polarization effects due to fiber birefringence can degrade signal quality and can give rise to false artifacts within the OCT image. Finally and perhaps of greatest significance is that the position of the optical focus generated by the catheter optics cannot be adjusted. In this situation the focused transverse spot size must be sufficiently large (15-20 um) in order to allow for imaging across the OCT scan range (2-3 mm depth of field). This constraint limits the capability to achieve high resolution imaging performance with small axial and transverse resolution capability.

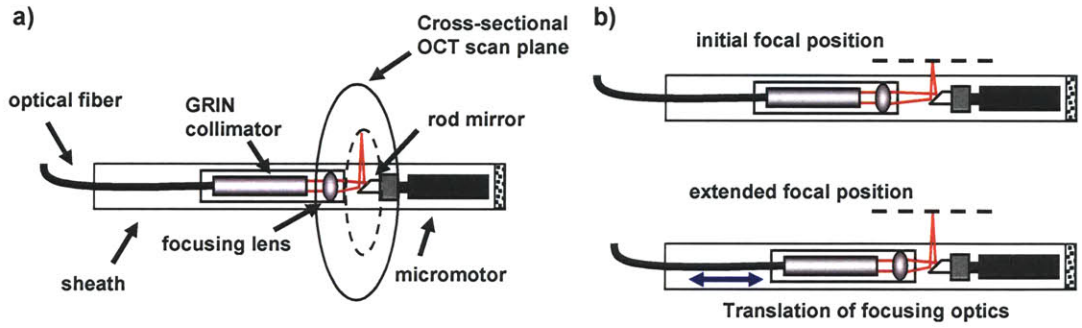

Figure 4-15. Concept of micromotor catheter

Distal rotational scanning is achieved by a rotating micromotor located at the end of the catheter. Adjustment of the optical focus is done by translating the optical elements independently of the catheter sheath position.

To address these limitations a new, high resolution micromotor endoscope with adjustable focus capability was developed. In the new catheter design, the mechanical scanning and micro-optic components were located at the distal end of the probe thereby eliminating the need for proximally actuated rotating elements and a rotary fiber coupling. Figure 4-15 shows the concept of the micro-motor catheter. The catheter would be initially placed within a lumen and rotational scan OCT imaging could be performed as with previous catheter designs. With the new catheter however, independent control of the optical beam focus position relative to the catheter sheath can be achieved by translating the focusing optics assembly (Figure 4-15b). This gives capability to use high numerical aperture optics and focus on a region of interest within the tissue at a high transverse resolution.

Several micromotor assemblies are commercially available at this stage due to increased interest in compact, mechanical actuation systems. The micromotor used for this catheter was manufactured by Micro Precision Systems AG and consisted of design similar to a three phase brushless dc motor. The rotor was comprised of a bipolar rare-earth permanent magnet mounted on a steel shaft with the stator made of three coils mounted inside a nickel-iron stator yoke.

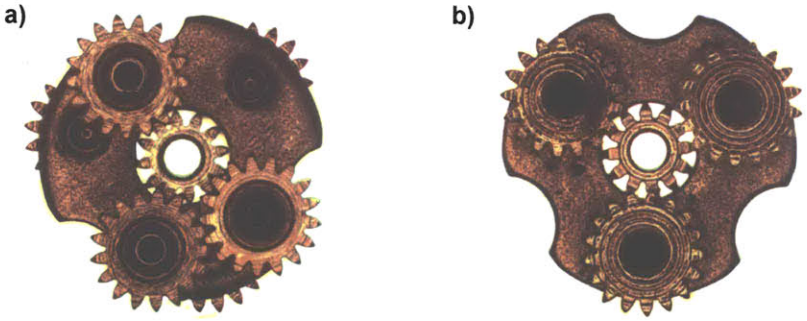

Figure 4-16. Micromotor planetary gear system

Optical microscope images of motor gearhead assembly viewed from the a) top and b) bottom perspective.

The gear heads were a planetary design and were initially configured in a two stage configuration resulting in a 25:1 gear reduction ratio. With a load speed specification of 15,000 rpm this would allow as OCT frame rate of up to 100 Hz. After initial testing it was determined that a higher gear ratio of 125:1 would increase performance and enable better imaging stability at the OCT scan rates of 1-4 Hz which are typically implemented. Optical microscope images of the front and back gear assemblies are shown in Figure 4-16 with a scanning electron micrograph of the assembled motor inside the exposed housing shown in Figure 4-17.

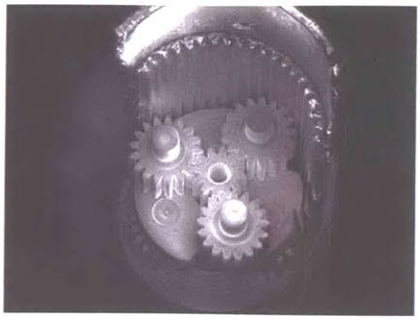

Figure 4-17. Scanning electron micrograph of micromotor gear assembly

Individual gear size was measured to be 1 mm in diameter with 200um wide gear teeth.

To accurately set and stabilize the motor rotation speed a vertical Hall sensor built into the motor was used for synchronous closed loop control. The motor had a maximum outer diameter of 5mm and an operating voltage of 5V. A single-sided voltage signal of 0-2.5V was used as an input to the motor control electronics to set the rotational speed.

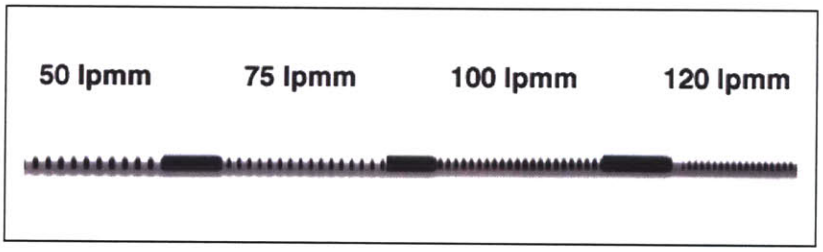

Figure 4-18. Characterization of micromotor optics

Focused spot size measurement using a 1330nm light source on a ruled grating target infers an 8.3 um transverse resolution with 120 lines per millimeter resolved.

Characterization of the optical performance of the micromotor catheter optical subassembly was also completed. An indirect measurement of the optical spot size was done by focusing the optical beam onto a ruled grating with calibrated arrays of varying line density. On OCT image was generated by translating the optical assembly and measuring the back reflected signal intensity from the reflective grating surface. Figure 4-18 shows that a line density of 120 lines per millimeter could be resolved using a 1330 nm center wavelength light source. This corresponds to a transverse spot size resolution of 8.3 um at 50% contrast.

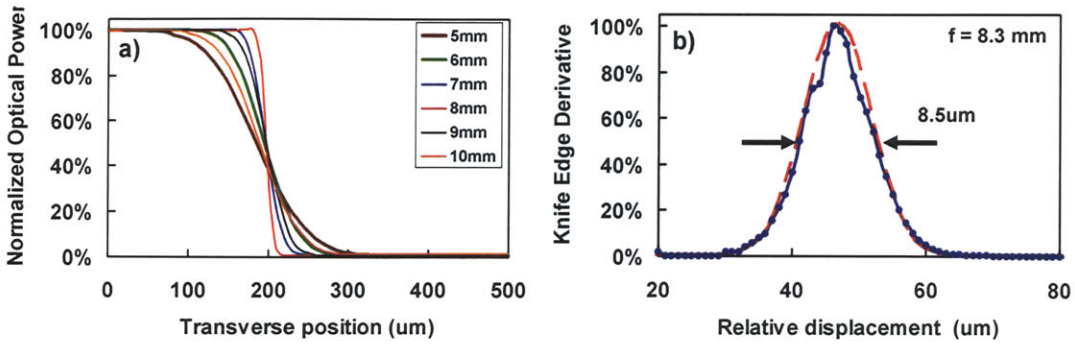

Figure 4-19. Direct measurement of micromotor catheter spot size

a) Power transfer function using a knife edge technique to measure focused spot size. Placement of the knife edge closer to the optical focus results in a steeper transfer function slope. b) Derivative of a measured transfer function indicating a spot size of 8.5um at a focal length of 8.3 mm from the focusing lens.

A direct measurement of the focused spot size was also performed by using a knife edge method [23]. For this technique, the optical power of the focused beam was measured as a cleaved edge of a silicon wafer was passed in front of the beam. This measurement was performed at several distances close to the lens focal position to determine the minimum spot size at the beam focus (Figure 4-19a). By taking the derivative of the power transfer function as a function of the knife edge position, a direct measurement of the focused spot size was possible shown in Figure 4-19b. An optical focal length of 8.3mm was determined to have a Gaussian-fit spot size of 8.5 um using a 1330 nm light source.

The symmetry of the transfer function derivative indicates that the knife edge face was nearly perpendicular to the incident beam. If it had not been perpendicular to the optical axis a skew in the transfer function derivative towards one side or another would be seen. This resolution value agrees well with the indirect measurement performed.

After mechanical and optical assemblies were tested a first micromotor catheter was built. The photograph in Figure 4-20 shows the optical assembly and micromotor with attached rod lens enclosed within a transparent plastic sheath. A double wound, stainless steel speedometer cable was affixed to the optical assembly to protect the inner optical fiber and allow for mechanical translation of the optical elements. The micromotor was held in place by non-conducting epoxy which also served to seal the catheter tubing from the external environment.

Figure 4-20. Photograph of initially constructed micromotor catheter

After initial testing of the catheter for both *ex vivo* and *in vivo* imaging, it was seen that two factors could be improved upon in the catheter design. The first was the modification to increase the motor gear ratio in order to produce smoother scanning at slower imaging frame rates. Dislocation jumps in the OCT scan image were seen at approximately 15 degree intervals using the 25:1 gear ratio motor. Increasing the gear ratio reduced the severity of these dislocations and resulted in a smoother OCT image scan. The second modification made was to modify the catheter housing to increase the mechanical strength of the catheter and improve the alignment tolerances between the optical subassembly and the micromotor center axis of rotation. During *in vivo* imaging it was observed that the plastic sheath did not have sufficient rigidity to prevent plastic deformation during operation. Using a thicker wall sheath material could have increased mechanical strength however was not implemented as it would have also resulted in decreased optical performance. Mechanical stress during insertion of the catheter in a live animal also caused misalignment of the optical beam axis with the center of the spinning rod mirror resulting in a distorted OCT image.

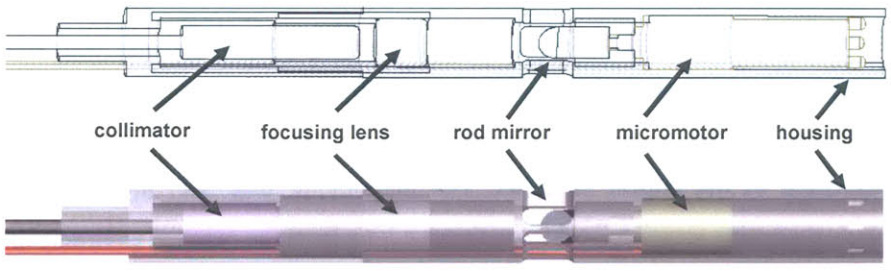

Figure 4-21. Schematic and solid model of redesigned micromotor assembly

Solid model and wireframe cutaway showing the catheter assembly with fiber collimator, focusing lens, rod mirror, and micromotor enclosed in housing.

Figure 4-21 shows a wireframe cut-away and solid model of the redesigned micromotor catheter. In this improved version a solid housing for the complete assembly was implemented to provide mechanical rigidity and precise alignment of the optical beam axis and rod mirror axis of rotation. The total outer diameter of the catheter was maintained at 5mm by using thin walled stainless steel tubing for the housing. Precision alignment and constrained motion of the optical subassembly were designed into the new device to prevent the focusing optics from colliding with and possibly damaging the spinning motor components.

A photograph of the micromotor catheter parts before assembly is shown in Figure 4-22. The redesigned catheter probe was able to perform high resolution *in vivo* imaging in an animal model. The design modifications made improved imaging performance, probe robustness, and mechanical stability during operation. It is possible that with further improvements in the mechanical and optical capabilities of the micromotor catheter future devices could have increased utility in other medical imaging applications.

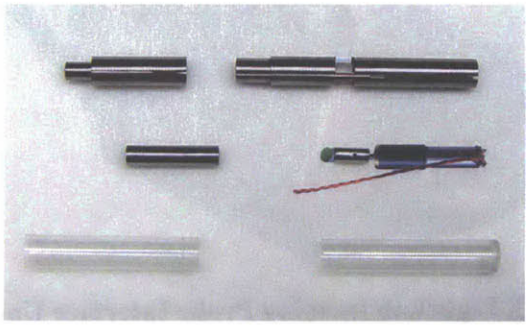

Figure 4-22. Micromotor imaging catheter components

Photograph of second revision micro-motor catheter components. Shown is the stainless steel housing, movable collimator housing, micro-motor with rod lens adapter and attached rod lens, and catheter sheath.

Advanced Rotary Scanning Catheter

For some of the imaging studies completed in this work a collaboration was established with LightLab Imaging, a company that is developing OCT systems for use in cardiology and gastroenterology applications. The collaboration was established to leverage the engineering expertise, manpower, and resources available at LightLab Imaging with the advanced technology development at MIT. Specifically a LightLab imaging engine which consisted of the optical interferometer, reference arm and digital demodulation was modified to support broadband operation and enable ultrahigh resolution imaging. As part of the collaboration, specially

designed LightLab imaging catheters consisted of fusion spliced GRIN lens components and reflectors were used. While very similar in concept to the rotary catheter described previously the engineering design is significantly more advanced and employs specialized hydrophilic catheter tubing and index-matched oil immersion for low friction operation and optimal beam focusing characteristics. In addition the fusion splicing of the optical elements makes alignment very precise and enables a core catheter fiber and lens diameter of 125 um.

Shown in Figure 4-23 is the Probe Interface Unit (PIU) that is employed to connect the catheters to the LightLab imaging engine. The PIU uses a square flange ST/PC fiber connector to rapidly attach or detach the fiber optic catheter to the OCT system. Control buttons on the interface unit allowed manual adjustment of the catheter scanning characteristics however were typically not used as the computer interface provided more readily adjustable performance.

Figure 4-23. LightLab Imaging Probe Interface Unit (PIU)

OCT fiber optic catheter is shown in the lower left portion of the image. A ST/ST connector allows attachment of the catheter to the PIU and imaging engine. Courtesy of LightLab Imaging.

Inside the PIU an advanced rotary and translating scanning system allowed for both high speed rotational OCT imaging and spiral OCT scanning. For the rotary scanning mechanism an ST/PC connector is rotated through the use of a pulley system attached to a small DC motor. The optical coupling from the connector to the OCT system is then achieved by using a miniature rotary optical coupling.

The miniature rotary coupling achieves the identical function as the optical fiber coupling from Figure 4-14 however is much more robust and applicable for clinical imaging studies. In addition to high speed rotational scanning, the PIU was also designed to perform OCT pullback scans whereby the inner optical fiber of the catheter would be pulled backwards while scanning in a rotary fashion. This would produce a spiral scanning of the OCT imaging beam and enabled visualization of tissue architecture all imaging planes perpendicular to the axis of rotation.

In addition a linear mechanism could be used to pull back the catheter in the spiral scanning mode. It consisted of a stepper motor and lead screw that could move the catheter at translation rates of 0.5, 1.0, or 2.0 mm/sec. At the typical OCT imaging rate of 4 frames per second this would correspond to one OCT image at 125um, 250um, or 500um spaced interval. As the transverse image resolution for the catheters was 15um much of the tissue area would not be scanned (i.e. under sampled) however it was possible to linearly translate the radially scanning catheter tip over as much as 40 mm thereby surveying a large area of interest. Additionally the system was capable of increasing the OCT frame rate to as high as 20 fps, high image spiral scan densities were achievable however at the cost of lower signal to noise performance.

Linear Scanning Catheter

In addition to rotation scanning, a linear scanning OCT catheter was developed with LightLab Imaging. A linear scanning catheter was pursued for several reasons. One was that it would allow imaging of tissue architecture though a lumen surface at a cross-sectional plane perpendicular to the rotational scanning method. The rotary scanning mode allows for imaging around a lumen however suffers from the fact that longitudinal disruptions cannot be seen in the image. Morphological changes along the length of a lumen are often characteristic in both arterial and gastrointestinal tissue systems and allow for visualization of transition regions which can be used to identify disease states. Another benefit of longitudinal scanning is that the image pixel density and axial scan density remain constant throughout the whole image cross-section. This is because a linear translation of the optical elements is mapped into a linear image representation. For rotational scanning, the distance between axial scans increases at larger radii. Thus the spaces between A-scans at the end of the scan contain no data resulting in a loss of information density.

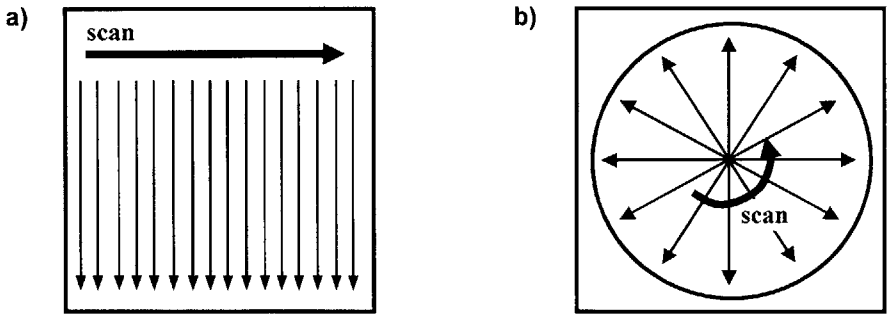

Figure 4-24. Representation of axial scan density for linear and rotary scan modes

a) Linear and b) rotary scan protocols. Rotational scanning results in significantly decreased axial scan density at greater depth position thereby reducing image resolution.

One of the major challenges in implementing a linear scanning catheter device is to find a suitable drive mechanism that can actuate the catheter over a large scan range at high speed. For OCT scan rates of 4 Hz over a 4-5 mm scan range this translates into 15-20 mm/sec at constant velocity. In addition due to rapid turn arounds at the beginning and end of the scan strokes high acceleration and deceleration profiles are required. For a 250msec single frame scanning window, if 10% of the scan time was allotted to turn around at each scan edge that would require an acceleration/deceleration value of 1600 mm/sec^2 ($\Delta v = 40$mm/sec over a $\Delta t = 50$ msec window). Several linear actuator designs were investigated however most all of the ones tested did not have the required torque or load capacity to drive the catheters under such conditions.

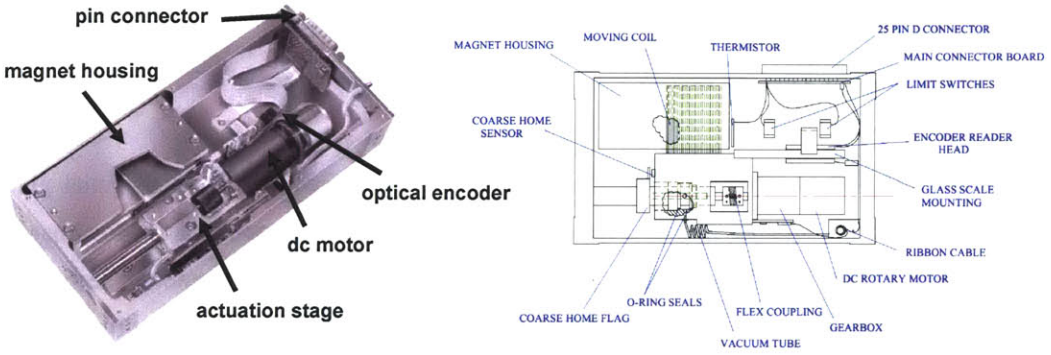

Figure 4-25. Linear voice coil actuator implemented for high speed scanning

Compact linear actuator from SMAC allows for precise and high speed motion with position feedback [24].

Figure 4-25 shows a graphic and schematic of the final actuator used to achieve a high speed linear scanning catheter for OCT studies. The actuator uses a copper voice coil to provide linear motion. Force is generated by applying and controlling a known current through the coil and allows for monitoring of force feedback in the system by the same means. An optical encoder is also incorporated into the system with a 1um resolution specification on positioning. The assembly is mounted onto a high specification linear guide and provides a robust unit capable of both applying and reporting force and position.

To integrate the linear actuator into the OCT system a separate control configuration was necessary and is shown in Figure 4-26. A PC was used to feed control commands into the linear actuator controller which sent out appropriate current and voltage signals to actuate the voice coil. An external control signal from the OCT system was used to synchronize the timing of the controller with the scanning frame rate of the OCT images. Using a higher level control language it was also possible to pre-program velocity and position profiles into the actuator controller that

would activate upon receiving a trigger signal from the external control. This was implemented as well to allow for turn-key operation during OCT imaging procedures.

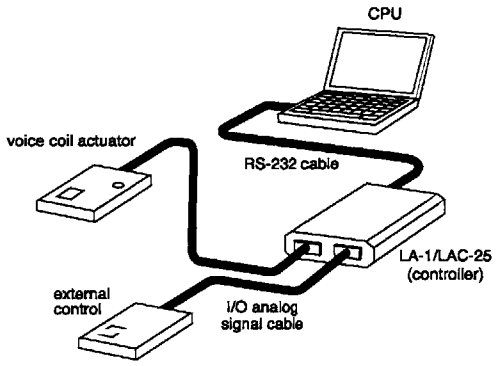

Figure 4-26. Control system for linear actuator

SMAC voice coil system used to program linear scanning profiles. The OCT catheter is attached to the moving actuator stage. Schematic modified from reference [198].

To physically implement the linear scanning catheter the actuator stage was mounted onto a machined adapter plate that interfaced with a removable handle. A handle was incorporated into the design so that the catheter could be operated in clinical imaging runs for endoscopy where the actuator would need to be placed close to the operating field due to the catheter length requirements (1.5-1.8 meters). Using longer catheters and placing an actuator at a more remote location was not feasible as frictional effects and play with long catheter lengths resulted in sub-optimal actuation performance.

In addition to high speed linear actuation, it was desired to design the catheter system to rotate the scan plane during imaging. This is a significant capability the enables various cross-section planes to be imaged during a procedure. To achieve this level of control a novel mounting method was devised that would allow rotation of the optical catheter elements independently of the linear scan actuation. A SolidWorks solid model of the designed mount is shown in Figure 4-27. The rotating element is a stage mount originally designed for the precise position and alignment of optical fibers for light coupling purposes. This mount was modified to match the dimensions of the linear scanning catheter and enable rotational control of the catheter's optical beam. The stabilization tube of the catheter was fixed in place by a small magnet and clamping arm on the rotary mount. This stabilization tube attached to the fiber and optical elements at the distal end of the catheter. A second clamp attached to a plastic Luer fixture that was part of the catheter sheath. The second clamp was designed and machined to attach to the moving actuator

stage and was capable of being tightened using one handed operation. This was a beneficial feature as the actuator operator had to use their other hand to hold the actuator handle during any procedure. By actuating the Luer, relative motion between the catheter sheath and optical fiber enabled linear scanning of the catheter optics.

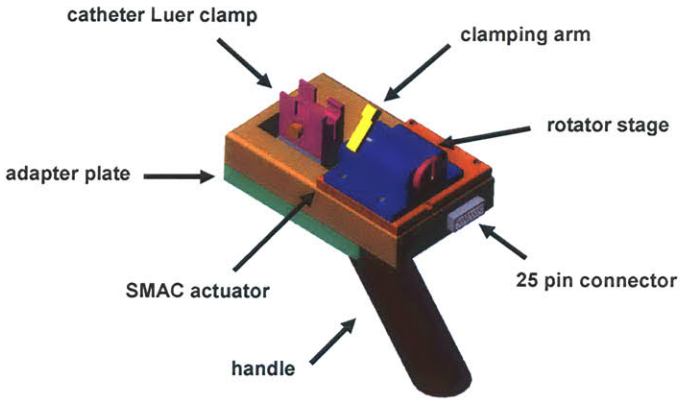

Figure 4-27. Solid model of handheld actuator for linear scanning catheter

An input signal to the actuator controller was used to trigger the linear motion of the catheter. The signal corresponded to start of and OCT image frame where acquired data would be displayed on the computer screen. As a sawtooth drive signal was used for the actuator (see Figure 4-6a), there was a region of the scan during the retrace that was not usable. This back re-trace is a highly compressed and inverted version of the data contained in the forward portion of the scan. This retrace effect is visualized in Figure 4-28.

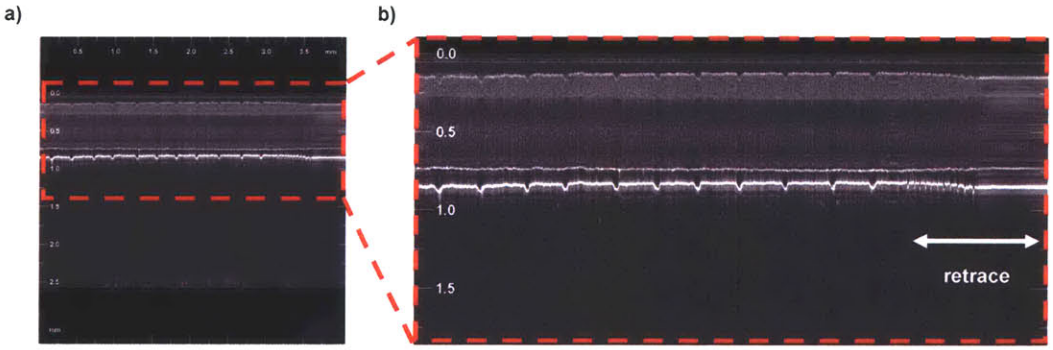

Figure 4-28. Visualization of back retrace of linear actuator on a ruled target

The retrace portion of the sawtooth drive produces a compressed and inverted image of the data acquired on the forward scan of the actuator. The target used was a ruler with each indentation corresponding to 1 mm.

Due to mechanical effects such as friction and actuator response time of the linear scanning system, a time lag existed between the electrical trigger signal and the actual motion of the distal catheter optics. As the OCT acquisition software used the electrical signal to initiate data acquisition for an OCT image frame, this resulted in a physical offset of the start of scan position seen on the video monitor.

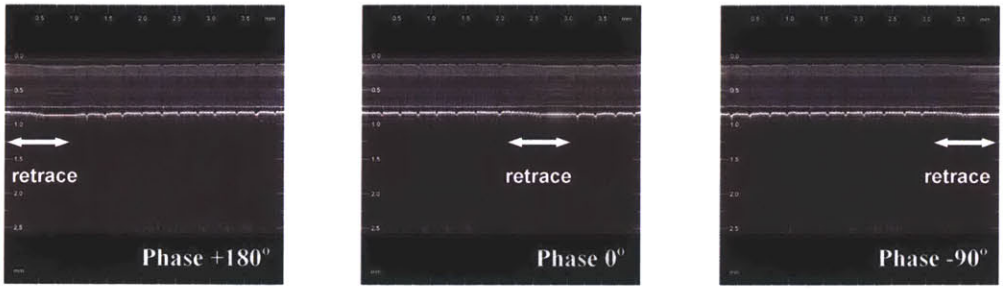

Figure 4-29. Modification of trigger phase for image synchronization

By changing the phase of the frame start signal relative to the image acquisition signal it was possible to correct for mismatch between the electronic start of scan signal edge and physical position of the scanning optics.

Fortunately because the time differential was highly repeatable it was possible to introduce a constant phase shift between the trigger signal and the data acquisition start time to account for this mechanically induced effect. This was done by using the output of a function generator running at the same frame rate frequency as the OCT system to trigger a pulse generator. The output from the pulse generator was produced at a delayed phase relative to the initial trigger signal and fed into the data acquisition system to synchronize the visually displayed image with the physical scan location. This correct is shown in Figure 4-29 with optimal phase matching occurring at -90°.

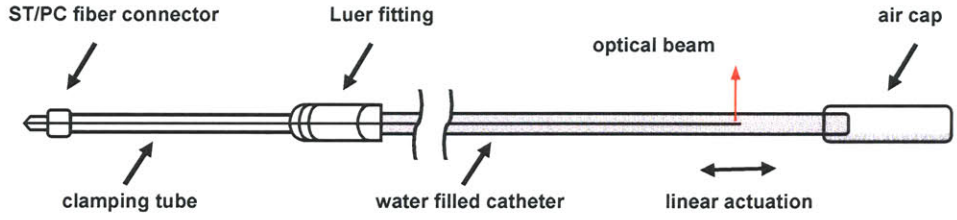

Figure 4-30. Sealed linear catheter design

The final consideration that was necessary to consider was the physical, mechanical, and optical design of the linear scanning catheter. To simplify the process the optical configuration

used for the radial catheters described previously was utilized again however modifications were made to the catheter sheath to allow for high speed linear actuation. In particular, as linear push-pull actuation was now required rather than a rotational motion it was necessary to allow compression of sheath fluid at the distal end. The catheters were water filled to allow for smooth actuation however a small, air filled cap was implemented at the catheter tip. This cap allowed compression of air during the linear actuation in a sealed catheter design and is shown schematically in Figure 4-30. Some problems were encountered such as small air pockets migrating backwards and interfering with the optical beam as well as dehydration of the water inside the catheter sheath after several weeks of operation.

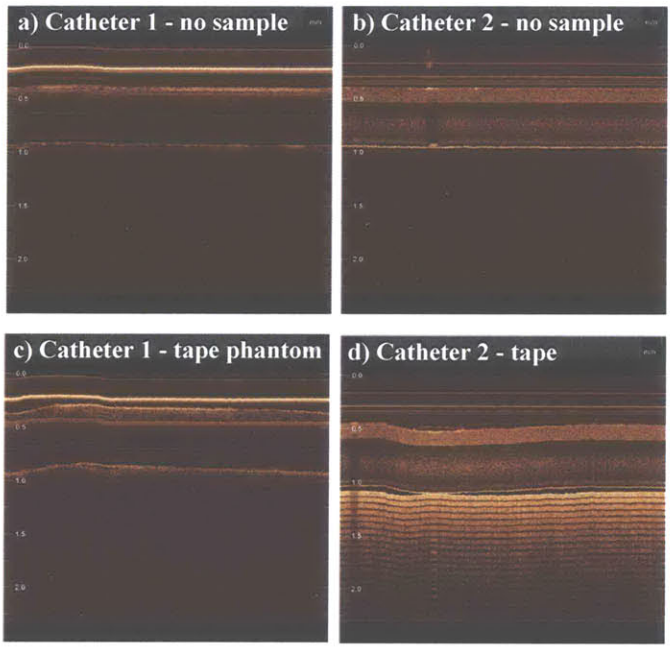

Figure 4-31. Characterization of optical performance for linear scanning catheters

Despite having no visible defects catheter #1 shows significantly degraded imaging performance. Optical and mechanical characterization of each catheter must be performed prior to clinical use.

During the use and operation of the linear scanning catheters it was necessary to remove and replace the plastic sheaths due to disinfection procedures in the experiments. Because the micro-optics located at the distal end of the catheter were highly sensitive to being damaged and there existed the possibility of air bubbles being trapped over the scanning region each catheter had to be optically tested. As the fusion spliced lenses and reflecting rod inside the catheter consisted of 125 um diameter glass rods it was not feasible to check them via an optical microscope. The most straightforward and practical method to evaluate catheter performance was

to scan a stationary tape phantom target and inspect the OCT image quality. Figure 4-31 shows the results of testing two linear scanning catheters both without a sample (a), (b) and with a phantom target composed of multiple 62 um thick layers of transparent tape (c), (d).

MEMS Scanner Catheter

Imaging technologies such as scanning confocal microscopy, and multiphoton microscopy, and optical coherence tomography allow imaging to be performed in living tissues at or near cellular level resolution. All of these imaging technologies however require the delivery and scanning of an optical beam at the site being imaged. As was seen in the previous sections, the development of linear and rotary scanning systems was pursued to enable two-dimensional cross sectioning imaging using OCT. To further enhance the capability of OCT and other imaging modalities investigation into microelectromechanical systems (MEMS) for minimally invasive optical scanning was pursued. There has been increased interest in the development of MEMS for biomedical imaging applications as well as demonstration of integrating MEMS with OCT imaging [25, 26]. The integration of MEMS technology with fiber optics was pursued in this work to construct next generation medical imaging technologies which can perform microscopic resolution, internal body imaging. As previous work demonstrated one dimensional optical beam scanning using thermoelectric or capacitive electrostatic effects [25-27], novel actuation methods were implemented in our studies with the capability of dimensional scanning along multiple axes. This would not only enable arbitrary axis imaging for OCT applications but also would provide the basis for two dimensional en-face imaging techniques such as confocal microscopy, two photon microscopy, and optical coherence microscopy. To pursue the development of a MEMS based OCT scanning system a collaboration was established with the Microelectronics Group at UCLA under the direction of Professor Ming Wu.

There were several design goals for the integration of a raster scanning MEMS device for with the high resolution OCT imaging systems. It was desirable to have a large mirror scan angle for the MEMS based mirror in order to achieve a reasonable number of resolvable imaging spots. In addition fast scanning rates of several hundred Hz to kHz would allow high speed scanning. In order to make a device that could be demonstrated for *in vivo* imaging in an animal model it was necessary to maintain a small scanner, optics, and packaging footprint. Low voltage and low current operation was also required to reduce the risk of electrical shock as well as avoid excessive heating which could damage the device or surrounding tissue.

The combination of high desired optical aperture, large scan range, and high speed scanning made the design of MEMS endoscopic scanners challenging. Previous MEMS scanners

have in large part focused on electrostatic, parallel plate actuation for one and two dimensional scanning [28, 29]. One of the main drawbacks for parallel plate scanners however is the requirement for high actuation voltages which is due to the large gap between the mirror and the biasing electrodes. This is undesirable for endoscopic applications or other applications where a MEMS based scanner would be used for internal body imaging. In addition, the parallel plate scanners also suffer from a "pull-in" phenomenon. This occurs when the actuation voltage exceeds a certain threshold called the pull-in voltage whereby the mirror will abruptly tilt and lock to the maximum angle possible. The useful scan range is limited to less than half of the maximum mechanical angle to avoid this effect.

The microelectronics group at UCLA had developed a novel angled vertical comb (AVC) drive actuation scheme [30] which has several benefits over parallel plate MEMS actuators. These comb drive actuators do not suffer from pull-in instability [31] and have been proposed to reduce the operating voltage and extend the stable scan range [32, 33]. In addition comb drive actuators can achieve higher levels of mechanical torque due to the short interaction distance between comb fingers compared to parallel plate actuation methods.

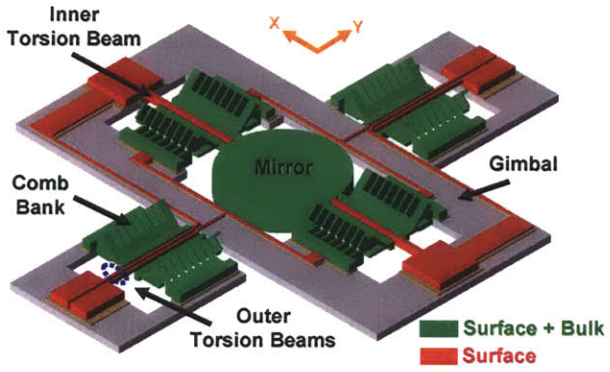

Figure 4-32. Angled Vertical Comb Drive MEMS Device Design

Two axis scanning is possible by implementing a gimbal mirror design that uses two sets of vertical comb drives for each rotation axis. Courtesy of UCLA Microelectronics Group.

Figure 4-32 shows a schematic of the designed two-axis MEMS scanner. Previous work at UCLA demonstrated that this scanner could achieve decoupling of the x-axis and y-axis scanning through the use of surface and bulk micromachining techniques [34]. For the new device a simple 3-photomask process was developed using MUMPS chips (Multi-User MEMS Process [35]) to build a high aspect ratio, large diameter single crystalline silicon mirror that could be integrated into an optical scanning system. The use of a single crystal silicon surface was important to minimize surface roughness and achieve good optical performance. Additionally

the mirror surface was coated with a 50nm thick gold layer to allow for high reflectivity in the infrared wavelength regime.

The silicon micromirror was suspended inside a gimbal frame by a pair of polysilicon torsion beams. The gimbal frame itself was supported by an additional pair of torsion beams. Four vertical comb banks each were used to actuate the gimbal frame and the MEMS micromirror. Each comb bank consisted of one fixed set of combs and one angled set of combs that were fabricated in a self-aligned masking process thereby ensuring good performance without the need for critical alignment procedures [36]. Polysilicon latching mechanisms were also built to enable the vertical comb actuators to be locked into place for mirror operation. Several additional process steps including CMP polishing, DRIE plasma etching, PE CVD, and BOE wet etching were performed at the UCLA Nanofabrication facility to achieve the final AVC MEMS scanner shown in Figure 4-33. Fabrication processing details are described in the PhD thesis of Wibool Piyawattanametha who collaborated in this work [37].

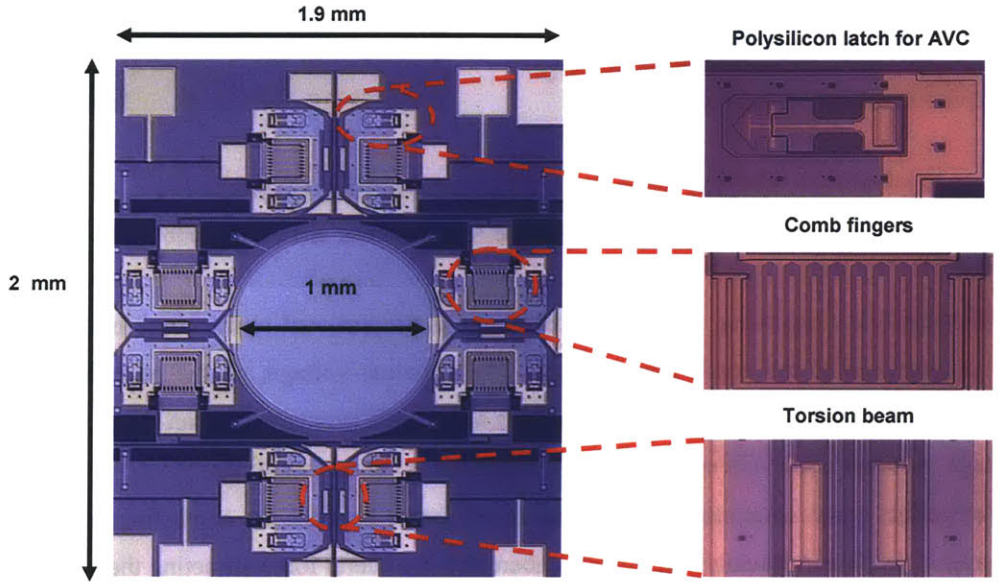

Figure 4-33. Fabricated MEMS 2-D Scanner

Optical microscope images of the 2D AVC MEMS scanner [38]. Total chip size was ~4mm^2. Courtesy of UCLA.

SEM micrographs of the MEMS mirror and angled vertical comb drive are shown in Figure 4-34. The movable comb of the AVC is tilted upward in the out-of-plane direction, while the fixed comb remains flat. When a voltage is applied between the combs, the electrostatic torque will twist the angled comb until it lines up with the fixed comb. The angled comb drives

provide several advantages over the conventional vertical comb drives. The first is a larger scan range for a given drive voltage. The scan range is not limited by the thickness of the comb fingers.

The scan range is determined by the initial tilting angle of the moveable comb. A second advantage of the AVC is that the self-aligned comb fingers and improved lateral stability. The moveable comb and the fixed comb are patterned in the same lithographic and etching steps, and are completely self-aligned. This will improve the lateral stability against lateral pull-in. Finally the AVC has a lower drive voltage, higher force density, and higher resonant frequency that standard vertical comb drive actuators.

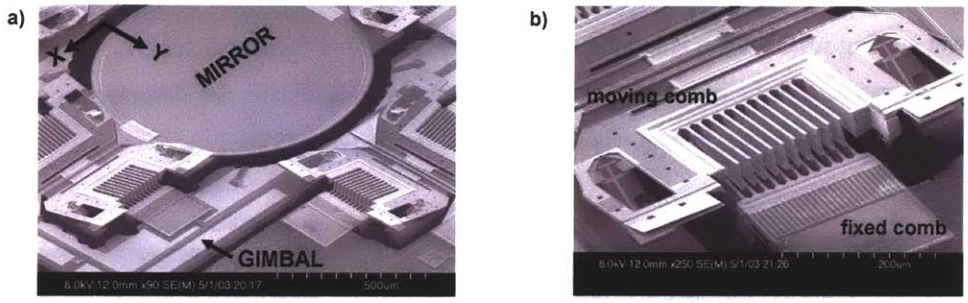

Figure 4-34. MEMS Mirror and Angled Vertical Comb Drive

Scanning electron micrographs of the fabricated MEMS mirror and AVC comb drive. Courtesy of UCLA.

For quasi-static scanning, the mirror scan range is proportional to the comb height and inversely proportional to the comb finger length. The actuation voltage, on the other hand, is proportional to the comb finger length. Thus there is a trade-off between the scan range and the drive voltage. Another issue with comb actuators in general is lateral instability.

For perfect comb structures, the in-plane lateral forces between the comb fingers cancel out. However if the finger spacing is asymmetric there is a net lateral force attracting the movable combs laterally towards the fixed combs. This results in a lateral "pull-in" effect. This can cause electrical shorting and possible catastrophic damage to the actuator. If the upper and lower comb fingers in the vertical comb structure are patterned separately in two lithography steps, they are prone to misalignment and lateral instability. This could limit the maximum voltage that can be applied to the actuator and reduce the practically achievable scan range. This is one reason a self-aligned fabrication process was chosen to create the AVC comb banks.

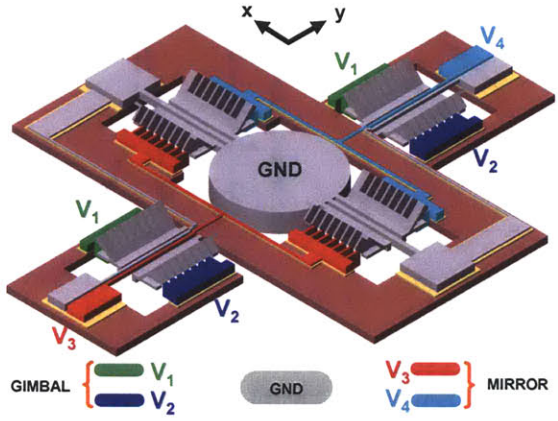

Figure 4-35. Electrical Biasing Configuration for MEMS Scanner

Four control voltages are used to apply a differential bias to the AVC combs for scanning. Courtesy of UCLA.

A differential biasing scheme was used to drive the MEMS scanner on two axes. Figure 4-35 shows schematic of the scanner and electrical biasing configuration. Because the actuator deflection is governed by the square of the net applied voltage it is important that this voltage be controlled in a precise manner. The differential biasing uses four voltages to control the x-axis and y-axis mirror actuation. These voltages are given by

$$V_1 = V_{bias} + V_y/2$$
$$V_2 = V_{bias} - V_y/2$$
$$V_3 = V_{bias} + V_x/2$$
$$V_4 = V_{bias} - V_x/2$$

where the gimbal, or y-axis, is controlled by V_1 and V_2 and the micro-mirror is controlled by V_3 and V_4. By superimposing the voltages over a bias it is possible to increase the linear response range [39]. A characterization of the electrical response transfer characteristics was carried out by UCLA to quantify the differential operation of the AVC MEMS scanner and is shown in Figure 4-36. The DC transfer curves show the mechanical rotation angle for the scanner as a function of applied voltage on each axis (V_x, V_y) and a bias voltage of 35V. The curves were found by measuring the static deflection as a function of DC voltage with a Wyko RTS 500 surface profiler. The measured data points fit well with the numerical solution derived from the UCLA theoretical model shown as the solid curves.

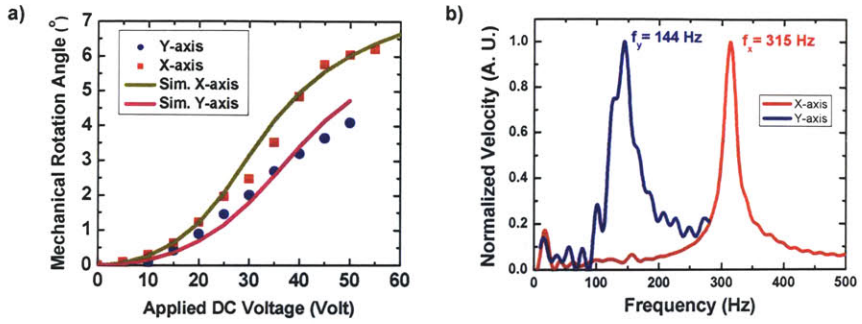

Figure 4-36. DC Transfer Curves and Resonant Frequency Response

a) Mechanical rotation as a function of applied DC electrode voltage shows good agreement with the UCLA theoretical model and mechanical deflection angles as high as 6 degrees. b) Resonance response shows that the MEMS mirror (x-axis) had a higher resonance frequency than the gimbal (y-axis). Courtesy of UCLA.

The resonant frequencies for the scanning micromirrors were characterized with a Polytech Vibrascan laser Doppler vibrometer. Resonant frequencies of 316 Hz and 144 Hz respectively for the x- and y-axes were measured. Mirror deflection at resonance, though not measured, is expected to be approximately twice as large as the DC rotation angles. As there was some process variation in the device fabrication the exact resonance frequencies of different MEMS scanners varied slightly but were all within a similar range as the data shown.

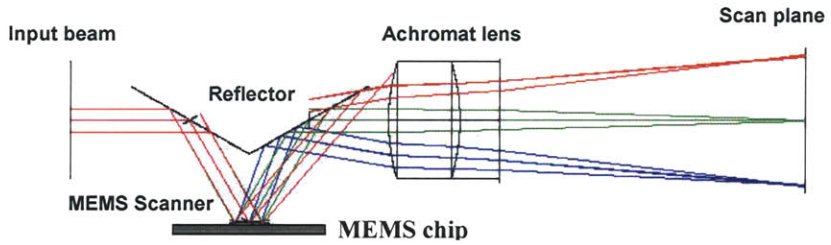

Figure 4-37. MEMS Optical Design Configuration 1

Pre-objective beam scanning allows for a smaller MEMS package however gives reduced optical performance.

In additional to the electrical characterization of the device done by UCLA, optical design simulations using ZEMAX were conducted to determine the optimal configuration for the beam focusing and scanning parameters. Figure 4-37 shows one optical layout that was considered. In this configuration the MEMS scanner is placed horizontally. While this reduces the dimensional footprint of the MEMS chip it also introduces increased complexity in the optical alignment due to the reflector. Two further disadvantages are that the input beam diameter is

limited to the diameter of the MEMS scanner and that by scanning the optical beam before the focusing objective lens, off axis aberration can be more significant.

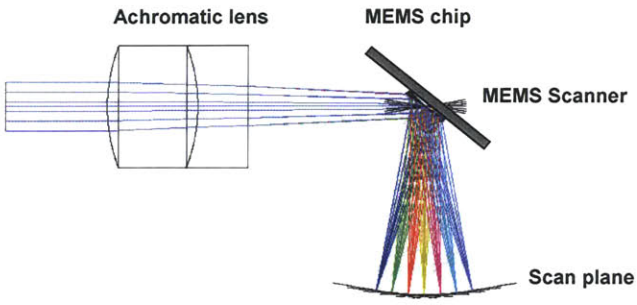

Figure 4-38. MEMS Optical Design Configuration 2

A side scanning optical design allowed for improved beam propagation while maintaining a small package size.

To simplify the device alignment and improve optical performance a side scanning, post-objective configuration was implemented and is shown in Figure 4-38. While this design required the MEMS chip to be angled thereby increasing the package size and reducing the available effective mirror area it proved to be the best option by allowing tighter focusing of the optical beam, better off-axis optical performance, and a reasonable working distance (2-3mm) for the device.

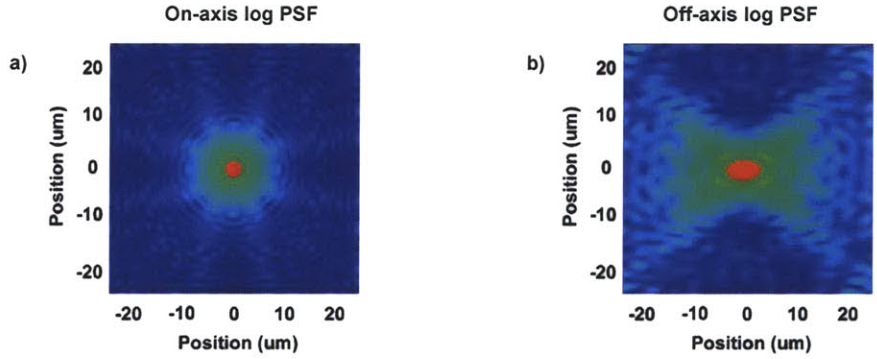

Figure 4-39. Contour Maps of Transverse Point Spread Functions (Simulation)

a) On-axis and b) off-axis transverse point spread functions of the side scan MEMS configuration in Figure 4-38. Simulation results from ZEMAX.

Further characterization of the side scanning MEMS catheter was done with ZEMAX to determine the optical performance of the device. Logarithmic contour maps of the on-axis (central ray) and off-axis (corresponding 5 degree mechanical rotation of MEMS mirror) transverse point spread functions (PSF) at the optical focus are shown in Figure 4-39. The

simulation used a Gaussian beam input and assumed linear beam propagation throughout the system. With a post-objective lens scanning design it was possible to maintain good spatial beam coherence and symmetry however some aberrations are seen in the off-axis focus.

In contrast, the post-objective lens scan design shown in Figure 4-37 resulted in off-axis aberrations that increased the beam size and asymmetry. These effects would theoretically translate into degraded imaging performance therefore providing increased motivation to use a post-objective scan design. In addition for future imaging studies that may possible implement higher numerical aperture optics, thereby resulting in even smaller focused spot sizes, off-axis aberrations become more severe and it is important to try maintain beam integrity throughout the optical system.

The final consideration that was investigated for the MEMS micro-scanner catheter was the device packaging. In order to achieve a low cross-sectional profile for the device a modular design was implemented which would allow for relatively simple machining of the MEMS package as well as capability to finely adjust the elements necessary for optical alignment. A schematic of the packing design is shown in Figure 4-40.

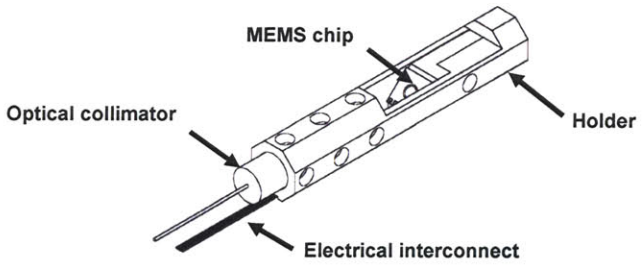

Figure 4-40. MEMS Packaging Design

Compact endoscopic MEMS package designed by UCLA. Machining of package was done at UCLA.

Machining and assembly of the MEMS package was done at UCLA under the direction of Dr. Li Fan. Figure 4-41 shows two photographs of the MEMS scanner placed inside the packaging assembly. Wire bonding of the MEMS chip electrodes was performed before insertion into the package assembly and rough alignment of the MEMS chip with the package was implemented through the use of a 3-axis translation stage. Next, insertion of the focusing lens and optical collimator through the back end of the package (shown in Figure 4-42) was done and a HeNe laser was coupled into the fiber to reflect off the MEMS mirror. Precise alignment of the optical beam was achieved by using small set screws to change the vertical, horizontal, and tilt position of the GRIN lens collimator (Figure 4-42).

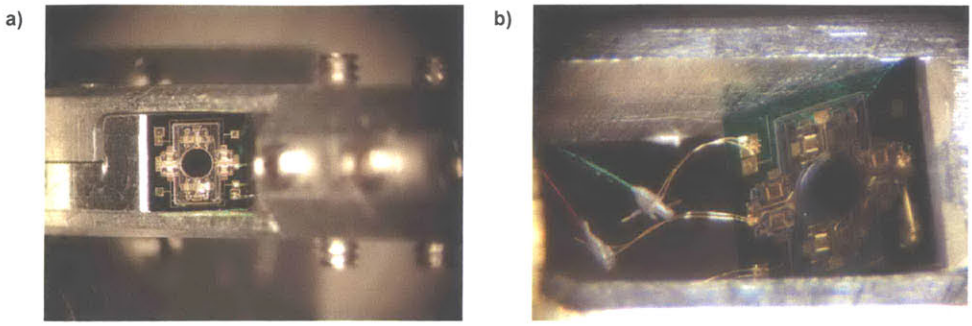

Figure 4-41. Aligned MEMS Scanner with Wiring

a) Top down view of the MEMS chip inside the packaging assembly. b) Side view of the MEMS chip with wire bonded interconnects shown.

The set screws were left in place for initial bench-top experiments with the OCT MEMS scanner. For endoscopic imaging *in vivo* however the set screws were removed and the GRIN lens collimator was held in place by UV cured epoxy. The top portion of the MEMS catheter used a small transparent ITO glass substrate which provided a flat scan surface for the optical beam to pass through. As the MEMS mirror scanned a flat scan plane, use of a flat rectangular glass allowed minimal optical distortion and was used preferential over a rounded catheter sheath used in the previous catheter designs.

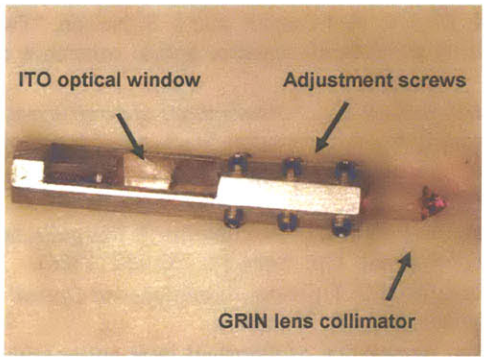

Figure 4-42. Assembled MEMS OCT Catheter Endoscope

The integration of MEMS technology with fiber optics was pursued in this work to construct next generation medical imaging technologies which can perform microscopic resolution, internal body imaging. This would represent a major advance, enabling a wide range of basic as well as clinical studies. Ultimately, the ability to fabricate these devices in a cost effective manner suitable for medical devices, combined with further clinical research, could significantly improve diagnosis and treatment in many clinical situations. OCT imaging results using MEMS scanner technology will be presented in subsequent chapters.

References

1. J. A. Izatt, N. D. Sankey, F. Partovi, M. Fitzmaurice, R. P. Rava, J. Itzkan, and M. S. Feld, *"Ablation of calcified biological tissue using pulsed hydrogen fluoride laser radiation,"* IEEE Journal of Quantum Electronics, **26**, 2261-70 (1990).
2. J. M. Krauss and C. A. Puliafito, *"Lasers in ophthalmology,"* Lasers in surgery and medicine, **17**, 102-59 (1995).
3. J. Bewersdorf, R. Pick, and S. W. Hell, *"Multifocal multiphoton microscopy,"* Opt Lett, **23**, 655-658 (1998).
4. W. Denk, J. Strickler, and W. Webb, *"Two-photon laser scanning fluorescence microscopy,"* Science, **248**, 73-76 (1990).
5. R. H. Webb, G. W. Hughes, and F. C. Delori, *"Confocal scanning laser ophthalmoscope,"* Appl Opt, **26**, 1492-1499 (1987).
6. T. Lazarus-Karaoglan, "Medical electronics [technology 1999 analysis and forecast]," IEEE Spectrum, **36**, 79-83 (1999).
7. D. Huang, E. A. Swanson, C. P. Lin, J. S. Schuman, W. G. Stinson, W. Chang, M. R. Hee, T. Flotte, K. Gregory, C. A. Puliafito, and J. G. Fujimoto, *"Optical coherence tomography,"* Science, **254**, 1178-81 (1991).
8. M. D. Kulkarni and J. A. Izatt, *"Spectroscopic optical coherence tomography,"* CLEO '96. Summaries of Papers Presented at the Conference on Lasers and Electro Optics, **9**, 59-60 (1996).
9. D. L. Farkas and D. Becker, *"Applications of spectral imaging: detection and analysis of human melanoma and its precursors,"* Pigment cell research / sponsored by the European Society for Pigment Cell Research and the International Pigment Cell Society, **14**, 2-8 (2001).
10. W. G. Zijlstra and W. P. Meeuwsen-van der Roest, "Absorption spectra of human fetal and adult oxyhemoglobin, de-oxyhemoglobin, carboxyhemoglobin, and methomoglobin," Clin. Chem., **37**, 1633-1638 (1991).
11. W. F. Cheong, S. A. Prahl, and A. J. Welch, *"A review of the optical properties of biological tissues,"* IEEE Journal of Quantum Electronics, **26**, 2166-85 (1990).
12. J. F. De Boer, T. E. Milner, M. J. C. van Gemert, and J. S. Nelson, "Two-dimensional birefringence imaging in biological tissue by polarization-sensitive optical coherence tomography," Optics Letters, **22**, 934-6 (1997).
13. Y. Yang, L. Wu, Y. Feng, and R. K. Wang, *"Observations of birefringence in tissues from optic-fibre-based optical coherence tomography,"* Measurement Science & Technology, **14**, 41-6 (2003).
14. M. Tateda and T. Horiguchi, *"Advances in optical time domain reflectometry,"* Lightwave Technology, Journal of, **7**, 1217-1224 (1989).
15. J. G. Fujimoto, S. De Silvestri, E. P. Ippen, C. A. Puliafito, R. Margulis, and A. Oseroff, *"Femtosecond Optical Ranging in Biological Systems,"* Opt. Lett., **11**, 150-152 (1986).
16. D. Stern, W.Z. Lin, C..A. Puliafito, J.G. Fujimoto, *"Femtosecond Optical Ranging of Corneal Insision Depth,"* Invest. Opthalm. and Vis. Sci., **30**, 99 (1989).
17. S. L. Jacques, "Time resolved propagation of ultrashort laser pulses within turbid tissues," Appl Opt, **28**, 2223-2229 (1989).
18. H. H. Gilgen, R. P. Novak, R. P. Salathe, W. Hodel, and P. Beaud, *"Submillimeter optical reflectometry,"* IEEE Journal of Lightwave Technology, **7**, 1225-1233 (1989).
19. K. Takada, I. Yokohama, K. Chida, and J. Noda, "New measurement system for fault location in optical waveguide devices based on an interferometric technique," Applied Optics, **26**, 1603-1608 (1987).
20. R. Youngquist, S. Carr, and D. Davies, *"Optical coherence-domain reflectometry: a new optical evaluation technique,"* Optics Letters, **12**, 158-60 (1987).
21. C. Chamon Cde, C. K. Sun, H. A. Haus, and J. G. Fujimoto, *"High-speed optical coherence domain reflectometry,"* Optics Letters, **17**, 151-3 (1992).
22. A. F. Fercher, *"Optical coherence tomography,"* Journal of Biomedical Optics, **1**, 157-173 (1996).
23. C. K. Hitzenberger, "Optical measurement of the axial eye length by laser Doppler interferometry," Invest Ophthalmol Vis Sci, **32**, 616-624 (1991).

24. J. A. Izatt, M. R. Hee, E. A. Swanson, C. P. Lin, D. Huang, J. S. Schuman, C. A. Puliafito, and J. G. Fujimoto, "*Micrometer-scale resolution imaging of the anterior eye in vivo with optical coherence tomography,*" Archives of Ophthalmology, **112**, 1584-1589 (1994).
25. E. A. Swanson, D. Huang, M. R. Hee, J. G. Fujimoto, C. P. Lin, and C. A. Puliafito, "*High-speed optical coherence domain reflectometry,*" Opt. Lett., **17**, 151-153 (1992).
26. X. Clivaz, F. Marquis-Weible, and R. P. Salathe, "*Optical low coherence reflectometry with 1.9 μm spatial resolution,*" Electronics Letters, **28**, 1553-1554 (1992).
27. J. M. Schmitt, A. Knuttel, and R. F. Bonner, "*Measurement of optical-properties of biological tissues by low-coherence reflectometry,*" Applied Optics, **32**, 6032-6042 (1993).
28. D. Huang, Swanson, E. A., Lin, C. P., Schuman, J. S., Stinson, W. G., Chang, W., Hee, M. R., Flotte, T., Gregory, K., Puliafito, C. A., Fujimoto, J. G., "*Optical coherence tomography,*" Science, **254**, 1178-1181 (1991).
29. E. A. Swanson, J. A. Izatt, M. R. Hee, D. Huang, C. P. Lin, J. S. Schuman, C. A. Puliafito, and J. G. Fujimoto, "*In vivo retinal imaging by optical coherence tomography,*" Opt Lett, **18**, 1864-1866 (1993).
30. M. Ramaswamy, A. S. Gouveia-Neto, D. K. Negus, J. A. Izatt, and J. G. Fujimoto, "*In vivo retinal imaging by optical coherence tomography,*" Optics Letters, **18**, 1864-6 (1993).
31. M. R. Hee, J. A. Izatt, E. A. Swanson, D. Huang, C. P. Lin, J. S. Schuman, C. A. Puliafito, and J. G. Fujimoto, "*Optical coherence tomography of the human retina,*" Archives of Ophthalmology, **113**, 325-332 (1995).
32. K. Kobayashi, J. A. Izatt, M. D. Kulkarni, J. Willis, and M. V. Sivak, "High-resolution cross-sectional imaging of the gastrointestinal tract using optical coherence tomography: preliminary results," Gastrointestinal Endoscopy, **47**, 515-523 (1998).
33. B. E. Bouma, G. J. Tearney, C. C. Compton, and N. S. Nishioka, "*High-resolution imaging of the human esophagus and stomach in vivo using optical coherence tomography,*" Gastrointestinal Endoscopy, **51**, 467-474 (2000).
34. J. G. Fujimoto, S. A. Boppart, G. J. Tearney, B. E. Bouma, C. Pitris, and M. E. Brezinski, "*High resolution in vivo intra-arterial imaging with optical coherence tomography,*" Heart, **82**, 128-133 (1999).
35. M. E. Brezinski, G. J. Tearney, B. E. Bouma, S. A. Boppart, M. R. Hee, E. A. Swanson, J. F. Southern, and J. G. Fujimoto, "*Imaging of coronary artery microstructure (in vitro) with optical coherence tomography,*" Am J Cardiol, **77**, 92-93 (1996).
36. M. E. Brezinski, G. J. Tearney, B. E. Bouma, S. A. Boppart, M. R. Hee, E. A. Swanson, J. F. Southern, and J. G. Fujimoto, "*High-resolution imaging of plaque morphology with optical coherence tomography,*" Circulation, **92**, 103-103 (1995).
37. J. M. Herrmann, C. Pitris, B. E. Bouma, S. A. Boppart, J. G. Fujimoto, and M. E. Brezinski, "*High resolution imaging of normal and osteoartheritic cartilage with optical coherence tomography,*" Journal of Rheumatology, **26**, 627-635 (1999).
38. P. R. Herz, S. Martin, P. Hsiung, X.D. Li, A.D. Aguirre, N. Patel, K. Saunders, D. Stamper, T.H. Ko, J.G. Fujimoto and M. Brezinski, "*High Resolution in vivo Imaging of Osteoarthritic Cartilage,*" OSA Biomedical Meeting, **MD6(1)**, 331-333 (2002).
39. S. A. Boppart, M. E. Brezinski, B. E. Bouma, G. J. Tearney, and J. G. Fujimoto, "*Investigation of developing embryonic morphology using optical coherence tomography,*" Developmental Biology, **177**, 54-63 (1996).
40. M. D. Kulkarni, W. Tobocman, and J. A. Izatt, "*Optical coherence tomography of embryonic morphology during cellular differentiation,*" OSA Trends in Optics and Photonics on Advances in Optical Imaging and Photon Migration, **2**, 231-3 (1996).
41. A. M. Cormack and G. N. Hounsfield, "1979 Nobel Prize in Physiology or Medicine: The development of computer assisted tomography," (1979).
42. J. H. Duyn and Y. Yang, "*Fast Spiral Magnetic Resonance Imaging with Trapezoidal Gradients,*" Journal of Magnetic Resonance, **128**, 130-134 (1997).
43. F. Kremkau, Diagnostic ultrasound: principles, instrumentation, and exercises. 2nd ed. 1984, Philadelpha: Grune and Stratton.

44. S. E. Nissen, J. C. Gurley, D. C. Booth, and A. N. DeMaria, "*Intravascular ultrasound of the coronary arteries: current applications and future directions,*" American Journal of Cardiology, **69**, 18H-29H (1992).
45. R. H. Hawes, "*New staging techniques: Endoscopic ultrasound,*" Cancer, **71**, 4207-4213 (1993).
46. H. Yanai, T. Yoshida, T. Harada, Y. Matsumoto, M. Nishiaki, and T. Shigemitsu, "Endoscopic ultrasonography of superficial esophageal cancers using a thin ultrasound probe system equipped with switchable radial and linear scanning modes," Gastrointestinal Endoscopy, **44**, 578-582 (1996).
47. A. T. Stavros, C. L. Rapp, and S. H. Parker, *Breast Ultrasound.* 2003: Lippincott Williams & Wilkins.
48. Computed Tomography and Magnetic Resonance Imaging of the Whole Body. 4 ed, ed. R.C. Gilkeson. 2002: Mosby.
49. J. P. Hornack, "*The Basics of MRI,*" http://www.cis.rit.edu/htbooks/mri/inside.htm (2004).
50. W. Drexler, U. Morgner, R. K. Ghanta, F. X. Kärtner, J. S. Schuman, and J. G. Fujimoto, "*Ultrahigh-resolution ophthalmic optical coherence tomography,*" Nature medicine, **7**, 502-7 (2001).
51. S. A. Boppart, G. J. Tearney, B. Bouma, J. G. Fujimoto, and M. E. Brezinski, "*Single mode fiber-optic catheter/endoscope for optical coherence tomography,*" CLEO '96. Summaries of Papers Presented at the Conference on Lasers and Electro Optics, **9**, 57-8 (1996).
52. A. Katsevich, J. George, and A. Ramm, "*Biomedical diagnostics using optical coherence tomography,*" OSA Trends in Optics and Photonics on Advances in Optical Imaging and Photon Migration, **2**, 196-9 (1996).
53. "*http://nucmed.richis.org/case/CV/MIRmi1201.htm,*"
54. "*www.the-scientist.com/yr2003/mar/upfront6_030310.html,*"
55. "*www.atd.ucar.edu/homes/granger/family/2002-12/,*"
56. "*http://lambda.meph.univie.ac.at/Forschung/medical_laseroptics/OCT_Resolution_improvement,*"
57. "*http://www.uni-kl.de/FB-Biologie/AG-Deitmer/Confocal/IC-neuron.htm,*"
58. "*http://www.brc.cornell.edu/brcinfo/mif/Gallery/gallery.html#Gallery,*"
59. W. Drexler, U. Morgner, F. X. Kartner, C. Pitris, S. A. Boppart, X. D. Li, E. P. Ippen, and J. G. Fujimoto, "*In vivo ultrahigh-resolution optical coherence tomography,*" Optics Letters, **24**, 1221-3 (1999).
60. J. M. Schmitt, M. Yadlowsky, and R. F. Bonner, "*Subsurface imaging of living skin with optical coherence tomography,*" Dermatology, **191**, 93-98 (1995).
61. C. Pitris, A. Goodman, S. A. Boppart, J. J. Libus, J. G. Fujimoto, and M. E. Brezinski, "*High-resolution imaging of gynecologic neoplasms using optical coherence tomography,*" Obstetrics and Gynecology, **93**, 135-9 (1999).
62. S. A. Boppart, B. E. Bouma, C. Pitris, G. J. Tearney, J. G. Fujimoto, and M. E. Brezinski, "*Forward-imaging instruments for optical coherence tomography,*" Optics Letters, **22**, 1618-1620 (1997).
63. A. H. Gandjbakhche, V. Chernomordik, R. F. Bonner, R. Nossal, and G. H. Weiss, "*High resolution intraarterial imaging with optical coherence tomography,*" OSA Trends in Optics and Photonics on Advances in Optical Imaging and Photon Migration, **2**, 200-2 (1996).
64. G. J. Tearney, M. E. Brezinski, S. A. Boppart, B. E. Bouma, N. Weissman, J. F. Southern, E. A. Swanson, and J. G. Fujimoto, "*Catheter-based optical imaging of a human coronary artery,*" Circulation, **94**, 3013 (1996).
65. X. D. Li, C. Chudoba, T. Ko, C. Pitris, and J. G. Fujimoto, "*Imaging needle for optical coherence tomography,*" Optics Letters, **25**, 1520-1522 (2000).
66. J. G. Fujimoto, C. Pitris, S. A. Boppart, and M. E. Brezinski, "Optical coherence tomography: an emerging technology for biomedical imaging and optical biopsy," Neoplasia, **2**, 9-25 (2000).
67. W. Drexler, U. Morgner, F. X. Kärtner, C. Pitris, S. A. Boppart, X. D. Li, E. P. Ippen, and J. G. Fujimoto, "*In vivo ultrahigh resolution optical coherence tomography,*" Optics Letters, **24**, 1221-1223 (1999).
68. Biomedical Photonics Handbook, ed. T. Vo-Dinh. 2003.
69. E. A. Swanson, J. A. Izatt, M. R. Hee, D. Huang, C. P. Lin, J. S. Schuman, C. A. Puliafito, and J. G. Fujimoto, "*In vivo retinal imaging by optical coherence tomography,*" Optics Letters, **18**, 1864-6 (1993).

70. M. R. Lee, J. A. Izatt, E. A. Swanson, D. Huang, J. S. Schumun, C. P. Lin, C. A. Puliafito, and J. G. Fujimoto, "*Optical coherence tomography for ophthalmic imaging: new technique delivers micron-scale resolution,*" IEEE Engineering in Medicine and Biology Magazine, **14**, 67-76 (1995).
71. Y. Pan and D. L. Farkas, "Noninvasive imaging of living human skin with dual-wavelength optical coherence tomography in two and three dimensions," Journal of Biomedical Optics, **3**, 446-55 (1998).
72. C. K. Hitzenberger, M. Danner, W. Drexler, and A. F. Fercher, "*Measurement of the spatial coherence of superluminescent diodes,*" Journal of Modern Optics, **46**, 1763-74 (1999).
73. U. Morgner, F. X. Kartner, S. H. Cho, Y. Chen, H. A. Haus, J. G. Fujimoto, E. P. Ippen, V. Scheuer, G. Angelow, and T. Tschudi, "*Sub-two-cycle pulses from a Kerr-lens mode-locked Ti:sapphire laser,*" Optics Letters, **24**, 411-413 (1999).
74. F. X. Kartner, N. Matuschek, T. Schibli, U. Keller, H. A. Haus, C. Heine, R. Morf, V. Scheuer, M. Tilsch, and T. Tschudi, "*Design and fabrication of double-chirped mirrors,*" Optics Letters, **22**, 831-833 (1997).
75. N. Matuschek, "*Theory and design of double-chirped mirrors,*" Swiss Federal Institute of Technology: Zurich (1999).
76. B. Bouma, G. Tearney, I. Bilinsky, B. Golubovic, and J. Fujimoto, "*Self-phase-modulated Kerr-lens mode-locked Cr:forsterite laser source for optical coherence tomography,*" Optics Letters, **21**, 1839-42 (1996).
77. G. D. Sanders, C. K. Sun, B. Golubovic, J. G. Fujimoto, and C. J. Stanton, "*Self-phase-modulated Kerr-lens mode-locked Cr:forsterite laser source for optical coherence tomography,*" Optics Letters, **21**, 1839-41 (1996).
78. I. Hartl, P. Hsiung, T. H. Ko, J. G. Fujimoto, W. Wadsworth, T. Birks, U. Bunting, and K. Kopf. *High resolution OCT imaging using a spectrally broadened femtosecond Nd:Glass laser.* in *Conference on Lasers and Electro-Optics.* 2002. Long Beach, CA: Optical Society of America and IEEE.
79. W. Watanabe, Y. Masuda, and K. Itoh, "*Dispersive coherence spectrotomography with white-light continuum,*" Optical Review, **6**, 455-8 (1999).
80. N. Nishizawa and T. Goto. Generation and characterization of widely broadened supercontinuum using highly nonlinear fibers and fiber laser. in OFC 2002. 2002.
81. I. Hartl, X. D. Li, C. Chudoba, R. K. Ghanta, T. H. Ko, J. G. Fujimoto, J. K. Ranka, and R. S. Windeler, "*Ultrahigh-resolution optical coherence tomography using continuum generation in an air-silica microstructure optical fiber,*" Optics Letters, **26**, 608-610 (2001).
82. M. Bashkansky, M. D. Duncan, L. Goldberg, J. P. Koplow, and J. Reintjes, "*Characteristics of a Yb-doped superfluorescent fiber source for use in optical coherence tomography,*" Optics Express, **3** (1998).
83. S. D. Personick, *Optical Fiber Transmission Systems.* 1982: Plenum Press.
84. A. B. Carlson, *Communication Systems.* 1975: McGraw Hill.
85. L. H. Enloe and J. L. Rodda, Proc. IEEE, **53**, 165-166 (1965).
86. O. E. Delange and A. F. Dietrich, Bell Syst. Tech. J., **47**, 161-178 (1968).
87. T. G. Hodgkinson, *Coherence, Amplification and Quantum Effects in Semiconductor Lasers.* Pure and Applied Optics, ed. Y. Yamamoto. 1991: John Wiley & Sons.
88. S. D. Personic, Bell Syst. Tech. J., **52**, 843-886 (1971).
89. G. L. Abbas, V. W. S. Chan, and T. K. Yee, "*Local-oscillator excess-noise suppression for homodyne and heterodyne detection,*" Optics Letters, **8**, 419-421 (1983).
90. G. L. Abbas, V. W. S. Chan, and T. Yee, "*A dual-detector optical heterodyne receiver for local oscillator noise supression,*" J Lightwave Technol, **2**, 1110-1122 (1985).
91. M. Hammer, D. Schweitzer, L. Leistritz, M.Scibor, K. Donnerhacke, and J. Strobel, "*Imaging Spectroscopy of the Human Ocular Fundus In Vivo,*" J. Biomed. Opt., **418** (1997).
92. U. Morgner, W. Drexler, X. Li, F. X. Kaertner, C. Pitris, S. A. Boppart, E. P. Ippen, and J. G. Fujimoto, "*Spectroscopic optical coherence tomography,*" Optics Letters, **25**, 111-113 (2000).
93. J. Herbst, K. Heyne, and R. Diller, "Femtosecond Infrared Spectroscopy of Bacteriorhodopsin Chromophore Isomerization," Science, **297**, 822-825 (2002).
94. M. Kohl, U. Lindauer, U. Dirnagl, and A. Villringer, "Separation of changesin light scattering and chromophore concentrations during cortical spreadingdepression in rats," Opt. Lett., **23**, 555 (1998).

95. S. W. Hell, K. Bahlmann, M. Schrader, A. Soini, H. Malak, I. Gryczynski, and J. R. Lakowicz, "*Three-Photon Excitation in Fluorescence Microscopy,*" J. Biomed. Opt., **71** (1996).
96. M. Dellinger and M. Gèze, "Detection of mitochondrial DNA in living animal cells with fluorescence microscopy," Journal of Microscopy, 196-202 (2001).
97. Y. C. Cao, R. Jin, and C. A. Mirkin, "Nanoparticles with Raman Spectroscopic Fingerprints for DNA and RNA Detection," Science, **297**, 1536-1540 (2002).
98. F. Tokumasu and J. Dvorak, "Development and application of quantum dots for immunocytochemistry of human erythrocytes," Journal of Microscopy, **211**, 256-261 (2003).
99. S. A. Prahl, N. Kollias, and R. R. Anderson, "*Light scattering in biologic tissues,*" Photochem. Photobiol., (1992).
100. H. van de Hulst, *Light Scattering by Small Particles*. 1957, New York: John Wiley & Sons.
101. L. T. Perelman, V. Backman, M. Wallace, G. Zonios, R. Manoharan, A. Nusrat, S. Shields, M. Seiler, C. Lima, T. Hamano, I. Itzkan, J. Van Dam, J. M. Crawford, and M. S. Feld, "*Observation of periodic fine structure in reflectance from biological tissue: a new technique for measuring nuclear size distribution,*" Physical Review Letters, **80**, 627-630 (1998).
102. L. T. Perelman, W. Jun, C. Kun, I. Itzkan, R. R. Dasari, and M. S. Feld, "*Photon paths in turbid media: from smooth to random,*" OSA Trends in Optics and Photonics on Advances in Optical Imaging and Photon Migration, **2**, 18-20 (1996).
103. C. F. Bohren and D. R. Huffman, *Absorption and Scattering of Light by Small Particles*. 1983, New York: John Wiley & Sons.
104. A. Maki, Y. Yamashita, Y. Ito, E. Watanabe, and H. Koizumi, "*Origins of tissue optical properties in the UVA, visible, and NIR regions,*" OSA Trends in Optics and Photonics on Advances in Optical Imaging and Photon Migration, **2**, 364-71 (1996).
105. J. S. Saidi, S. L. Jacques, and F. K. Tittel, "*Mie and Rayleigh modeling of visible-light scattering in neonatal skin,*" Appl. Opt., **34**, 7410 (1995).
106. R. Drezek, A. Dunn, and R. Richards-Kortum, "Light scattering from cells: finite-difference time-domain simulations and goniometric measurements," Applied Optics, **38**, 3651-3661 (1999).
107. A. Dunn and R. Richards-Kortum, "*Three-Dimensional Computation of Light Scattering From Cells,*" IEEE Journal of Selected Topics in Quantum Electronics, **2**, 898-905 (1996).
108. Y. Pan, R. Birngruber, J. Rosperich, and R. Englehardt, "*Low-coherence optical tomography in turbid tissue: theoretical analysis,*" Appl Opt, **34**, 6564-6574 (1995).
109. A. E. Profio, "*Light transport in tissue,*" Appl Opt, **28**, 2250-2255 (1989).
110. A. H. Hielscher, R. E. Alcouffe, K. M. Hanson, and J. S. George, "Comparison of finite difference transport and diffusion calculations for photon migration in homogenous and heterogeneous tissues," OSA Trends in Optics and Photonics on Advances in Optical Imaging and Photon Migration, **2**, 55-9 (1996).
111. S. Prahl, "*http://omlc.ogi.edu/classroom/ece532/class3/index.html,*").
112. M. Kempe, A. Z. Genack, W. Rudolf, and P. Dorn, "*Ballistic and diffuse light detection in confocal and heterodyne detection,*" J. Opt. Soc. Am. A, **14**, 216-223 (1997).
113. G. Popescu and A. Dogariu, "*Ballistic attenuation of low-coherence optical fields,*" Appl Opt, **39**, 4469-4472 (2000).
114. M. E. Brezinski, G. J. Tearney, B. E. Bouma, S. A. Boppart, M. R. Hee, E. A. Swanson, J. F. Southern, and J. G. Fujimoto, "*Imaging of coronary artery microstructure (in vitro) with optical coherence tomography,*" The American journal of cardiology, **77**, 92-3 (1996).
115. S. Jackle, N. Gladkova, F. Feldchtein, A. Terentieva, B. Brand, G. Gelikonov, V. Gelikonov, A. Sergeev, A. Fritscher-Ravens, J. Freund, U. Seitz, S. Soehendra, and N. Schrodern, "*In vivo endoscopic optical coherence tomography of the human gastrointestinal tract--toward optical biopsy,*" Endoscopy, **32**, 743-9 (2000).
116. W. Jung, B. Kao, K. M. Kelly, L.-H. L. Liaw, J. S. Nelson, and Z. Chen, "*Optical coherence tomography for in vitro monitoring of wound healing after laser irradiation,*" IEEE Journal of Selected Topics in Quantum Electronics, **9**, 222-6 (2003).
117. A. V. D'Amico, M. Weinstein, X. Li, J. P. Richie, and J. Fujimoto, "Optical coherence tomography as a method for identifying benign and malignant microscopic structures in the prostate gland," Urology, **55**, 783-7 (2000).

118.J. G. Fujimoto, "Optical coherence tomography for ultrahigh resolution in vivo imaging," Nature biotechnology, **21**, 1361-7 (2003).
119.E. V. Zagaynova, O. S. Streltsova, N. D. Gladkova, L. B. Snopova, G. V. Gelikonov, F. I. Feldchtein, and A. N. Morozov, "*In vivo optical coherence tomography feasibility for bladder disease,*" The Journal of urology, **167**, 1492-6 (2002).
120.U. Seitz, J. Freund, S. Jackle, F. Feldchtein, S. Bohnacker, F. Thonke, N. Gladkova, B. Brand, S. Schroder, and N. Soehendra, "*First in vivo optical coherence tomography in the human bile duct,*" Endoscopy, **33**, 1018-21 (2001).
121.*Functional Histology*, ed. P.R. Wheater, H.G. Burkitt, and V.G. Daniels. 1987: Churchill Livingston.
122.H. W. Ott, "*Noise Reduction Techniques in Electronic Systems,*" John Wiley & Sons, 2nd edition, (1988).
123.F. Grum and R. J. Becherer, *Radiometry*. Optical Radiation Measurements. Vol. 1. 1979: Academic Press.
124.A. Rollins and J. Izatt. SNR Analysis of conventional and optimal fiber-optic low-coherence interferometer topologies. in Proc. SPIE 3915. 2000.
125."New Focus Nirvana Auto-Balanced Photoreceivers,"
126.H. Stadt, Astron. Astophys., **36** (1974).
127.B. M. Oliver. in *Proc IRE*. 1961.
128.H. P. Yuen and V.Chan, Opt Lett, **8**, 177 (1983).
129.A. Rollins and J. Izatt, "*Optimal interferometer designs for optical coherence tomography,*" Optics Letters, **24**, 1484-1486 (1999).
130.H. A. Haus and M. Mecozzi, "*Noise of mode-locked lasers,*" IEEE J Quantum Electron, **29**, 983-996 (1993).
131.H. A. Haus, M. Margalit, and C.X.Yu, "*Quantum Noise of a Modelocked Laser,*" Opt. Soc. America., **17**, 1240-1256 (2000).
132.F. Rana and R. J. Ram, "Noise and timing jitter in active and hyvrid mode-locked semiconductor lasers," OSA, 6-7 (2001).
133.F. Rana, H. Lee, R. J. Ram, M. E. Grein, L. A. Jiang, E. P. Ippen, and H. A. Haus, "*Characterization of the noise and correlations in harmonically mode-locked lasers,*" Opt. Soc. America., **19**, 2609-2621 (2002).
134.K. Takada, IEEE J Quant Electron, **34**, 1098-1108 (1998).
135.Selected Papers on Adaptive Optics and Speckle Imaging, ed. D.G. Crowe. 1993: SPIE Milestone.
136.J. D. McKinney, M. A. Webster, K. J. Webb, and A. M. Weiner, "Characterization and imaging in optically scattering media by use of laser speckle and a variable-coherence source," Opt Lett, **25**, 4 (2000).
137.R. Feiel and P. Wilksch, "High-Resolution Laser Speckle Correlation for Displacement and Strain Measurement," Applied Optics, **39**, 54 (2000).
138.S. H. Xiang, L. Zhou, and J. M. Schmitt. Speckle noise reduction for optical coherence tomography. in SPIE. 1997.
139.J. M. Schmitt, S. H. Xiang, and K. M. Yung, "*Speckle in optical coherence tomography,*" Journal of Biomedical Optics, **4**, 95-105 (1999).
140.A. F. Fercher, W. Drexler, C. K. Hitzenberger, and T. Lasser, "*Optical coherence tomography-principles and applications,*" Reports on Progress in Physics, **66**, 239-303 (2003).
141.W. Li, "*1/f Noise,*" http://www.nslij-genetics.org/wli/1fnoise/ (2004).
142.K. Takada, H. Yamada, and M. Horiguchi, "*Optical low coherence reflectometry using a 3x3 fiber coupler,*" IEEE Photon. Tech. Lett., **6**, 1014-1016 (1994).
143.T. Waite, Proc. IEEE, **54**, 334 (1966).
144.R. H. Dicke, Rev Sci Instrum, **17**, 268 (1946).
145.G. L. Abbas, V. Chan, and T. K. Yee, "Oscillator excess intensity suppression for homodyne and heterodyne detection," Opt. Lett., **8** (1983).
146.W. Drexler, U. Norgner, F. X. Kaertner, C. Pitris, S. A. Boppart, X. Li, M. Brezinski, E. P. Ippen, and J. G. Fujimoto. *In vivo ultrahigh resolution optical coherent tomography using a Kerr-lens*

modelocked Ti:Al_2O_3 laser. in *Conference on Lasers and Electro-Optics*. 1999. Baltimore, MD: Optical Society of America and IEEE.

147. U. Morgner, P. Wagenblast, R. Ell, W. Seitz, E. P. Ippen, J. G. Fujimoto, and F. X. Kartner, "*Broadband laser light sources for commercial and biomedical applications,*" Proceedings of SPIE, **4978**, 32-37 (2003).

148. ANSI, "American National Standard for Safe Use of Lasers, ANSI Z136.1-2000," (2000).

149. R. J. Thomas, B. A. Rockwell, W. J. Marshall, R. C. Aldrich, S. A. Zimmerman, and J. R. Rockwell, "A procedure for multiple-pulse maximum permissible exposure determination under the Z136.1-2000 American National Standard for Safe Use of Lasers," Journal of Laser Applications, **13**, 134-140 (2001).

150. B. A. Rockwell, C. P. Cain, W. P. Roach, and R. J. Thomas. Safe use of ultrashort lasers. in Proceedings of the 1999 Commercial and Biomedical Applications of Ultrafast Lasers. 1999. San Jose, CA.

151. K. K. Ranka, A. I. Gaeta, A. Baltuska, M. S. Pshenichnikov, and D. A. Wiersma, "*Autocorrelation measurement of 6-fs pulses based on the two-photon induced photocurrent in a GaAsP photodiode,*" Opt Lett, **22**, 1344-1347 (1997).

152. J. W. Nicholson, J. Jasapara, W. Rudolph, F. G. Omenetto, and A. J. Taylor, "*Full-field characterization of femtosecond pulses by spectrum and cross-correlation measurements,*" Opt Lett, **24**, 1774-1776 (1999).

153. Y. Yasuno, S. Makita, Y. Sutoh, M. Itoh, and T. Yatagai, "Birefringence imaging of human skin by polarization-sensitive spectral interferometric optical coherence tomography," Optics Letters, **27**, 1803-5 (2002).

154. M. C. Pierce, B. Hyle Park, B. Cense, and J. F. de Boer, "Simultaneous intensity, birefringence, and flow measurements with high-speed fiber-based optical coherence tomography," Optics Letters, **27**, 1534-6 (2002).

155. J. F. de Boer and T. E. Milner, "Review of polarization sensitive optical coherence tomography and Stokes vector determination," Journal of Biomedical Optics, **7**, 359-71 (2002).

156. X. D. Li, W. Drexler, C. Pitris, R. Ghanta, C. Jesser, J. Hermann, D. Stamper, D. Golden, S. Martin, J. G. Fujimoto, and M. E. Brezinski. *Imaging of osteoarthritic cartilage with optical coherence tomography: micronstructure and polarization sensitivity.* in *Conference on Lasers and Electro-Optics*. 1999. Baltimore, MD: Optical Society of America and IEEE.

157. C. Saxer, J. de Boer, B. Park, Y. Zhao, Z. Chen, and J. Nelson, "*High-speed fiber-based polarization-sensitive optical coherence tomography of in vivo human skin,*" Optics Letters, **25**, 1355-1357 (2000).

158. J. A. Izatt, W. Hsing-Wen, M. Kulkarni, K. Kobayashi, M. I. Canto, and M. V. Sivak, "*Optical coherence tomography and microscopy in gastrointestinal tissues,*" OSA Trends in Optics and Photonics on Advances in Optical Imaging and Photon Migration, **2**, 203-6 (1996).

159. G. Tearney, B. Bouma, and J. Fujimoto, "High speed phase- and group delay scanning with a grating-based phase control delay line," Optics Letters, **22**, 1811-13 (1997).

160. A. Rollins, M. Kulkarni, S. Yazdanfar, R. Ung-arunyawee, and J. Izatt, "*In vivo video rate optical coherence tomography,*" Optics Express, **3** (1998).

161. G. Tearney, B. Bouma, S. Boppart, B. Golubovic, E. Swanson, and J. Fujimoto, "*Rapid acquisition of in vivo biological images by use of optical coherence tomography,*" Optics Letters, **21**, 1408-10 (1996).

162. V. Gelikonov, G. Gelikonov, N. Gladkova, V. Leonov, F. Feldchtein, A. Sergeev, and Y. Khanin, "*Optical Fiber Interferometer with PZT Scanning of Interferometer Arm Optical Length,*" Optical Coherence Technologies, Inc. (1999).

163. R. Windecker, M. Fleischer, B. Franze, and H. J. Tiziani, "*Two methods for fast coherence tomography and topometry,*" Journal of Modern Optics, **44**, 967-77 (1997).

164. C. Su, "Achieving variation of the optical path length by a few millimeters at millisecond rates for imaging of turbid media and optical interferometry: a new technique," Optics Letters, **22**, 665-7 (1997).

165. J. Ballif, R. Gianotti, P. Chavanne, R. Walti, and R. Salathe, "*Rapid and scalable scans at 21 m/s in optical low-coherence reflectometry,*" Optics Letters, **22**, 757-9 (1997).

166.A. M. Rollins, M. D. Kulkarni, S. Yazdanfar, R. Ung-arunyawee, and J. A. Izatt, *"In vivo video rate optical coherence tomography,"* Optics Express, **3** (1998).
167.J. P. Heritage, A. M. Weiner, and R. N. Thurston, *"Picosecond pulse shaping by spectral phase and amplitude manipulation,"* Optics Letters, **10**, 609-611 (1985).
168.R. Thurston, J. Heritage, A. Weiner, and W. Tomlinson, *"Analysis of picosecond pulse shape synthesis by spectral masking in a grating pulse compressor,"* IEEE J Quantum Electronics, **QE-22**, 682-96 (1986).
169.O. E. Martinez, "3000 times grating compressor with positive group velocity dispersion: Application to fiber compensation in the 1.3-1.6um region," IEEE J. Quant. Elect., **23**, 59-64 (1987).
170.A. V. Zvyagin and D. D. Sampson, *"Achromatic optical phase shifter-modulator,"* Optics Letters, **26**, 187-190 (2001).
171.J. A. Izatt, M. R. Hee, G. M. Owen, E. A. Swanson, and J. G. Fujimoto, *"Optical coherence microscopy in scattering media,"* Optics Letters, **19**, 590-2 (1994).
172.A. D. Aguirre, P. Hsiung, T. H. Ko, I. Hartl, and J. G. Fujimoto, *"High-resolution optical coherence microscopy for high-speed, in vivo cellular imaging,"* Opt Lett, **28**, 2064-6 (2003).
173.S. Donati, Photodetectors: Devices, Circuits, and Applications. 2000: Prentiss Hall.
174."Analog Devices AD8015 Differential Oputput Transimpedance Amplifier,").
175."Anadigics ATA005001 Transimpedance Amplifier,"
176."Vitesse VSC7710 Integrated Photodetector/Transimpedance Amplifier,"
177."Analog Devices AD8310 Logarithmic Amplifier,"
178.D. Smith, ARRL Handbook for Radio Communications: Digital Signal Processing. 2003.
179.T. Ko, "High Speed Data Acquisition System for Optical Coherence Tomography," in Electrical Engineering and Computer Science Massachusetts Institute of Technology: Cambridge. p. 59 (2000).
180.C. H. Lee, H. Y. Chiang, and H. Y. Mong, "Sub-diffraction-limit imaging based on the topographic contrast of differentail confocal microscopy," Opt Lett, **28**, 1772-175 (2003).
181.T. Wilson, ed. *Confocal Microscopy*. 1990, Academic Press: London.
182.T. D. Wang, M. J. Mandella, C. H. Contag, and G. S. Kino, *"Dual-axis confocal microscope for high-resolution in vivo imaging,"* Optics Letters, **28**, 414-416 (2003).
183.K. H. Kim, C. Buehler, and P. T. C. So, *"High-speed, two-photon scanning microscope,"* Applied Optics, **38**, 6004-6009 (1999).
184.W. Denk, D. W. Piston, and W. W. Webb, *Two-Photon Molecular Excitation in Laser-Scanning Microscopy*, in *Handbook of Biological Confocal Microscopy*, J.B. Pawley, Editor. 1995, Plenum Press: New York. p. 445-458.
185.D. Bird and M. Gu, "Compact two-photon fluorescence microscope based on a single-mode fiber coupler," Optics Letters, **27**, 1031-1033 (2002).
186.A. Zoumi, A. Yeh, and B. J. Tromberg, *"Imaging cells and extracellular matrix in vivo by using second-harmonic generation and two-photon excited fluorescence,"* Proceedings of the National Academy of Sciences USA, **99**, 11014-11019 (2002).
187.G. Tearney, "Optical Biopsy of In Vivo Tissue Using Optical Coherence Tomography," in Electrical Engineering and Computer Science MIT: Cambridge (1996).
188.G. J. Tearney, M. R. Hee, B. Bouma, J. A. Izatt, J. G. Fujimoto, M. B. Brezinski, J. F. Southern, and E. A. Swanson, *"Optical biopsy in human tissue by using optical coherence tomography and microscopy,"* CLEO '95. Summaries of Papers Presented at the Conference on Lasers and Electro Optics, **349** (1995).
189.T. Corle, C. Chou, and G. Kino, *"Depth response of confocal optical microscopes,"* Optics Letters, **11**, 770-772 (1986).
190.J. M. Herrmann, C. Pitris, B. E. Bouma, S. A. Boppart, C. A. Jesser, D. L. Stamper, J. G. Fujimoto, and M. E. Brezinski, *"High resolution imaging of normal and osteoarthritic cartilage with optical coherence tomography,"* The Journal of rheumatology, **26**, 627-35 (1999).
191.G. J. Tearney, S. A. Boppart, B. E. Bouma, M. E. Brezinski, N. J. Weissman, J. F. Southern, and J. G. Fujimoto, *"Scanning single-mode fiber optic catheter-endoscope for optical coherence tomography,"* Optics Letters, **21**, 543-5 (1996).

192. J. G. Fujimoto, S. A. Boppart, G. J. Tearney, B. E. Bouma, C. Pitris, and M. E. Brezinski, "*High resolution in vivo intra-arterial imaging with optical coherence tomography,*" Heart, **82**, 128-33 (1999).
193. C. Pitris, M. E. Brezinski, B. E. Bouma, G. J. Tearney, J. F. Southern, and J. G. Fujimoto, "*High resolution imaging of the upper respiratory tract with optical coherence tomography - A feasibility study,*" American Journal of Respiratory and Critical Care Medicine, **157**, 1640-1644 (1998).
194. J. A. Izatt, M. D. Kulkarni, W. Hsing-Wen, K. Kobayashi, and M. V. Sivak, Jr., "*Optical coherence tomography and microscopy in gastrointestinal tissues,*" IEEE Journal of Selected Topics in Quantum Electronics, **2**, 1017-28 (1996).
195. A. M. Sergeev, V. M. Gelikonov, G. V. Gelikonov, F. I. Feldchtein, R. V. Kuranov, N. D. Gladkova, N. M. Shakhova, L. B. Suopova, A. V. Shakhov, I. A. Kuznetzova, A. N. Denisenko, V. V. Pochinko, Y. P. Chumakov, and O. S. Streltzova, "*In vivo endoscopic OCT imaging of precancer and cancer states of human mucosa,*" Optics Express, **1** (1997).
196. A. M. Rollins, R. Ung-arunyawee, A. Chak, R. C. K. Wong, K. Kobayashi, M. V. Sivak, Jr., and J. A. Izatt, "Real-time in vivo imaging of human gastrointestinal ultrastructure by use of endoscopic optical coherence tomography with a novel efficient interferometer design," Optics Letters, **24**, 1358-60 (1999).
197. A. E. Siegman, M. W. Sasnett, and T. F. Johnston, "*Choice of clip levels for beam width measurements using knife-edge techniques,*" IEEE J Quant Electron, **27**, 1098-1104 (1991).
198. "*http://www.smac-mca.com/smac/SMAC603.pdf*,"
199. Y. Pan, H. Xie, and G. K. Fedder, "Endoscopic optical coherence tomography based on a microelectromechanical mirror," Optics Letters, **26**, 1966-8 (2001).
200. J. M. Zara, S. Yazdanfar, K. D. Rao, J. A. Izatt, and S. W. Smith, "*Electrostatic micromachine scanning mirror for optical coherence tomography,*" Optics letters, **28**, 628-30 (2003).
201. D. L. Dickensheets and G. S. Kino, "*Silicon-micromachined scanning confocal optical microscope,*" J Microelelectromech Systems, **7**, 38-47 (1998).
202. K. E. Peterson, "*Silicon torsional scanning mirror,*" IBM J Res Develop, **24**, 631 (1980).
203. P. Hagelin and O. Solgaard, "*Optical raster-scanning display based on surface-micromachined polysilicon mirrors,*" IEEE J Select Topics in Quantum Electronics, **5**, 67 (1999).
204. A. Selvakumar, K. Najafi, W. H. Juan, and S. Peng. *Vertical comb array microactuators*. in *IEEE Workshop on Micromechanical Systems*. 1995. Amsterdam, Netherlands.
205. W. C. Tang, T.-C. H. Nguyen, and R. T. Howe. Laterally driven polysilicon resonant microstructures. in Proc IEEE Micro Electro Mechanical Systems Workshop. 1989.
206. J. T. Nee, R. A. Conant, R. S. Muller, and K. Y. Lau. Lightweight, optically flat micromirrors for fast beam steering. in IEEE/LEOS International Conference on Optical MEMS. 2000.
207. H. Schenk, P. Durr, T. Haase, D. Kunze, U. Sobe, H. Lakner, and H. Kuck, "*Large deflection micromechanical scanning mirrors for linear scans and pattern generation,*" IEEE J Select Topics in Quantum Electron, **6**, 715 (2000).
208. W. Piyawattanametha, P. R. Patterson, D. Hah, H. Toshiyoshi, and M. C. Wu. A 2D scanner by surface and bulk micromachined angular vertical comb actuators. in IEEE/LEOS Int. Conf. on Optical MEMS. 2003. Hawaii, USA.
209. D. Koester, A. Cowen, R. Mahadevan, M. Stonefield, and B. Hardy, *PolyMUMPs Design Handbook*. Vol. 10. 2003.
210. D. H. P. Patterson, H. Nguyen, H. Toshiyoshi, R. Chao, M.C. Wu. A scanning micromirror with angular comb drive actuation. in Int. Conf. on Micro Electro Mechanical Syst. 2002. Las Vegas, USA.
211. W. Piyawattanametha, "2D Microelectromechanical Scanner by Surface and Bulk Micromachined using Angular Vertical Comb Actuators," in Electrical Engineering UCLA: Los Angeles (2004).
212. H. Toshiyoshi, W. Piyawattanametha, C.-T. Chan, and M. C. Wu, "*Linearization of electrostatically actuated surface micromachined 2-D optical scanner,*" J. Microelectromechanical Systems, **10**, 210-214 (2001).

Chapter 5 – Biological Imaging in Animal Models

Introduction

Several possibilities exist to demonstrate the potential of OCT as a biological and biomedical imaging modality. While initial OCT studies looked at tissue architecture in scattering medium using *ex vivo* specimens, the state of the art has moved to *in vivo* imaging in both animal and human models. *In vivo* imaging is significant both scientifically and clinically as the detection, monitoring, and progression of disease at various stages of development can be achieved. In addition surgical guidance by optical biopsy is possible if the OCT system is capable of distinguishing pathologically relevant architecture. Finally the effects of therapeutic drug and interventional procedures can be monitored *in situ* and in real time without excision of tissue.

Animal models play an important role in both the development of imaging techniques and the demonstration of imaging capability in a controlled experimental environment. Not only can induction of a specified disease progression be controlled but precise correlation of imaging results with physical architecture can be done with histological sectioning of animal tissue post-mortem. For this reason, several animal models were employed to demonstrate the high capability of OCT systems developed in this work for both high resolution imaging of tissue architecture and for the demonstration of minimally invasive diagnostic imaging with novel devices.

In this chapter animal imaging results from multiple experiments will be presented. This first study involves the imaging of artificially induced osteoarthritis disease in a rat knee. The study is significant both clinically and scientifically as the progression and quantification of osteoarthritis is not fully understood. The capability to visualize cartilage changes *in vivo* has important implications for monitoring the progression of the disease and has applicability in the gauging the efficacy of possible anti-osteoarthritis drug treatments.

A second animal study involves *in vivo* imaging of the rabbit gastrointestinal and respiratory tracts. There were several goals for imaging in the rabbit model. The first goal was to demonstrate minimally invasive catheter-based imaging with multiple novel diagnostic probes. A second goal was to allow for correlation of cross-sectional OCT images to histological tissue cross-sections. Histology processing is currently the gold standard used in the identification of disease pathology and provides a standard baseline to compare against in the imaging of tissue. Demonstrating that OCT can visualize tissue architecture and morphology with close agreement to histology is an important step in the use of OCT for the detection and diagnosis of disease. Achieving good correlation in an animal study adds credibility to OCT images obtained in a human model where variability in tissue architecture and disease pathology is expected to be greater. The third goal of

using the rabbit animal model was to demonstrate multiple imaging scan protocols such as rotation, linear, and spiral OCT scan methods with catheter devices and to compare the efficacy of each of these methods in visualizing tissue structure.

Imaging of Osteoarthritis and Cartilage Degeneration *(Rat model)*

Osteoarthritis (OA) is a degenerative joint disease that necessitates several thousand orthopedic procedures every year. Articular cartilage, essential for joint function, often exhibits morphological changes during the preliminary stages of many arthritic diseases and could be used as an early indicator of disease induction [1]. The early detection of cartilage wear can be used to monitor the progression of OA and to effectively diagnose a therapeutic response. In addition, the capability to visualize articular cartilage would also enable the efficacy of anti-arthritic drugs to be evaluated. This work was don in collaboration with Dr. Mark Brezinski of Harvard Medical School and his medical students Mark Roberts and Samuel Adams. The histopathologist for the study was Dr. Debra Stamper. Individuals assisting with the imaging procedures from MIT included Dr. Stephane Bourquin, Pei-lin Hsiung, and Tony Ko.

Several imaging technologies have been used to image articular cartilage in an attempt to evaluate and detect the onset of OA. Current diagnostic techniques include X-ray radiography, minimally invasive needle arthroscopy, magnetic resonance imaging (MRI) and high frequency ultrasound (HF-US). Although bone erosions are the most specific indication of arthritis [2, 3] they typically manifest much later than cartilage erosion. Historically serial radiographs of joint space width (JSW), as an approximation of cartilage thickness, have been used to assess OA progression. This technique however can produce inconsistent results as minimum JSW can be dependent on several variables such as joint placement, reproducible joint orientation and beam alignment [4, 5]. In addition JSW measurements can also be significantly affected by surrounding tissue such as the meniscus [6, 7].

The use of arthroscopy, while minimally invasive, is somewhat limited in assessing cartilage structure because only surface features can be evaluated. Substantial progress has been made in the measurement of articular cartilage thorough the use of magnetic resonance imaging. Although MRI can provide full volumetric information on the knee joint [8] and has been used to identify cartilage variations, image acquisition times are often quite long (10 minutes to several hours) and are dependent on the spatial resolution desired. High field (> 8T) MRI systems have shown the capability to image at 60 um resolution ex vivo but required acquisition times on the order of 12 hours [9]. Experimental and clinical systems typically operate at lower field strengths of 2-2.5 T and 0.5-1.5 T respectively, resulting in a corresponding decrease in image resolution

(100-25 um) [10, 11]. The size and cost of MRI equipment also makes widespread clinical use more difficult.

High frequency ultrasound has shown the capability to provide quantitative information on cartilage structure and composition with reasonable imaging times [12, 13]. However similar to the situation with MRI, HF-US resolution is limited to 50-100 um and requires the presence of a transducing medium and a rather large transducer.

Experiments with OCT have demonstrated the capability to image articular cartilage both in vitro and in vivo and cartilage thickness, fibrosis, fibrillations and joint microstructures have been able to be identified [14, 15]. It is also known that with the progression of OA, collagen architecture becomes more disorganized resulting in a change in polarization sensitivity. Because OCT uses a low coherence light source as the transducing signal, the birefringence of collagen can be used to provide information on cartilage matrix integrity. Polarization sensitive OCT has been used to identify and grade collagen disorganization previously [16].

In this experiment, high resolution OCT was performed to visualize cartilage breakdown and the progression of osteoarthritic degeneration in a longitudinal animal study. The goal of the study was to visualize the progression OA in articular cartilage induced by intra-articular injections of sodium iodoacetate. Iodoacetate has been used in several studies to examine anti-inflammatory and potential chondroprotective agents and is a well established model for chemically induced cartilage damage [17, 18]. Cartilage thinning, osteochondral remodeling and fibrillation of articular surfaces are typically observed within 10-15 days of iodoacetate introduction [19] and similar disease progression was seen in this study.

In the study the Cr4+:Forsterite modelocked laser was used as the broadband light source to enable high resolution imaging. An operating bandwidth of 180-220 nm at a center wavelength of 1250 nm enabled axial resolutions of 3-5 um. High power and bandwidth operation was maintained over several imaging dates with consistent performance. A transverse spot size resolution of 18 um was obtained using a 18 mm focal length lens to focus the light onto the sample via the handheld imaging probe. Using dual balanced detection to reduce background laser intensity noise, a sensitivity of 95 dB was measured with 10 mW of power on the sample. Polarization controllers (PC) in the sample and reference arms were used to optimize the image contrast by adjusting the heterodyne signal strength. Two dimensional cross sectional images were obtained by scanning the optical beam in the sample arm with a mechanical galvanometer. A 4 Hz repetition rate allowed real-time imaging to be performed with the compact handheld probe described previously.

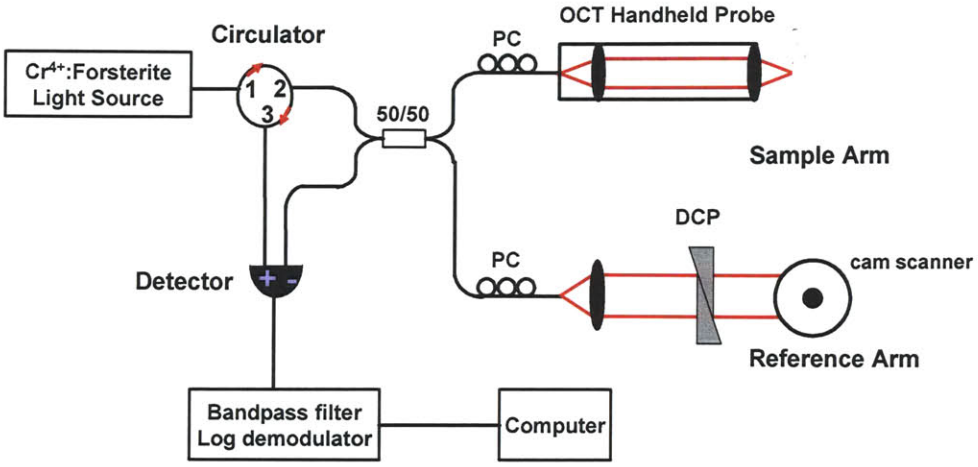

Figure 5-1. Experimental setup for rat knee imaging

A handheld probe and broadband light source were used for high resolution imaging of osteoarthritic changes in the rat knee model.

Experimental osteoarthritis was induced in 12 male Wistar rats (body weight of 180-200 grams) by injecting 3 mg of sodium iodoacetate dissolved in 50 ul of sterile saline into the left knee under the patellar ligament. A saline injection of 50 ul was administered into the right knee as a control solution. Rats 1-6 (Group A) were injected on Day 0 while rats 7-12 (Group B) were injected on Day 0 and Day 5 (3 mg iodoacetate for each injection). Imaging was performed over a period of 60 days with imaging and sacrifice dates shown in Figure 5-2.

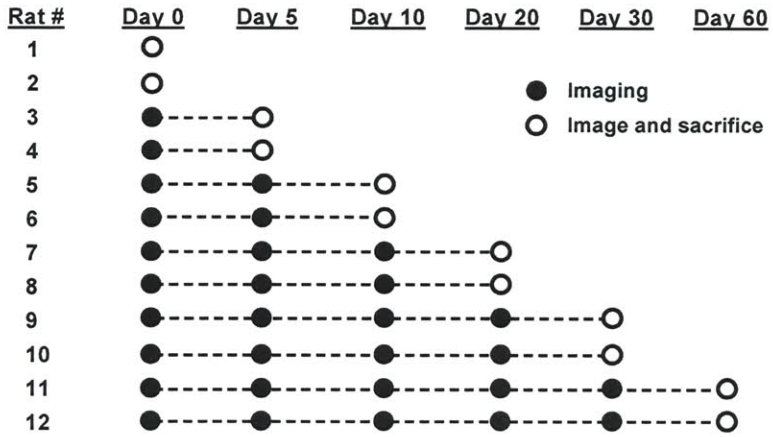

Figure 5-2. Longitudinal imaging timeline with imaging and sacrifice dates

Osteoarthritic degeneration was seen 10-15 days following induction via sodium iodoacetate injections.

For both imaging and injection of sodium iodoacetate or saline solution, knee joints were opened under sterile conditions via a medial parapatellar incision. Once the knee capsule was opened and cartilage exposed, OCT imaging was performed with a handheld probe. After imaging, each joint was sutured closed under sterile conditions. All procedures were performed with the rats under gas anesthesia.

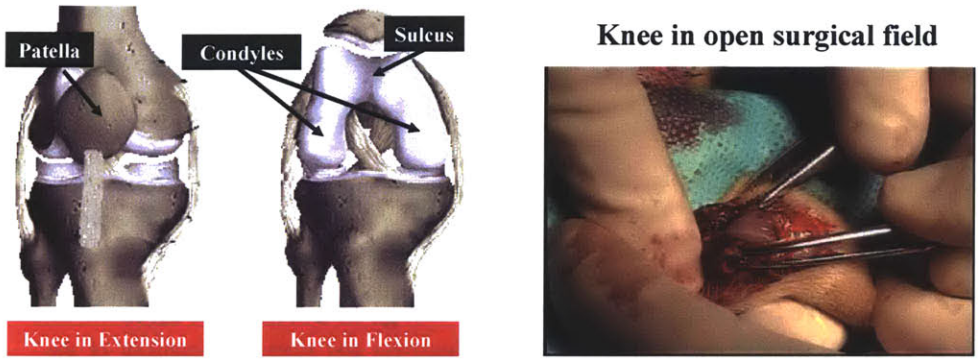

Figure 5-3. Schematic of knee joint and photograph of rat open knee procedure

a) Schematic of knee joint both in extension and flexion positions. Imaging of the condyle and sulcus regions of both iodoacetate injected and control knees was performed. b) Photograph of surgical field with exposed rat knee. The patella was placed to the side of the surgical field during imaging.

OCT imaging was performed on the left and right knees at each time point (Day 0, 5, 10, 20, 30 and 60) by reopening the suture site. At each time point one animal from each imaging group (A and B) was sacrificed. Rat knees were imaged longitudinally along the right and left medial condyles as well as within the sulcus region. During imaging the handheld probe was clamped in place above the knee and accurately positioned with a micrometer stage. To aid OCT image orientation with histology registration, two orientation marks (red dots) were placed at the start and end scan points within each knee.

Imaging of normal knees was performed to provide a baseline reference of articular structure in knees without osteoarthritic degeneration. Figure 5-4a shows an OCT image of the rat knee condyle and sub-patellar region. The cartilage-bone interface can be clearly delineated with the top cartilage layer exhibiting a highly backscattering and laminar appearance. It was also possible to accurately measure a cartilage thickness of 150 um +/-10 um. Below the cartilage was a layer with low signal intensity corresponding to the cartilage-bone interface followed by subchondral bone. Imaging of the knee sulcus showed similar backscattering properties and uniform cartilage layer thickness (Figure 5-4b).

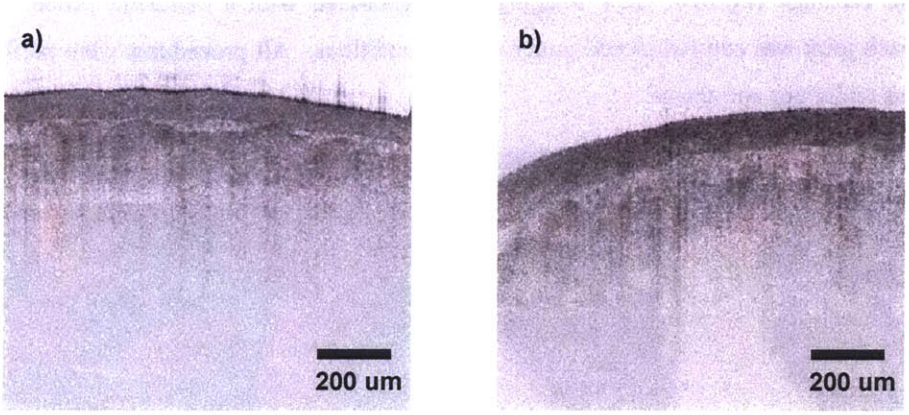

Figure 5-4. High resolution OCT image of normal rat knee

Rat knee a) condyle and b) sulcus regions. Thickness and scattering intensity of the cartilage layer is seen to be uniform indicating a healthy tissue state.

In addition to normal cartilage structure, several architectural changes were visible by OCT after injection of iodoacetate. Figure 5-5 shows a time progression of the knee degeneration imaged at Days 0, 20 and 60. Marked cartilage thinning was observed in the condyle regions indicative of osteoarthritis progression. Thinning was more pronounced on condyles of the injected knees than on the sulcus region in the same knee. This indicated that the observed deterioration was due to wear from load bearing on the rat knee rather than cartilage dissolution due to reaction with the sodium iodoacetate solution.

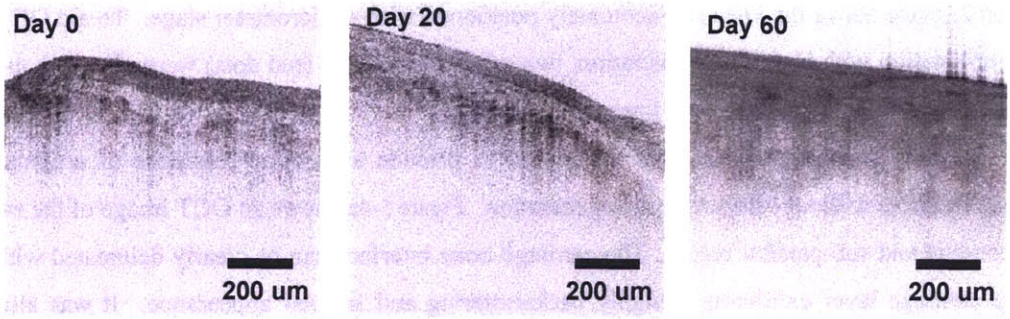

Figure 5-5. Cartilage thinning in knee condyle regions

Thinning can be seen in time progression. Degeneration was visible by Day 20 with severe cartilage erosion seen by Day 60.

Imaging of the knee sulcus regions located between the condyles was also performed with results shown in Figure 5-6. Minimal degeneration was observed in the sulcus and confirmed the model hypothesis for acceleration of osteoarthritic wear by iodoacetate induction.

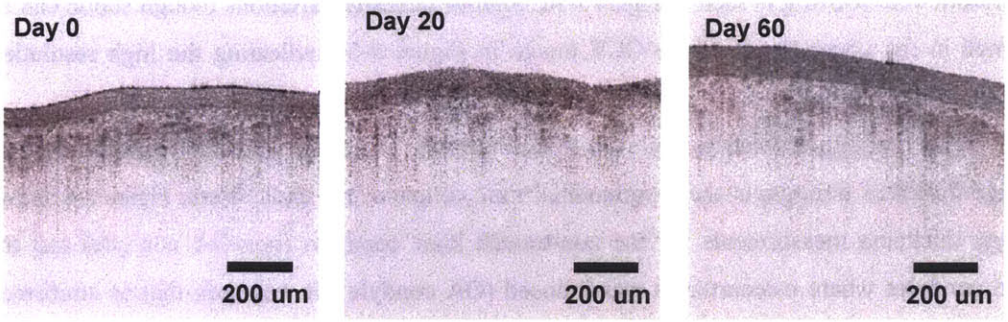

Figure 5-6. Imaging of knee sulcus regions in injected knees

Cartilage degeneration was not observed indicating that accelerated osteoarthritic progression occurred in the load bearing condyle regions.

In order to validate architectural morphology observed in OCT images, histopathology sectioning and staining was performed on the knees of sacrificed animals. Figure 5-7 shows OCT images and corresponding trichrome stained histology of a iodoacetate treated knee condyle at Day 0 (Figure 5-7a,b) and at Day 60 (Figure 5-7c,d).

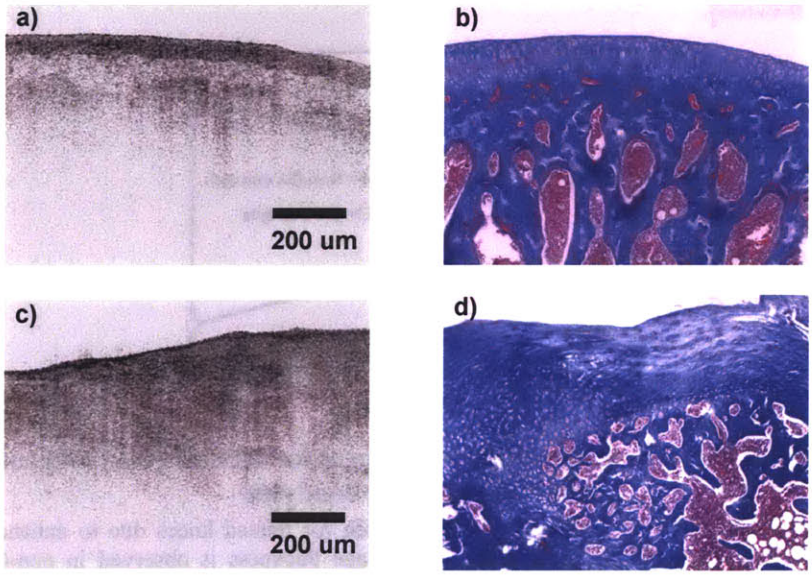

Figure 5-7. OCT images and histopathology of treated rat knees

OCT imaging of iodoacetate treated rat knee condyles at a) Day 0 and c) Day 60. Histopathology stained cross-sections of the same knee condyles (b,d) after animal sacrifice show corresponding architectural morphology and correlation to features seen observed in the OCT images.

Similar cartilage thickness can be seen before induction of osteoarthritis with the cartilage osteocyte layer well delineated in both the OCT image and histology. The cartilage-bone inteface is also apparent however sub-chondral features within the bone are difficult to visualize due to limited image penetration depth. Full degeneration of the condyle cartilage layer with fibrotic-like scarring is seen in Figure 5-7d. Similar intensity variations though subtle can be discerned in the upper layers of the OCT image in Figure 5-7c indicating the high resolution capability of the system.

With the high resolution achieved it was possible to conduct precise measurements of cartilage thickness throughout the longitundinal time course of the experiment. Figure 5-8 shows cartilage thickness measurments for the non-treated knee condyles (non-OA condyle) and the treated condyles where osteoarthritis was induced (OA condyle). It was seen that as confirmed visually a marked decrease in cartilage thickness occurred in the treated knee condyles. Remarkably an increase was observed in the condlye thickness of the untreated, control knee over the 60 day time course. This can be explained by the healing and regenartive repair processes that occurred on the untreated knees. Due to having multiple surgical procedures performed at 5-10 day intervals, the control (saline injected) rat knees were exposed to external damage from the surgical procedure. Due to the increased metabolism in the rat, these knee condyles initiated healing processes by which the cartilage was regrown to slightly larger thickness than previous.

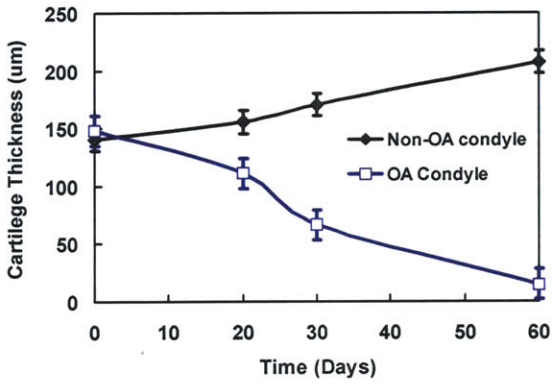

Figure 5-8. Time course of cartilage thickness for treated (OA) and control (non-OA) rat knee condyles

A dramatic decrease in cartilage thickness is seen for treated knees due to enhanced osteoarthritic degeneration. An increase in cartilage thickness is observed in non-OA knees due to healing and regenerative processes.

Finally it was possible to resolve cartilage-bone interfaces and osteochondral features below the tissue surface (Figure 5-9a,b) which are important in determining regions of disruption that may be indicative of the early onset of osteoarthritis progression. Cartilage remodeling and

fibrillations were also distinctly apparent with the high resolution capability of the system (Figure 5-9b).

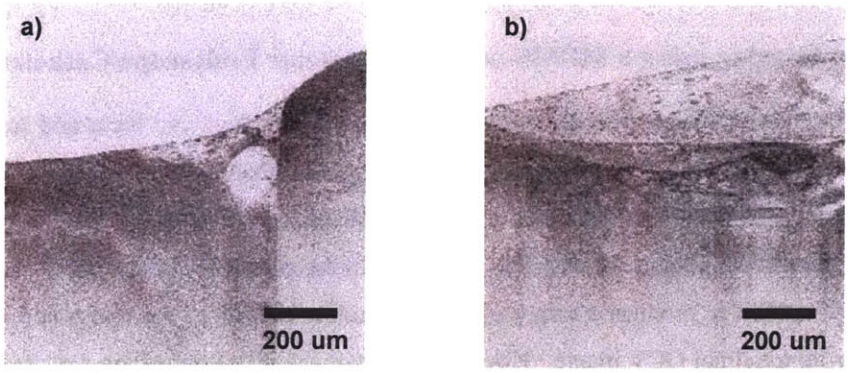

Figure 5-9. High resolution images of knee architecture

(a) OCT image of rat knee condyle. Cartilage thickness can be measured precisely and the cartilage-bone interface is clearly discerned. (b) Cartilage remodeling and fibrillations can be seen below the tissue surface.

The ability to assess disease progression in an animal model will have important applications for drug discovery and pharmaceutical trails. Although this study was performed with a hand held probe, OCT imaging is also possible using arthroscopes or minimally invasive devices such as imaging needles. From these initial results OCT promises to be a useful imaging modality in both osteoarthritis research and clinical diagnosis.

Imaging of Gastrointestinal at Respiratory Architecture *(Rabbit model)*

Endoscopic high resolution imaging of the upper and lower gastrointestinal tracts as well as the respiratory tract was investigated using minimally invasive catheters. The rabbit is an excellent animal model for performing ultrahigh resolution imaging surveys of various organ systems. Comparison of images with corresponding histology provided a baseline for image interpretation for both ex vivo and in vivo future animal and human studies. The results of these studies established the feasibility of catheter and endoscopically-based OCT imaging devices and identified key factors necessary to achieve optimal system design and performance.

The development of scanning, fiber optic endoscope catheters [20] was an important advance which enabled in vivo OCT imaging applications in different organ systems [21]. The first imaging studies in human subjects were performed using a novel, magnetically actuated,

forward imaging fiber scanning probe [22, 23]. Linear as well as rotary scanning fiber optic endoscope catheters have been demonstrated for imaging the gastrointestinal tract in human subjects [24, 25]. Clinical endoscopic OCT imaging studies have been performed by several groups and demonstrates the ability of OCT imaging to visualize pathologies of the upper and lower gastrointestinal tracts [23, 26-29].

Endoscopic Imaging using a MEMS-based Micromotor Endoscope/Catheter Probe

Minimally invasive endoscope catheter imaging probes which can focus and scan a beam inside the body have been a key technology for enabling endoscopic OCT imaging studies. The most common probe design to date uses a mechanical cable, optical fiber, and lens assembly housed in a transparent plastic sheath. The cable within the sheath is either rotated or translated in a push-pull motion to produce a rotary or linear scanning motion of the optics and generate a transverse or longitudinal OCT image. However, because the distal optics are actuated from the proximal end of the long probe, this design can result in non-uniform scanning motion which introduces artifacts in the OCT image. Imaging speeds and duty cycles are limited. In addition, for rotary scan designs, a proximally located rotary optical coupling is required. Forward imaging designs avoid these problems, but scan ranges can be limited. Recent developments in novel microelectromechancial system (MEMS) scanning technologies promise to enable distal beam scanning which would improve the speed and reduce image distortion in endoscopic imaging [30, 31]. In spite of these advances, previous endoscope catheter probe designs could not provide focus adjustment during OCT imaging. For this reason, relatively large spot sizes were necessary in order to preserve a sufficient depth of field to enable OCT imaging in intraluminal structures. This limits the transverse image resolution.

In this experiment a new, high resolution, MEMS-based micro-motor endoscope catheter with adjustable focus capability was demonstrated. The mechanical scanning and micro-optic components were located at the distal end of the probe, thereby eliminating the need for proximally actuated rotating or translating elements. Distal actuation provides better uniformity of beam scanning with reduced image distortion artifacts and improved range of image speeds. Standard OCT imaging probes usually require long depth of fields and therefore the minimum transverse focused beam sizes are limited. With the ability to independently adjust the optical beam focal position and use higher numerical aperture optics, transverse image resolution can be improved. In addition, an adjustable focus device can enable C-mode OCT imaging (acquiring images with several focal planes and fusing them together) to overcome depth of field limitations [32]. The micro-motor imaging probe also has a larger field of view than conventional OCT

endoscope catheter devices thereby allowing larger diameter lumens to be more readily visualized. The characterization of the micro-motor probe is described previously in this thesis.

Figure 5-10 shows a schematic of the experimental setup. The compact, broadband Cr4+:Forsterite laser combined with a dispersion shifted fiber was used to generate spectral bandwidths of 210 nm at a center wavelength of 1250 nm with 40 mW output power. The operation and laser performance characterists of this light sourec are described earlier in this work. Light was coupled into a broadband optical circulator and fiber optic beam splitter and dual balanced detection was used to reduce background intensity noise from the laser source and increase signal to noise. To enable real time imaging a rapidly rotary cam scanning delay line was used in the reference arm. Polarization controllers (PC) were used in both the sample and reference arms. Dispersion compensating prisms (DCP) and an air gap coupling (AGC) were used to match material dispersion and achieve broadband, high resolution operation.

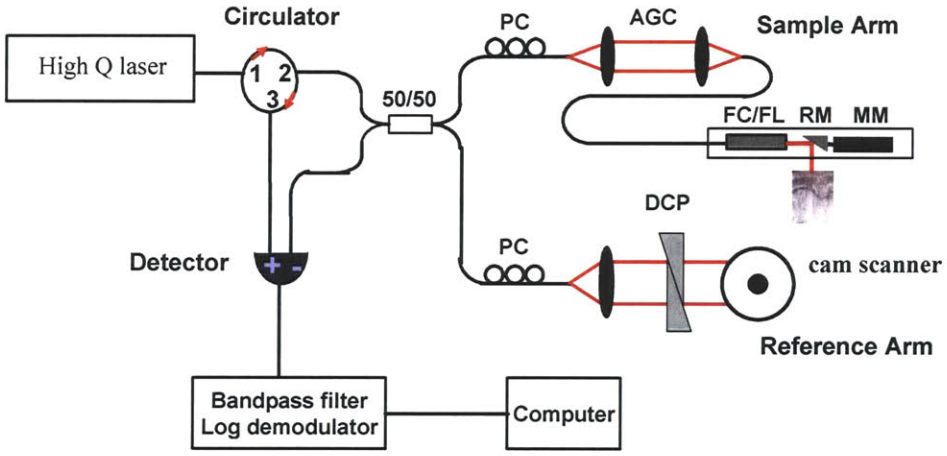

Figure 5-10. OCT system used for micromotor imaging

The broadband Cr4+:Forsterite light source for the micro-motor imaging experiment. Accurate dispersion matching through the use of an air gap coupling and dispersion compensating prisms enables broadband, high resolution operation.

The initial design of the endoscope probe consisted of a fiber optic collimator and focusing lens with a rod mirror mounted onto the micro-motor. The endoscope probe and housing fit within a 5 mm diameter, transparent plastic sheath. The control wires for the micro-motor were fed through to the proximal end of the endoscope and attached to control electronics. The fiber collimator and focusing lens assembly were mounted at the end of a speedometer cable and the focus could be adjusted distally by translating the assembly with respect to the rotating mirror. The assemblem micromotor and schematic are shown in Figure 5-11. Real time imaging was performed at 4 frames per second with 1600 axial scans per second. The OCT signal was

filtered and demodulated at a heterodyne frequency of 9.8 MHz. Image data was acquired with a 5 MHz, 12 bit A/D converter and displayed on the computer screen.

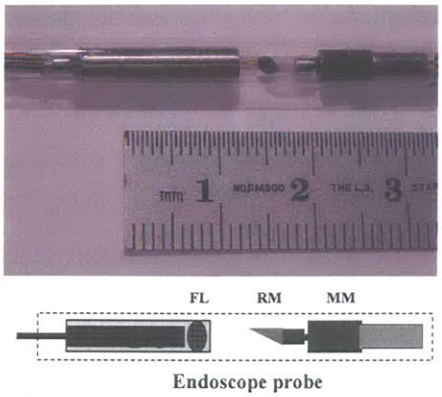

Figure 5-11. A photograph and schematic of the assembled adjustable-focus probe

The probe consisted of a fiber collimator (FC), focusing lens (FL), rod mirror (RM) and micro-motor (MM). The micro-motor located at the distal end of the endoscope allows accurate scanning of the optical beam with no non-uniform rotation distortion.

The OCT system achieved a transverse resolution of 8 um and an axial resolution of 8 um resulting in a uniform imaging volume at the optical focus of 8um x 8um x 8um. Figure 5-12 shows an image of two finger pads grasping the endoscope sheath housing. Cross correlation processing and bilinear interpolation were employed to create high resolution polar images. Both the stratum corneum and dermal-epidermal junction can be resolved at high resolution with good image contrast. By varying the micro-motor rotation speed, the transverse pixel and frame rate could also be adjusted. For large diameter structures such as the esophagus, high pixel densities are necessary to achieve high transverse resolutions. Novel display methods to visualize these structures are necessary as the image sizes at high resolution will be extremely large.

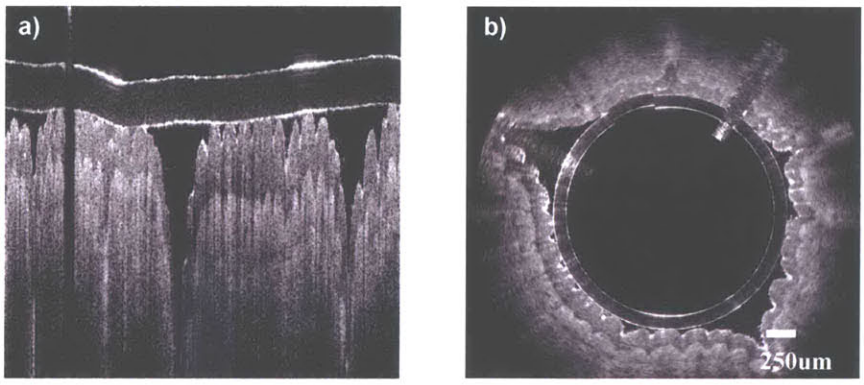

Figure 5-12. Human finger pad OCT image from the micromotor catheter

The original data set (a) and transformed (b) into an accurate polar mapping. Skin structure is discernable with good demarcation of the stratum corneum, dermal and epidermal layers.

To demonstrate focus tracking in scattering media, chicken skin and muscle were initially imaged ex vivo. Figure 5-13 shows two radial scans acquired with the beam focus at the tissue surface (a) and 1 mm within the sample (b) respectively. The focal position was varied by translating the collimator assembly with an electronically controlled motion stage. Several features deeper within the tissue can be resolved more clearly at the further beam focus position (circled regions).

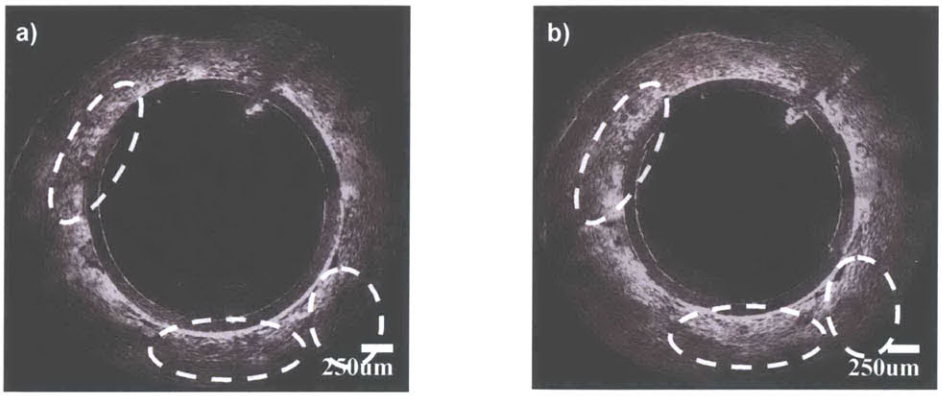

Figure 5-13. Image of chicken muscle and skin tissue *ex vivo*

Images are taken at two different focal positions. Several structural features can be resolved with greater detail using an adjustable focus located deeper within the sample (b). The focused spot size is 8 um corresponding to a confocal parameter of 75 um.

After the initial demonstration of the micro-motor scanning probe endoscopic imaging was performed in vivo on an anesthesized New Zealand White rabbit. For the experimental procedure, the lower gastrointestinal tract of a female rabbit was imaged by manual introduction of the endoscope probe through the rectum. To minimize animal discomfort and reduce the risk of damaging the colonic mucosa, a 5.0 French introducer and sterile bacteriostatic lubricant were used during catheter insertion. Imaging at multiple locations within the colon was conducted and at each imaging position, OCT scans were taken at multiple focus positions on the optical beam to demonstrate the adjustable focusing capability of the probe. The beam focal position was changed by translation of the collimator and focusing lens assembly with respect to the fixed motor assembly. The rabbit was anesthetized with 35 mg/kg Ketamine and 5 mg/kg Xylazine injected intramuscularly as per MIT CAC (Committee on Animal Care) protocol specifications. Acepromazine (0.75 mg/kg) was also administered with the initial ketamine/xylazine induction. During the procedure the rabbit heart rate was monitored with an EKG to ensure adequate sedation. When the heart rate increased by more than 25% above the sedated heart rate of 110 bpm, maintenance anesthesia of 8 mg/kg Ketamine and 1 mg/kg Xylazine was administered via a

marginal ear vein. After imaging the animal was euthanized with 250 mg/kg of sodium pentobarbital.

Figure 5-14 shows the first in vivo imaging results using the micro-motor scanning probe in the rabbit colon. Colonic epithelium and muscular mucosa layers are well defined and clearly differentiated in the image. Image penetration depth of approximately 750-1000 um is observed. Looking at an enlarged section of the image, it was seen that at high resolution there existed slight scan irregularites that showed up as small jumps in the OCT image (arrows in Figure 5-14b).

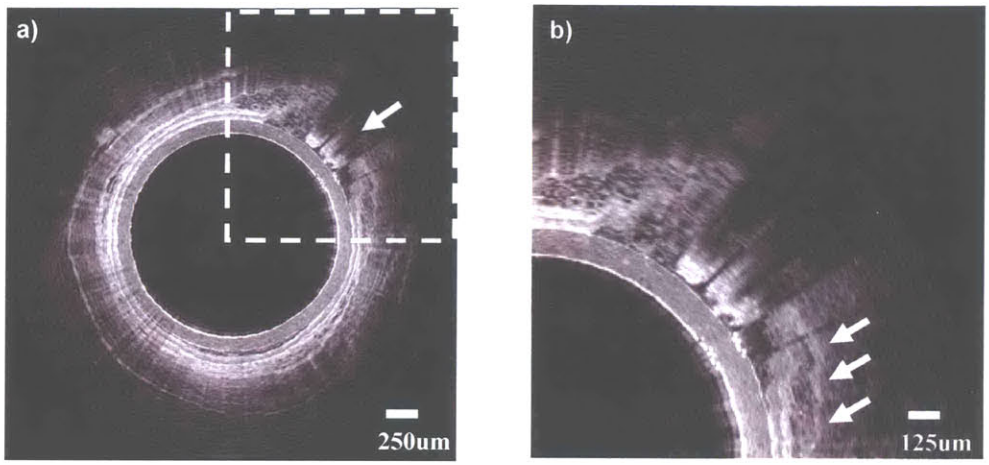

Figure 5-14. *In vivo* OCT image of the rabbit colon

The micro-motor control wires occlude a small portion of the scan field and are indicated with an arrow. b) Enlarged view of the OCT scan shows slight scan irregularities or jumps due to non-uniform micro-motor rotational motion.

It was determined that these jumps corresponded to the number of gear teeth that the micro-motor had in the inner MEMS gearing with a 25:1 gear reduction ratio. As this effect was inherent to the micro-mechanical construction of the motor assembly the solution to remove the non-uniformity I rotation was to implement a higher gear ratio of 125:1 in a second micro-motor design. This would result in much finer gear steps that would improve the OCT image quality.

Figure 5-15 shows an OCT image obtained with the redesigned and higher gear ratio micro-motor probe. The image was with the probe inserted 3 cm inside the rabbit colon. In the image the probe sheath radius is 2.5 mm, while the OCT scan depth extends an additional 2 mm beyond the sheath. The OCT image was able to clearly delineate upper mucosa (um), muscularis mucosae (mm), and submucosa (sm) regions within the colon with smooth radial motion.

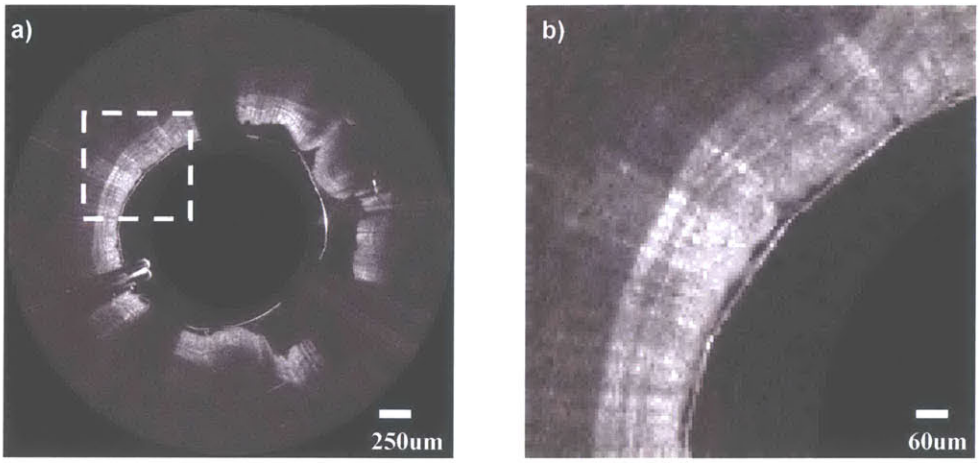

Figure 5-15. OCT image of rabbit colon *in vivo*

Imaging was performed with < 4 um axial resolution. b) Visualization of colonic upper mucosa (um), muscularis mucosae (mm), and submucosa (sm) layers is clear within the colon with smooth radial motion in the enlarged image.

Adjustment of the optical beam focus in real time was also demonstrated. Figure 5-16 shows enlarged OCT images of a region in the colon with two different beam focus positions. When the focus was set shallower, closer to the probe sheath it was possible to resolve detailed features near the colonic upper mucosa more clearly (Figure 5-16a). Focusing deeper inside the tissue, farther from the probe sheath, improved the visualization of deeper layers (Figure 5-16b). Figure 5-16c shows two radial A-scans plotted along the dashed lines in the Figure 5-16a and Figure 5-16b. A clear difference in the A-scan intensity behavior is observed when the focus was set closer to the tissue surface (Figure 5-16a) versus deeper in the tissue (Figure 5-16b).

The micro-motor imaging probe design has several attractive features. Adjustable focus enables the use of smaller focused spot sizes and shorter depth of field than was previously feasible. The resulting improvement in image resolution could improve the performance of ultrahigh resolution OCT imaging by enabling better visualization of tissue pathology.

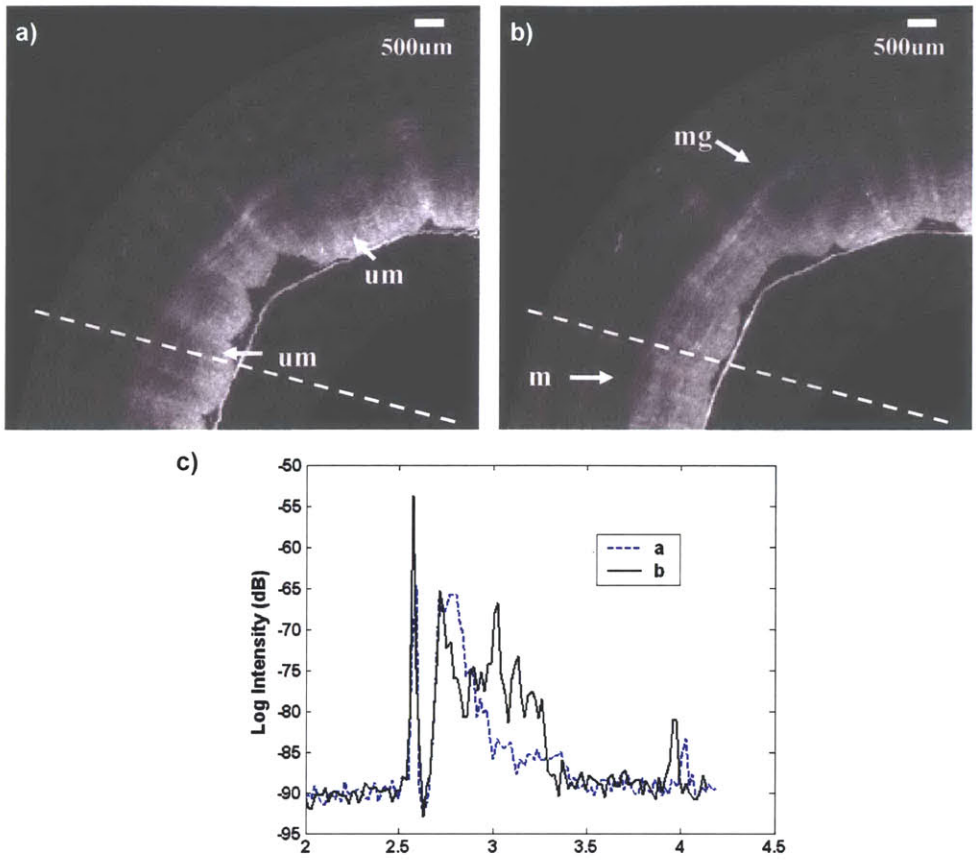

Figure 5-16. OCT images at two different focus settings

a) Beam focus set near the tissue surface provides higher contrast within the colonic upper mucosa (um). b) Setting the focus 500 um deeper enhances visualization of deeper mucosal layers (ml) and glandular structure (mg). c) Plots of axial scans along the dashed lines for the two focus depth settings (a and b) illustrate the signal enhancement at different depths inside the tissue.

With additional engineering, it should be possible to perform dynamic focusing where the focal position is adjusted as a function of rotary beam position. This would enable focus tracking in cases where the endoscope catheter probe was not centered in the lumen. The use of a micromotor for distal actuation reduces the motion non-uniformity which could occur with previous proximally actuated endoscope catheter probes. A wider range of imaging speeds can be achieved with improved duty cycle. Finally, although this prototype imaging probe was 5 mm in diameter, a reduction in probe size is possible through the use of smaller micro-motors in the future.

Imaging of Biological Systems with 2-Axis MEMS Scanner

The implementation of microelectromechanical (MEMS) scanners with high resolution OCT imaging systems was purseued in this work to demonstrate the next step towards minimally invasive diagnostic imaging devices. Typical medical imaging devices have relatively small sized dictated by the need to insert these devices into various organ systems of the body. For example, cardiac catheters have a typical diameter of 1 mm. While high resolution optical imaging can be performed using devices such as catheters and endoscopes and has been demonstrated in this work, the lack of a beam scanning and focusing technology is a drawback in their design and utility.

The integration of MEMS technology, fiber optics, and biomedical imaging can be used to construct next generation medical imaging technologies which can perform microscopic resolution, internal body imaging. The demonstration of this technology would represent an advance which would establish a basis for future experimental and clinical studies. Ultimately, the ability to fabricate these device in a cost effective manner suitable for medical devices, combined with clinical research, could have a significant impact on health care.

Figure 5-17 shows a schematic and photograph of the the assembled MEMS chip. The OCT signal beam is delivered via a single mode fibe collimator and focused onto the MEMS chip for a post-objective scanning configuration. This results in a slightly curved scan field however significantly reduces off-axis optical abberations.

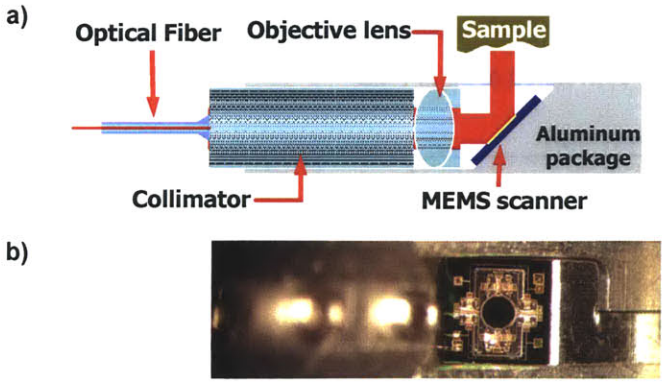

Figure 5-17. Schematic and photograph of MEMS OCT scanner

a) The MEMS probe consists of a single mode optical fiber pigtailed to a fiber collimator. An objective lens focuses the beam on the MEMS chip which scans the beam across the sample. b) Photograph of the assembled MEMS chip inside the package.

Figure 5-18 shows the OCT system setup used for the experiment. The High Q modelocked light source was used to generate broadband optical spectra with a bandwidth of 100 nm at a center wavelength of 1090 nm. The laser output was 167 mW with 97 mW of power coupled into the fiber.

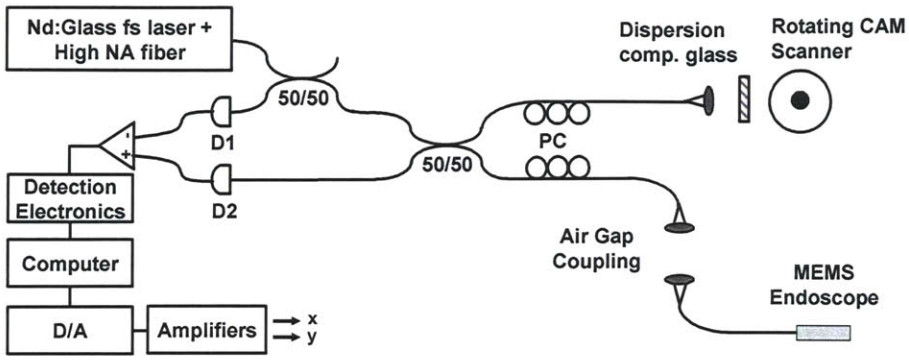

Figure 5-18. Experimental setup for MEMS imaging at 1 um

A high power throughput interferometer configuration was used to maximize signal strength. Dispersion compensating glass and an air gap coupling were utilized to achieve high resolution and broadband operation.

The high axial resolution achieved with the MEMS endoscope is shown in Figure 5-19. The axial point spread function has a FWHM of 1.10 usec which at the Doppler scan speed of 3920 mm/sec corresponds to an axial resolution of 4.3 um in air or ~3 um in tissue. The log demodulated function is shown on the left and exhibits low interference fringe sidelobes that are approximately -55 dB below the beak signal. The total signal indicates a high signal to noise of 112 dB with a calibrated conversion of 31 mV/dB

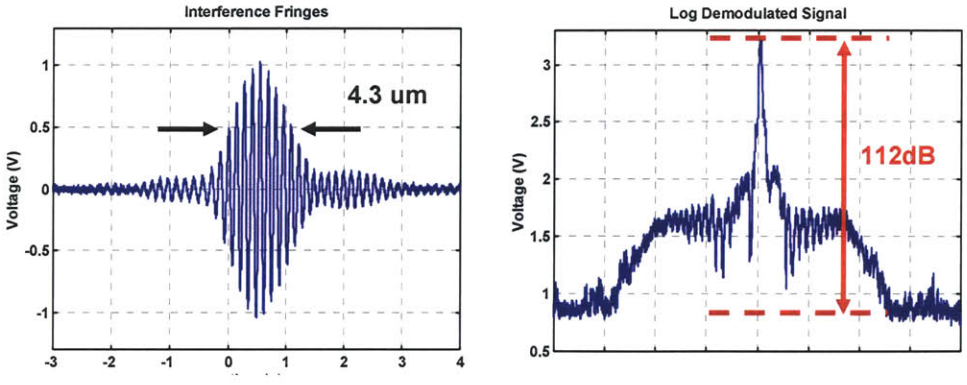

Figure 5-19. Linear and log demodulated axial points spread functions

a) High axial resolution of 4.3 um in air was achieved with good signal to noise performance b) of over 100 dB.

In order to characterize the scanning performance of the MEMS chip, a ruled optical grating was imaged along each scanning axis. A representative scan for the x-axis scan is shown in Figure 5-20a and illustrates that a slight scan curvature exists as expected (seen as a non-flat grating field). The MEMS mirror scan range at the focal plane of the optical beam is estimated to be ~925 um with a working distance from the endoscope package of 1.1 mm. Using the known voltage input range and grating characteristics it was possible to plot the scan transfer curve for the mirror which is shown in Figure 5-20b. While the scan is not completely linear (dashed line) it performs well between the expected operating voltage range of 30-120 Volts. The y-axis scan range was approximately 200 um over the same voltage range.

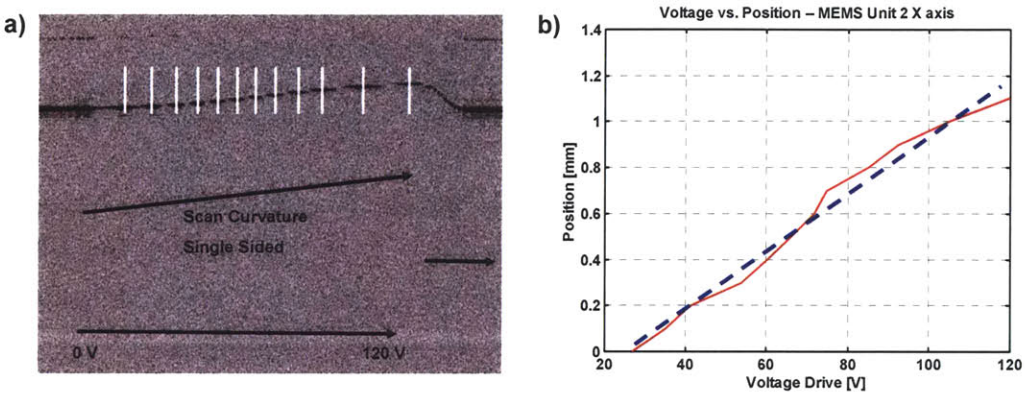

Figure 5-20. Scan linearity of MEMS chip

a) OCT scan across a ruled grating of 10 lines per mm shows an approximate scan range of 925 um. b) Scan transfer characteristic indicates that the MEMS chip scan range is fairly linear of the voltage range from 30-120 Volts.

For initial testing of the MEMS device, imaging scans were performed of human skin *in vivo*. Figure 5-21 shows two scans of the human volar finger pad. Each cross-sectional image was taken from one image of a volume scan set performed by the 2D MEMS scanner. The volume scan was performed by stepping the y-axis of the scanner after each successive transverse scan (which is performed by x-axis). From Figure 5-21a, delineation of the stratum corneum (SC) and epidermis (E) underneath the finger is possible as well as the initial opening to a sweat duct. At a later scan in the volume sweep, the full sweat duct is visualized in Figure 5-21b. Some slight image distortions can be seen at the far right portion of the images due to the decreased scan linearity at the edges of the scan range. To the best of this author's knowledge, this was the first demonstration of multi-plane OCT imaging using a two dimensional scanning MEMS mirror.

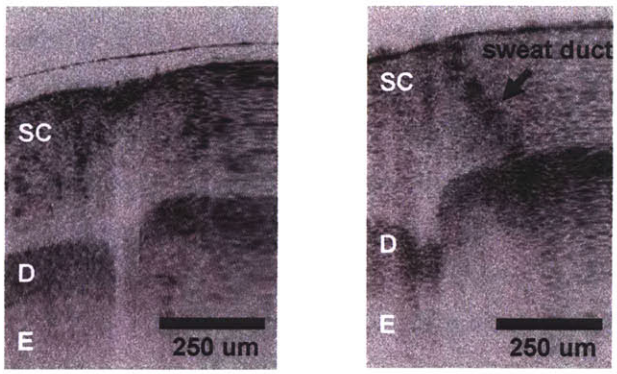

Figure 5-21. Image of human finger volar pad *in vivo*

Two images taken from a 2-dimensional volume scan sequence are able to visualize the tissue structure of the stratum corneum (SC), epidermis (E), and dermis (D) layers in the skin.

Imaging was also done on the animal model of brachydanio rerio zebrafish. This model is of importance in developmental biology and has served as a useful imaging specimen for previous work. Figure 5-22 shows a set of two OCT image scans, again taken from a volume scan sequence, of an embryonic zebrafish. In the first scan the optic primordium (OP), ventral midbrain (VM), and embryonic yolk sac (YS) are visualized in the OCT image. Scanning through the body of the animal, a later scan shows distinct features of the dorsal midbrain (DM).

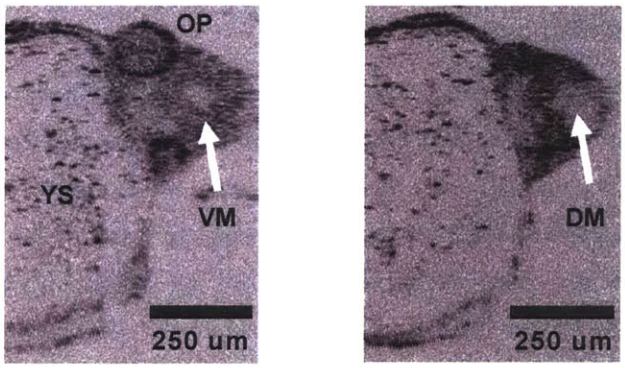

Figure 5-22. OCT images of embryonic zebrafish

Two OCT scans taken from a 3-D volume scan show distinguishing features in the zebrafish midbrain as well as development of the optic primordium.

Using the two-dimensional MEMS scanner, 3-D volumetric reconstruction of OCT data was also demonstrated. Figure 5-23 shows a reconstructed volume image of lime pulp that was imaged by the OCT MEMS scanner. The scan volume measures 1.6mm x 0.92 mm x 0.2 mm and was

imaged with 4um axial resolution and 8um transverse resolution. Discrete boundaries of the lime pulp compartemnts can be seen.

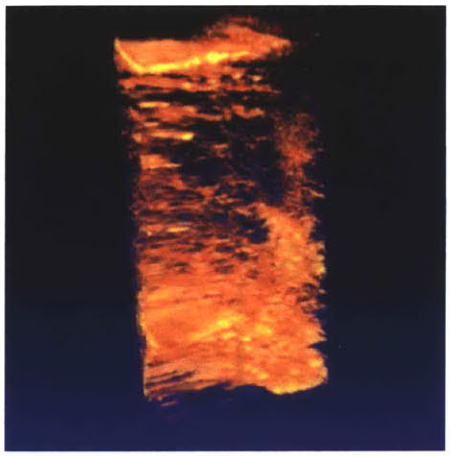

Figure 5-23. Three dimensional volume of lime pulp imaged with MEMS scanner

With the advanced scanning capabilities of these probes demonstrated there exist many opportunities to conduct further experimental investigations into minimally invasive diagnostic imaging for both *ex vivo* and *in vivo* tissue systems.

Ultrahigh Resolution Endoscopic Imaging with Minimally Invasive Catheters

An expansive experiment involving OCT imaging of the GI tract was also performed utilizing an advanced OCT system engineered by LightLabs Corporation. One of the goals of this work was to demonstrate the capability of ultrahigh resolution OCT imaging to visualize tissue architecture in both animal and human models. As most available OCT system and almost all previous OCT endoscopic imaging studies at 1300 nm wavelength have had image resolutions on the order 10-30 um, the implementation of a 4-5 um resolution system would be an important demonstration of the next generation of imaging performance. Imaging was performed in this study in collaboration with Dr. Joseph Schmidt, Dr. Chris Peterson, and Amanda Koski of LightLab Imaging. Individuals assisting with imaging from MIT included Dr. Yu Chen, Aaron Aguirre, and animal specialist Katie Madden of the Division of Comparitive Medicine.

Figure 5-24 shows a schematic of the OCT imaging system. This system used the LightLabs imaging engine hwoever was modified for ultrahigh resolution performance. Light was coupled into a broadband optical circulator and a 90/10 fiber optic coupler, which transmitted 90% of the incident light to the sample. A rapid scanning delay line consisting of a

rotational cam scanner in the reference arm provided real-time imaging at up to 3125 axial scans per second. Imaging was typically performed at a frame rate of 4 Hz which corresponded to a transverse pixel image density of up to 780 axial scans per image. In the experiment, the OCT beam was scanned in both longitudinal and rotational scan protocols to generate cross-sectional images of tissue structure in orthogonal imaging planes. Polarization controllers were used in both the sample and reference arms to optimize signal strength and interference fringe contrast.

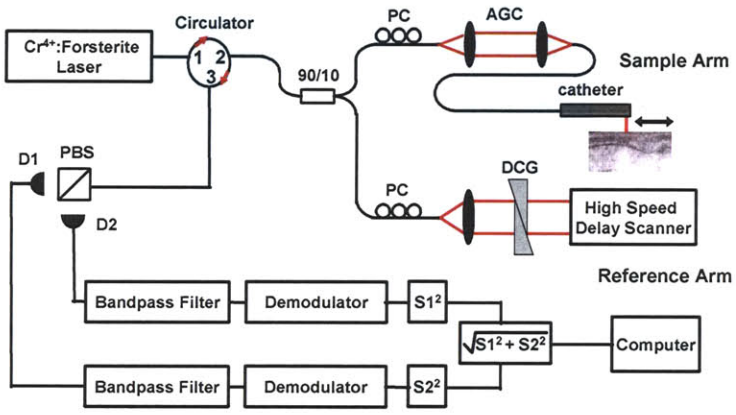

Figure 5-24. Schematic of endoscopic OCT imaging system

To match optical dispersion within the system, SFL6 and LaKN22 dispersion-compensating glass was inserted in the reference arm and an air gap coupling was used in the sample arm. The use of the air coupling allowed precise dispersion compensation and enabled broadband operation for ultrahigh resolution imaging performance. The backcoupled OCT signal was divided into two orthogonal polarization channels by a polarizing beam splitter and the two detector outputs were digitally demodulated using a DSP board. A polarization diversity signal was obtained from the square root of the sum of the squared signal intensities from the two polarization channels.

The compact, broadband Cr^{4+}:Forsterite laser combined with a nonlinear fiber was used to generate a spectral bandwidth greater than 200 nm at a center wavelength of 1250 nm. An output power of 50 mW was coupled into a single-mode fiber. The Cr^{4+}:Forsterite laser is somewhat similar to one previously demonstrated in our laboratory [33, 34], however used broadband double-chirped mirrors [35] to compensate intra-cavity dispersion and achieve a compact, prismless laser design. A compact Yb fiber laser was used as the pump source. Figure 5-25a shows the optical spectrum generated by the Cr^{4+}:Forsterite laser and nonlinear fiber. The bandwidth is 210 nm FWHM. Due to bandwidth limitations in the optical circulator, shorter

wavelengths were attenuated and the transmitted spectrum was reduced to 150 nm bandwidth (also shown).

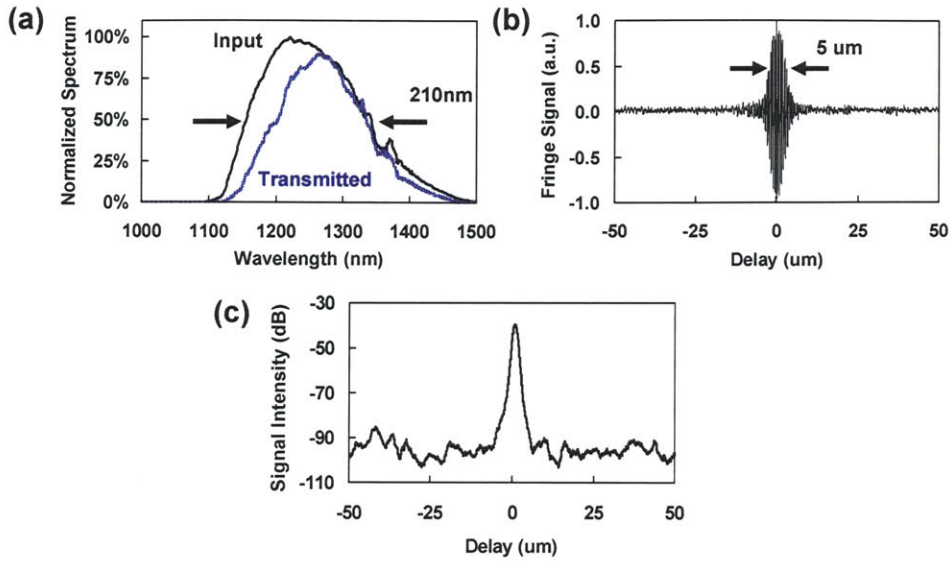

Figure 5-25. System characteristics for high resolution operation

(a) Optical bandwidth of the Cr^{4+}:Forsterite light source at the input to the OCT system and transmitted through to the sample. The modelocked laser has high output power, excellent noise performance and enables a 3-fold improvement in axial image resolution over standard endoscopic OCT systems using a superluminescent diode light source. (b) Measured axial resolution of 5 um in air, corresponding to 3.7 um resolution in tissue. (c) Plot of the logarithmic point spread function shows low sidelobes in the point spread function. The measured sensitivity was 102 dB with 10 mW of incident power on the sample.

The measured axial point spread function shown in Figure 5-25b has a resolution of 5 um in air, close to the calculated theoretical value of 4.6 um for the bandwidth. This corresponds to an axial resolution of 3.7 um in tissue, assuming an index of refraction of ~1.37, and is a three-fold improvement in resolution compared to previous endoscopic OCT systems. It is expected that with improvements in bandwidth of the optical interferometer components, even higher axial resolutions can be achieved. The system detection sensitivity was measured to be 102 dB with 10 mW of power on the sample.

The OCT beam was delivered through a 1.5 mm outer diameter imaging catheter with a focal spot size of 15 um ($2w_o$) and a focal distance of 0.5 mm from the outer wall of the catheter sheath. For linear scan imaging, a push-pull catheter was driven by a magnetic actuator to create a linear cross-sectional imaging plane through the tissue surface. It was possible to adjust the scan length by modifying the input control voltages on the magnetic actuator. The physical

position of the OCT beam was synchronized with both image acquisition software and timing signals to generate the OCT image. Rotational imaging was also performed using a rotary-scanning catheter design. Images were formed by rotating the optical fiber within the catheter sheath to acquire data in an orthogonal imaging plane.

OCT imaging of the upper and lower gastrointestinal tracts, as well as the respiratory tract, of New Zealand White rabbit was performed. All imaging procedures were performed at MIT facilities with protocol approval by the MIT Committee on Animal Care. The rabbits were initially sedated and anesthesia was administered during the procedure via a marginal ear vein. The OCT catheter was manually introduced into the upper gastrointestinal tract (esophagus) through the oral pharynx. Imaging was performed from the esophagus to the proximal stomach, with particular emphasis placed on imaging the distal esophagus and the gastroesophageal junction. In human subjects, these sites are of primary interest for the evaluation of Barrett's esophagus, which occurs near the gastroesophageal junction [36]. Barrett's esophagus is a metaplastic condition associated with chronic gastroesophageal reflux disease and patients with this condition have elevated risk for esophageal adenocarcinoma [37]. If endoscopic OCT could detect dysplastic changes which occur as a precursor to adenocarcinoma, endoscopic guidance of excisional biopsy could be performed, improving sensitivity and reducing sampling errors.

For imaging of the lower gastrointestinal tract, the OCT imaging catheter was introduced through the rectum. To minimize animal discomfort and reduce the risk of damaging the colonic mucosa, a 5.0-French introducer and sterile bacteriostatic lubricant were used during catheter insertion. Imaging was performed from the distal colon to the rectum in both rotational and linear scanning modes. The respiratory tract was also imaged to assess the ability of OCT to delineate tissues inside the pulmonary tract. After disinfection, the catheter was introduced via a midline transverse incision made in the skin and the supportive tissue of the anterior neck, just below the hyoid bone. A puncture in the cricothyroid membrane was made and the OCT catheter was inserted through the orifice. OCT imaging was done while the catheter was advanced through the trachea until the tracheal bifurcation was reached. After *in vivo* endoscopic imaging was complete, the animal was euthanized with sodium pentobarbital administered intravenously. Tissues from the esophagus, colon, and trachea were resected for tissue harvest and histological processing. Before the tissues were prepared for histology, *ex vivo* imaging was performed on selected organ tissues. This was done to provide precise registration of the COT imaging area with histological sectioning. After imaging was complete, tissue samples were placed in 10% buffered formalin and processed with hematoxylin and eosin as well as trichrome staining.

In vivo imaging was conducted using both linear and rotary scanning protocols. Figure 5-26a shows an *in vivo* OCT image of the esophagus taken with the linear scanning catheter. The corresponding histology is shown in Figure 5-26b. The layered structure of the esophagus is delineated clearly, with good definition of the squamous epithelium (e), lamina propria (lp), muscularis mucosa (mm), submucosa (sm), inner (im) and outer muscular (om) layers.

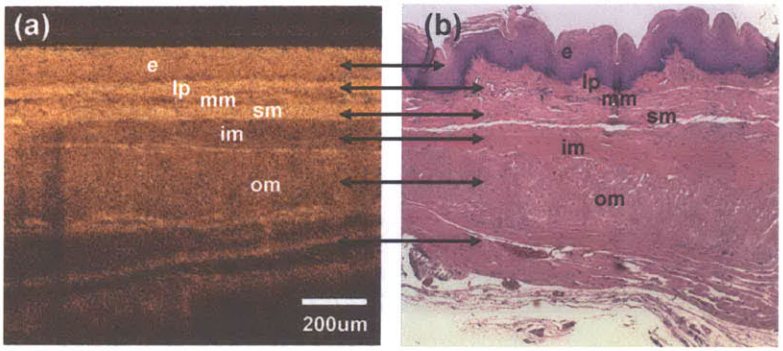

Figure 5-26. *In* vivo OCT image of rabbit esophagus with corresponding histology
Good correlation is seen between OCT and histology. The epithelium (e), lamina propria (lp), muscularis mucosa (mm), submucosa (sm), inner (im) and outer muscular (om) layers are visible on both the OCT image and histology.

The OCT image correlates well with the histology in both the order of layers and the layer thickness. This result is in agreement with previous OCT imaging studies of the esophagus in the rabbit [21]. Changes in the orientation of muscular fiber bundles in the inner and outer muscular layers correlated with different scattering patterns in the corresponding layers seen in the OCT image. Epithelial folds evident in the histology resulted from artifacts introduced by the preparation and staining process. The esophagus contracts when excised thereby producing a roughened appearance of the epithelium. Since the linear catheter was placed in contact with the esophageal surface to allow for high image contrast, the epithelial layer in the OCT images appears smooth.

Figure 5-27a shows an *in vivo* OCT image of the esophagus and trachea. The tracheal hyaline cartilage (hc) is visible through the esophageal wall, demonstrating the ability of the endoscopic OCT system to image deeply within the tissue. In addition, the structural details of the tracheal mucosa and trachealis muscle are visible. The vacuous region below the tracheal wall located at the bottom of the image is the tracheal airway. The corresponding histology section in Figure 5-27b shows very good correlation with the architecture seen in the OCT image. Trichrome staining was used in the histological section to enhance delineation of cartilage rings in the trachea.

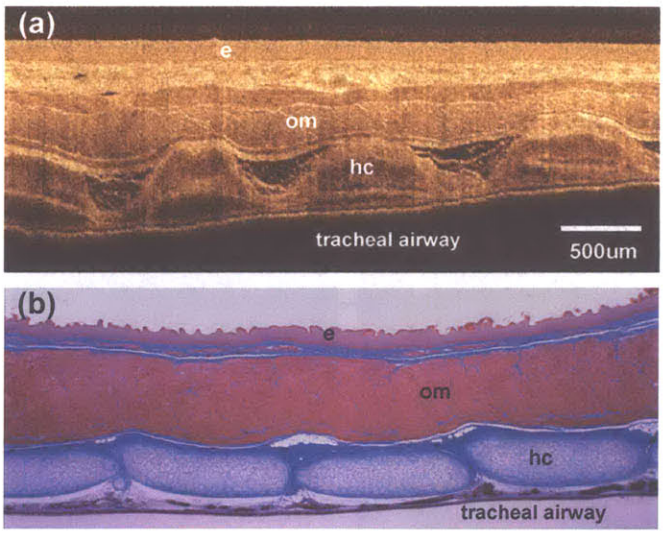

Figure 5-27. *In* vivo OCT image and histology of rabbit esophagus and trachea

Image is viewed intraluminally from the esophagus. Tracheal hyaline cartilage (hc) between the tracheal mucosa and trachealis muscle is well defined. The image demonstrates the ability of the endoscopic OCT system to image deeply within the tissue. Trichrome stain was used to highlight cartilage and muscle layers.

With the high speed of the OCT system used for this study, it was possible to image large regions within the gastrointestinal tract while maintaining high axial and transverse image resolutions. Figure 5-28 shows a composite image of five OCT linear scans acquired sequentially as the catheter was withdrawn during imaging. Images were acquired over a 12 mm scanning range from the epiglottis to the inner esophagus. This image illustrates the capability to visualize continuous morphology over a large field of view at ultrahigh resolution, a method that permits suspect regions to be rapidly surveyed.

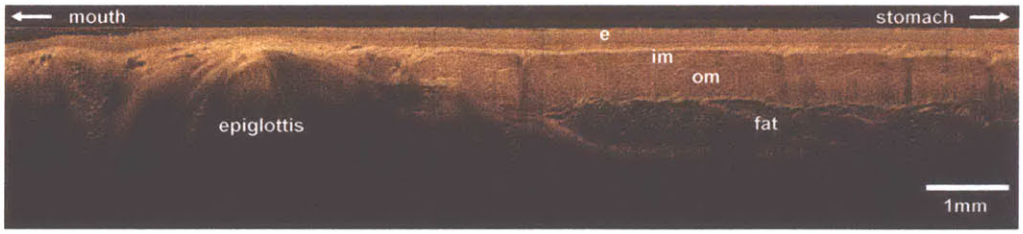

Figure 5-28. *In* vivo image showing sequential OCT scans spanning the rabbit epiglottis and esophagus

Ultrahigh-resolution imaging capability is maintained over a large field allowing detailed discrimination of tissue structure. Architectural morphology of the proximal esophagus is well defined, as is the transition from the mouth to the esophagus at the epiglottis.

Figure 5-29a shows a large field OCT image of rabbit esophagus, gastroesophageal (GE) junction, and gastric mucosa (stomach) acquired *in vivo*. The transition region between the esophagus and stomach can be clearly visualized. This region is important in humans because it is the site of metaplastic changes associated with Barrett's esophagus. Architectural changes from the laminar esophageal mucosa to the gastric mucosa are well differentiated with good correlation to the histological cross-section shown in Figure 5-29b. Reduced penetration was observed within the stomach due to high scattering of the gastric mucosa and is consistent with observations in previous OCT studies in animals and humans [29, 38].

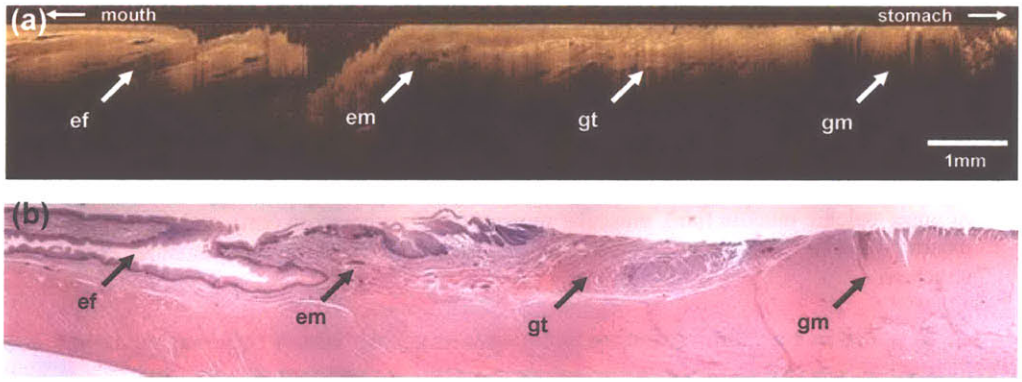

Figure 5-29. Large field scan of rabbit esophagus *in vivo*

The OCT image shows the transition region from the esophagus to the proximal stomach. There is excellent differentiation of esophageal versus gastric mucosa. Visible structures include epithelial folds (ef), esophageal mucosa (em), gastric transition (gt), and gastric mucosa (gm). (b) Corresponding histological cross section stained with hematoxylin and eosin.

In Figure 5-30 an *in vivo* OCT image and corresponding histology of the rabbit colon are shown. The OCT image shows a highly scattering and multi-structured layer at the surface that correlates with the upper colonic mucosa. Individual crypts of Lieberkuhn can be seen in the OCT image and correlate well with the histological cross-section. Increased detail of crypts and features within the colon are visualized in the 2x magnification images on the right of Figure 5-30. Crypt boundaries within the lamina exhibit high scattering intensity in the OCT image, thereby increasing the contrast between individual crypts. This allows the colonic crypt structure to be visualized clearly. The capability to resolve crypt features within the colon is important in the clinical diagnosis of conditions such as inflammatory bowel disease and colon cancer. The submucosa appears as a highly scattering layer that separates the muscularis mucosa from the muscularis externa. Sets of cylindrical fiber bundles, which are oriented transverse to the OCT catheter beam, are also visible within the OCT image (arrows).

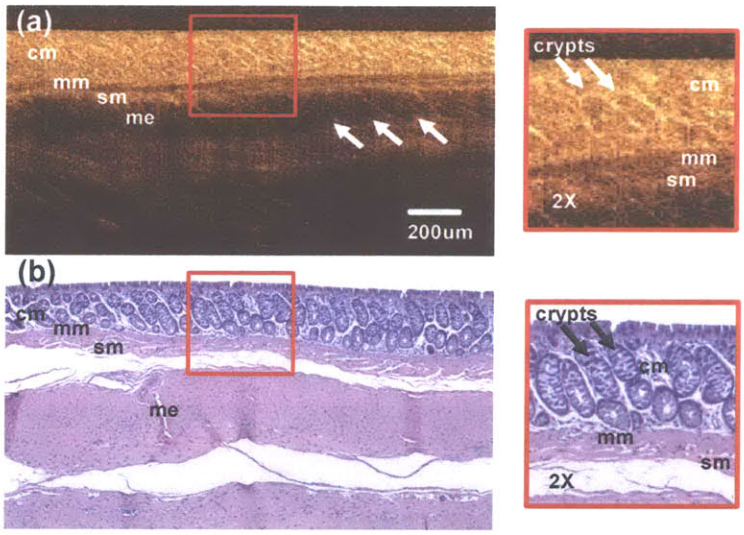

Figure 5-30. In vivo OCT image and corresponding histology of rabbit colon

(a) Endoscopic OCT image of rabbit colon with (b) corresponding histology. Delineation of upper colonic mucosa (cm), muscular mucosa (mm), submucosa (sm), and muscularis externa (me) is possible. Enlarged images show the capability to visualize crypt structure.

In addition to lateral scanning, rotational scanning within the esophagus and colon was also performed. Figure 5-31 shows cross-sectional images of the rabbit esophagus and stomach generated by rotational scanning at 4 frames per second. The lamina layers are well defined in the esophagus and the epithelial, mucosal, and submucosal regions can be readily distinguished. The rotational image in the stomach of the rabbit (Figure 5-31b) shows the characteristic, highly scattering behavior of gastric mucosa as seen in the longitudinal images.

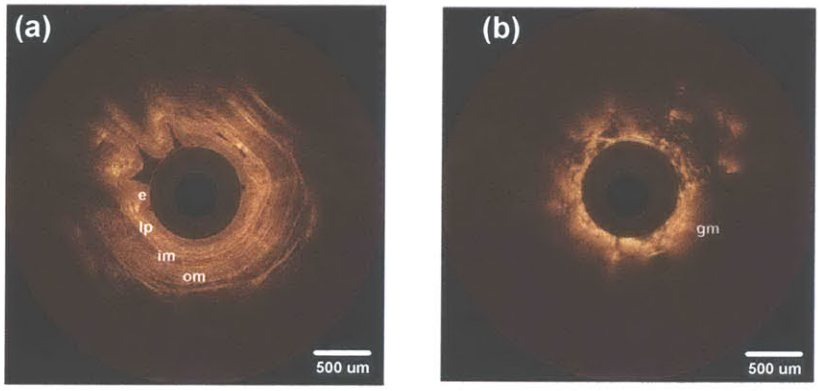

Figure 5-31. Rotational OCT images of rabbit esophagus and stomach

(a) Rotational scanning images of rabbit esophagus and (b) proximal stomach *in vivo*. The esophageal lamina structure is well distinguished. Epithelium (e), lamina propria (lp), inner muscularis (im), and outer (om) muscularis layers can be seen. Increased scattering with reduced image penetration is observed in the stomach which is indicative of gastric mucosa architecture (gm).

Figure 5-32 illustrates a pullback imaging technique that is useful for surveying luminal structures. To generate this image, the optical fiber was pulled back within the catheter sheath at a constant rate of 0.5 mm/sec while imaging in a rotational scan mode at 4 rotations per second. Maintaining the external catheter sheath stationary during the pullback scan minimized any motion artifacts or image distortions that would have been caused by movement of the outer sheath surface sheath relative to the colonic wall.

Figure 5-32 shows one rotational scan in the pullback sequence. The location of this scan is indicated by the solid line in the full pullback cross section (Figure 5-32b). The full cross-sectional image of the colon over a 35 mm scan range was acquired in 70 seconds. The orientation of the cross-sectional imaging plane is seen on the rotational scan image (Figure 5-32a) as the dashed line in the figure. The rotational and cross-sectional pullback images allow simultaneous views of the colon from two aspects. The longitudinal scan format can be valuable in cases where the extent and dimensions of atypical tissue structures must be identified. With the ultrahigh resolution capability of the system, delineation of the colonic mucosa and muscularis was possible.

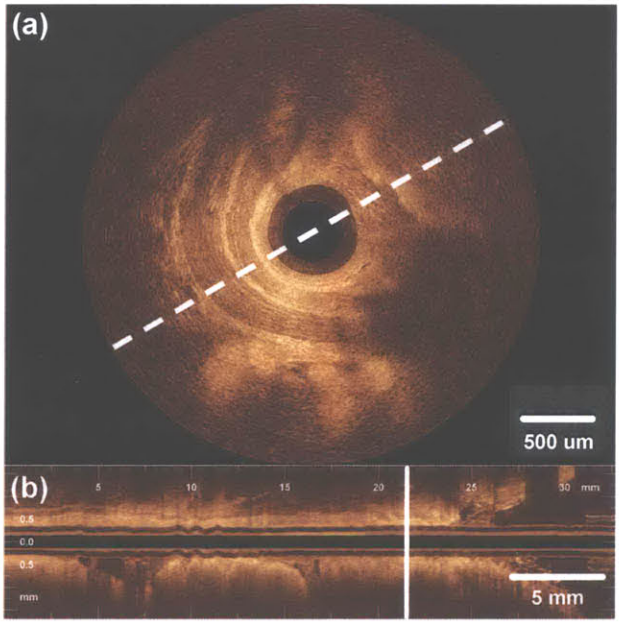

Figure 5-32. Pullback imaging of the rabbit colon

(a) Rotational scan and (b) longitudinal pullback cross-section of rabbit colon *in vivo*. Architectural detail is distinguished over the large scan field seen in lower image. The location of the rotational image (a) in the pullback sequence is indicated by the solid line in (b).

Pullback imaging of the esophagus was also performed with similar performance. The full rotational scan data sets acquired from both the colon and esophagus provided sufficient information for reconstruction of three-dimensional images of the gastrointestinal tract. At this imaging speed, the separation of the successive image planes and corresponding pixel spacing is 125 um in the pullback direction. At increased imaging speeds, higher pixel density three-dimensional image reconstruction is possible.

After *in vivo* imaging was completed, tissue biopsy samples were taken from selected organ systems after animal euthanasia. These specimens were imaged under the OCT microscope configuration described previously in Chapter 3. During imaging, the precise location of the OCT scan beam on the tissue was marked with India dye inks to register cross-sectional cutting planes for histological processing. By pursuing this methdology precise co-alignment of both the OCT scan plane and tissue histology should be possible providing close correlation of the tissue architecture provided that the OCT system resolution is high enough.

Figure 5-33 shows an *ex vivo* OCT image and corresponding histology of the rabbit GE junction. The distinction between the uniform squamous epithelium (se) in the esophagus and the columnar epithelium (ce) of the gastric mucosa can be seen by differences both in scattering intensity and depth of light penetration. In the enlarged regions to the right, the Z-line transition between the esophagus and stomach corrleates well between the OCT and histology.

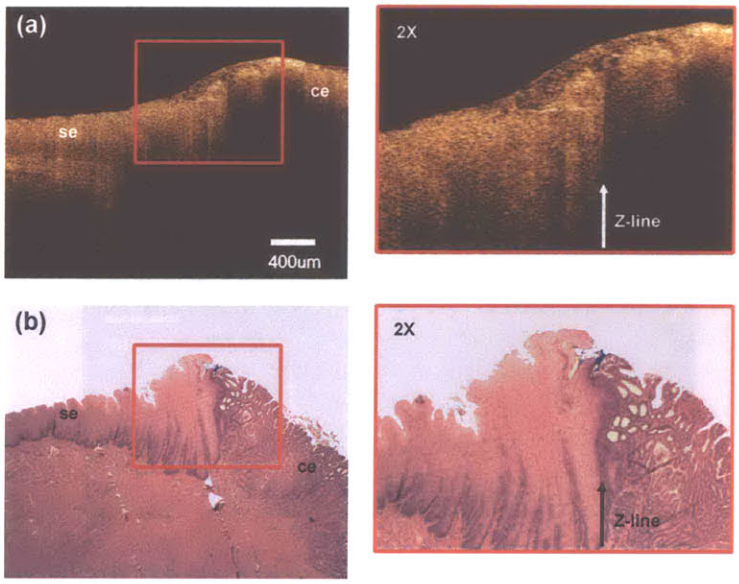

Figure 5-33. *Ex vivo* OCT image of rabbit gastrointestinal junction and histology

Stratified squamous epithelium with the esophagus exhibits high scattering intensity while the columnar epithelium (ce) of the gastric mucosa has reduced image penetration. Visualization of the Z-line interface between the esophagus and stomach is well delineated in the OCT image.

Another region imaged *ex vivo* was the small intestine of the rabbit. As this organ was difficult to access endoscopically, imaging of biopsy tissue provided a good opportunity to access the capability of the high resolution OCT system to visualize important architecture in the small intestine. Figure 5-34 shows an OCT image and corresponding histology of the rabbit small intestine. Very good correlation was seen to visualize intestinal villi and small glandular structures below the villous layer. This results is encouraging as it may be possible to distinguish pathological changes in the small intestine for future high resolution imaging studies.

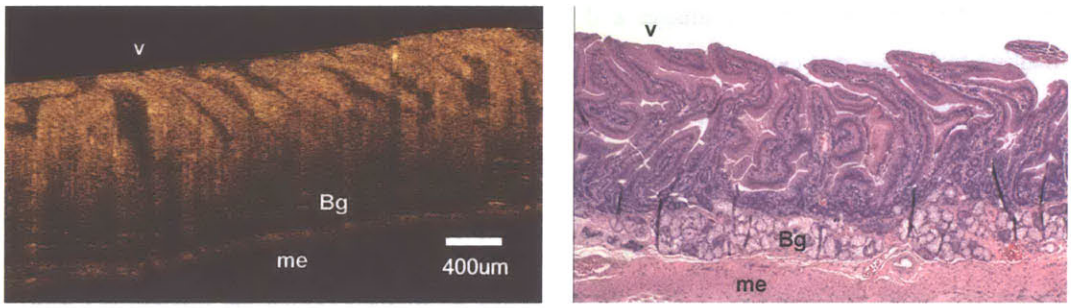

Figure 5-34. *Ex vivo* OCT image of rabbit small intestine with histology
Intestinal villi (v) can be distinguished in the OCT image with low scattering observed for Brunner's glands (Bg) and muscularis externa (me).

In recent years there has been a substantial increase in the number of endoscopic procedures aimed at the early detection and diagnosis of gastrointestinal diseases. While video endoscopy is the most established clinical technique, its diagnostic utility is limited by its inability to image below the tissue surface. Although endoscopic ultrasound allows sub-surface imaging within the GI tract, its resolution is limited to features with dimensions larger than 100 um. OCT is emerging as a new and powerful technique in endoscopic imaging that can image at resolutions 10-20 times greater than conventional ultrasound or MRI and has the potential to detect changes in tissue structure associated with disease pathogenesis. Clinical studies have been performed in humans on both the upper and lower gastrointestinal tracts and indicate that OCT can differentiate normal from diseased tissue states, such as specialized intestinal metaplasia in Barrett's esophagus and adenocarcinoma.

While standard resolution OCT systems have demonstrated the ability to visualize architectural changes associated with Barrett's esophagus, ultrahigh-resolution OCT could significantly increase the ability to visualize morphological changes characteristic of dysplasia. In particular, the ability to visualize high grade dysplasia would enable endoscopic OCT to be used to guide excisional biopsy, thereby reducing sampling errors and improving sensitivity.

To obtain ultrahigh-resolution OCT images, axial resolution can be increased through the use of broadband optical light sources. Standard OCT systems and most previous studies

have used superluminescent diodes. The optical bandwidths of these superluminescent diodes are typically 30-60 nm at a central wavelength of 1300 nm, which corresponds to 10-20 um axial resolution in tissue. In this experiment, the broadband high-power Cr^{4+}:Forsterite laser developed in our laboratory was used to image at ultrahigh resolution. The delivered optical bandwidth of the laser on the sample was 150 nm, which resulted in a 5 um axial resolution measured in air corresponding to a resolution of 3.7 um in tissue. The higher resolution achieved with this system provided enhanced visualization of tissue morphology. In addition, the excellent correspondence between the OCT images and histopathology suggests the capability of OCT as an imaging technique that can perform optical biopsy *in situ* and in real time. The results from this animal model demonstrate the potential of ultrahigh-resolution endoscopic OCT imaging of gastrointestinal pathologies. Improvement of imaging resolution in OCT may enhance the capability to detect early neoplastic changes in gastrointestinal tissue.

The OCT scan format also has an important influence on image quality. For luminal structures, the most common format used for OCT is a radial scan formed by rotating the fiber optic catheter along its central axis. A benefit of this scan format is that the OCT catheter can be pulled back during the rotational motion to obtain a scan over a large tissue volume. By using rotational scanning with catheter pull-back in this study, it was possible to obtain a spiral OCT scan over a large tissue volume. This is a powerful technique to identify regions of interest within a gastrointestinal lumen for subsequent diagnosis or identification of biopsy sites. It is also possible to use this scanning method to form three-dimensional images of the lumen by volume reconstruction methods.

In the linear-scanning mode, the catheter was moved in a push-pull manner to create a line scan along a section of the lumen. With linear scanning, the cross-sectional image can have a higher pixel density and better transverse image resolution than radial scanning. This is because in a radial scan format pixel density is decreased at more distant radial positions in the scan. A linear scanning method does not suffer from this effect however it usually requires a more complex scanning mechanism for actuation and is more prone to non-uniform motion. In this study, a magnetic voice coil actuator was used to achieve precise linear actuation over the OCT scan range. It is also challenging to orient the radial direction of the optical beam while the catheter is scanning in a linear mode. Design modifications were implemented in the catheter construction and mounting configuration to allow the operator to simultaneously rotate the catheter orientation while scanning in a linear mode.

In this experiment ultrahigh-resolution OCT images were obtained of the rabbit esophagus, trachea, and colon with minimally invasive catheter devices. Using a broadband

Cr^{4+}:Forsterite laser endoscopic OCT imaging *in vivo* was demonstrated, to the best of our knowledge, at the highest resolutions attained to date. A linear scanning protocol was used to generate high pixel density images at a real-time imaging rate of 4 frames per second. Histological cross sections were obtained from *in vivo* imaging sites and excellent correspondence of architectural detail was seen between histopathology and OCT scans. Identification of clinically relevant tissue morphology was possible at ultrahigh resolution in agreement with histological findings. By imaging in real time it was possible to construct large-field, ultrahigh-resolution OCT images from consecutive lateral scans. High image penetration in tissue was realized and enabled imaging through the complete esophagus and tracheal walls in the rabbit. Visualization of individual colonic crypts was also achieved at ultrahigh resolution. These results demonstrate the feasibility of using ultrahigh-resolution endoscopic OCT to identify architectural features within the gastrointestinal tract. Ongoing advances in the development of turn-key and commercial broadband optical light sources promise to give investigators wider access to ultrahigh-resolution OCT imaging capability. To assess the performance of ultrahigh-resolution endoscopic OCT in human subjects, results from clinical trial studies will be presented in the following chapter.

References

1. A. Wluka, S. Stuckey, J. Snaddon, and F. Cicuttini, "*The determinants of change in tibial cartilage volume in osteoarthritic knees.,*" Arthritis Rhuem, **46**, 2065-72 (2002).
2. A. Brook and M. Corbett, "*Radiographic changes in early rheumatoid disease.,*" Ann Rheum Dis, **36**, 71-73 (1977).
3. I. Kobayashi and M. Ziff, "*Electron microscopic studies of the cartilage-pannus junction in rheumatoid arthritis.,*" Arthritis Rheum, **18**, 475-583 (1975).
4. M. C. Hochenberg, "*Quantitative radiography in osteoarthritis: analysis,*" Clin Rheumatol, **10**, 421-428 (1996).
5. M. LaValley, T. McAlindon, C. Chaisson, D. Levy, and D. Felson, "*The validity of different definitions of radiographic worsening for longitudinal studies of knee osteoarthritis,*" J Clin Epidemiol, **54**, 30-39 (2001).
6. J. P. Raynauld, "*Magnetic resonance imaging of articular cartilage: toward a redefinition of "primary" knee osteoarthritis and its progression,*" J Rheum, **29**, 1809-1810 (2002).
7. J. Adams, T. McAlindon, M. Dimassi, J. Carey, and S. Eustace, "*Contribution of meniscal extrusion and cartilage loss to joint space narrowing in osteoarthritis,*" Clin Radiol, **54**, 502-509 (1999).
8. F. Cicuttinni, A. Wiluka, and S. Stuckey, "*Tibial and femoral changes in knee osteoarthritis,*" Am Rheum Dis, **60**, 977-980 (2001).
9. D. Loeuille, P. Gonord, C. Guingamp, P. Gillet, A. Blum, M. Sauzade, and P. Netter, "*In vitro magnetic resonance microimaging of experimental osteoarthritis in the rat knee joint,*" J Rheumatol, **24**, 133-139 (1997).
10. T. Carpenter, J. Everett, L. Hall, G. Harper, R. Hodgson, M. James, and P. Watson, "*High-resolution magnetic resonance imaging of arthritic pathology in the rat knee,*" Skeletal Radiol, **23**, 429-437 (1999).
11. J. Tyler, R. Watson, and K. Hwee-Ling, "*Detection and monitoring of progressive degeneration of osteoarthritic cartilage by MRI.,*" Acta Orthop Scand, **66**, 130-138 (1995).
12. H. Nieminen, J. Toyras, J. Rieppo, M. Nieminen, J. Hirvonen, R. Korhonen, and J. Jurvelin, "*Real-time ultrasound analysis of articular cartilage degradation in vitro,*" Ultrasound Med Biol, **28**, 519-525 (2002).
13. S. Myers, K. Dines, D. Brandt, K. Brandt, and M. Albrecht, "*Experimental assessment by high frequency ultrasound of articular cartilage thickness and osteoarthritic changes,*" J Rheumatol, **22**, 109-116 (1995).
14. J. M. Herrmann, C. Pitris, B. E. Bouma, S. A. Boppart, J. G. Fujimoto, and M. E. Brezinski, "*High resolution imaging of normal and osteoartheritic cartilage with optical coherence tomography,*" Journal of Rheumatology, **26**, 627-635 (1999).
15. P. R. Herz, S. Martin, P. Hsiung, X.D. Li, A.D. Aguirre, N. Patel, K. Saunders, D. Stamper, T.H. Ko, J.G. Fujimoto and M. Brezinski, "*High Resolution in vivo Imaging of Osteoarthritic Cartilage,*" OSA Biomedical Meeting, **MD6(1)**, 331-333 (2002).
16. W. Drexler, D. Stamper, C. Jesser, X. Li, C. Pitris, K. Saunders, S. Martin, M. B. Lodge, J. G. Fujimoto, and M. E. Brezinski, "*Correlation of collagen organization with polarization sensitive imaging of in vitro cartilage: implications for osteoarthritis,*" The Journal of rheumatology, **28**, 1311-8 (2001).
17. D. Kalbhen, *Proteoglycan synthesis and cartilage protection in the hen model of osteoarthritis.*, in *Diclofenac (Voltaren) and Cartilage in Osteoarthritis*, K. Hirohata, Editor. 2001, Hogrefe & Huber: New York. p. 22-30.
18. J. Williams and E.-M. Thonar, "*Early osteophyte formation after chemically induced articular cartilage injury,*" Am J Sports Med, **17**, 7-15 (1989).
19. J. Dunham, S. Hoedt-Schmidt, and D. Kalbhen, "*Structural and metabolic changes in articular cartilage induced by iodoacetate,*" Int J Exp Path, **73**, 455-464 (1992).
20. G. J. Tearney, S. A. Boppart, B. E. Bouma, M. E. Brezinski, N. J. Weissman, J. F. Southern, and J. G. Fujimoto, "*Scanning single-mode fiber optic catheter-endoscope for optical coherence tomography,*" Optics Letters, **21**, 543-5 (1996).

21. G. J. Tearney, M. E. Brezinski, B. E. Bouma, S. A. Boppart, C. Pitvis, J. F. Southern, and J. G. Fujimoto, "*In vivo endoscopic optical biopsy with optical coherence tomography,*" Science, **276**, 2037-9 (1997).
22. A. M. Sergeev, V. M. Gelikonov, G. V. Gelikonov, F. I. Feldchtein, R. V. Kuranov, N. D. Gladkova, N. M. Shakhova, L. B. Suopova, A. V. Shakhov, I. A. Kuznetzova, A. N. Denisenko, V. V. Pochinko, Y. P. Chumakov, and O. S. Streltzova, "*In vivo endoscopic OCT imaging of precancer and cancer states of human mucosa,*" Optics Express, **1** (1997).
23. F. I. Feldchtein, G. V. Gelikonov, V. M. Gelikonov, R. V. Kuranov, A. Sergeev, N. D. Gladkova, A. V. Shakhov, N. M. Shakova, L. B. Snopova, A. B. Terent'eva, E. V. Zagainova, Y. P. Chumakov, and I. A. Kuznetzova, "*Endoscopic applications of optical coherence tomography,*" Optics Express, **3**, 257 (1998).
24. A. M. Rollins, R. Ung-arunyawee, A. Chak, R. C. K. Wong, K. Kobayashi, M. V. Sivak, Jr., and J. A. Izatt, "*Real-time in vivo imaging of human gastrointestinal ultrastructure by use of endoscopic optical coherence tomography with a novel efficient interferometer design,*" Optics Letters, **24**, 1358-60 (1999).
25. B. E. Bouma and G. J. Tearney, "*Power-efficient nonreciprocal interferometer and linear-scanning fiber-optic catheter for optical coherence tomography,*" Optics Letters, **24**, 531-3 (1999).
26. S. Jäckle, N. Gladkova, F. Feldchtein, A. Terentieva, B. Brand, G. Gelikonov, V. Gelikonov, A. Sergeev, A. Fritscher-Ravens, J. Freund, U. Seitz, S. Schröder, and N. Soehendra, "*In vivo endoscopic optical coherence tomography of esophagitis, Barrett's esophagus, and adenocarcinoma of the esophagus,*" Endoscopy, **32**, 750-5 (2000).
27. M. V. Sivak, Jr., K. Kobayashi, J. A. Izatt, A. M. Rollins, R. Ung-Runyawee, A. Chak, R. C. Wong, G. A. Isenberg, and J. Willis, "*High-resolution endoscopic imaging of the GI tract using optical coherence tomography,*" Gastrointestinal endoscopy, **51(4) Pt 1**, 474-9 (2000).
28. X. D. Li, S. A. Boppart, J. Van Dam, H. Mashimo, M. Mutinga, W. Drexler, M. Klein, C. Pitris, M. L. Krinsky, M. E. Brezinski, and J. G. Fujimoto, "*Optical coherence tomography: advanced technology for the endoscopic imaging of Barrett's esophagus,*" Endoscopy, **32**, 921-30 (2000).
29. B. E. Bouma, G. J. Tearney, C. C. Compton, and N. S. Nishioka, "*High-resolution imaging of the human esophagus and stomach in vivo using optical coherence tomography,*" Gastrointestinal endoscopy, **51(4) Pt 1**, 467-74 (2000).
30. Y. Pan, H. Xie, and G. K. Fedder, "*Endoscopic optical coherence tomography based on a microelectromechanical mirror,*" Optics Letters, **26**, 1966-8 (2001).
31. J. M. Zara, S. Yazdanfar, K. D. Rao, J. A. Izatt, and S. W. Smith, "*Electrostatic micromachine scanning mirror for optical coherence tomography,*" Optics letters, **28**, 628-30 (2003).
32. W. Drexler, U. Morgner, F. X. Kartner, C. Pitris, S. A. Boppart, X. D. Li, E. P. Ippen, and J. G. Fujimoto, "*In vivo ultrahigh-resolution optical coherence tomography,*" Optics Letters, **24**, 1221-3 (1999).
33. B. E. Bouma, G. J. Tearney, I. P. Bilinsky, and B. Golubovic, "*Self phase modulated Kerr-lens mode locked Cr:forsterite laser source for optical coherence tomography,*" Optics Letters, **21**, 1839-1841 (1996).
34. C. Chudoba, J. G. Fujimoto, E. P. Ippen, H. A. Haus, U. Morgner, F. X. Kärtner, V. Scheuer, G. Angelow, and T. Tschudi, "*All-solid-state Cr:forsterite laser generating 14 fs pulses at 1.3 μm,*" Optics Letters, **26**, 292-294 (2001).
35. F. X. Kartner, N. Matuschek, T. Schibli, U. Keller, H. A. Haus, C. Heine, R. Morf, V. Scheuer, M. Tilsch, and T. Tschudi, "*Design and fabrication of double-chirped mirrors,*" Optics Letters, **22**, 831-833 (1997).
36. M. Conio, G. Lapertosa, S. Blanchi, and R. Filiberti, "*Barrett's esophagus: an update,*" Critical Reviews in Oncology Hematology, **46**, 187-206 (2003).
37. S. Haag and G. Holtmann, "*Reflux disease and Barrett's esophagus,*" Endoscopy, **35**, 112-7 (2003).
38. M. V. Sivak, Jr., K. Kobayashi, J. A. Izatt, A. M. Rollins, R. Ung-Runyawee, A. Chak, R. C. Wong, G. A. Isenberg, and J. Willis, "*High-resolution endoscopic imaging of the GI tract using optical coherence tomography,*" Gastrointest Endosc, **51**, 474-9 (2000).

Chapter 6 – Clinical Imaging in Humans

Imaging of Barrett's Esophagus and Esophageal Adenocarcinoma

The use of ultrahigh resolution endoscopic OCT for imaging in human patients *in vivo* was pursued as a clinical implementation of the advanced OCT systems built and developed in this work. The system development involved finding solutions to both technological and logistical issues in transitioning ultrahigh resolution OCT imaging from a laboratory setting to the clinical environment. OCT catheters, detection electronics, hardware, and software components were optimized and integrated for clinical use and demonstration of ultrahigh resolution endoscopic OCT imaging in humans was achieved. Optimal imaging parameters such as speed, scan field, pixel density, image resolution, scanning protocol, and actuation method were investigated to image esophageal microstructure *in vivo*. This work was done in collaboration with LightLabs Imaging for OCT system development as well as the VA Boston Healthcare System (VABHS) for access to patients undergoing endoscopy procedures. Collaborators from our group who assisted in system development and imaging runs at the VABHS were Dr. Yu Chen and graduate student Pei-lin Hsiung. The results from this work demonstrate that OCT is capable to distinguish normal and Barrett's esophagus at resolutions not previously possible. In addition the ability to identify structural changes in tissue architecture indicative of dysplasia and adenocarcinoma is demonstrated providing evidence that OCT may be a powerful imaging modality in the screening and surveillance of Barrett's esophagus, early detection of esophageal cancer, and localization of suspect lesions for the screening and guidance of excisional biopsy.

Clinical Relevance

The identification of early changes in pre-malignant tissue before full progression to cancer remains a critical objective in clinical cancer diagnosis and treatment since, once the tissue becomes metaplastic, patient survival rate decreased significantly. Biopsy and histopathology are the current gold standards for the diagnosis of dysplasia or carcinoma however can suffer from sampling errors and are cumbersome for screening and surveillance applications. A technology such as OCT which is capable of performing optical biopsy (imaging at a resolution comparable to histopathology without the need for tissue removal) could significantly improve the ability of clinicians to identify and treat malignancies at an early stage of disease progression. Large areas could be screened in real time at high resolution and relatively low cost. High resolution imaging of architectural morphology may allow the *in situ*

assessment of early neoplastic changes such as dysplasia. If successful, this technology could be coupled with excisional biopsy to reduce sampling errors and false negative rates. In this work the feasibility of optical biopsy with ultrahigh resolution OCT was investigated for the identification of the detection and diagnosis of disease states in the gastrointestinal tract. The experiments conducted in this study emphasize the clinical implementation of a diagnostic technology where current methods of excisional screening have limitations. This is particularly important for the early diagnosis of neoplastic changes in a pre-malignant condition in gastrointestinal endoscopy known as Barrett's esophagus which can lead to esophageal cancer.

Epidemiology of Barrett's Esophagus and Esophageal Cancer

Esophageal cancer is among the most lethal of all cancers. The five-year survival rate for esophageal cancer is less than 15% and in 2003 over 13,000 new esophageal cancer cases are expected in the United States alone [1]. In addition, once diagnosed, the cost of patient care is high [2]. Adenocarcinoma accounts for greater than 50% of these esophageal cancers and the incidence of esophageal adenocarcinoma in white males has increased by 21% per year in the United States, a rate greater than that for any other cancer in that group [3]. Other industrialized countries have shown similar trends and incidence rates have also been on the rise for black males and white females.

Gastroesophageal reflux disease (GERD) is one of the most common gastrointestinal disorders, affecting up to one third of the adult population [4]. The duration of GERD symptoms and presence of erosive esophagitis have been shown to be consistent risk factors for Barrett's esophagus. Barrett's in turn, is a precursor lesion that has been correlated with increased risk of esophageal cancer. The prevalence of Barrett's was reported to be 10% to 15% in 97 patients with chronic reflux symptoms that had endoscopy and biopsy performed [5]. Within this group, those with erosive esophagitis had a prevalence of Barrett's of 35%. In patients with esophagitis, the likelihood of Barrett's was 2- to 3-fold higher than in patients without esophagitis, with both the duration of GERD and age of onset associated with the prevalence of Barrett's [6]. Patients with duration of GERD symptoms between 1 and 5 years had a 3-fold increase in odds for Barrett's [7]. These and other data derived from the medical literature over the last few decades formed the basis for recommendations to screen for Barrett's in patients with chronic GERD symptoms (i.e. greater than 5 years duration) [8].

Barrett's esophagus has a well-established association with esophageal adenocarcinoma [4] and is an acquired condition resulting from severe esophageal mucosal injury. It is a condition where the normal squamous epithelium of the distal esophagus is replaced by columnar

epithelium typically observed in the gastric, or stomach, region [9, 10]. It is believed that this change is the result of chronic regurgitation (gastroesophageal reflux or GERD) of the stomach contents up into the esophagus. The contents of the stomach contain digestive acid and other chemicals which damage the normal lining of the esophagus. Once the metaplastic cells have replaced the normal ones, the patient frequently feels less discomfort since the metaplastic areas seem to be less sensitive than the normal tissue. Unfortunately, patients with intestinal metaplasia are at increased risk of developing cancer of the esophagus over those without it, so being symptom-free does not equate with being disease free [11]. This is why the detection of Barrett's and identification of possible metaplastic changes is significant and being pursued in this work.

The prevalence of Barrett's within the US population is between 0.3% and 2% [12] and among patients undergoing endoscopy for symptoms of GERD, the prevalence is as high as 6-12% [13, 14]. The prevalence of Barrett's also increases significantly in the later decades of life with the majority of cases occurring in patients between the ages of 40-80 years of age (see Figure 6-1).

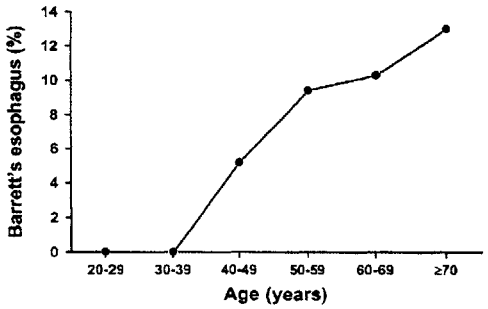

Figure 6-1. Prevalence of Barrett's esophagus in different age groups
Data from 200 subjects show a progressively increasing occurance of Barrett's esophagus after age 40. Frequency in males was twice as high as in females. From reference [15].

Barrett's esophagus can be classified according to the length of columnar epithelium as either short-segment Barrett's (< 3 cm, SSBE) or long-segment Barrett's esophagus (≥ 3 cm, LSBE) [9]. Neoplastic changes in Barrett's esophagus develop through stages from non-dysplastic metaplasia, often termed specialized intestinal metaplasia or SIM [16], to increasing grades of dysplasia (low and high grade) and eventually adenocarcinoma [9]. Several studies have linked the presence of intestinal metaplasia as a symptomatic indicator of future progression to dysplasia [16, 17]. Detection of short-segment Barrett's esophagus is more challenging due to the difficulties in distinguishing SSBE from the displaced gastroesophageal junction [18]. Thus a high resolution imaging technique such as OCT could prove valuable in detecting the location and extent of short segment Barrett's as well as identifying localized regions of metaplasia.

Over time or with repeated mucosal injury, the intestinal metaplasia associated with Barrett's esophagus can progress to low-grade, then high-grade dysplasia. If left untreated there exists a high probability that high grade dysplasia will progress to adenocarcinoma which is usually fatal for the patient. Dysplasia is characterized by cytologic and architectural disarray in the tissue structure and often occurs in various stages depending on the degree of mucosal damage [19]. Figure 6-2 illustrates the morphological and cellular changes associated with metaplasia and the progression from Barrett's esophagus to invasive carcinoma [11]. The normal lining of the esophagus is a stratified squamous structure showing normal cellular maturation in the esophagus epithelium. As the tissue becomes metaplastic, goblet cells and pit structures similar to those found in the gastric stomach form. Also in the progression from low to high grade dysplasia an increase in the architectural disorientation is seen with increased numbers of glandular features within the tissue and higher nuclear to cytoplasm ratio. At the stages of high grade dysplasia and invasive carcinoma, nuclear atypia is highly pronounced with altered nuclear alignment occurring and invasion of the cancer below the basal membrane.

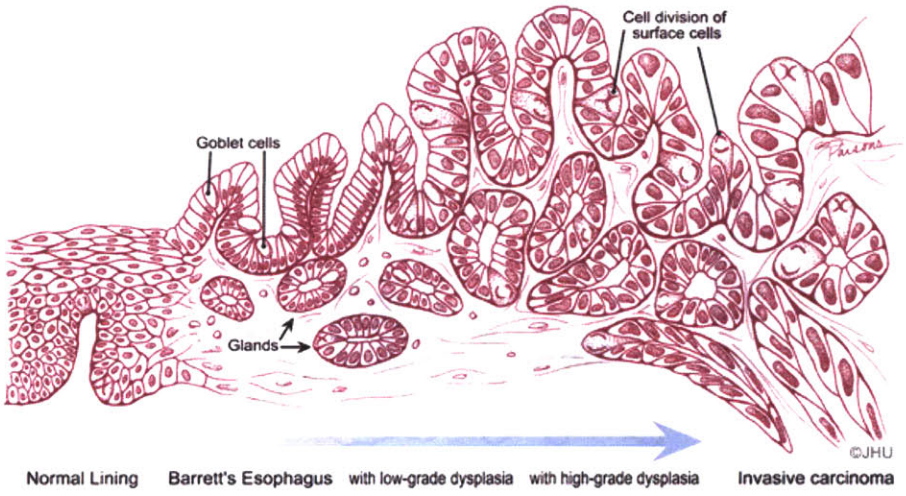

Figure 6-2. Illustration of metaplastic progression to esophageal cancer

Dysplatic progression to carcinoma shows distrupted architecture with increased glandular proliferation, increased architectural complexity, and loss of surface maturation. Reprinted from reference [11].

High-grade dysplasia is associated with a high risk of developing adenocarcinoma with a rate from 14-59% in 3-5 years [20, 21]. Preventative therapy treatment achieves high levels of regression in patients with dysplasia [22] thereby validating the importance of early detection. The esophageal cancer risk for patients with Barrett's esophagus is estimated to be 30-125 times greater than the general population [23-25]. It is also estimated that as many as 20 cases of

Barrett's esophagus go undetected for each known case [26]. The incidence of progression to adenocarcinoma in patients with Barrett's is approximately 7-9% [27, 28]. For this reason, endoscopic surveillance of Barrett's epithelium every 6-18 months is recommended.

Unfortunately dysplasia is not typically visible endoscopically and the focal nature of dysplasia makes accurate targeted biopsy highly difficult. With standard endoscopy, dysplastic tissue does not exhibit an altered appearance visually unless specialized staining techniques are used. Pinch biopsy however is still considered the gold standard for endoscopic determination of Barrett's esophagus and is the major diagnostic and surveillance method in practice today [29]. Targeted four-quadrant biopsies are taken every 2 cm along a suspect region, however significant sampling errors exist and procedures are prone to miss small foci of carcinoma [30, 31]. This is an important consideration in the screening of Barrett's and dysplasia.

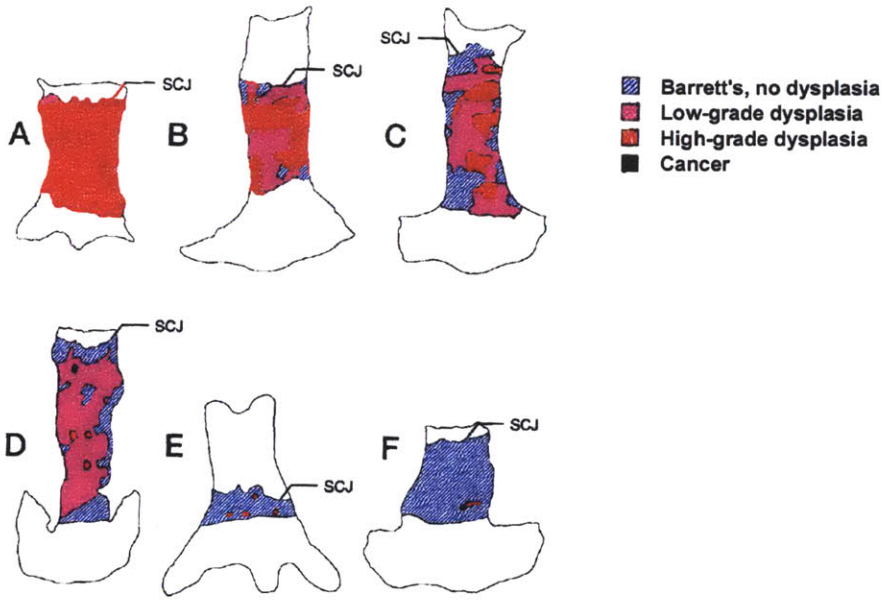

Figure 6-3. Histological mapping of Barrett's, dysplasia, and adenocarcinoma

Six cases of esophagectamy resection show A) HGD across almost all of Barrett's region; B) large area of HGD with intersperesed areas of low-grade and nondysplastic Barrett's; C) multiple areas of HGD and LGD; D) scattered small foci of HGD with a small focus of intramucosal adenocarcinoma; E) short segment Barrett's with HDG foci; F) small interamucosal adenocarcinoma adjacent to HGD focus. SCJ - squamocolumnar junction. Modified from reference [32].

In a pathological study of Barrett's, dysplasia, and adenocarcinoma the localization and distribution of each tissue grade was investigated for resected esophagi [32]. Data from this study shown in Figure 6-3 and Figure 6-4 demonstrates the high degree of localization and multiple distinct foci of dysplastic or cancerous tissue in the esophagus. Of the 19 initial patients undergoing surgery for high grade dysplasia, only 2 cases exhibited submucosal carcinoma.

Surgery was also performed on a second set of 11 patients that had biopsy established diagnoses of adenocarcinoma or suspicion of adenocarcinoma. Of these 11 resections, esophageal mapping confirmed carcinoma in only 5 patients (< 46%). From the esophagectomies, the median surface areas for each tissue type were 32 cm^2 for Barrett's, 13 cm^2 for low-grade dysplasia, 1.3 cm^2 for high-grade dysplasia, and 1.1 cm^2 for adenocarcinoma

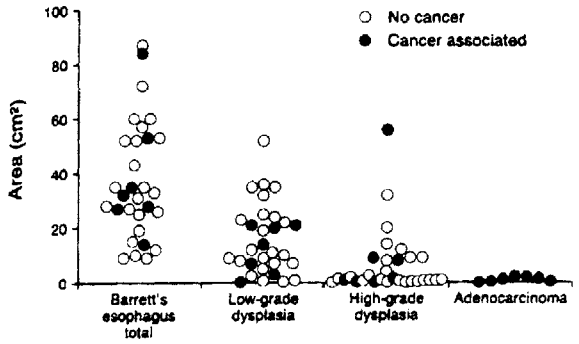

Figure 6-4. Surface area involved with Barrett's, LGD, HGD, and adenocarcinoma

Esophageal mappings show high localization of dysplastic and cancerous tissue within significantly larger regions of Barrett's for 30 patient resections. From reference [32].

Because of the imprecision and high cost associated with screening, new methods are required to identify high risk patients. Endoscopic ultrasound (EUS) has been used for the staging of advanced Barrett's esophagus with high-grade dysplasia or intramucosal carcinoma [33] however it has limited resolution of 100-200 um [34]. A high-resolution imaging technology such as OCT for guiding biopsy could reduce sampling errors, thereby improving sensitivity. In addition the early detection of dysplasia in Barrett's esophagus followed by preventive therapy could lead to significant decreases in patient morbidity and mortality.

Review of Previous Work in Endoscopic OCT

The first demonstration of *in vivo* endoscopic OCT was performed by our group (Tearney, et al. Science, 1997) [35]. This study demonstrated high speed OCT imaging of the GI and pulmonary tracts in the rabbit using a 1 mm fiber optic catheter and demonstrated the capability of OCT to visualize histologically significant structural layers within the GI lumen of the animal. Endoscopic OCT imaging was first demonstrated in humans by Sergeev et al. [36]. All layers of esophageal wall were able to be identified and tumor tissues were compared with healthy tissues. Disruption of the well-defined stratified mucosa structure in the tumor tissue was observed and representative images are shown in Figure 6-5. The imaging speed of their OCT system was slow (1 image per second) however and did not provide real-time imaging.

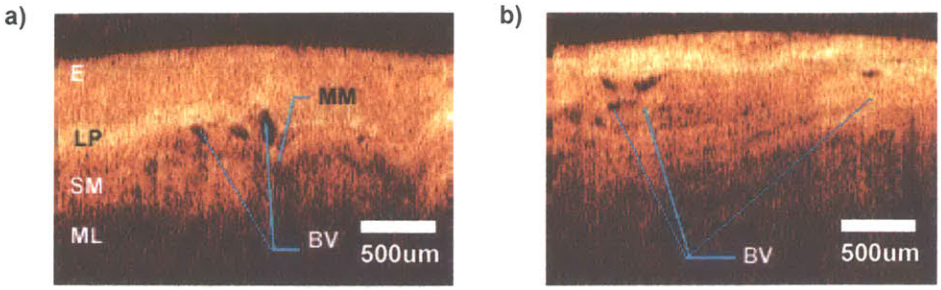

Figure 6-5. First *in vivo* endoscopic OCT imaging in humans

a) Normal and b) tumor tissue regions within the esophagus. Normal tissue exhibits good differentiation and segmentation of esophageal layers while the tumor region shows a disrupted submucosa (sm) and lack of a uniformly scattering epithelium (e). From reference [36].

Real time OCT imaging of the gastrointestinal tract was demonstrated by Bouma et al. [37] using a novel linear actuated catheter and Rollins et al. [38] using a novel high sensitivity interferometer design. Sivak et al. [39] have used a 2.4 mm radial scanning OCT probe inserted through the endoscope for real-time imaging (6.7 images per second) at a resolution of ~10 um, demonstrating OCT imaging of gastrointestinal tissues including esophagus, stomach, duodenum, rectum, colon and terminal ileum *in vivo* from 38 patients. The work by both Rollins et. al and Sivak et. al. utilized a rotary catheter design to image the esophagus in cross-section. While useful to gain a full 360 degree circumferential view of one depth location within the esophagus, it is somewhat more difficult to distinguish subtle changes in tissue architecture as a result of the decreased image pixel density combined with standard axial resolution OCT. This was one of the reasons that a linear scanning protocol was implemented in the high resolution OCT imaging of this work. Images of the rotational scanning results from these two studies are shown in Figure 6-6.

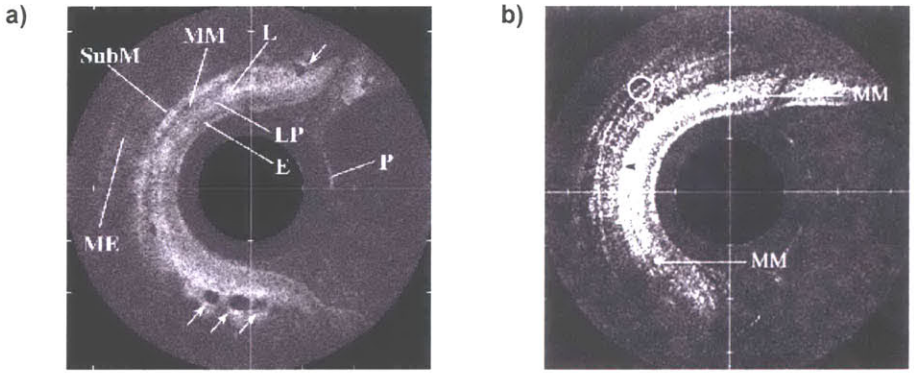

Figure 6-6. Rotational OCT scans of the esophagus

Structural layers are apparent in the rotational OCT image from the a) Rollins and b) Sivak work however subtle acrhictectural changes may be more difficult to distinguish due to lower image resolution (15um axial resolution). From references [38] and [39].

Bouma et al. [40] imaged upper gastrointestinal tract on 32 patients (including 20 patients with Barrett's esophagus) with a longitudinal scanning probe and ~10 um axial resolution. Barrett's esophagus was differentiated from normal esophageal mucosa, and esophageal adenocarcinoma was distinguished from normal esophagus and Barrett's esophagus. Li et al. [41] from our research group performed a comparative study of longitudinal and radial scanning for *in vivo* imaging of normal and Barrett's esophagus and demonstrated ultrahigh resolution and spectroscopic imaging of Barrett's esophagus *ex vivo*. Figure 6-7 shows imaging results from that study which are the most recent results to date from our laboratory previous to this work.

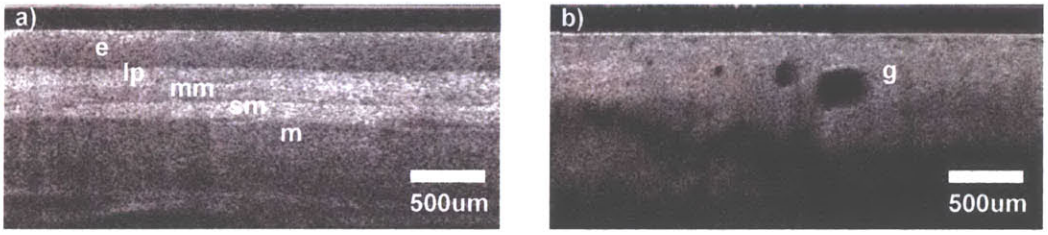

Figure 6-7. Previous *in vivo* standard resolution OCT imaging results

Linear scan OCT images of a) normal esophagus and b) Barrett's from our research group prior to this work. Disruption of the muscularis and gland regions (g) can be seen in the Barrett's tissue. The color scale has been inverted from reference [41] for consistency.

Jackle et al. [42, 43] described OCT clinical studies imaging the normal gastrointestinal tract tissues (esophageal, gastric and colonic mucosa) as well as colonic adenoma and carcinoma. With 10 um resolution, they found distinct patterns of normal, inflammatory, premalignant and malignant tissues in OCT images. Endoscopic OCT has also been shown to provide complementary information to endoscopic ultrasound for potential applications in staging of endoscopic tumor resection [44, 45]. Zuccaro et al. [46] reported the OCT images of esophagus and stomach in 69 patients with distinct appearance of squamous mucosa, gastric cardia, Barrett's esophagus and carcinoma.

In a study by Poneros et al., OCT was shown to have high sensitivity and specificity for the detection of specialized intestinal metaplasia (SIM) [47]. In the study a database of biopsy correlated OCT images from 166 esophagus and stomach biopsy specimens was generated as a training set to establish OCT criteria for SIM. Criteria were established by analyzing known images of SIM (n=75) and comparing them to OCT images of gastric and squamous mucosa. An OCT image and corresponding histology of cardiac epithelium is shown in Figure 6-8. Low image penetration and the presence of pit and crypt structures can be seen in the OCT image. Imaging parameters were axial and transverse resolution of 10um and 25um respectively with an image acquisition rate of 4 frames per second.

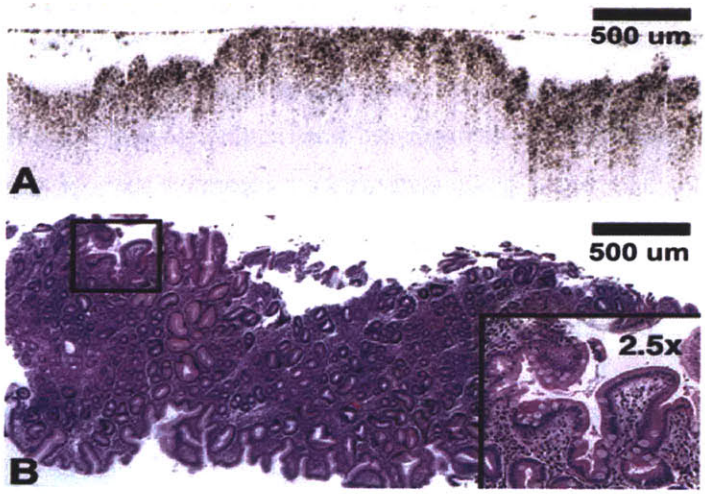

Figure 6-8. OCT image of gastric epithelium and corresponding histology

Low image penetration is seen in the OCT image of the gastric mucosa with the presence of "pit and crypt" architecture. Axial resolution is 10um. Reprinted from reference [47].

The criteria used for the qualification of SIM in the OCT images were 1) absence of a layered normal structure of squamous epithelium and the presence of vertical "pit and crypt" morphology seen in the gastric mucosa, 2) disorganized tissue architecture with inhomogeneous tissue contrast and an irregular mucosal surface, and 3) presence of submucosal glands. Testing retrospectively a sensitivity of 100% and specificity of 93% were achieved. With prospective testing the sensitivity and specificity values were 97% and 92% respectively. In general the lack of normal squamous or gastric mucosa and inhomogeneous tissue contrast were the most important criteria for diagnosis of SIM from the OCT images.

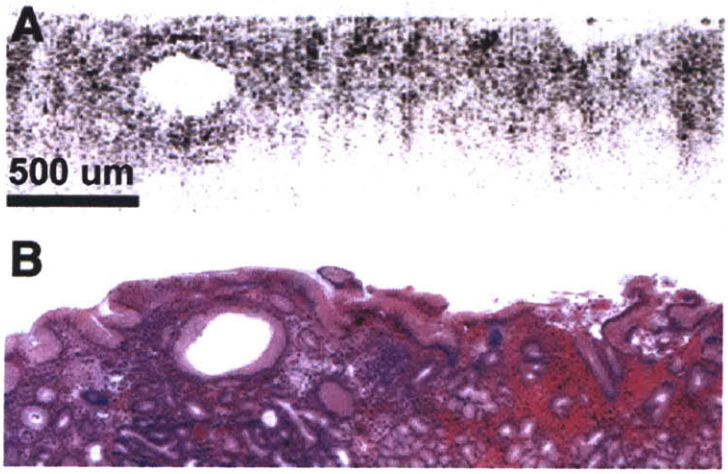

Figure 6-9. OCT image of and corresponding histology of SIM

Irregular glandularity with increased cellularity in the lamina propria is seen. Axial resolution is 10um. Reprinted from reference [47].

Recent work by Pfau et al. looked at criteria to diagnosis dysplasia by OCT and showed that OCT could distinguish hyperplastic from adenomatous polyps in the colon [48]. In that study 44 polyps were imaged in 24 patients (30 adenomas and 14 hyperplastic polyps). During the imaging the endoscopist subjectively rated the OCT images of normal mucosa and polyps based on two criteria; 1) the degree of organized histologic structure and organization and 2) degree of light scattering. Both gradings were on a scale from 0 to 5 with 5 representing the most organized or most highly scattering of each criteria. It was observed that adenomatous polyps exhibited lower light scattering properties and appeared darker in the OCT images. With increased light scattering scores, polyps were found to be 66% less likely to be adenomatous. Using a computer algorithm to quantify the degree of light scattering within specific regions of normal and polyp tissues, a correlation was found between the real-time evaluated light scattering grading and the computer-determined values. With respect to tissue organization, polyps were found to be 69% less likely to be adenomatous with increasing organization scores. Representative OCT images from the study of adenomatous and hyperplastic polyps are shown in Figure 6-10. The study implemented a rotational scan mode which results in somewhat lower resolution in the image however differences in scattering properties were observable between the two types of polyps.

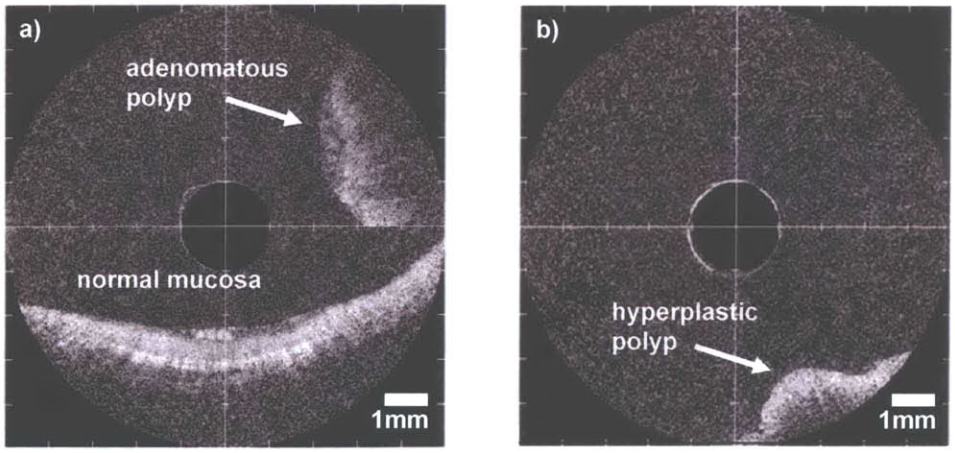

Figure 6-10. OCT images of adenomatous and hyperplastic polyps in the colon

a) Normal mucosa (6 o'clock position) exhibits a well organized linear crypt pattern that is not seen in the adenoma (2 o'clock position). Light scattering is also decreased within the polyp when compared to the normal mucosa. b) OCT image of a hyperplastic polyp shows brighter scattering than normal mucosa with a maintained crypt pattern. Reprinted from reference [48].

These previous endoscopic studies demonstrated that OCT imaging could be readily integrated with endoscopic procedures and provide valuable diagnostic information. However, all clinical studies to date have been performed using standard OCT with 10-15 um resolution and

the ability to differentiate high grade dysplasia has not yet been demonstrated. In addition the image fidelity and subsequent ability to readily distinguish morphological architecture indicative of Barrett's esophagus, dysplasia, and adenocarcinoma has been sub-optimal. By increasing the resolution capability of OCT imaging, its use for image guided biopsy could significantly improve the sensitivity of biopsy by reducing false negative rates.

Study Design and Imaging Protocols

One of the goals of this work was to demonstrate the use of OCT as an ultrahigh resolution, real time, and *in situ* imaging technique in the gastrointestinal tract for the identification and differentiation of metaplastic changes associated with dysplasia and adenocarcinoma. Human imaging studies were performed on both *ex vivo* tissue samples as well as endoscopically *in vivo*. The studies were performed in collaboration with Dr. Hiroshi Mashimo, M.D., Ph.D., Chief of Gastroenterology and Dr. Marcos Pedrosa, M.D. in the VA Boston Healthcare System. Additional major collaborators at the VABHS were nurse practitioner Marisa Figueiredo and endoscopists Dr. Saleem Desai, M.D. and Dr. Mihir Wagh, M.D. The pathology department at the West Roxbury campus and administrative assistance Sandra Johnson provided access to histopathology slides and analysis. Participants from the MIT lab included Dr. Yu Chen and graduate student Pei-lin Hsiung. Preliminary results in the previous chapter demonstrated ultrahigh resolution endoscopic OCT in an animal model and provided the framework from which to conduct the human trials.

Imaging of the upper gastrointestinal tract in humans was performed on two sets of specimens. *In vivo* endoscopic OCT imaging was performed on a group of 20 patients diagnosed with Barrett's esophagus, esophageal neoplasia, or carcinoma and who were scheduled for routine endoscopic surveillance of Barrett's esophagus. All procedures were conducted in accordance with human study protocols approved by the MIT Committee on the Use of Humans as Experimental Subjects and the VABHS Human Studies Internal Review Board and Research Committee. During standard diagnostic endoscopy, the patient oropharynx was desensitized with a 4% lidocaine topical spray. A single or dual-channel Olympus endoscope was introduced into the esophagus with the patient under sedation of midazolam and meperidine, given intravenously. During the procedure live video images were viewed and recorded via an endoscopic CCD camera. When the endoscope was within the patient stomach region, a disinfected OCT imaging catheter was inserted through the accessory channel of the endoscope and passed into the field of view. The OCT imaging catheter was positioned within the esophagus and transverse (linear) scanning, ultrahigh resolution OCT was performed at regions with Barrett's metaplasia and

suspected dysplasia. Several areas within the stomach and across the gastroesophageal junction were imaged as well as at proximal regions of normal esophagus. OCT imaging was performed for approximately 10-15 minutes per patient with an average of 800-1000 digital OCT images obtained per patient. A photograph of the OCT catheter extending out of one port of the Olympus endoscope is shown in Figure 6-11.

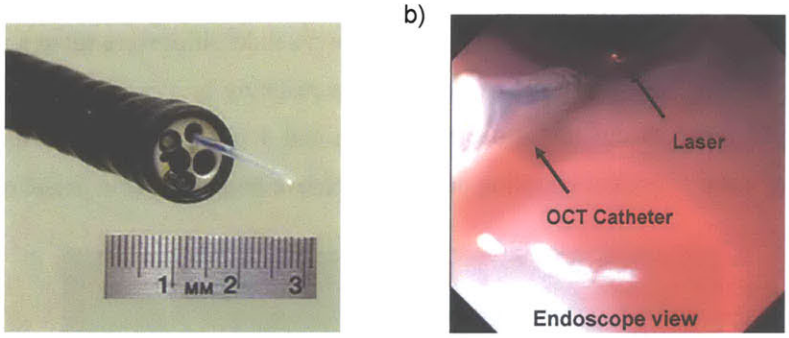

Figure 6-11. Clinical implementation of endoscopic OCT

a) Photograph of the OCT catheter extending beyond the distal end of the endoscope. b) Endoscopic view captured by CCD camera of the OCT catheter imaging inside the patient esophagus. The red aiming laser beam is used to visualize the area being imaged.

After *in vivo* imaging was conducted, four-quadrant pinch biopsies were taken every 2 cm in regions of Barrett's esophagus as well as biopsies from target sites of suspect lesions. OCT imaging of these esophageal pinch biopsies was conducted immediately after excision. The surgical specimens were expected to exhibit a spectrum of pathologies ranging from Barrett's to dysplasia to adenocarcinoma. Imaging was performed in the endoscopy suite with the portable ultrahigh resolution imaging system developed for this work. Biopsies were oriented and imaged inward from the mucosal face within 5 minutes of excision. Isotonic saline was applied to insure tissue hydration and approximate conditions *in vivo*. Since these specimens are from pinch biopsies and are small, the entire extent of the specimen was imaged in order to enable registration and correlation of OCT images with subsequent histology. Immediately after imaging, biopsy specimens were fixed in a 10% formalin solution and underwent standard histopathology processing at the West Roxbury VABHS facility. Histological images were compared with OCT images to obtain image correspondence relative to pathological disease states.

OCT System Design and Characterization

The imaging configuration employed for this study utilized the ultrahigh resolution OCT system described previously in this thesis. A Cr^{4+}:Forsterite laser was used as the light source

with a typical operating bandwidth of 180 nm achieving an axial resolution of 5 um measured in air. A linear scanning protocol was implemented with the push-pull catheter design and magnetic coil SMAC actuator system. The scanning parameters were optimized such that 3200 axial scans were taken per second at a 4 Hz frame rate giving 800 axial scans per image. A longitudinal scan length of 4 mm was used to give a high transverse pixel density while maintaining a reasonable scan range to view tissue architectural changes. The scan depth set by the acquisition window on the reference arm scanner was set to 2.5 mm. The image pixel densities were set to a minimum of 2000 pixels in both the transverse and axial directions resulting in a minimum pixel sampling density of 1 pixel per 1.25 um in the depth direction and 1 pixel per 2 um in the transverse direction. This allowed sufficient sampling density to achieve high resolution image quality.

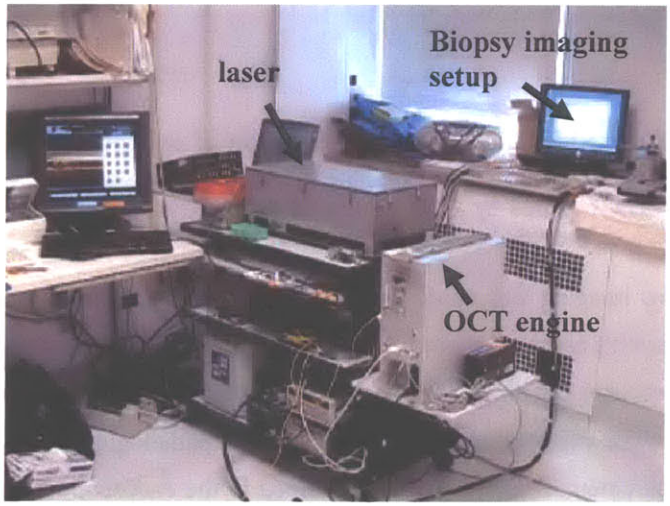

Figure 6-12. Photograph of portable high-resolution OCT system in the clinic

Before each procedure all catheters were disinfected under standard procedures in place at the VABHS hospital system consisting of a 30 minute soak in Cidex solution followed by water rinsing and drying. During the procedure typically three operators were present for the OCT system control. One operator controlled the catheter positioning and remained near the patient while the other two operators respectively recorded notes during the procedure and saved digital OCT images onto the computer system. A photograph of the complete system in the clinic is shown in Figure 6-12. During the procedure there was typically one endoscopist present and one nurse attendee to aid the doctor. A separate disinfected catheter was used for the OCT imaging in each patient.

Clinical Imaging Results

In order to establish a baseline for detecting disease pathologies, imaging of normal regions of the esophagus was conducted in several patients. Figure 6-13 shows an ultrahigh resolution OCT image of a patient in the upper esophagus region. Cephalad and caudad correspond to the direction toward the patient's head and towards the patient rectum respectively and is the same orientation used for all the OCT images. The squamous epithelium (e) exhibits a uniform scattering intensity with an epithelial thickness of 300-400 um. Under the epithelium, the lamina propria (LP) is seen as a highly scattering band located directly above the muscularis mucosa (mm) which has lower scattering intensity. The submocosa (sm) is seen as a second bright layer and is situated above the smooth muscle layer of the muscularis externa (ext).

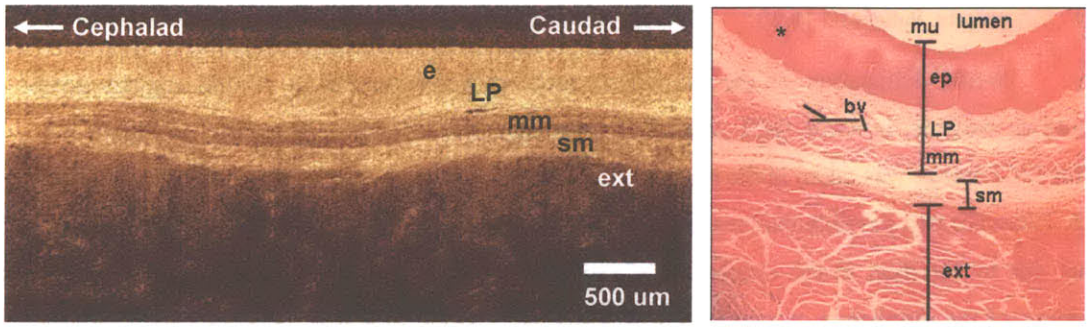

Figure 6-13. Ultrahigh resolution image of normal esophagus and histology
OCT image of normal esophagus and corresponding histology from reference [49]. Patient ID 8-3.

Several significant features should be noted in the high resolution OCT image. First is the uniformity of the stratified squamous epithelium. It will be seen in later results that disruption of the uniform squamous layer is indicative of Barrett's esophagus. Another important architectural detail to note is the well defined layering of the healthy esophagus. In particular good definition of the muscularis mucosa with continuity across the esophagus in the longitudinal (horizontal) direction is observed. For later disease states suggestive of dysplasia or cancer, this muscularis layer becomes disrupted and distinct breaks in the layer continuity are observed. Finally the lack of high brightness scattering centers or conversely dark regions of very low scattering indicate a uniform structure without any glandular bodies or mucus inclusions.

The boundary between the lamina propria and epithelium is distinct, but can be marked by irregularities where connective tissue papillae push into the epithelium. In some of the high resolution OCT images mottling of the squamous epithelium with highly scattering regions extending from the lamina propria were seen which may be indicative of Rete pegs. These features have been difficult to observe in previous OCT studies and can be visualized with the

high resolution system developed in this work. Figure 6-14 shows an OCT image detailing these structures.

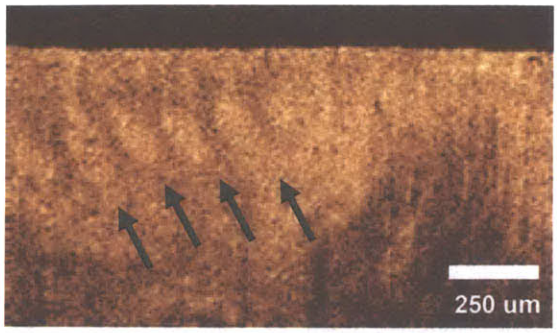

Figure 6-14. Enlarged region of squamous epithelium showing Rete pegs

Small variations in scattering intensity may be indicative of Rete pegs within the lamina propria. Patient ID 18-10.

While delineation of the muscularis mucosa was observed in several regions across multiple patients, in some OCT scans this layer appeared absent as illustrated in Figure 6-15. This OCT image was taken in the same patient and in the same location as the image in Figure 6-13. There are two possible explanations for this apparent loss of the muscularis layer. The first is that due to variation in the esophagus, the muscularis mucosa layer may be thinner in certain regions of the esophagus. A previous endoscopic OCT study in which the five-layered structure of Figure 6-13 was not seen in the mid-esophagus showed similar results [46]. Another possibility is that the muscularis may become compressed between the lamina propria and submocosa layers. The effect would be that a single region of increased backscattering would be seen in the OCT image. This effect has been also observed previous endoscopic OCT experiments by Rollins et. al where slight compression of the tissue caused an increase in scattering intensity [50]. More investigation into these possibilities is encouraged.

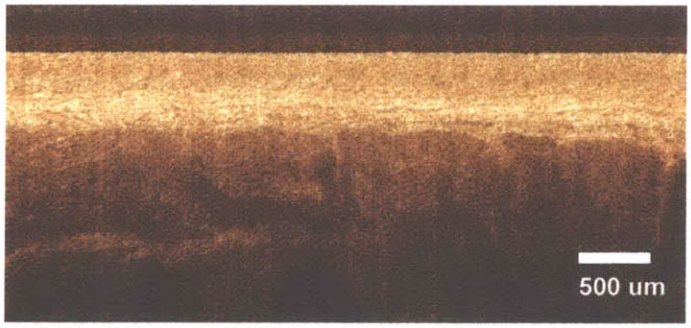

Figure 6-15. Increased scattering intensity due to possible tissue compression

The lamina propria, muscularis mucosa, and submucosa collapse into one band of highly scattering tissue under compression. Patient ID 8-3.

Looking at a cross section of patients, similar features are seen for normal, healthy esophagus. Namely a uniformly scattering squamous epithelium, a highly backscattering layer corresponding to the lamina propria and submocosa, and connective smooth muscle present below. A selection of OCT images taken in the esophagus is shown in Figure 6-16.

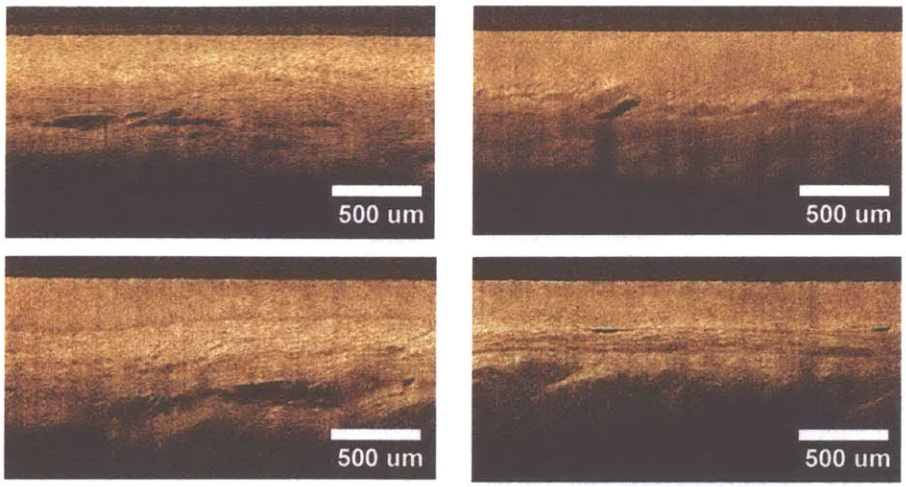

Figure 6-16. Series of OCT images of healthy esophagus

Variations across patients of normal esophagus show that a uniformly scattering epithelium is consistent across patients. Patient ID 2-1,6-2,9-4,14-6.

Both across patients and within one patient there exists some variability in the architecture seen in normal esophagus. Figure 6-17 shows an OCT scan of a normal region within a patient that may initially look highly disrupted to the untrained observer. In fact however, looking at the top 400-500 um, the uniform intensity and non-disrupted epithelial layers indicates that the tissue is health esophagus. What is of interest and importance is the fact that the OCT image can visualize features that would be impossible to see via histological examination.

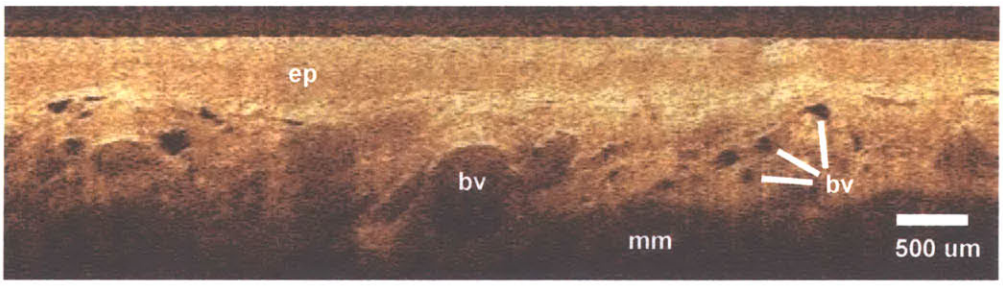

Figure 6-17. Architecture of normal esophagus

The normal esophagus can exhibit many architectural features such as glands and blood vessels. Composite image from 3 sequential OCT scans. Patient 3-1.

The ability to discern this level of architectural detail is exciting as many relevant features can be seen and investigated. The ability to see small vessels for example opens opportunities to conduct Doppler flow OCT imaging. Furthermore, structures visualized below the surface may at some point exhibit pathological characteristics that would not be seen with normal endoscopic techniques

A comparison of an enlarged portion of the above OCT image compared with histology is shown in Figure 6-18. Esophageal layers of the stratified squamous epithelium (ep), lamina propria (lp), and muscularis mucosa (mm) are well defined in both images. Good correlation is of architectural features such as blood vessels (bv) is also seen. Delineation of lymph nodes (ln) is more difficult to definitively distinguish in the OCT image.

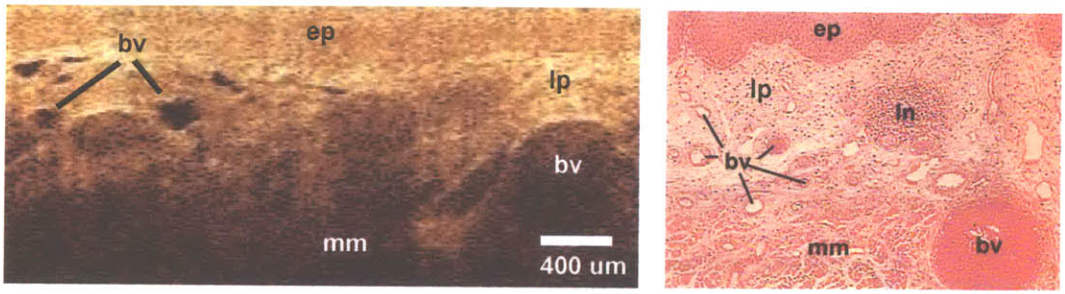

Figure 6-18. Comparison of normal esophagus with histology

Good coorelation is seen between the high resolution OCT image and textbook histology. Esophageal layers and structures within the lamina propria are apparent in both images. Patient ID 3-1, histology from reference [51].

As the development of Barrett's esophagus is characterized by a metaplastic change in cell and tissue type from the normal squamous epithelium found in the esophagus to a tissue resembling that found in the stomach, imaging of the gastric mucosa is also important to determine the relevant architectural features and morphology. Figure 6-19 shows a gross photograph of the stomach to give an idea of the relative position of different regions imaged.

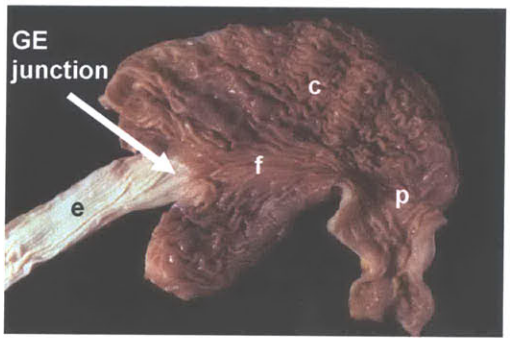

Figure 6-19. Gross photograph of stomach

Sections imaged by OCT include the esophagus (e), fundus (f), corpus (c), and pyloris (p) of the stomach. From reference [52].

Figure 6-20 shows an OCT image and corresponding representative histology the proximal stomach. As can be seen the scattering properties of the gastric mucosa are strikingly different than what was seen in the esophagus. In particular, regions of high scattering are well localized into areas of vertical striping. These correspond to tubular pits comprised of columnar mucus-secreting cells typically found in cardiac or junctional-type mucosa [53]. Also seen in the gastric mucosa is a distinct lack of the banded layered structure seen in the esophagus as well a decrease in image penetration.

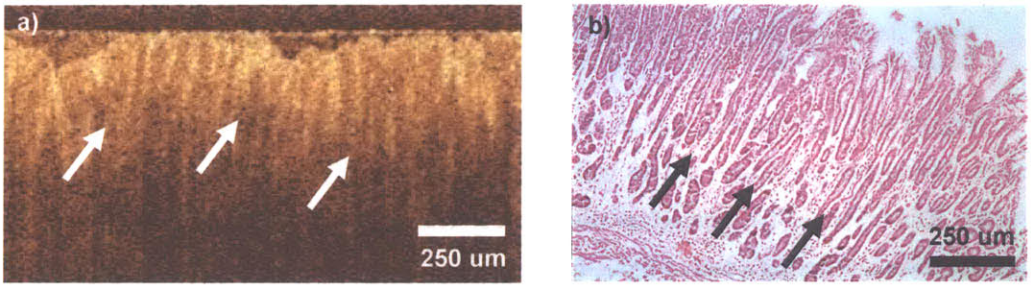

Figure 6-20. OCT image of proximal stomach and representative histology

Vertical striping in the OCT image can be seen to correlate well to gastric pit linings in the histology cross section. Patient ID 8-3. Histology from reference [49].

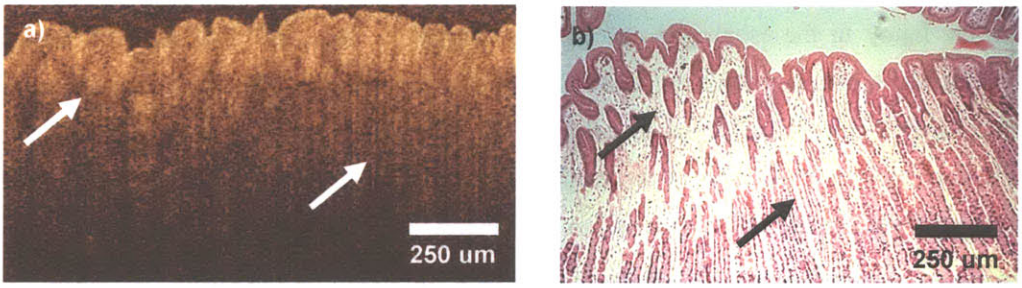

Figure 6-21. OCT image and histology of stomach corpus

Glandular features can be seen in both the OCT image and histology cross-section. Patient ID 6-2. Histology from reference [49].

In Figure 6-21 the more muscular type of gastric architecture is seen when imaging deeper within the stomach corpus region. This architecture corresponds to the denser and increased glandular-like structure (arrows) found in the body of the stomach. This region is where food is churned and undergoes peristalsis thus leading to a more resilient tissue structure. The differentiation between the two tissue types can be clearly visualized in the OCT images.

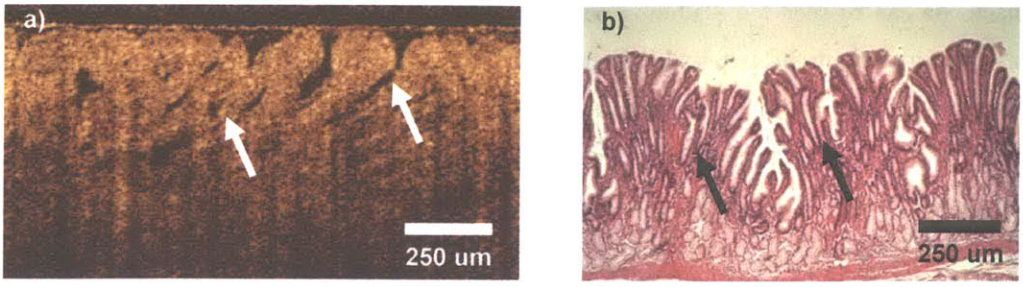

Figure 6-22. OCT image of distal stomach and representative histology

Large glands with finger-like projections are visualized well in the high resolution OCT image. Patient ID 5-2. Histology from reference [49].

Figure 6-22 shows a final region imaged within a patient stomach of the pylorus or distal stomach. The highly glandular features indicative of the stomach lower atrium can be seen very distinctly. This region of the stomach is where a majority of the acid secretion via parietal cells occurs thereby engendering a more villous-type of architecture.

Between the esophagus and stomach lies a boundary termed the gastroesophageal junction or GE junction. This area is of particular clinical interest and importance because often repetitive esophageal damage due to gastroesophageal reflux (GERD) occurs near this region. Repetitive injury to the esophagus can lead to metaplastic changes associated with Barrett's esophagus which may develop over time into dysplasia or carcinoma. Moreover, identification of intestinalization from biopsies taken below the GE junction do not bear the same clinical implications as intestinalization in the esophagus and do not confirm the presence of Barrett's esophagus. Therefore the ability to visualize this boundary is of clinical importance.

Figure 6-23. OCT image across the GE junction

The OCT scan spans from the distal esophagus to proximal stomach showing the alteration of tissue type from squamous epithelium (se) to columnar epithelium (ce). Composite image from two sequential OCT scans. Patient ID 8-3.

Figure 6-23 demonstrate the capability of the high resolution system to visualize the GE junction. On the far left of the image the squamous epithelium (se) is discernible at the distal esophagus. Within the proximal stomach on the right side, the transition to the vertical striping of columnar epithelium (ce) seen in gastric mucosa is also readily apparent. The ability to take high resolution, large scan range images at high frame rates allows clear delineation of the architecture across this transition region.

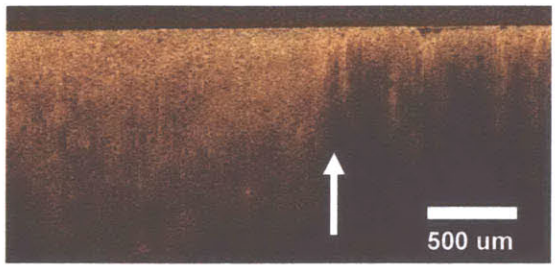

Figure 6-24. GE junction and Z-line of normal patient

A clear Z-line transiton can be seen between squamous epithelium in the esophagus and columnar epithelium in the stomach. Patient ID 1-1.

Figure 6-24 shows a distinct transition at a classic Z-line interface between the esophagus and stomach. As will be seen in later images, loss of this distinct boundary between is common in a diseased tissue state such as Barrett's esophagus or dysplasia. The ability to visualize this boundary clearly establishes the capability of the high resolution system to distinguish normal from abnormal architectural morphology in patients imaged.

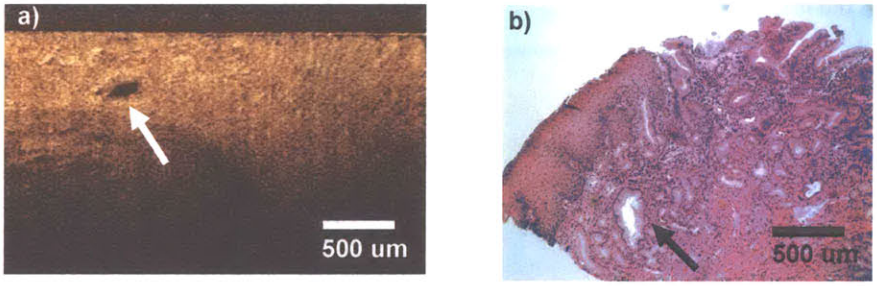

Figure 6-25. OCT image and biopsy histology of GE junction

Squamous epithelium has more uniform scattering appearance in the OCT image. Glandular features are apparent across the junction as well as identification of a large gland below the epithelium (arrow). Patient ID 9-4.

Following *in vivo* OCT imaging of the patients, several biopsies were taken to obtain representative histology of the areas scanned. The biopsies serve as one method to validate the high resolution OCT imaging results and good correspondence between the OCT image and histology allow greater confidence in the interpretation of OCT images where histology is not available. Figure 6-25 shows an OCT image and histology taken from a patient across the GE

junction region. As can be seen the transition between the squamous epithelium of the esophagus and columnar epithelium is clear. Microscopic examination of biopsy from the squamocolumnar junction indicated active inflammation and hyperplasia as seen by the numerous glands below the squamous epithelium. No specialized columnar epithelium of Barrett's was seen however

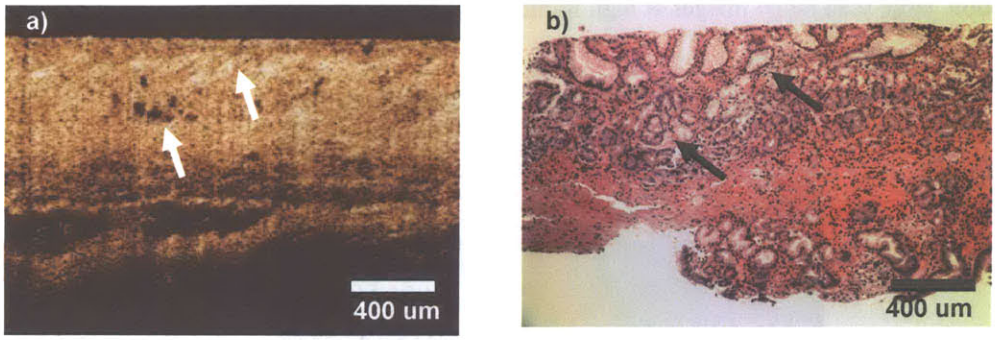

Figure 6-26. OCT image and corresponding histology of Barrett's esophagus

a) The OCT image shows high intesity scattering in the region of Barrett's. b) Corresponding histology diagnosed with specialized intestinal metaplasia (SIM) shows high glandular density with disruption of the muscularis layer. Patient ID 14-6.

Even with the large degree of variation among tissue pathologies in patients, consistent architectural patterns were observed in the OCT images of Barrett's esophagus. Figure 6-26a shows an OCT image from a patient with Barrett's esophagus (Figure 6-26b). The OCT image shows high intensity scattering clusters in the region of Barrett's that correspond to glandular structures in the histology.

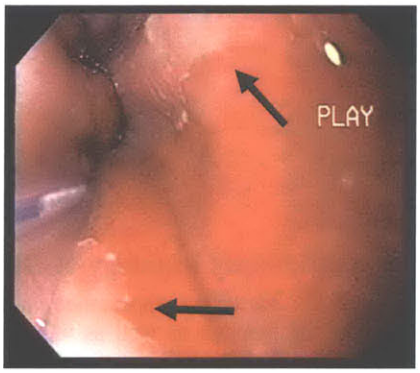

Figure 6-27. Endoscope view of Barrett's region imaged

Finger projections of squamous epithelium (arrows) are apparent in the area imaged near the gastroesophageal junction. Patient ID 14-6.

Small dark regions within the tissue may correspond to pockets of mucin observed similarly in the gastric mucosa and support the hypothesis of gradual metaplastic change in the disease progression. Disruption of the muscularis layer is another indication of the disease which

will be seen to become more pronounced in cases of suspected dysplasia and adenocarcinoma. Figure 6-27 shows the correlated endoscopic view of the region imaged in the esophagus for the OCT image of Figure 6-26. Squamous regions with ragged boundaries are apparent at the GE junction (arrows). The imaging catheter is in the lower left of the CCD captured image.

Figure 6-28 shows another demonstration of Barrett's pathology the high resolution OCT imaging is capable of distinguishing. Disruption of the muscularis is apparent while prominent non-scattering inclusions of low intensity indicative of cystic dilations are seen to be present.

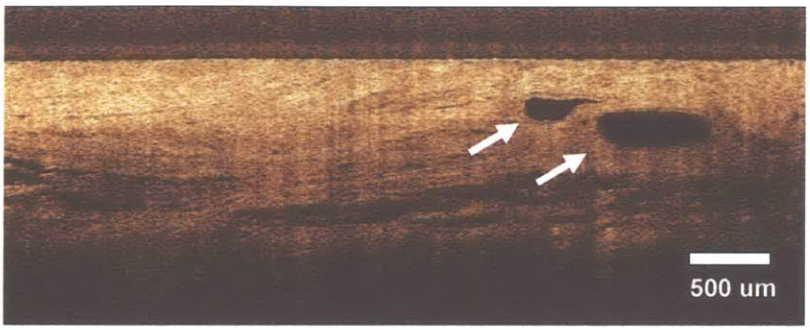

Figure 6-28. OCT image of Barrett's esophagus with large cystic dilations

Large regions of low-scattering inclusions (arrows) are apparent as well as strong disruption of the muscularis mucosa. High scattering areas are also seen indicative of Barrett's. Composite image from two sequential OCT scans. Patient ID 4-1.

These cystic dilations have appeared in multiple patients with Barrett's esophagus and appear to be a possible accumulation of mucous or interstitial fluid within the esophagus. As Barrett's is a disease where glands progress in a follicular type of reaction (i.e. budding outwards from a central follicle submerged below the surface), such interstitial fluid may build up below the surface of the esophagus if there is no avenue for discharge into the intestinal tract. Figure 6-29 shows another OCT image of a region imaged with Barrett's that has similar high scattering within the epithelium in addition to cystic dilations which may be caused by edematous glands.

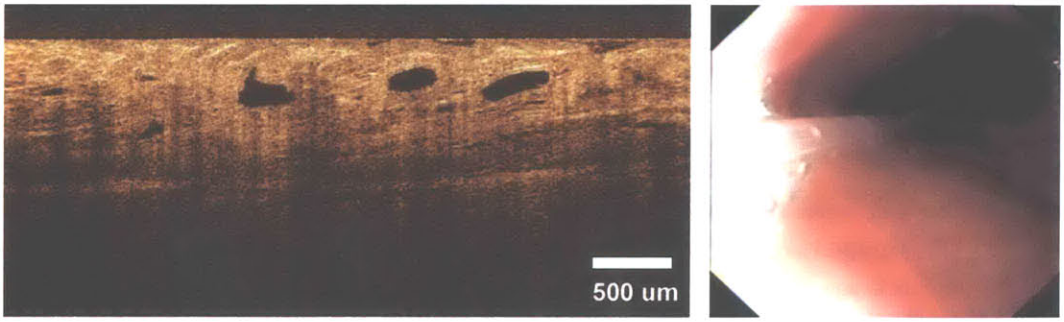

Figure 6-29. OCT image and endoscope view of Barrett's region imaged

Striations of bright scattering regions within the epithelium are visible with several cystic dilations. Patient ID 19-10.

In one patient with a very long segment (>10 cm) and lengthy history of Barrett's, such dilations were seen both within the distal esophagus as well as within the proximal stomach as shown in Figure 6-30. As these dilations exist several hundreds of microns below the surface they would not be captured in a standard endoscopic biopsy. Even with a jumbo biopsy method, such dilations would likely collapse and might be poorly visualized in histopathology sectioning.

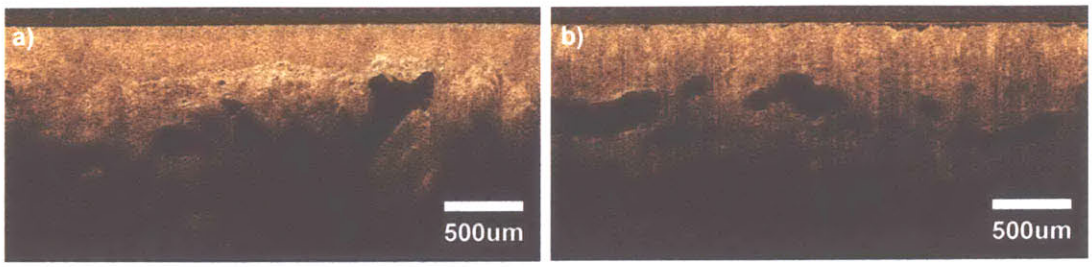

Figure 6-30. Cystic dilations in a patient with long segment Barrett's

Large dilations >500um is size are seen in both the distal esophagus (a) and proximal stomach (b). The presence of these dilations may indicate a long history of Barrett's. Patient ID 1-1.

There may be a possible correlation between the duration of Barrett's within the patient and the presence of these dilations. Further investigation into possible causes and implications of these dilations are being pursued and the ability to visualize these dilations *in vivo* using OCT may prove to be an indication of duration or severity of Barrett's or dysplasia within patients.

Another technique to qualification of disease state and quantification of disease severity using OCT is to pursue image processing techniques and algorithms to analyze and segment architectural features within high resolution OCT images. While low-scattering regions are more readily visible, regions of high scattering may be washed out in the high intensity background seen in Barrett's epithelium.

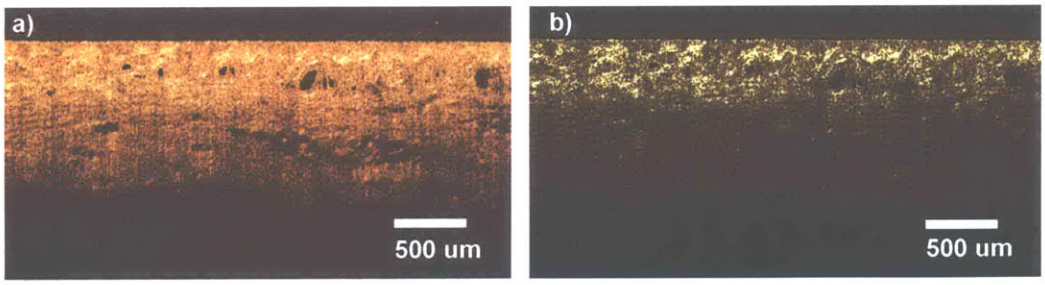

Figure 6-31. Image thresholding to identify regions of high scattering in Barrett's

a) Original image. b) Original image overlayed with 70% intensity threshold. Regions of highest intensity are shown in white. Patient ID 5-2.

Figure 6-31a shows an OCT image of a Barrett's region in the original OCT format. Using a conversion to grayscale with a 70% intensity threshold, an overlay of the segmented

regions of high intensity is shown in Figure 6-31b. It is apparent that using algorithmic approaches such as these for OCT image analysis would allow quantification of Barrett's esophagus as demonstrated by Pfau et. al in endoscopic OCT of colon polyps [48].

As a comparison, an identical 70% threshold operation was performed on an OCT image of normal esophagus. The differences in the images are apparent as the Barrett's pathology exhibits distinctly more disorganized scattering centers interspersed within the epithelium. In addition the normal physiology of the esophagus has a clear layering of the individual esophageal layers with good continuity of each layer maintained across the field. The distribution and density of the high scattering regions in the healthy tissue is more uniform and regular than in Barrett's-altered tissue.

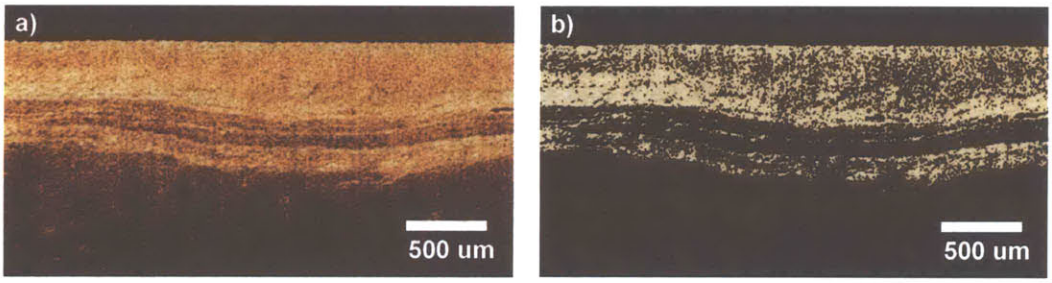

Figure 6-32. Image threshold of normal esophagus region

a) Original image. b) Original image overlayed with 70% intensity threshold. The epithelium exhibits a region of uniform high intensity. Patient ID 8-3.

The capability to accurately detect and diagnose regions of Barrett's esophagus is significant for several reasons. The extent of Barrett's within a patient, while usually visible endoscopically, can be well determined with the high resolution capability of OCT. Qualification of the severity of Barrett's through several methods including degree of architectural disruption, presence of distinguishing low or high scattering morphology, and image processing techniques could also help determine the extent of metaplastic tissue and disease progression. In addition, for patient cases where short segment Barrett's (SSBE) exists, it is often difficult to identify or visually localize suspect areas. The ability to see sub-surface architectural disruptions is also significant as Barrett-like conditions such as a disrupted muscularis mucosa may exist underneath apparently normal tissue. Finally using high resolution OCT it possible to scan large transverse regions of the esophagus to where the tissue may undergo morphological alterations from normal to Barrett's, from Barrett's to dysplasia, and from dysplasia to cancer. The capability to visualize these transitional tissue states may prove critical in establishing criteria to identify areas of dysplasia which are not visible under standard endoscopy procedures.

Figure 6-33. Transverse scan of GE junction

Transition between the normal squamous epithelium of the esophagus (left) to the columnar-lined epithelium of the stomach (right) is seen. Composite image from three sequential OCT scans. Patient ID 5-3.

Figure 6-33 demonstrates a transition across the GE junction of a patient diagnoses with Barrett's. In the far left region of the OCT scan an area of normal squamous esophagus is present while at the far right of the image, vertical striping of the gastric mucosa is seen indicating imaging in the patient's stomach. Between these two areas is a transitional region with rich architectural detail and varying degrees of structural disruption. The ability to see a large portion of the GE junction within the patient has significant implications for the use of OCT to guide directed biopsy. Obtaining images such as these with a significant scan field at high resolution images, *in vivo* and at high speed is not possible with any other imaging modality available.

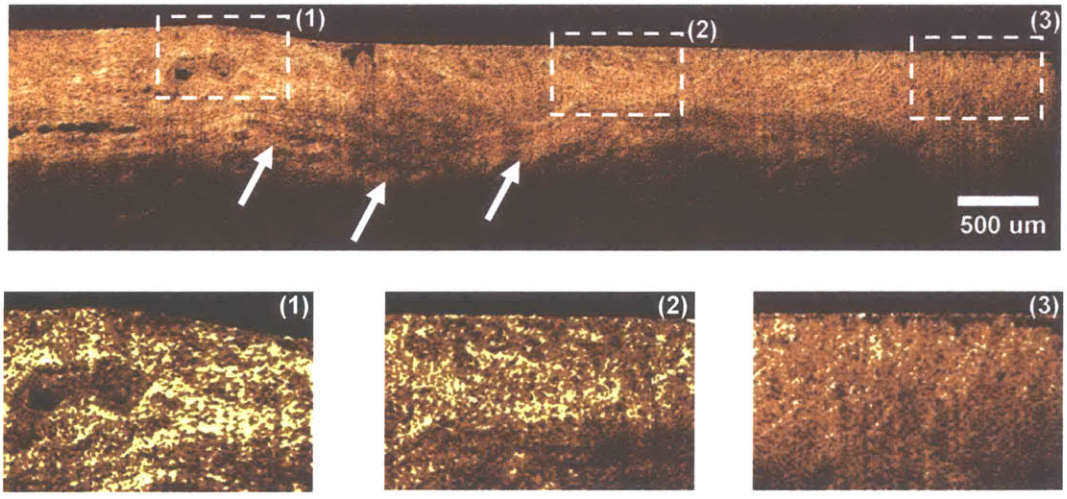

Figure 6-34. Cross-sectional scan of metaplastic transitions in Barrett's

Enlarged regions (1), (2), (3) across the metaplastic GE junction show quantification of architectural disruption via image thresholding. Composite image from three sequential OCT scans. Patient ID 9-4.

To demonstrate the power the high resolution OCT in visualizing and quantify these metaplastic transitional regions an OCT scan is shown in Figure 6-34 with image intensity thresholding applied to various regions across the GE junction. From the full length scan, the metaplastic transition from squamous to columnar epithelium is apparent as seen previously. Of importance also is the visualization of a greater degree of disruption in the muscularis mucosa spanning the region (arrows). Using a 70% intensity threshold across several regions of interest it is possible to see that areas of increased architectural disorder can be readily identified (Figure 6-34 enlarged regions). This is highly encouraging and suggests that quantitative metrics to grade disease localization and severity are possible in future studies.

With high resolution OCT it was also possible to identify very short segments of Barrett's-like epithelium as shown in Figure 6-35. A suspect region of tissue alteration was seen by OCT surrounded by normal squamous epithelium (enlarged regions of Figure 6-35). As this area is only ~1 mm in length it is highly likely to be missed using standard biopsy procedures.

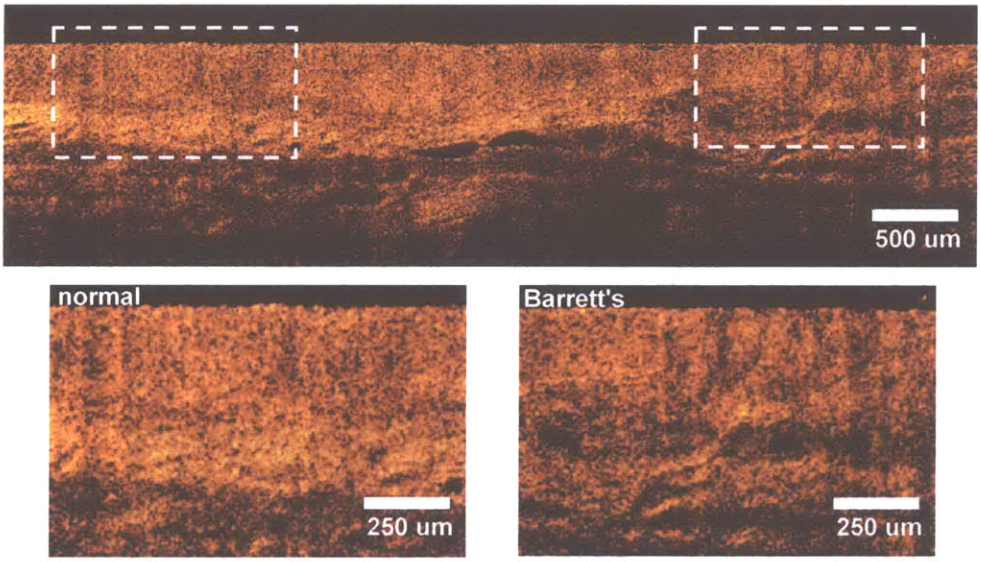

Figure 6-35. OCT scan identifying a suspect region of short segment Barrett's

With the high resolution capability of the system a small 1mm segment of disrupted tissue was identified. Composite image from three sequential OCT scans. Patient ID 8-9.

The endoscopic view of the region imaged in Figure 6-35 is shown in Figure 6-36. The region of normal squamous epithelium is identified as being light pink in color and is located proximally in the image. The transition does not exhibit ragged boundaries or squamous islands which are often indicative of Barrett's. The OCT image in Figure 6-35 shows the capability to detect and localize regions of Barrett's which are subtle and may be difficult to detect visually by standard endoscopy.

Figure 6-36. Endoscopic view of transition between normal and Barrett's

The transition region across the normal squamous epithelium of the esophagus is imaged. Patient ID 8-9.

A beautiful demonstration of the resolution capability of the high performance system developed in this work is shown in Figure 6-37. In the OCT image an apparently normal layer of squamous epithelium can be seen near the surface of the tissue. Using white light endoscopy or even chromoendoscopy staining techniques, it is highly likely that this region would appear as normal healthy tissue. In the high resolution OCT image, a uncharacteristic region can be seen approximately 500 um below the surface. Previous biopsies from the squamocolumnar junction region in this patient showed diagnoses of underlying granulation tissue and regenerative atypia of both the squamous and glandular mucosa. In addition this patient had a long history of GERD as well as esophagitis therefore this sub-surface disruption may represent an abnormal region that has had epithelial regrowth over it. This is an excellent example of the ability of OCT to visualize sub-surface architecture.

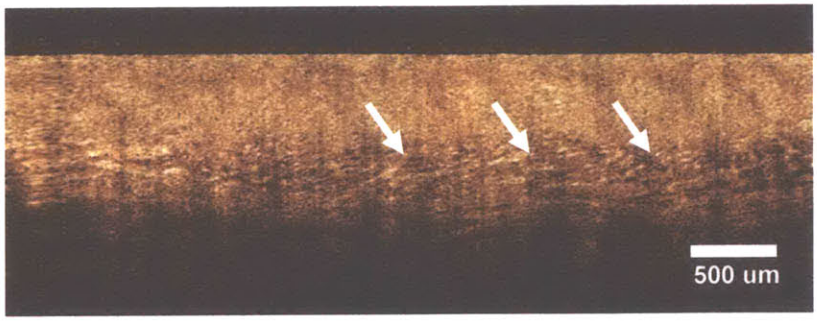

Figure 6-37. Visualization of sub-epithelial morphology

High scattering centers of tissue below normal squamous epithelium suggest the re-formation of healthy tissue over a region of treated Barrett's esophagus. Patient ID 11-5.

As shown above, the OCT performance realized in this work demonstrates some of the highest resolution and best quality results for endoscopic OCT imaging. This has implications

beyond the ability to just get 'nicer pictures', as studies using even standard resolution OCT have shown the ability to identify regions of Barrett's esophagus. These studies have been able to do so and demonstrate high sensitivity and specificity [47] for Barrett's as well as visualize regions of esophageal adenocarcinoma [40, 54]. The increased image fidelity and delineation of architectural morphology achieved in this work can be directly applied to both improve analysis and achieve quantification of early esophageal disease pathologies by OCT imaging. This can positively impact sensitivity and specificity metrics as well increase the efficacy of OCT to detect and diagnose diseased tissue states at a pre-malignant state. This is of importance as early diagnosis of dysplasia or adenocarcinoma allows preventative therapy to be initiated and can substantially affect patient quality of life and survival rate.

While the capability to accurately visualize Barrett's is significant and has several important implications for the use of OCT as a medical diagnostic imaging modality, the demonstration to also detect early dysplastic changes would be a highly monumental achievement in the field of gastrointestinal endoscopy. One difficulty in demonstrating this capability is the scarcity of patients that have diagnoses of low grade or high grade dysplasia. As dysplasia is typically not visible by standard endoscopy and due to high sampling error rates the chance to image dysplastic areas, as well as the availability of diagnosed patients with this stage of disease progression, is low. Furthermore upon detection of high grade dysplasia or adenocarcinoma the recommended patient protocol usually involves surgical resection or interventional therapy to remove the diseased tissue. This allows only a small time window within which the patient may be available for imaging.

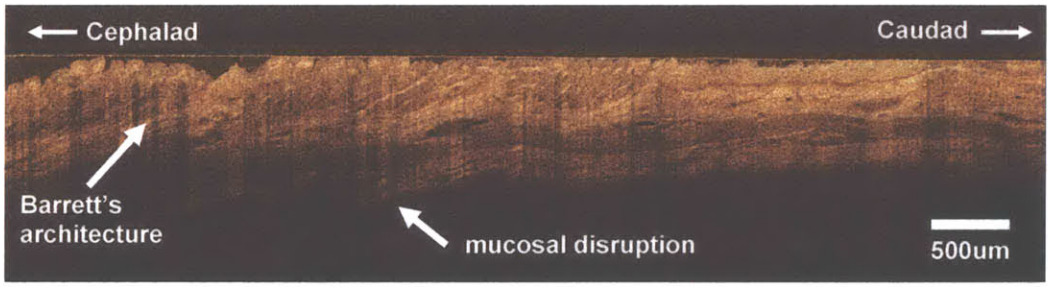

Figure 6-38. Region of metaplasia visualized with OCT

Gastric-like villous architecture is seen in regions distal to the stomach. Disruption of the muscularis mucosa is observed in the area showing transition region between metaplastic tissue states. Composite image from four sequential OCT scans. Patient ID 5-2.

Fortunately in the studies conducted in this work there existed multiple opportunities to image patients diagnosed with varying stages of dysplasia as well as adenocarcinoma. Having access to these pathologies allowed a comparison to be made from the previous imaging results

of patients with Barrett's to determine what characteristics in the OCT images were differentiable and indicative of dysplasia. Shown in Figure 6-38 is a large area scan of a region of obvious metaplasia in a patient that was diagnosed with low grade dysplasia.

Of immediate note is the highly gastric-like architecture in the esophagus that exists *distal* to the stomach (cephalad direction) in the region of Barrett's. Normally tissue characteristic of the gastric mucosa would be localized just below the gastroesophageal junction. Furthermore in a healthy patient the esophagus would have the squamous epithelium with layered structuring of the lamina propria and muscularis mucosa. What is seen in this patient with dysplasia however is a glandular tissue architecture that is more significantly advanced in the metaplastic tissue transformation process. This morphology is appreciably more distinct than the scattering regions seen in OCT images of Barrett's esophagus observed above. Disruptions of both the muscularis mucosa and lamina propria are evident indicating the disease stage is of concern.

Figure 6-39. Imaging of nodule with high grade dysplasia

a) Endoscopic view of esophagus with OCT catheter placed to image dysplastic nodule. b) OCT image of dysplastic nodule showing dense tissue structure with highly disrupted glandular morphology. Composite image from two sequential OCT scans. Patient 10-4.

A particularly valuable endoscopy case was one where the patient was diagnosed with both high grade dysplasia and adenocarcinoma of the esophagus. Shown in Figure 6-39 is an endoscopic view of a dysplastic nodule with the OCT imaging catheter placed on it and the corresponding image of the nodule. It was fortunate to have a highly discrete landmark from which to image and obtain a biopsy specimen with a high degree of precision. In the OCT image the nodule region is seen to have several characteristics that are distinct and indicative of a dysplastic tissue region

A cap region of dense, highly amorphous tissue is present near the surface of the nodule while the interior region exhibits a highly disrupted morphology with a scattered network of glandular components. No uniform layers of epithelium or muscularis mucosa are present. In addition there are no highly scattering centers or localized regions of gastric-like architecture as observed in OCT images of Barrett's. Figure 6-40 shows an OCT image and corresponding

histological cross section of the nodule region diagnosed with adenocarcinoma. The high glandular density and disrupted architecture is apparent in both the OCT and histology.

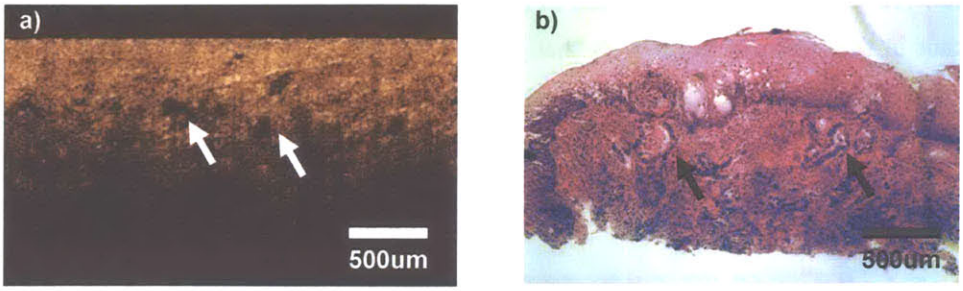

Figure 6-40. OCT image and histopathology of high grade dysplasia

The OCT image shows a squamous upper region with disrupted glands in a shotgun pattern below the surface. b) The corresponding histology diagnosed with high grade dysplasia and adenocarcinoma exhibits increased nuclear proliferation and sub-epithelial glands. No layering of the lamina or muscularis is apparent in either image Patient ID 10-4.

Imaging other areas in the same patient yielded OCT images exhibiting similar characteristics of the dysplastic nodule indicating that a large area of the esophagus was affected by the disease progression. Figure 6-41 shows two OCT images taken within the esophagus (a) and at the gastroesophageal junction (b). Both images are further distal from the nodule region imaged in Figure 6-39 and Figure 6-40. High gland density with a scattered shotgun distribution is visible with no discernible layers of esophageal mucosa. In Figure 6-41a a small region located distal to the stomach shows some epithelial characteristics but contains dysplastic structure underneath. This may be a region of epithelial regrowth or a small region that is not yet affected by the dysplastic tissue growth. In Figure 6-41b a very sharp Z-line transition can be seen at the GE junction however what is significant is that the dysplastic-like architecture seems to be present at the junction region. This indicates that the patient may have a severe and long-term reflux condition that has resulted in a metaplastic change of the esophageal tissue.

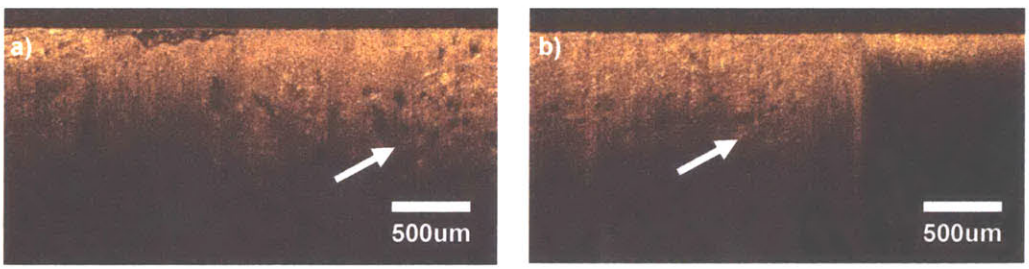

Figure 6-41. OCT imaging of regions with possible high grade dysplasia

a) Region of dysplastic tissue within the esophagus. b) Transition across the GE junction shows tissue architecture indicative of dysplasia. Patient ID 10-4.

One area of interest that was imaged in the patient with HGD had a suspicious distension that was apparent just below the tissue surface. This area also exhibited the dense tissue structure with scattered glandularity (arrows) seen in the previous high grade dysplasia images. What is significant in this scenario however is that just above and surrounding the suspect region is somewhat normal appearing epithelial tissue exhibiting diffuse and uniform scattering properties. The ability for OCT to detect this sub-surface lesion has important implications for localized cancer detection in scenarios where dysplasia is not as pronounced or profuse as was observed in this patient.

Figure 6-42. OCT image of region with possible high grade dysplasia
A dense nodule is seen below the tissue surface localized within a region of squamous epithelium. Patient ID 10-4.

Several biopsies were taken from the dysplastic regions seen in the patient under consideration. After 50 days the patient was brought back to the clinic for a follow-up endoscopy procedure and to determine if a surgical option was necessary. OCT imaging was again conducted during the procedure and the imaging results indicated the strong likelihood of high grade dysplasia existing at several locations within the esophagus. As the nodule imaged in the previous procedure provided a distinct landmark from which to reference the imaging, the same region from which the biopsies were taken was imaged in this follow-up procedure.

Shown in Figure 6-43 are two OCT images of the tissue. It is exciting to note that while some re-epithelialization has occurred in the surrounding tissue, there exist regions where the tissue disruption and scattering properties would indicate the presence of residual Barrett's tissue. It can be seen that the sub-epithelial disruption seen in Figure 6-43b (arrows) is similar is structure to the disruption seen previously in Figure 6-37. It may be possible that while removal of the dysplastic tissue was achieved with the biopsy procedure, the residual Barrett's tissue remaining may cause reoccurrence of dysplasia at a later stage. This region could be imaged at a later date to follow up for diagnostic assessment. An endoscopic view is shown in Figure 6-44.

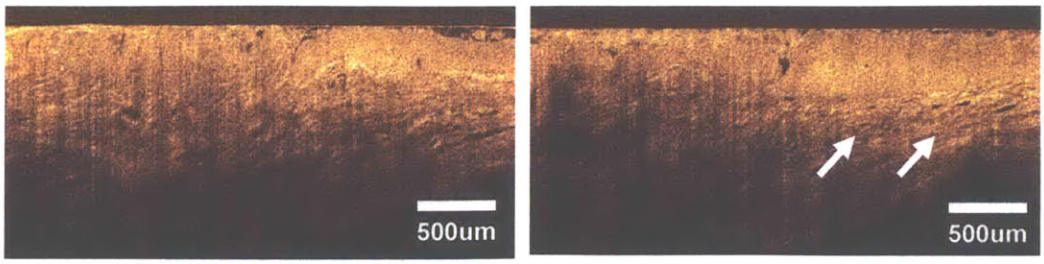

Figure 6-43. Imaging of previous dysplastic region after biopsy

Despite re-epithelialization of surrounding tissue after biopsy, sub-surface disruption and scattering characteristics indicate that residual Barrett's tissue may be present. Patient ID 10-7.

When these images are compared across multiple patients, the scattered glandular regions with dense tissue structure are seen as well. In a separate patient a similar OCT result was obtained with the patient biopsy diagnosed as low grade dysplasia. As can be seen in the OCT and histopathology shown in Figure 6-45 show similar characteristics to the low scattering glandular features seen in Figure 6-40 and Figure 6-41. The correlated endoscopy view of the region imaged is shown in Figure 6-46 with an enlarged region of interest shown to the right.

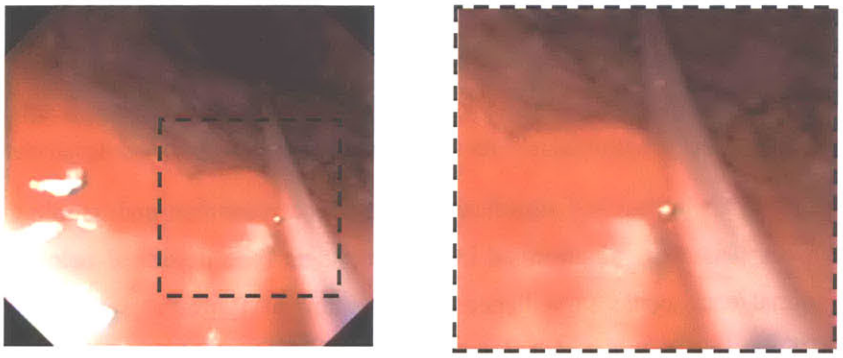

Figure 6-44. Endoscopic view of post-biopsy region imaged in Figure 6-43

A re-epithelialized nodular area is visible in the endoscopic view of the region imaged.

While these regions of low scattering structures are interesting and appear to be consistent across multiple patients with low grade and high grade dysplasia, it should be noted that due to the small number of patient cases with diagnosed dysplasia (n=4), additional investigation is necessary to confirm these initial finding. What is apparent however is that these dysplastic tissue regions exhibit unique scattering properties when compared to OCT images of Barrett's esophagus. This allows an initial baseline of imaging criteria to be established for further investigation of Barrett's and dysplasia using the high resolution OCT systems used in this work.

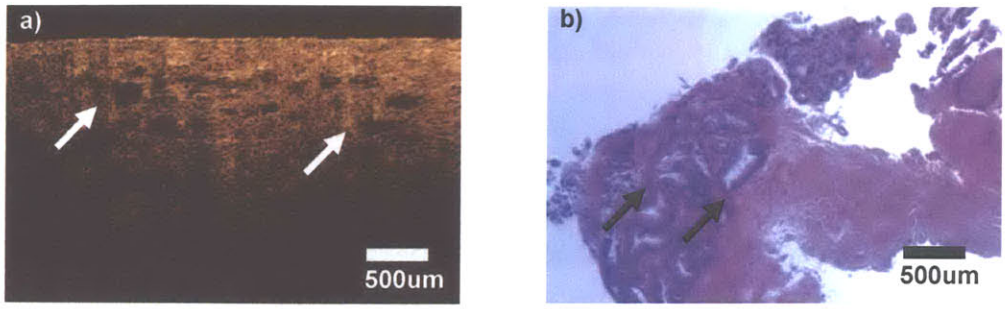

Figure 6-45. OCT image and histopathology of low grade dysplasia

a) Localized regions of dark gland structures in a scattered configuration are seen in the OCT iamge. b) The corresponding histology shows increased glandular density for a low grade dyzsplasia diagnosis. Patient ID 15-7.

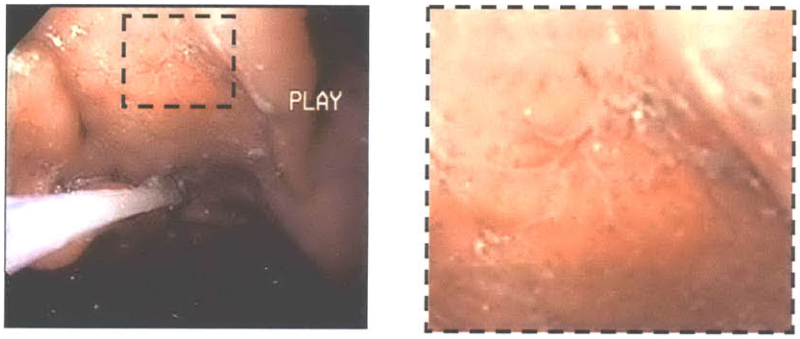

Figure 6-46. Endoscopic view of region imaged in Figure 6-45

A small region of disrupted tissue in the tissue imaged is visible in the endoscope view.

The diagnostic impact and significance of the high resolution endoscopic OCT system built in this work was also demonstrated in a final patient case described below. The patient underwent normal endoscopic surveillance for screening of Barrett's esophagus. During the procedure OCT imaging was recorded simultaneously with video endoscopy images to correlate the OCT image location to position within the esophagus. Under routine visual examination, no regions were seen to be suspect within the patient's esophagus. During the procedure however, the OCT images picked up an area that looked highly suspect of disrupted and atypical architecture. Figure 6-47 shows the OCT image captured during rapid acquisition and corresponding endoscopic video capture of the same region. It should be noted that the area of interest was initially recognized as being suspect from the OCT images and not by the video camera view of the endoscope. Only after the area was identified, the endoscope was passed forward past the area and retroflexed back upon itself in the cephalad direction (towards the patient's head) to view the region within a stomach of the patient. This is clear in the video capture picture as the endoscope body can be seen in the upper left portion of the image. The

suspect region of interest (arrows in Figure 6-47b) was seen to have a discolored surface appearance that warranted further investigation.

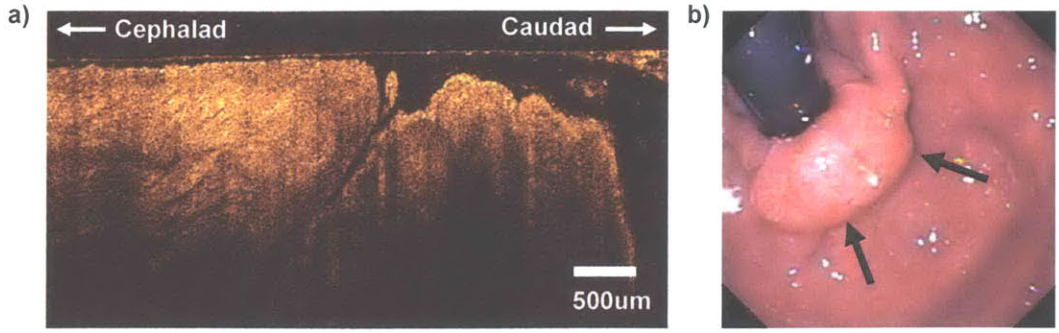

Figure 6-47. Endoscopic view and OCT image of suspect region

An unusual tissue architecture is observed across the boundary of patient's haital hernia. Patient ID 12-6.

After identifying this region as a site or significantly altered tissue architecture, the endoscope was withdrawn backwards from the position shown in Figure 6-47b and the OCT catheter was placed across the junction. The area was imaged in multiple cross-sectional planes, one of which is shown in Figure 6-48. On the left side of the image a relatively normal appearing squamous region can be seen that extends up to a fold in the tissue that exists at the junction (vertical arrow) between the esophagus and stomach. Below the squamous region there is a relatively large area of tissue 500um wide by 250um thick that appears dense and may be a metaplastic nodule below the squamous epithelium. On the distal side of the junction, the tissue architecture is highly disrupted with low scattering regions of tissue branching and localized areas of small glands.

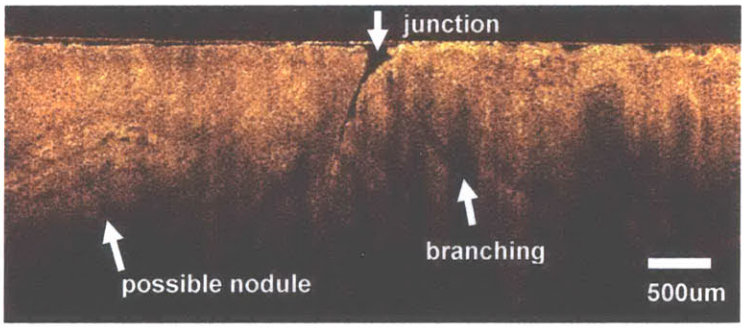

Figure 6-48. OCT image across suspect region across the hiatal hernia junction

Further investigation shows branching structures beneath the surface and an are of dense tissue that may be a sub-epithelial nodule. Patient ID 12-6.

It was apparent from the OCT images obtained during the procedure that this area within the patient was highly unusual. Further interrogation was conducted and imaging of the lesion across a larger area was done. Figure 6-49 shows a composite image formed of 3 sequential OCT scans spanning 6-7mm across the junction. What is can be seen in the high resolution image is a transition from a somewhat disrupted architecture at left to a highly metaplastic tissue morphology on the right. The ability to see the detailed structure of this metaplastic transition is empowering in that it is possible to qualify how severe the tissue progression towards dysplasia.

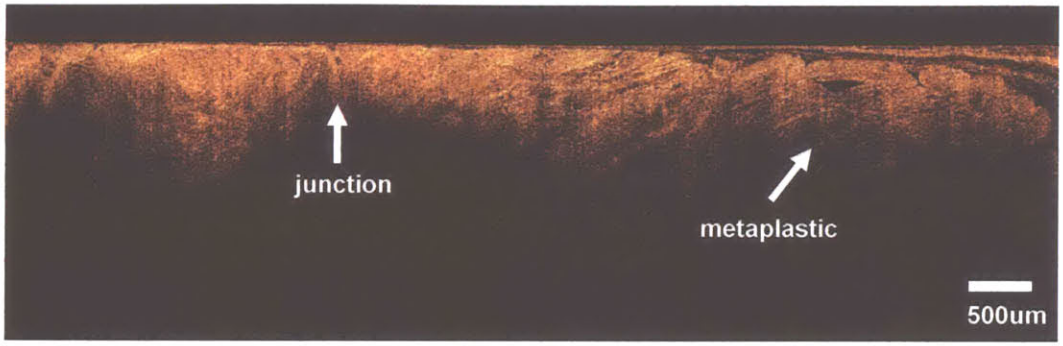

Figure 6-49. Interrogation of suspect region across a large area

The suspect region shows metaplastic tissue architecture with villous-like composition. Combined image from four sequential OCT scans. Patient ID 12-6.

The glandularity and villous appearance of the distal tissue region indicates that there is a strong possibility of dysplasia at this area within the patient. Figure 6-50 shows an enlarged view of the dysplastic region which allows clear visualization of low scattering areas within the glandular architecture. This scattered architecture is consistent with previously observed OCT images of dysplasia as shown in Figure 6-39 and Figure 6-40.

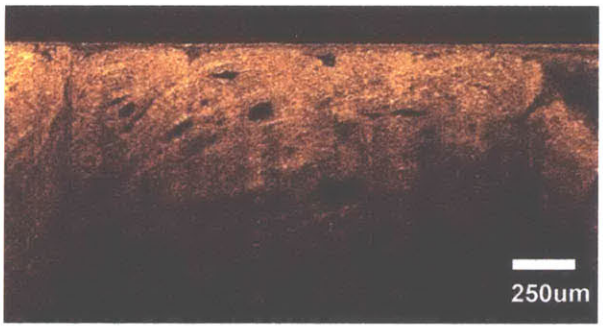

Figure 6-50. Enlarged view of metaplastic region

Scattered glandular structures and low scattering indicative of previously observed dysplastic tissue are observed in the OCT image. Patient ID 12-6.

Two endoscopic views of this region imaged are shown in Figure 6-51. Of interest and note is the web-like network seen clearly in the image. This mesh appearance in the tissue surface was observed previously in this study. In particular, a very similar pattern was observed under magnification endoscopy for the patient diagnosed with high grade dysplasia and adenocarcinoma (Patient ID 10-4).

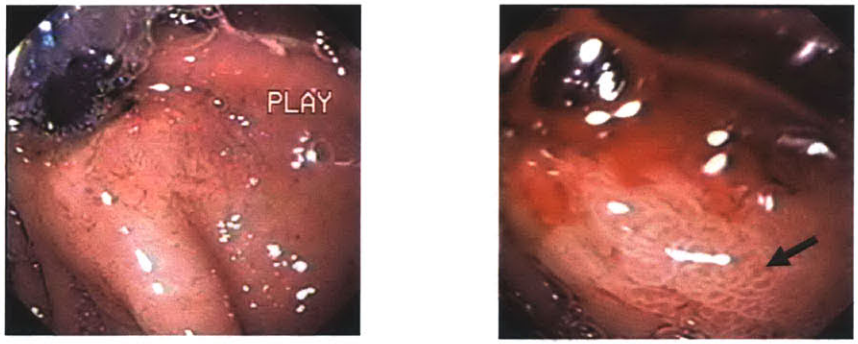

Figure 6-51. Endoscope views of metaplastic region

An interesting mesh pattern was observed on the region suspected to have dysplasia. This pattern was consistent with a previous patient diagnosed with HGD and cancer. Patient ID 12-6.

A magnification endoscopy view of Patient 10-4 exhibiting a similar mesh-like network on the tissue surface is shown in Figure 6-52. These mucosal patterns have been investigated with magnification endoscopy techniques and have been shown to correlate to the presence of intestinal metaplasia [55]. The ability of OCT to visualize significant architectural differences indicative of these regions may be useful in their diagnosis as it is difficulty to see these areas during normal endoscopic procedures.

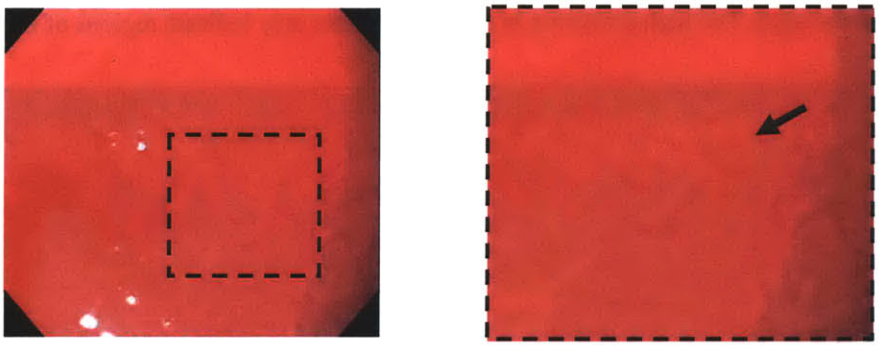

Figure 6-52. Endoscopic view of previous mesh pattern in HGD patient

Under magnification endoscopy a mesh-like pattern in the tissue surface was observed. Biopsies from this pateint in this region were diagnosed with high grade dysplasia and adenocarcinoma. Patient ID 10-4.

Conducting further imaging slightly beyond the tissue junction region and further into the stomach, a region of interesting architecture was observed. Figure 6-53 shows this area to have a villous appearance similar to the lower atrium of the stomach where the tissue architecture is adapted to high levels of acid secretion. In the OCT image it can be seen that there are areas of high scattering across the tissue. These high scattering areas are indicative of fibrosis and are likely the regenerative response of the tissue in response to esophageal reflux and damage. The tissue morphology here and its close proximity to the metaplastic region strengthens the hypothesis that the region shown near the junction in Figure 6-49 and Figure 6-50 may be dysplastic.

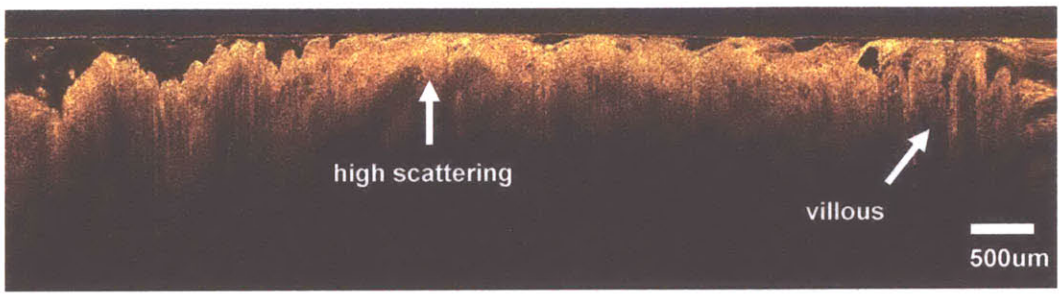

Figure 6-53. Imaging of tissue beyond the esophageal junction

Regions of high scattering within gastric like architecture may be indicative of fibrotic tissue formed during tissue regenreation. Composite image from four sequential OCT scans. Patient ID 12-6.

It is interesting to note that these regions of high scattering with gastric like architecture and low depth penetration were also observed in previous patients. One patient in particular had a history of chronic gastritis with active inflammation and reactive epithelial changes observed in esophageal biopsy specimens. Shown in Figure 6-54 are image scans taken over surface lesions within the esophagus. The high scattering in the OCT images may indicate regions of fibrosis.

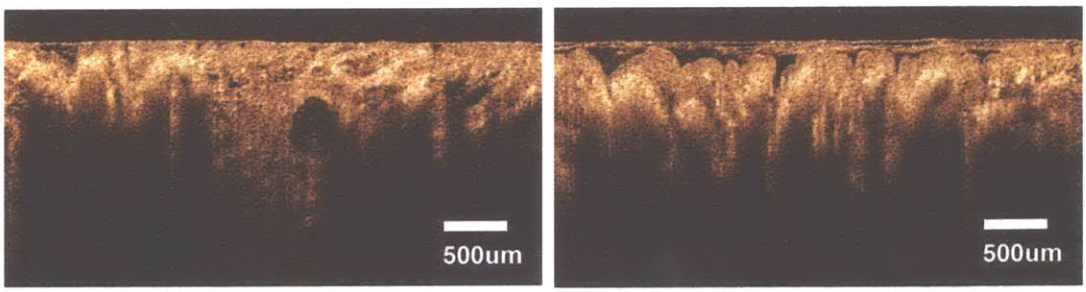

Figure 6-54. Regions of high scattering may indicate tissue fibrosis

Highly scattering surface within the OCT images may be indicative of tissue fibrosis during regeneration and correlated to surface lesions. Patient ID 13-6.

The corresponding endoscopic view of the area visualized in the OCT images of Figure 6-54 is shown in Figure 6-55. The whitish area in the lower left portion of the CCD camera field was subsequently imaged and corresponds to the OCT images shown above in Figure 6-54.

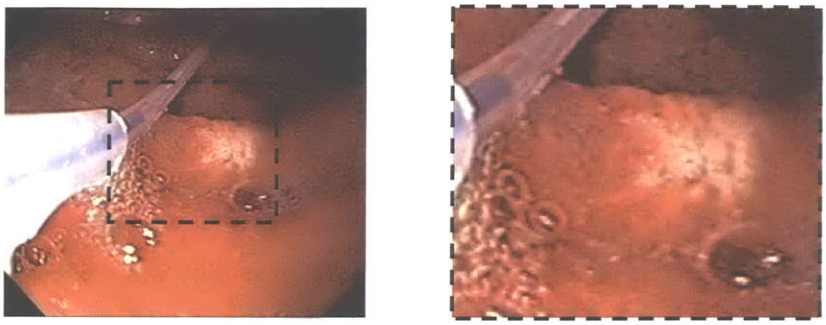

Figure 6-55. Corresponding endoscope view for OCT images in Figure 6-54

The whitish region in the endoscope image may indicate tissue fibrosis and correlate to the high scattering regions seen in the OCT iamges.

Several imaging passes were made of the suspect region to visualize the full extent of the dysplastic area. In one of the cross-sectional scans across the junction a highly porous morphology was observed in the high resolution OCT image. The area had a flaky and friable consistency which is similar to previous observations in patients with esophageal adenocarcinoma. Cancerous tissue and nodules are very loosely attached to the tissue lamina and can easily crumble or be perforated when touched with a catheter or endoscope biopsy forceps. While conclusive determination is currently not possible due to the small number of cases seen, this mesh-like network of tissue is very fine and would likely be missed using standard resolution OCT systems. In addition as the area is highly localized, it would be very difficult to locate and identify using standard endoscopy techniques.

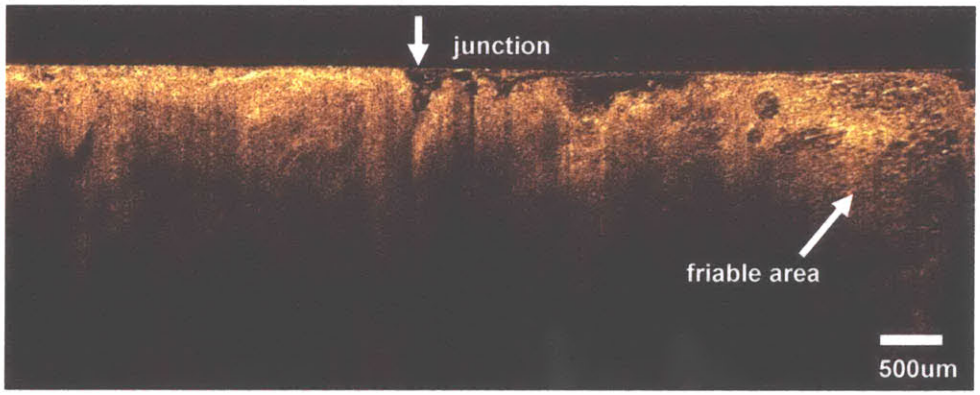

Figure 6-56. OCT image across suspect region with friable texture

Friable region seen may be indicative of a serious disease state. Composite image from three sequential OCT scans. Patient ID 12-6.

Summary

In this study the clinical implementation and demonstration of ultrahigh resolution endoscopic OCT imaging was achieved. Successful transition of the systems from the laboratory setting was completed and a range of disease pathologies were imaged in 20 human subjects. Identification of both normal tissue architecture within the esophagus and stomach was possible with high degrees of correlation with standard histological cross sections, the current gold standard used for disease diagnosis. Imaging results indicated the clear ability of ultrahigh resolution OCT to distinguish with increased fidelity the tissue architectures within the esophagus and stomach regions of the human gastrointestinal tract. The ability to differentiate Barrett's esophagus, a pre-cancerous tissue state, at varying degrees of severity was shown as well as the ability to effectively visualize highly localized regions that would be difficult to see endoscopically.

Significantly, disrupted architectural features with corresponding histology diagnosed with low grade and high grade dysplasia were also identified. While the lack of a large data set of dysplastic patient cases and difficulty with exact biopsy site correlation made it difficult to conduct quantitative statistical analyses, definitive changes in tissue structure were identified with the high resolution OCT system. These changes were distinct from both normal esophagus and gastric tissue as well as differentiated from observed and correlated OCT images of Barrett's esophagus.

Additional morphological features such as sub-epithelial cystic dilations, tissue re-epithelialization over Barrett's' tissue, and highly scattering fibrotic tissue were also imaged in detail. These pathologies may provide additional insight to the progression and treatment of Barrett's esophagus. The ability to detect these architectures, localize and diagnose Barrett's esophagus, and identify regions of possible early dysplasia before the development of esophageal adenocarcinoma could significantly improve patient prognosis and quality of life through early intervention and treatment.

References

1. A. Jemal, T. Murray, A. Samuels, A. Ghafoor, E. Ward, and M. J. Thun, "*Cancer statistics, 2003,*" CA Cancer J Clin, **53**, 5-26 (2003).
2. M. A. Eloubeidi, R. K. Homan, M. D. Martz, K. E. Theobald, and D. Provenzale, "*A cost analysis of outpatient care for patients with Barrett's esophagus in a managed care setting,*" American Journal of Gastroenterology, **94**, 2033-6 (1999).
3. E. Bollschweiler, E. Wolfgarten, C. Gutschow, and A. H. Holscher, "*Demographic variations in the rising incidence of esophageal adenocarcinoma in white males,*" Cancer, **92**, 549-555 (2001).
4. S. Haag and G. Holtmann, "*Reflux disease and Barrett's esophagus,*" Endoscopy, **35**, 112-7 (2003).
5. J. Winters, C. and e. al., "*Barrett's esophagus. A prevalent, occult complication of gastroesophageal reflux disease,*" Gastroenterology, **92**, 118-124 (1987).
6. G. M. Eisen, R. S. Sandler, S. Murray, and M. Gottfried, "*The relationship between gastroesophageal reflux disease and its complications with Barrett's esophagus,*" American Journal of Gastroenterology, **92**, 27-31 (1997).
7. D. A. Lieberman, M. Oehlke, and M. Helfand, "*Risk factors for Barrett's esophagus in community-based practice,*" American Journal of Gastroenterology, **92**, 1293-1297 (1997).
8. R. E. Sampliner, "*Updated guidelines for the diagnosis, surveillance, and therapy of Barrett's esophagus,*" American Journal of Gastroenterology, **97**, 1888-1895 (2002).
9. M. Conio, G. Lapertosa, S. Blanchi, and R. Filiberti, "*Barrett's esophagus: an update,*" Critical Reviews in Oncology Hematology, **46**, 187-206 (2003).
10. R. W. Phillips and R. K. H. Wong, "*Barrett's esophagus: natural history, incidence, etiology, and complications,*" Gastro. Clinics of North America, **20**, 791-815 (1991).
11. "*http://pathology2.jhu.edu/beweb/menu_understanding.cfm,*"
12. A. L. Taylor, "*The epithelial heterotopias of the alimentary tract,*" J. Pathol. Bacteriol., **30**, 415-449 (1927).
13. M. H. Johnston, A. S. Hammond, W. Laskin, and D. M. Jones, "*The prevalence and clinical characteristics of short segments of specialized intestinal metaplasia in the distal esophagus,*" Gastroenter., **91**, 1507-1511 (1996).
14. G. W. Falk, "*Barrett's Esophagus,*" Gastroenter., **122**, 1569-1591 (2002).
15. Y. Romero, A. J. Cameron, D. J. Schaid, S. K. McDonnell, L. J. Burgart, C. L. Hardtke, J. A. Murray, and G. Locke, "*Barrett's Esophagus: Prevalence in SYmptomatic Relatives,*" Am. J. Gastroenterol., **97**, 1127-1132 (2002).
16. W. K. Hiroto, T. M. Loughney, D. J. Laza, C. L. Maydonovitch, V. Rholl, and R. K. Wong, "*Specialized instestinal metaplasia, dysplasia, and cencer of the esophagus and esophagogastric junction: prevelance and clinical data,*" Gastroenter., **116**, 227-285 (1999).
17. M. Moreto, "*Diagnosis of Esophagogastric Tumors,*" Endoscopy, **35**, 36-42 (2003).
18. C. P. Wild and L. J. Hardie, "*Reflux, Barrett's oesophagus and adenocarcinoma: Burning questions,*" Nature Reviews Cancer, **3**, 676-684 (2003).
19. R. H. Riddell and F. R. C. Path, "*Premalignant and early malignant lesions in the gastrointestinal tract: Definitions, terminology, and problems,*" American Journal of Gastroenterology, **91**, 864-872 (1996).
20. N. S. Buttar, K. K. Wang, T. J. Sebo, D. M. Riehle, K. K. Krishnadath, L. S. Lutzke, M. A. Anderson, T. M. Petterson, and L. J. Burgart, "*Extent of high-grade dysplasia in Barrett's esophagus correlates with risk of adenocarcinoma,*" Gastroenterology, **120**, 1630-1639 (2001).
21. B. J. Reid, D. S. Levine, G. Longton, P. L. Blount, and P. S. Rabinovitch, "*Predictors of progression to cancer in Barrett's esophagus: Baseline histology and flow cytometry identify low- and high-risk patient subsets,*" American Journal of Gastroenterology, **95**, 1669-1676 (2000).
22. B. F. Overholt, M. Panjehpour, and J. M. Haydek, "*Photodynamic therapy for Barrett's esophagus: follow-up in 100 patients,*" Gastrointestinal Endoscopy, **49**, 1-7 (1999).

23. S. J. Spechler, A. H. Robbins, H. B. Rubins, M. E. Vincent, T. Heeren, W. G. Doos, T. Colton, and E. M. Schimmel, "*Adenocarcinoma and Barrett's esophagus. An overrated risk?,*" Gastroenterology, **87**, 927-933 (1984).
24. A. J. Cameron, B. J. Ott, and W. S. Payne, "*The incidence of adenocarcinoma in columnar-lined (Barrett's) esophagus,*" N Engl J Med, **313**, 857-859 (1989).
25. W. Hameeteman, G. Tytgat, and H. J. Hoffman, "*Barrett's esophagus: Development of dysplasia and adenocarcinoma,*" Gastroenter., **96**, 1249-1256 (1989).
26. A. J. Cameron, A. R. Zinsmeister, D. J. Ballard, and J. A. Carney, "*Prevalence of Columnar-Lined (Barrett) Esophagus - Comparison of Population-Based Clinical and Autopsy Findings,*" Gastroenterology, **99**, 918-922 (1990).
27. A. J. Cameron, B. J. Ott, and W. S. Payne, "*The incidence of adenocarcinoma in columnar-lined (Barrett's)esophagus,*" New England Journal of Medicine, **313**, 857-859 (1985).
28. M. G. Sarr, S. R. Hamilto, G. C. Marrone, and J. L. Cameron, "*Barrett's esophagus: its prevelance and association with adenocarcinom in patients with symptoms of gastroesophageal reflux,*" Am J Surg, **149**, 187-193 (1985).
29. R. C. Fitzgerald, I. T. Saeed, D. Khoo, M. J. G. Farthing, and W. R. Burnham, "*Rigorous surveillance protocol increases detection of curable cancers associated with Barrett's esophagus,*" Digestive Diseases and Sciences, **46**, 1892-1898 (2001).
30. P. Rozen, M. Baratz, F. Fefer, and T. Gilat, "*Low incidence of significant dysplasia in a successful endoscopic surveillance program of patients with ulcerative colitis,*" Gastroenter., **108**, 1361-1370 (1995).
31. A. T. Axon, "*Cancer surveillance in ulcerative colitis-- a time for reappraisal,*" Gut, **35**, 587-589 (1994).
32. A. J. Cameron and H. A. Carpenter, "*Barrett's Esophagus, High-Grade Dysplasia, and Early Adenocarcinoma: A Pathological Study,*" Am. J. Gastroenterol., **92**, 586-591 (1990).
33. I. A. Scotiniotis, M. L. Kochman, J. D. Lewis, E. E. Furth, E. F. Rosato, and G. G. Ginsberg, "*Accuracy of EUS in the evaluation of Barrett's esophagus and high-grade dysplasia or intramucosal carcinoma,*" Gastrointestinal Endoscopy, **54**, 689-696 (2001).
34. P. Fockens, "*Future developments in endoscopic imaging,*" Best Practice & Research Clinical Gastroenterology, **16**, 999-1012 (2002).
35. G. J. Tearney, M. E. Brezinski, B. E. Bouma, S. A. Boppart, C. Pitvis, J. F. Southern, and J. G. Fujimoto, "*In vivo endoscopic optical biopsy with optical coherence tomography,*" Science, **276**, 2037-9 (1997).
36. A. M. Sergeev, V. M. Gelikonov, G. V. Gelikonov, F. I. Feldchtein, R. V. Kuranov, N. D. Gladkova, N. M. Shakhova, L. B. Snopova, A. V. Shakov, I. A. Kuznetzova, A. N. Denisenko, V. V. Pochinko, Y. P. Chumakov, and O. S. Streltzova, "*In vivo endoscopic OCT imaging of precancer and cancer states of human mucosa,*" Optics Express, **1**, 432 (1997).
37. B. E. Bouma and G. J. Tearney, "*Power-efficient nonreciprocal interferometer and linear-scanning fiber-optic catheter for optical coherence tomography,*" Optics Letters, **24**, 531-3 (1999).
38. A. M. Rollins, R. Ung-arunyawee, A. Chak, R. C. K. Wong, K. Kobayashi, M. V. Sivak, Jr., and J. A. Izatt, "*Real-time in vivo imaging of human gastrointestinal ultrastructure by use of endoscopic optical coherence tomography with a novel efficient interferometer design,*" Optics Letters, **24**, 1358-60 (1999).
39. M. V. Sivak, K. Kobayashi, J. A. Izatt, A. M. Rollins, R. Ung-runyawee, A. Chak, R. C. K. Wong, G. A. Isenberg, and J. Willis, "*High-resolution endoscopic imaging of the GI tract using optical coherence tomography,*" Gastrointestinal Endoscopy, **51**, 474-479 (2000).
40. B. E. Bouma, G. J. Tearney, C. C. Compton, and N. S. Nishioka, "*High-resolution imaging of the human esophagus and stomach in vivo using optical coherence tomography,*" Gastrointestinal endoscopy, **51(4) Pt 1**, 467-74 (2000).
41. X. D. Li, S. A. Boppart, J. Van Dam, H. Mashimo, M. Mutinga, W. Drexler, M. Klein, C. Pitris, M. L. Krinsky, M. E. Brezinski, and J. G. Fujimoto, "*Optical coherence tomography: advanced technology for the endoscopic imaging of Barrett's esophagus,*" Endoscopy, **32**, 921-30 (2000).
42. S. Jäckle, N. Gladkova, F. Feldchtein, A. Terentieva, B. Brand, G. Gelikonov, V. Gelikonov, A. Sergeev, A. Fritscher-Ravens, J. Freund, U. Seitz, S. Schröder, and N. Soehendra, "*In vivo*

endoscopic optical coherence tomography of esophagitis, Barrett's esophagus, and adenocarcinoma of the esophagus," Endoscopy, **32**, 750-5 (2000).

43. S. Jäckle, N. Gladkova, F. Feldchtein, A. Terentieva, B. Brand, G. Gelikonov, V. Gelikonov, A. Sergeev, A. Fritscher-Ravens, J. Freund, U. Seitz, S. Soehendra, and N. Schrödern, *"In vivo endoscopic optical coherence tomography of the human gastrointestinal tract--toward optical biopsy,"* Endoscopy, **32**, 743-9 (2000).
44. A. Das, M. V. Sivak, Jr., A. Chak, R. C. Wong, V. Westphal, A. M. Rollins, J. Willis, G. Isenberg, and J. A. Izatt, *"High-resolution endoscopic imaging of the GI tract: a comparative study of optical coherence tomography versus high-frequency catheter probe EUS,"* Gastrointestinal endoscopy, **54**, 219-24 (2001).
45. I. Cilesiz, P. Fockens, R. Kerindongo, D. Faber, G. Tytgat, F. Ten Kate, and T. Van Leeuwen, *"Comparative optical coherence tomography imaging of human esophagus: how accurate is localization of the muscularis mucosae?,"* Gastrointestinal Endoscopy, **56**, 852-7 (2002).
46. G. Zuccaro, N. Gladkova, J. Vargo, F. Feldchtein, E. Zagaynova, D. Conwell, G. Falk, J. Goldblum, J. Dumot, J. Ponsky, G. Gelikonov, B. Davros, E. Donchenko, and J. Richter, *"Optical coherence tomography of the esophagus and proximal stomach in health and disease,"* American Journal of Gastroenterology, **96**, 2633-9 (2001).
47. J. Poneros, S. Brand, and B. Bouma, *"Diagnosis of specialized intestinal metaplasia by optical coherence tomography,"* Gastroenterology, **120**, 7-12 (2001).
48. P. R. Pfau, M. V. Sivak, A. Chak, M. Kinnard, R. C. K. Wong, G. A. Isenberg, J. A. Izatt, A. Rollins, and V. Westphal, *"Criteria for the diagnosis of dysplasia by endoscopic optical coherence tomography,"* Gastrointestinal Endoscopy, **58**, 196-202 (2003).
49. *"http://www.udel.edu/Biology/Wags/histopage/colorpage/colorpage.htm,"*).
50. A. M. Rollins, R. Ung-arunyawee, A. Chak, C. K. Wong, K. Kobayashi, M. V. Sivak, and J. A. Izatt, *"Real-time in vivo imaging of human gastrointestinal ultrastructure by use of endoscopic optical coherence tomography with a novel efficient interferometer design,"* Optics Letters, **24**, 1358-1360 (1999).
51. J. L. Boulnois, *" Photophysical processes in recent medical laser development: A review,"* Lasers Med. Sci., **1**, 47-66 (1986).
52. *"http://www-medlib.med.utah.edu/WebPath/GIHTML/GI194.html,"*).
53. D. W. Fawcett, *The esophagus and stomach.* 11 ed, ed. D.W.F. W. Bloom. 1986, Philidelphia: Sanders.
54. S. Jackle, N. Gladkova, F. Feldchtein, A. Terentieva, B. Brand, G. Gelikonov, V. Gelikonov, A. Sergeev, A. Fritscher-Ravens, J. Freund, U. Seitz, S. Schroder, and N. Soehendra, *"In vivo endoscopic optical coherence tomography of esophagitis, Barrett's esophagus, and adenocarcinoma of the esophagus,"* Endoscopy, **32**, 750-5 (2000).
55. M. Guelrud and E. E. Ehrlich, *"Endoscopic classification of Barrett's esophagus,"* Gastrointest Endoscopy, **59**, 58-65 (2004).

Chapter 7 – Conclusion

Summary and Conclusions

This research has successfully demonstrated the design, construction, and implementation of high resolution OCT systems for minimally invasive diagnostic imaging. The development of system components and their integration with broadband light sources to achieve the high resolution imaging results in a range of tissue and organ systems was demonstrated. *In vivo* imaging of animal models and successful transitioning of OCT technology from the laboratory to the clinical environment was achieved for *in vivo* human imaging trials.

In the introduction of this thesis an overview of current imaging modalities was presented to understand the benefits and drawback of current technology used to visualize and diagnose disease pathologies. OCT was seen to be a potentially significant diagnostic imaging technique as it allows for sub-surface imaging at resolutions greater than possible with other methods.

In the second chapter, the fundamental theory that forms the foundation of OCT was introduced. Relevant imaging parameters and their dependence on the components used in OCT systems was reviewed and optimal configurations implemented for the systems built in this work were discussed. Characteristics of the optical light sources implemented were presented and issues with tissue viability and the motivation to conduct *in vivo* imaging were discussed.

In Chapter 3, System Development and Characterization, the design, characterization, and implementation of multiple OCT systems developed for this work was presented. The source of noise and optimization of signal to noise through heterodyne detection, dual balancing, and electronic filtering was discussed with supporting system characterization data. Factors affecting optimal imaging performance such as dispersion, bandwidth support, and operation of pulsed laser oscillators were discussed. Finally mechanical scanning systems developed and system timing considerations for both hardware and software control were presented.

Chapter 4 presented several of the delivery systems and minimally invasive diagnostic probes developed in this work and implemented in imaging studies. The design and characterization of these devices was shown with a range of instruments from microscopes and handheld devices, to fiber optic catheters and MEMS based scanning chips. The mechanical, electrical, and optical considerations and characterization data was presented.

Moving into the imaging experiments, Chapter 5 presented results from biological studies in animal models. Animal models serve as a more controlled system for *in vivo* experimental imaging and multiple tissue systems were investigated. An extensive study looking at cartilage

degeneration in the rat knee was shown with indication that OCT could track osteoarthritic changes *in vivo*. Imaging of the gastrointestinal tract in a rabbit model was also presented using multiple imaging systems and diagnostic probe devices. Ultrahigh resolution imaging was performed in multiple scan modalities and OCT imaging results achieved excellent correspondence with histopathology sectioning of the tissues. This served as a demonstration and validation of ultrahigh resolution OCT to be capable of visualizing architectural details within the gastrointestinal tract with a high degree of accuracy.

Chapter 6 presented the implementation of the OCT systems from the laboratory into a clinical setting with *in vivo* imaging of Barrett's esophagus and esophageal cancer in humans. The significance of Barrett's was discussed as well as the motivations to develop systems to accurate detect and localize metaplastic tissue within the esophagus. Previous work with endoscopic OCT was reviewed showing representative results and recent findings in the field. Imaging performance of the ultrahigh resolution system was then presented for a range of tissue pathologies covering normal esophagus, the gastric mucosa (stomach), Barrett's esophagus, dysplasia, and adenocarcinoma (cancer). Representative and corresponding histology matches to the OCT imaging results were shown with good correlation of the architecture. It was seen that the high resolution OCT system was capable to clearly identify regions of Barrett's epithelium and distinguish these areas from normal tissue. Even more significantly, OCT images of highly disrupted tissue architecture indicated that the high resolution system was capable to detect low to high grade dysplastic tissue. This is important as previous work with standard resolution OCT has not shown the capability to distinguish the architectural detail associated with dysplasia. Finally the ability of OCT to detect abnormal tissue structures beyond the capability of standard endoscopic procedures was presented. The clear deviation of tissue architecture from a normal state was made apparent in the patient cases and demonstrated the potential to use OCT as an important clinical imaging modality.

Future Directions

The results from this study have demonstrated the great potential to use high resolution OCT as a diagnostic tool to image tissue pathologies. With this criteria established, there exists many opportunities to conduct further studies using OCT in scenarios where minimally invasive imaging plays a critical role. With respect to endoscopic OCT there are projects now underway that plan to look at artificially induced gastrointestinal disease in animal models thereby providing a well controlled system to investigate. In addition further work to optimize correlation between OCT imaging sites *in vivo* and representative biopsy sampling can be done. Studies

looking at the use of specialized therapies for esophageal disease such as photodynamic therapy or effects of diet or lifestyle can be investigated. Blinded studies using increased patient numbers with more cases of dysplasia and adenocarcinoma can provide statistical metrics to evaluate the efficacy of OCT in larger scale studies. Also the use of numerical algorithms to evaluate and grade OCT images holds the potential for rapid interpretation of OCT results and would enable quantitative methods to be employed in OCT imaging studies. With many investigators throughout the world pursuing research in OCT, its use in the diagnosis of clinical disease holds the promise of improved patient care and quality of life.